



DGK Ausschuss Geodäsie (DGK)
der Bayerischen Akademie der Wissenschaften

Reihe C

Dissertationen

Heft Nr. 956

Alexey Kupriyanov

**Investigation of Optical Accelerometry
and Novel Satellite Formations
for Future Gravimetry Missions**

München 2025

Verlag der Bayerischen Akademie der Wissenschaften, München

ISSN 0065-5325

ISBN-978-3-7696-5368-7

Investigation of Optical Accelerometry
and Novel Satellite Formations
for Future Gravimetry Missions

Von der Fakultät für Bauingenieurwesen und Geodäsie
der Gottfried Wilhelm Leibniz Universität Hannover
zur Erlangung des akademischen Grades
Doktor-Ingenieur (Dr.-Ing.)
genehmigte
Dissertation

von

Alexey Kupriyanov, M. Sc. (TUM)

geboren am 21. August 1996 in Moskau

München 2025

Verlag der Bayerischen Akademie der Wissenschaften, München

Adresse des Ausschusses Geodäsie (DGK)
der Bayerischen Akademie der Wissenschaften:



Ausschuss Geodäsie (DGK) der Bayerischen Akademie der Wissenschaften

Alfons-Goppel-Straße 11 • D – 80 539 München
Telefon +49 – 89 – 23 031 1113 • Telefax +49 – 89 – 23 031 - 1283 / - 1100
e-mail post@dgk.badw.de • <http://www.dgk.badw.de>

Prüfungskommission:

Vorsitzender: Prof. Dr.-Ing. Matthias Weigelt
Referent: Prof. Dr.-Ing. habil. Jürgen Müller
Korreferenten: Prof. Dr.-Ing. Nico Sneeuw (Universität Stuttgart)
PD Dr.-Ing. Hamza Alkhatib

Tag der mündlichen Prüfung: 17.02.2025

Diese Dissertation ist auf dem Server des Ausschusses Geodäsie (DGK)
der Bayerischen Akademie der Wissenschaften, München unter <http://dgk.badw.de/>
sowie unter Wissenschaftliche Arbeiten der Fachrichtung Geodäsie und Geoinformatik
der Leibniz Universität Hannover (ISSN 0174-1454), Nr. 406,
unter <https://doi.org/10.15488/19007>, Hannover 2025 elektronisch publiziert

© 2025 Ausschuss Geodäsie (DGK) der Bayerischen Akademie der Wissenschaften, München

Alle Rechte vorbehalten. Ohne Genehmigung der Herausgeber ist es auch nicht gestattet,
die Veröffentlichung oder Teile daraus zu vervielfältigen.

Abstract

Satellite gravimetry provides essential insight into Earth's mass change phenomena and is used in a wide range of applications. However, users and the scientific community need gravimetry data with improved spatio-temporal resolution. Therefore, new instruments and measurement concepts are investigated in this thesis.

Accelerometers (ACCs) are one of the key sensors in spaceborne gravimetry. Depending on the measurement principle, they can sense either the non-gravitational forces or gravity gradients. So far only electrostatic ACCs with increasing noise in the low-frequency domain were utilized in satellite gravimetry missions, restricting their performance. On the other hand, the LISA-Pathfinder mission demonstrated promising results by utilizing a Gravitational Reference Sensor (GRS) – an optical ACC. The test mass displacement in the LISA-Pathfinder GRS is measured by laser interferometry instead of capacitive sensing as in electrostatic sensor.

This study investigates how the gravity field measurements from space can be improved when applying advanced sensors and observation concepts. This dissertation focuses on multiple aspects: 1) Performance evaluation of a modeled wireless Simplified-GRS (SGRS) – an optical ACC, with the parameters based on the LISA-Pathfinder GRS, in spaceborne gravimetry at Low Earth Orbits. 2) Recovering of gravity field models, obtained from different sensors, e.g., Cold Atom Interferometry (CAI), electrostatic, hybrid in low-low Satellite-to-Satellite Tracking (ll-SST) and cross-track gradiometry and comparison w.r.t. each other. 3) Evaluation of different satellite formations that may be applied in subsequent missions. For these purposes, closed-loop simulation procedures were developed and applied in various studies, considering detailed orbital simulations, inertial sensor modeling and Gravity Field Recovery (GFR).

The noise budget of the modeled SGRS optical ACC, including various error sources, achieves $\sim 3 \times 10^{-12} \text{ (m/s}^2\text{)}/\sqrt{\text{Hz}}$ level of accuracy at 1 mHz. GFR simulations show that a combination of this modeled SGRS with the level of accuracy of the inter-satellite Laser Ranging Instrument anticipated for 2033, outperforms other instrument configurations, reduces the spatial residuals down to $\pm 5 \text{ mm}$ Equivalent Water Height (EWH) and shows a significant reduction of the North-South striping artifacts. Novel triple satellite formations demonstrate reducing of the residuals down to $\pm 2.5 \text{ mm}$ EWH. However, these formations present challenges, such as high relative range rates between the satellites in cross-track direction, which requires advancements in current Laser Ranging Interferometer (LRI) systems.

Also, other types of simulations, e.g. cross-track gradiometry, satellites with modified shapes, double-pair Bender constellation, etc. are evaluated in terms of GFR. Technical aspects, such as high-pass filtering for minimizing the impact of the low-frequency components in the modeled SGRS sensor is being discussed. Furthermore, the effect of the common mode gain uncertainty in the gradiometry use case and the scale factor for residual drag in ll-SST configuration are also investigated.

Keywords: Future gravimetry missions, ll-SST, Satellite Gradiometry, Optical accelerometry, Cold Atom Interferometry, Novel inertial sensors, Triple satellite formations

Zusammenfassung

Die Satellitengravimetrie liefert wesentliche Einblicke in die Phänomene der Massenveränderung auf der Erde. Die Anwender und die wissenschaftliche Community benötigen jedoch Gravimetriedaten mit verbesserter räumlicher und zeitlicher Auflösung. Daher werden in dieser Arbeit neue Instrumente und Messkonzepte untersucht.

Beschleunigungsmesser (ACCs) gehören zu den wichtigsten Sensoren in der weltraumgestützten Gravimetrie. Bisher wurden in der Satellitengravimetrie nur elektrostatische ACCs mit ansteigendem Rauschen im Niederfrequenzbereich eingesetzt, was ihre Leistungsfähigkeit einschränkt. Andererseits hat die LISA-Pathfinder-Mission vielversprechende Ergebnisse durch den Einsatz eines Gravitationsreferenzsensors (GRS) - eines optischen ACC - gezeigt. Beim GRS wird die Verschiebung der Testmasse durch Laserinterferometrie anstelle von kapazitiven Sensoren gemessen.

In dieser Studie wird untersucht, wie die Schwerefeldmessungen aus dem Weltraum durch den Einsatz moderner Sensoren und Beobachtungskonzepte verbessert werden können. Die Dissertation befasst sich mit mehreren Aspekten: 1) Der Leistungsbeurteilung eines modellierten drahtlosen vereinfachten GRS (SGRS) - eines optischen ACC, dessen Parameter auf dem Lisa-Pathfinder GRS basieren - für die weltraumgestützte Gravimetrie in erdnahen Umlaufbahnen. 2) Gewinnung von Schwerefeldmodellen, die von verschiedenen Sensoren, z.B. Kaltatominterferometrie (CAI), elektrostatischen, hybriden in ll-SST und Cross-Track-Gradiometrie, gewonnen wurden, und deren Vergleich untereinander. 3) Außerdem werden verschiedene Satellitenformationen bewertet, die bei späteren Missionen eingesetzt werden können. Für diese Zwecke wurde ein Closed-loop Simulationsverfahren entwickelt und angewendet.

Das Rauschbudget des modellierten SGRS optischen ACC, einschließlich verschiedener Fehlerquellen, erreicht $\sim 3 \times 10^{-12} \text{ (m/s}^2\text{)}/\sqrt{\text{Hz}}$ Genauigkeitsniveau bei 1 mHz. Durchgeführte Schwerefeldsimulationen zeigen, dass eine Kombination dieses modellierten SGRS mit dem für 2033 erwarteten Genauigkeitsniveau des Inter-Satellite Laser Ranging Instruments andere Instrumentenkonfigurationen übertreffen, die räumlichen Residuen auf $\pm 5 \text{ mm EWH}$ reduzieren und eine signifikante Reduzierung der in Nord-Süd Richtung verlaufenden Streifen-Effekte zeigen. Die untersuchten neuen Dreifach-Satellitenformationen zeigen eine Reduzierung der Residuen auf bis zu $\pm 2.5 \text{ mm EWH}$. Diese Formationen bringen jedoch Herausforderungen mit sich, wie z. B. hohe Relativgeschwindigkeit zwischen den Satelliten in Querrichtung, die eine Weiterentwicklung der derzeitigen LRI-Systeme erfordern.

Auch andere Arten von Simulationen, z. B. Cross-Track-Gradiometrie, Satelliten mit modifizierten Formen usw. wurden im Hinblick auf die Schwerefeldberechnung bewertet. Technische Aspekte, wie z.B. Hochpassfilterung zur Minimierung des Einflusses der niederfrequenten Komponente im modellierten SGRS-Sensor, werden diskutiert. Weiterhin wurde im Fall der Gradiometrie der Effekt der Common Mode Reduktion untersucht, und für die ll-SST-Konfiguration der Skalierungsfaktor für den Restwiderstand.

Schlagwörter: Zukünftige Schwerefeldmissionen, ll-SST, Satellitengradiometrie, Optische Beschleunigungsmessung, Kaltatominterferometrie, Neuartige Trägheitssensoren, Drei-Satelliten-Formationen

Contents

1	Introduction	1
1.1	Relevance of the Research	1
1.2	Research Questions and Objectives	3
1.3	Thesis Outline	4
2	Fundamentals	5
2.1	Spherical Harmonic Series	5
2.2	Measurement Principles in Satellite Gravimetry	6
2.2.1	High-low Satellite-to-Satellite Tracking	7
2.2.2	Low-low Satellite-to-Satellite Tracking	7
2.2.3	Satellite Gravity Gradiometry	9
2.2.4	Summary of Satellite Gravimetry Measurement Techniques	11
2.3	Amplitude Spectral Density Representation	12
2.4	Least-Squares Adjustment for Spherical Harmonics Estimation . .	15
2.5	Stochastic Modeling	16
2.6	Validation of the Retrieved Gravity Field Models	18
2.7	Regularization of Retrieved Gravity Field Solutions	20
2.8	Combination of Various Retrieved Gravity Field Solutions	22
2.9	Multi-step Integrator of Orbital Dynamics Simulator	22
2.10	Implemented Mathematics of the Accelerometer Modeling Environment	23
2.10.1	Test Mass Dynamics - Assumptions and Physical Model . .	24
2.10.2	Second-Order Integrator in Test Mass Dynamics	25
2.11	Chapter Summary	25
3	Past, Current and Future Satellite Gravimetry Missions and Technologies	27
3.1	Overview of Realised Gravity Missions and LISA-Pathfinder Flight Heritage	27
3.2	Accelerometers Used in Gravimetry Missions	32
3.3	Overview of Upcoming Gravimetry Missions	34
3.4	Novel Electrostatic Accelerometer Concepts	36
3.5	Chapter Summary	39
4	Simulation Procedure and Software Overview	41
4.1	Closed-loop Simulation Procedure	41
4.2	Satellites Dynamics Simulator	44
4.2.1	Environmental Background Models and Non-gravitational Forces	44
4.2.2	Description of the Simulated Orbits	47
4.3	Inertial Sensor Modeling Environment	48
4.3.1	Accelerometers Modeling	48

4.3.2	Gradiometer Modeling	54
4.4	Gravity Field Recovery Software	54
4.4.1	Gravity Field Retrieval for ll-SST Scenarios	55
4.4.2	Gravity Field Retrieval for Cross-track Gradiometry	55
4.5	Chapter Summary	56
5	Amplitude Spectral Densities of the Investigated Instruments	57
5.1	Errors of the Inertial Sensors	57
5.1.1	Filtering of Accelerometer Colored Noise at Low Frequencies	60
5.2	Errors of the Inter-satellite Ranging Instruments	61
5.3	Chapter Summary	62
6	Gravity Field Recovery Results from Simulations	63
6.1	Impact of Stochastic Modeling	63
6.1.1	Colored Noise at Low Frequencies	64
6.1.2	White Noise at Low Frequencies	69
6.2	low-low Satellite-to-Satellite Tracking	73
6.2.1	Performance of Accelerometers and Range Instruments	73
6.2.2	ll-SST Simulations with Time-variable Background Model- ing Errors	77
6.2.3	ll-SST Simulations with Modified Satellites Shapes	82
6.3	Cross-track Satellite Gravity Gradiometry	87
6.3.1	Cross-track SGG Instruments	87
6.3.2	Study of the Common Mode Gain Uncertainty in the SGG case	92
6.3.3	Combination of ll-SST and Cross-track SGG	94
6.4	Triple and Quadruple Satellite Formations	97
6.4.1	Double Satellite Pair ‘Bender’ Constellation	97
6.4.2	Scale Factor Study for Residual Drag in ll-SST Case	100
6.4.3	Investigation of the Regularization Techniques for ll-SST at the Standalone Inclined Orbit	102
6.4.4	Novel Triple Satellite Formations	107
6.5	Chapter Summary	115
7	Conclusions and Outlook	117
A	Appendix	123
A.1	Combination of ll-SST and Cross-track SGG	123
A.2	Regularization Techniques for ll-SST at the Standalone Inclined Orbit	124
	List of Figures	135
	List of Tables	141
	Acronyms	143
	Acknowledgments	147

Bibliography

149

1 Introduction

1.1 Relevance of the Research

In the beginning of the 21st century, spaceborne gravimetry has become a dedicated discipline providing valuable data about the Earth system and related processes. Satellite gravimetry has been realised by three past missions: Challenging Minisatellite Payload (CHAMP) (Torge et al., 2023), Gravity Recovery and Climate Experiment (GRACE) (Tapley et al., 2019; Chen et al., 2022; Panet et al., 2022), Gravity Field and Steady-State Ocean Circulation Explorer (GOCE) (Bruinsma et al., 2014; Flechtner et al., 2021) and two currently operating missions: GRACE-FO mission (Chen et al., 2020; Ciraci et al., 2020; Peidou et al., 2022) led by NASA-DLR collaboration and a similar one from China (Xiao et al., 2023).

The results of the satellite gravimetry missions help to understand the time-variable mass changes that take place in the Earth system, either due to natural causes or due to direct human impact (Flechtner et al., 2010; Rodell et al., 2018). Spaceborne gravimetry assesses various geophysical processes, for example, in glaciology (Wouters et al., 2019), in particular, in glacier mass balance analysis of Antarctica (Williams et al., 2014) and Greenland (Siemes et al., 2013; Otosaka et al., 2022), as well as Glacial Isostatic Adjustment estimation (Whitehouse et al., 2019; Kang et al., 2022). Moreover, continental hydrology can be investigated by spaceborne gravimetry (Rodell and Reager, 2023; Gerdener et al., 2023; Humphrey et al., 2023; Kvas et al., 2024). For instance, seasonal water storage changes in the Amazon river basin (Tourian et al., 2018), seasonal cycles of groundwater flows, e.g., in arid regions (Abdelmohsen et al., 2020), short-term hydro-meteorological fluxes from daily GRACE data (Eicker et al., 2020), groundwater depletion in the Indian subcontinent (Frappart and Ramillien, 2018; Asoka and Mishra, 2020), etc. Also, sea level rise (Fox-Kemper et al., 2021) and ocean mass estimation (Tapley et al., 2019; Barnoud et al., 2023) in the field of oceanography, as well as atmosphere mass variations (Horwath et al., 2022). In the solid Earth sciences, for example, estimation of the viscosity of the lower mantle (Argus et al., 2021), secular trends in Earth rotation parameters (Roy and Peltier, 2011), Earth's polar motion and length of day trends investigation (Zotov et al., 2022) benefit largely from the satellite gravimetry. Spaceborne gravimetry can also be used for natural hazards, such as floods and droughts assessment (Sun et al., 2017).

One of the challenges for all satellite gravimetry missions in low Earth orbits is their short lifetime due to strong non-conservative forces acting on the spacecraft, causing an orbit decay. The necessity of continuous and un-interrupted measurements together with increasing science and user needs mentioned by Pail et al. (2015) and Wiese et al. (2022) requires to continue satellite gravimetry measure-

ments with enhanced concepts and sensors. Future gravimetry missions suppose to improve both spatial (up to 100 km) and temporal (up to few days) resolution relative to the current GRACE-FO mission, that provides gravity fields up to 350 km spatial resolution (Dahle et al., 2014) with sub-monthly periods. Moreover, the US National Academies of Sciences, Engineering, and Medicine (2018) declared mass change among the five Earth’s Designated Observables over the next 2017-2027 decade (Wiese et al., 2022).

At the instrument level, so far only Electrostatic Accelerometers (EA) have been used as inertial sensors in spaceborne gravimetry missions. In this type of accelerometers, a displacement of the test mass under the acting non-gravitational forces is measured capacitively and kept centered in the electrode housing by electrostatic actuation forces. EA are one of the limiting factors in the current space gravimetry missions because of the dominating error contribution at low frequencies (below 1 mHz), so-called drift (Frommknecht et al., 2003; van Camp et al., 2021). This drift is mainly caused by the polarization wire connecting the test mass to the surrounding electrode housing, which is a significant source of stiffness (Christophe et al., 2015), and also by the thermal stability of the system (Dalin et al., 2020; Maquaire et al., 2023).

A lot of different studies were carried out in order to improve the accuracy of the retrieved gravity field models. In general, these studies can be divided into two major groups: the first one studied different satellite formations that should provide more measurements allowing better spatio-temporal resolution, and the second group evaluated enhanced and novel accelerometer concepts. Bender et al. (2003), Elsaka et al. (2014, 2015), Purkhauser and Pail (2020), Pail et al. (2023), Kupriyanov et al. (2024b) studied multiple satellite pairs, Pail et al. (2019) evaluated novel measurement concepts, in particular, high-low ranging. In Kupriyanov et al. (2024a) satellite formations that allow range measurements in cross-track direction were estimated and Pfaffenzeller and Pail (2023) assessed small satellite formations and constellations for observing sub-daily mass changes.

The second group of studies aimed on overcoming the drawback of EAs. For example, enhanced EAs with modified test mass parameters were analyzed by the French aerospace lab ONERA (Liorzou et al., 2023). EA without a polarization wire has been evaluated in Boulanger et al. (2020). There, a wireless ultraviolet light charge management system, that was on-board the Laser Interferometer Space Antenna (LISA) Pathfinder mission (Armano et al., 2021) and impeded charge buildup on the test mass, substituted the polarization wire. This allows to keep the electrostatic noise sources at an acceptable level at low frequencies (Sumner et al., 2020). Also, on-board LISA-Pathfinder, for the first time in space, so-called optical accelerometers were used, where the test mass displacement were sensed by laser interferometry (Armano et al., 2018a). Based on the promising results of optical accelerometers, also known as Gravitational Reference Sensor (GRS), multiple studies were carried out evaluating Simplified GRS (SGRS) (Dávila Álvarez et al., 2022; Weber et al., 2022). SGRS is an enhanced EA with capacitive test mass position readout and which inherited a wireless polarization system and a large gap between the test mass and surrounding elec-

trode housing from LISA-Pathfinder. SGRS with a wide range of parameters and different test mass readout schemes, electrostatic and optical, was modeled and evaluated by Kupriyanov et al. (2024b). Another interesting test mass displacement measurement system was demonstrated by Zoellner et al. (2017), where a differential optical shadow sensor was used to readout the sphere-shaped proof mass movements.

Cold Atom Interferometry (CAI) is another technology that could overcome the drawback of EAs in the low-frequency domain. In CAI accelerometers, atom clouds act as test masses (Alonso et al., 2022). Knabe et al. (2022) evaluated the performance of CAI accelerometry, while Douch et al. (2018), Trimeche et al. (2019) and Migliaccio et al. (2019) studied CAI gradiometry. Utilization of CAI accelerometers in space, on the one hand, allows longer interrogation times, but on the other hand, fast changing non-gravitational forces can not be observed. Hybridization of CAI and electrostatic accelerometers could overcome this issue. So-called hybrid sensors, as well as various ways of combining them, were studied by HosseiniArani et al. (2022, 2024); Zahzam et al. (2022) and Zingerle et al. (2024).

Novel satellite formations and inertial instruments' enhancement mentioned above are not the only areas for improvements of retrieved gravity products. There are ongoing developments on improving the time-variable background models that represent short-term mass variations in the atmosphere and oceans which are the main contributors to inaccuracies in GRACE(-FO) solutions, causing aliasing errors. For example, Release (RL) 06 by Dobslaw et al. (2017) and RL07 by Shihora et al. (2022) represent those Atmosphere and Ocean De-Aliasing Level-1B products.

1.2 Research Questions and Objectives

After introducing the state-of-the-art sensors, concepts and approaches in satellite gravimetry, the main research question, that this thesis addresses, is how the gravity field measurements from space can be improved when applying advanced sensors and observation concepts. Possible improvements are investigated for various satellite formations, e.g., GRACE-like, GOCE-like, novel triple satellite configuration and combination of low-low Satellite-to-Satellite Tracking (ll-SST) with cross-track Satellite Gravity Gradiometry (SGG).

The major research questions are:

- Is it possible to adapt optical accelerometry technology from the LISA-Pathfinder mission for satellite gravimetry missions in low Earth orbits, where non-gravitational forces have a big impact?
- Can modeled accelerometers and gradiometers, with an optical interferometer readout of the test mass displacements, outperform classical electrostatic, CAI and hybrid (electrostatic & CAI) instruments?

- Which novel satellite formations can be formed in order to utilize cross-track ranging measurements, taking into account enhanced laser ranging? Which technical challenges have to be solved for operating such missions?

In order to answer the research questions, the main objectives of this work are to:

- analyze the anticipated performance of optical accelerometers and gradiometers w.r.t. existing electrostatic ones as well as w.r.t. other instrument concepts, e.g enhanced electrostatic, CAI, hybrid, etc.,
- quantify benefits of optical accelerometry for future gravimetry missions via closed-loop simulations,
- estimate gravity field models from novel satellite formations and measurement concepts as well as evaluate the feasibility of such approaches.

1.3 Thesis Outline

In Chapter 2, a description of the main ‘fundamentals’ of this work is given. It includes used mathematics, algorithms and procedures. Chapter 3 gives an overview of the past and current satellite gravimetry missions and utilized technologies. Also, in this chapter, upcoming future gravimetry missions as well as existing concepts of inertial sensors are introduced. In Chapter 4, the simulation procedure is set up including the description of the used software components. Results of the gravity field recovery simulations are presented and discussed in Chapter 6. Finally, the summary of the research results and an outlook are given in Chapter 7.

2 Fundamentals

2.1 Spherical Harmonic Series

According to Heiskanen and Moritz (1967) the Earth's gravity potential W is a sum of the gravitational potentials of all masses V and the centrifugal potential due to the Earth's rotation Z :

$$W(x,y,z) = V(x,y,z) + Z(x,y,z) = G \int \int \int_{\text{Earth}} \frac{dM}{l} + \frac{1}{2} \omega^2 (x^2 + y^2), \quad (2.1)$$

where x,y,z are the geocentric coordinates of the Earth-fixed system, G is the gravitational constant, M the mass of the Earth, l the distance of the mass elements and ω the angular velocity of Earth's rotation. The Earth mass includes the masses of the atmosphere.

Since the gravitational potential V outside of attracting masses, or in other words outside of the Earth, is a harmonic function that satisfies the Laplace equation for the outer space ($\Delta V = 0$), it can be represented in a Spherical Harmonic (SH) series expansion (Hofmann-Wellenhof and Moritz, 2006):

$$V(r, \theta, \lambda) = \frac{GM}{R} \times \sum_{n=0}^{\infty} \left(\frac{R}{r}\right)^{n+1} \sum_{m=0}^n [\overline{C}_{nm} \cos m\lambda + \overline{S}_{nm} \sin m\lambda] \overline{P}_{nm}(\cos \theta), \quad (2.2)$$

where (r, θ, λ) are the spherical coordinates of a point on the Earth's surface, GM is gravitational constant times the mass of the Earth, R the equatorial radius of the Earth's reference ellipsoid, n,m the SH degree and order, $\overline{P}_{nm}(\cos \theta)$ the fully normalized associated Legendre functions and $\overline{C}_{nm}, \overline{S}_{nm}$ the cosine and sine normalized SH coefficients, which are the unknowns of the gravity field solutions.

Note: Since the atmospheric masses are always above the Earth's surface, the Laplace equation for satellite observation is only fulfilled under certain assumptions. Here, one can assume that the centers of masses of the atmospheric columns lie below the satellite's orbit and Laplace equation is still valid (Gruber et al., 2009). However, a specific correction has to be applied to gravity anomalies on ground (Hackney and Featherstone, 2002). Further theory and details of the correction computation are described in Moritz (1980).

Figure 2.1 shows the classification of the surface SH coefficients into three groups:

zonal, sectorial and tesseral. When the order is zero ($m = 0$), one has the zonal harmonics, when the degree equals to the order ($m = n$) they are called sectorial harmonics. In all other cases ($m \neq n$) they are tesseral components. Spherical harmonic representation is a convenient way that also describe some of the properties of the Earth. For example, C_{00} scales the total mass of the Earth, C_{20} reflects the Earth oblateness or polar flattening, C_{10}, C_{11}, S_{11} are the coordinates of the center of mass, etc. (Torge et al., 2023).

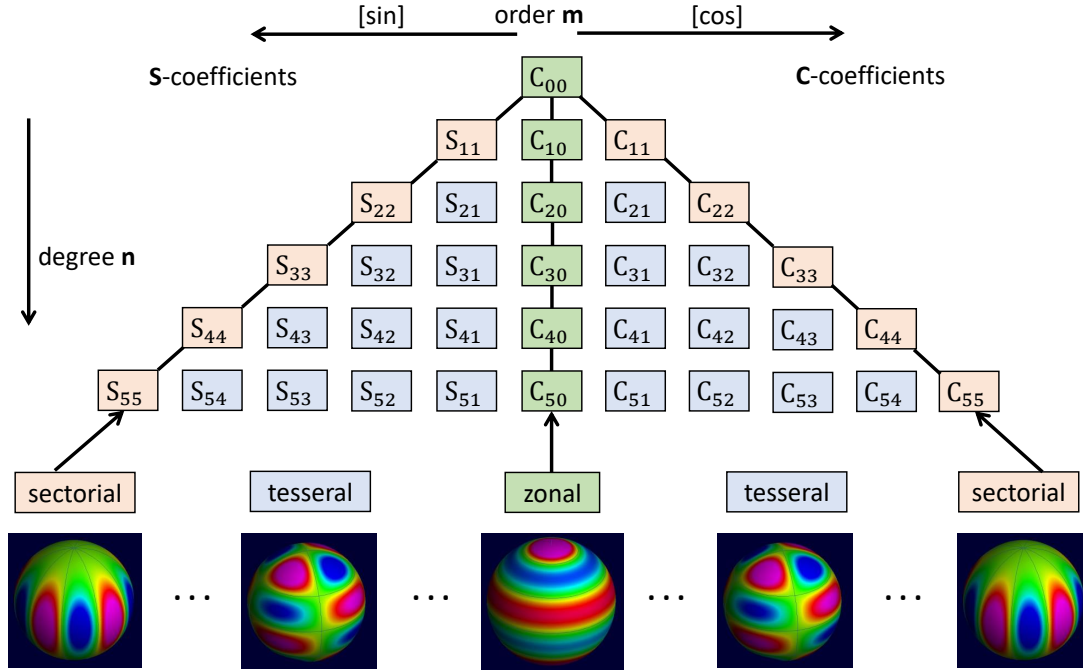


Figure 2.1: Surface spherical harmonics representation (modified from Rummel and Ince et al. (2019))

2.2 Measurement Principles in Satellite Gravimetry

Satellite gravimetry determines the spatial and temporal changes of the gravitational field on a global scale (Flechtner et al., 2021). Different measurement techniques and principles, e.g., high-low Satellite-to-Satellite Tracking (hl-SST), ll-SST, SGG that are introduced further, are utilized depending on the observable targets. While orbiting on Low Earth Orbit (LEO), various conservative e.g., Earth's non-spherical gravitation, solid Earth tides, ocean tides, third body attraction, etc., and non-conservative forces, e.g, air drag, solar and thermal radiation pressures, infrared irradiance and Earth albedo act on the satellite and cause an orbit perturbation. Equations of motion of the satellite can be described as (Jäggi and Arnold, 2017)

$$\ddot{\mathbf{r}} = -GM \frac{\mathbf{r}}{r^3} + \mathbf{f}_p(t, \mathbf{r}, \dot{\mathbf{r}}, Q_1, \dots, Q_d), \quad (2.3)$$

where $\ddot{\mathbf{r}}$ is the total acceleration of the satellite, G is the gravitational constant, M is the mass of the Earth, \mathbf{r} is the geocentric position of the satellite in the inertial frame, \mathbf{f}_p summarizes all accelerations due to gravitational and non-gravitational perturbing forces in the inertial frame. The force models comprising \mathbf{f}_p depend on the time t , position \mathbf{r} and velocity $\dot{\mathbf{r}}$, as well as additional parameters Q_1, \dots, Q_d that could be scaling factors of analytically (e.g., retrieved from a model of the Earth's gravity field) or numerically known (e.g., measured by accelerometers) accelerations. In this case, the whole satellite act as a test mass. Comparing the true orbit with the computed one, an analysis of orbit perturbations can be applied to improve the gravity field.

2.2.1 High-low Satellite-to-Satellite Tracking

Figure 2.2 depicts different measurement concepts that are used in satellite gravimetry. Precise orbit determination of LEO satellites is done with the Global Navigation Satellite System (GNSS), e.g., GPS. For this purpose, the **hl-SST** measurement principle is used (Reigber et al., 2002). The hl-SST was utilized for the first time at the CHAMP mission and as an additional measurement in the GRACE(-FO) and GOCE missions. Typically, long-wavelength observations or, in other words, large-scale structures (≈ 1000 km) of the gravitational field can be obtained more accurately by this principle (Reigber et al., 2006).

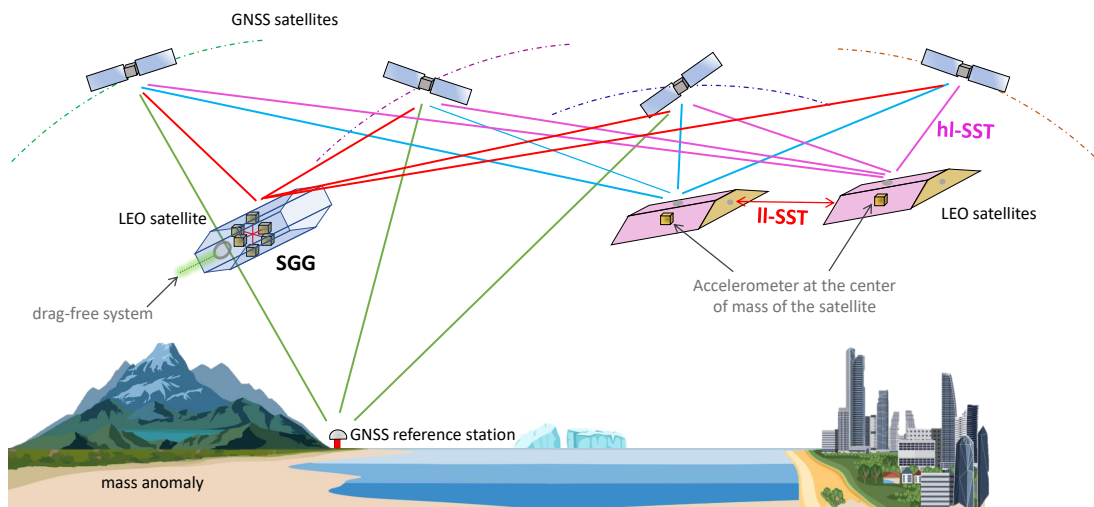


Figure 2.2: Scheme of the measurement concepts applied in satellite gravimetry. II-SST between two LEO spacecraft with accelerometers located at the center of mass of the satellites; hl-SST between the GNSS and LEO satellites; SGG realised by six 3-axis accelerometers on-board a single drag-free satellite (modified from Wöske (2021)).

2.2.2 Low-low Satellite-to-Satellite Tracking

GRACE and GRACE-FO missions utilized, in addition to hl-SST, **ll-SST**. Here, the major observable is the inter-satellite range change mainly due to the different

gravitational pull at the positions of the two satellites (see Figure 2.3), which are separated by roughly 220 km (Abich et al., 2019). The impact of the non-gravitational accelerations on the inter-satellite distance is removed using the measurements from the accelerometers that are located at the center of mass of each satellite. In the GRACE mission, a K-band Ranging (KBR) instrument (Kim and Lee, 2009) was used in order to measure the inter-satellite distance with μm precision, while in GRACE-FO a Laser Ranging Interferometer (LRI) was on-board as a technology demonstrator (Abich et al., 2019) that can achieve up to nm precision. The ll-SST principle is sensitive to the medium and fine structures ($\approx 200 - 350$ km) of the gravitational field (Dahle et al., 2014; Wöske, 2021).

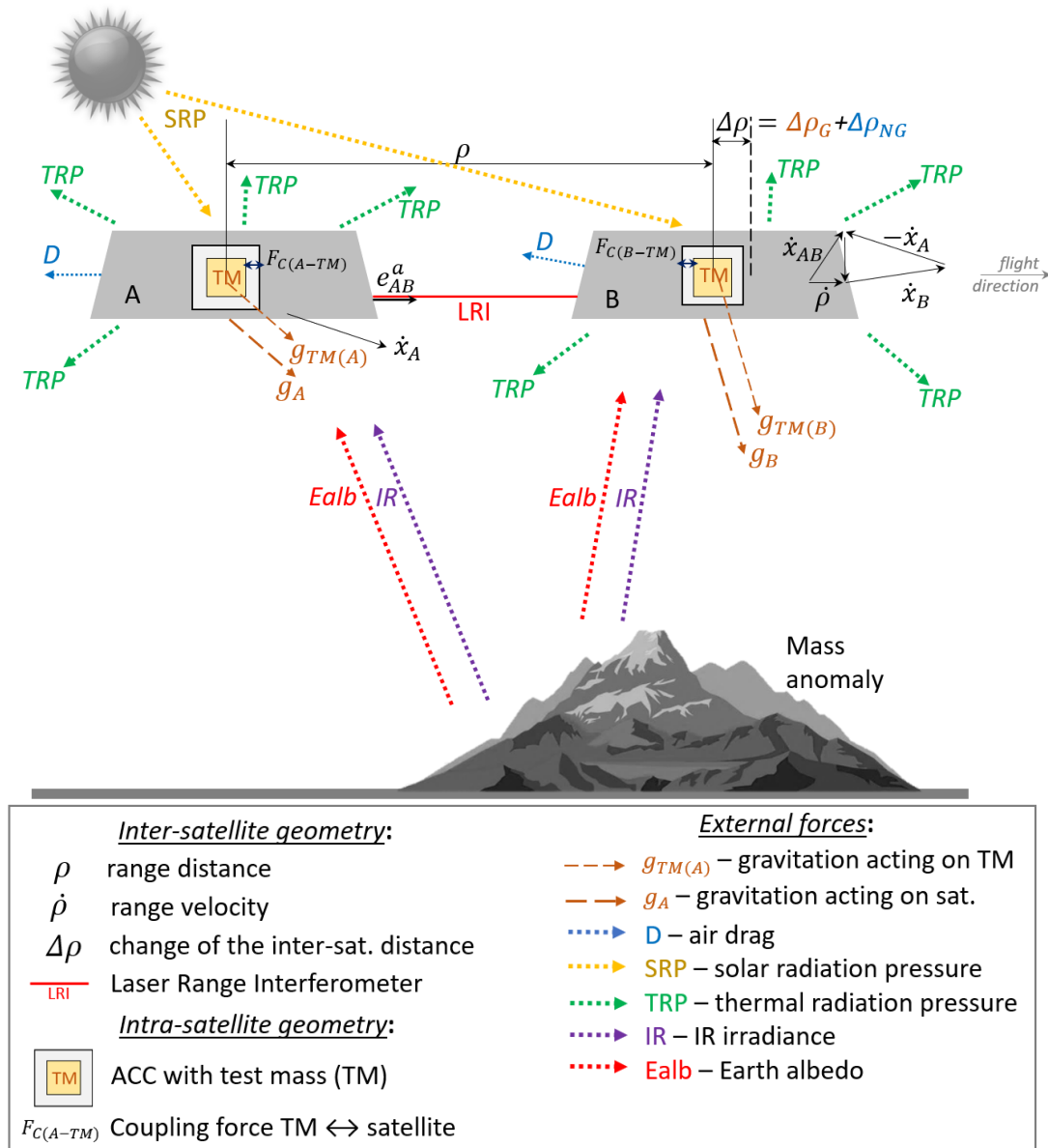


Figure 2.3: Measurement principle of the ll-SST for a GRACE-like mission (adapted from Kupriyanov et al. (2024b))

The equation of motion (2.4) from Weigelt (2017) for a GRACE-like case connects the observed range acceleration between the two LEO satellites A and B with the gradient of the gravitational field (see Figure 2.3):

$$\nabla V_{AB} \cdot \mathbf{e}_{AB}^a = \ddot{\rho} - \frac{1}{\rho} (\dot{\mathbf{x}}_{AB} \cdot \dot{\mathbf{x}}_{AB} - \dot{\rho}^2), \quad (2.4)$$

where ρ is the range between the satellites, \mathbf{x}_{AB} the relative position, \mathbf{e}_{AB}^a the unit vector along the Line of Sight (LOS) between the two spacecraft, $\dot{\mathbf{x}}_{AB}$ is the relative velocity vector, $\dot{\rho}$ the range velocity, $\ddot{\rho}$ the range acceleration and ∇V_{AB} the gravity gradient.

2.2.3 Satellite Gravity Gradiometry

The **SGG** principle consists of measuring the second derivative of the gravitational potential or, in other words, the gravity gradient tensor (Ditmar et al., 2003). SGG was first realized in the GOCE mission. Six free-floating test masses, located on three orthogonal axes, formed three arms of the gradiometer (see Figure 2.2). Differential mode accelerations are used to determine the gravitational gradients (Siemes, 2017):

$$\mathbf{a}_{dij} = \frac{(\mathbf{a}_i - \mathbf{a}_j)}{2} = -\frac{1}{2} (\mathbf{V} - \mathbf{\Omega}^2 - \dot{\mathbf{\Omega}}) (\mathbf{r}_i - \mathbf{r}_j), \quad (2.5)$$

where \mathbf{a}_{dij} is the differential acceleration between the accelerometer pairs i, j , \mathbf{V} the gravity gradient tensor, $\mathbf{\Omega}^2$ the centrifugal part, $\dot{\mathbf{\Omega}}$ the Euler part (angular acceleration of the satellite), $\mathbf{r}_{i,j}$ is the radius-vector from the satellite center of mass to the center of the i^{th} and j^{th} accelerometer.

Equation (2.5) can be also re-written in other form (Rummel et al., 2011) as:

$$\mathbf{D} = \mathbf{V} + \mathbf{\Omega}\mathbf{\Omega} + \dot{\mathbf{\Omega}}, \quad (2.6)$$

where \mathbf{V} is the gravitational gradient tensor (a second-order tensor field), $\mathbf{\Omega}\mathbf{\Omega}$ the centrifugal part, $\dot{\mathbf{\Omega}}$ the Euler part and \mathbf{D} is the matrix of the observed gradients.

In matrix form Equation (2.6) can be written as:

$$\begin{bmatrix} D_{xx} & D_{xy} & D_{xz} \\ D_{yx} & D_{yy} & D_{yz} \\ D_{zx} & D_{zy} & D_{zz} \end{bmatrix} = \begin{bmatrix} V_{xx} & V_{xy} & V_{xz} \\ V_{yx} & V_{yy} & V_{yz} \\ V_{zx} & V_{zy} & V_{zz} \end{bmatrix} + \begin{bmatrix} -(\omega_y^2 + \omega_z^2) & \omega_x\omega_y & \omega_x\omega_z \\ \omega_y\omega_x & -(\omega_z^2 + \omega_x^2) & \omega_y\omega_z \\ \omega_z\omega_x & \omega_z\omega_y & -(\omega_x^2 + \omega_y^2) \end{bmatrix} + \begin{bmatrix} 0 & -\dot{\omega}_z & \dot{\omega}_y \\ \dot{\omega}_z & 0 & -\dot{\omega}_x \\ -\dot{\omega}_y & \dot{\omega}_x & 0 \end{bmatrix}, \quad (2.7)$$

where ω_x , ω_y , ω_z are the angular rates of the satellite about the along-track, cross-track and nadir axes, respectively.

A matrix of the gravitational gradient tensor \mathbf{V} is symmetric and after re-arranging Equation (2.5), the diagonal gravity gradients components look like (Siemes, 2017):

$$V_{xx} = -2 \frac{a_{d14x}}{L_x} - \omega_y^2 - \omega_z^2, \quad (2.8)$$

$$V_{yy} = -2 \frac{a_{d25y}}{L_y} - \omega_x^2 - \omega_z^2, \quad (2.9)$$

$$V_{zz} = -2 \frac{a_{d36z}}{L_z} - \omega_x^2 - \omega_y^2. \quad (2.10)$$

Here a_{d14x} is the acceleration difference of the accelerometers 1 and 4 along the x -axis and L_x is the baseline of the gradiometer. The left side of Equation (2.7), the observed gradient element can be represented as (Rummel et al., 2011):

$$D_{xx} = \frac{\Delta a_x}{L_x}, \quad (2.11)$$

where Δa_x is the acceleration difference.

In this work within the gravity field recovery software, gradiometer noise time-series were calculated based on the following relation:

$$D = \frac{(\text{ACC}_1 - \text{ACC}_2) \cdot \sqrt{2}}{L}, \quad (2.12)$$

which is a modified version of Equation (2.11), taking into account a factor $\sqrt{2}$, which represents the same type of observations and instruments (accelerometers). This factor was considered from the assumption that uncorrelated observations from the ACC_1 and ACC_2 , that form a gradiometer, have the same variances and standard deviations. The covariance between the measurements of each pair of accelerometers were assumed negligible small.

As it was already mentioned, in SGG a second-order derivatives of the gravitational potential are measured, therefore in the Gradiometer Reference Frame (GRF), the measured gravity gradients along the axes x_i can be represented as (Wu, 2016):

$$V_{ij} = \frac{\partial^2 V}{\partial x_i \partial x_j}, \quad (2.13)$$

where V_{ij} are point-wise measured gravity gradients and $i, j = 1, 2, 3$ representing X, Y and Z axes of the GRF.

The SGG measurement principle is sensitive to the fine structures (≈ 100 km) of the gravity field (Gruber et al., 2011).

2.2.4 Summary of Satellite Gravimetry Measurement Techniques

This section aims to summarize the measurement techniques that are implemented in satellite gravimetry. Before representing a chart with the outline of key principles, quantities, etc., an important variable, the disturbing potential (T) shall be introduced. According to Torge et al. (2023), the Earth's gravity potential (W) and the normal gravity potential (U) contain gravitational and centrifugal parts: $W = V + Z$ and $U = V' + Z'$. The disturbing potential is defined as:

$$T = W - U = V + Z - (V' + Z'). \quad (2.14)$$

Considering that the Earth's centrifugal acceleration is precisely known, it is assumed that the centrifugal components of W and U are equal, i.e. $Z = Z'$ (Torge et al., 2023). Therefore, Equation (2.14) simplifies to:

$$T = V - V'. \quad (2.15)$$

Also, disturbing potential can be expressed by spherical harmonic expansion as (Heiskanen and Moritz, 1967; Liang et al., 2020):

$$T(r, \theta, \lambda) = \frac{GM}{r} \sum_{n=0}^{\infty} \left(\frac{a}{r}\right)^n \sum_{m=0}^n (\bar{C}_{nm} \cos m\lambda + \bar{S}_{nm} \sin m\lambda) \times \bar{P}_{nm}(\cos \theta), \quad (2.16)$$

where the variables have the same notation as in Equation (2.2).

The extended Meissl scheme given in Figure 2.4 shows the connections between the spectral components of the disturbing potential T_n of degree n and its first and second derivatives in radial direction. The lower row corresponds to the Earth's surface and the upper one to the satellite altitude h . The arrows show the directions, for which the eigenvalues, that connect the disturbing potential T_n and its derivatives per SH degree n , are applied. Mathematical operations depicted in the scheme applied per degree of the SH expansion. As mentioned in Rummel (2005), the arrows connecting the bottom row with the upper one correspond to the direction of smoothing (attenuation of high degrees SH coefficients) with altitude. The upper row reflects to the various satellite gravimetry measurement techniques. For example, the disturbing potential T_n can be observed by considering the whole satellite as a test mass and using precise orbit

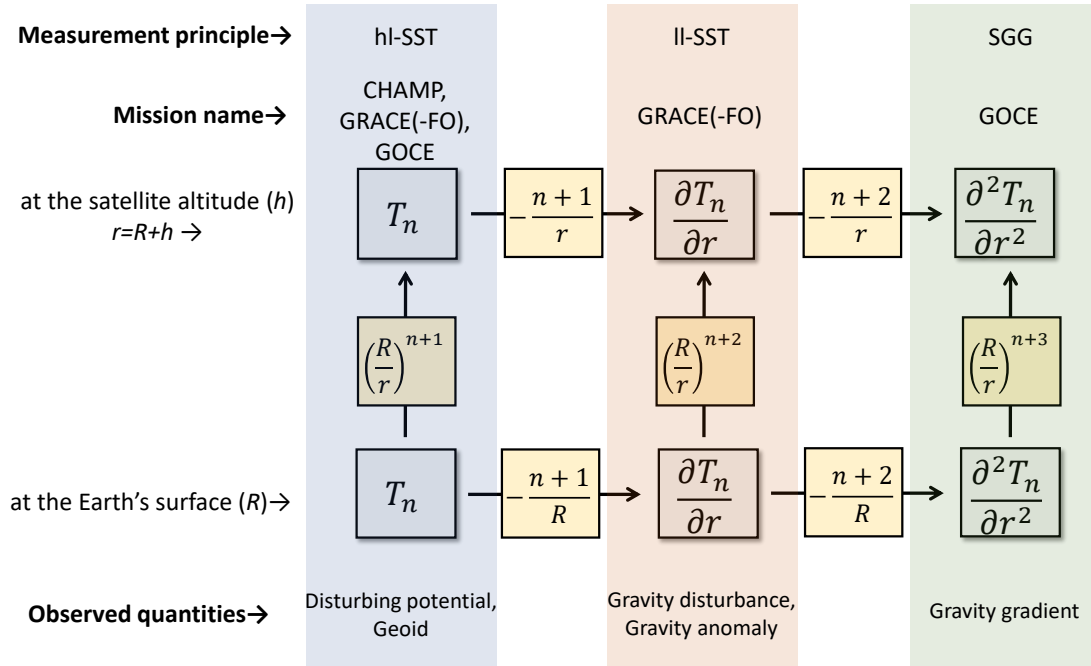


Figure 2.4: Extended Meissl scheme (modified from Rummel (2005), Pail and Gruber (2020) personal communication)

determination for tracking the true orbit. This is implemented within the hl-SST principle in multiple gravimetry missions (CHAMP, GRACE(-FO) and GOCE). First derivatives of the disturbing potential lead to the gravity disturbance or gravity anomalies (a difference between the real value of gravity and computed from the rotational ellipsoid), which can be observed by the ll-SST utilized in GRACE and GRACE-FO missions. Finally, second derivatives of the disturbing potential provide gravity gradients that are observed by the SGG in the GOCE mission.

2.3 Amplitude Spectral Density Representation

In this work, noise models of the instruments, in particular, accelerometers, gradiometers, inter-satellite range measurement sensors, etc., are represented as Amplitude Spectral Densities (ASD). A detailed overview of the estimation of spectra and spectral densities using Discrete Fourier Transform is given by Heinzl et al. (2002). A signal power in each infinitesimal frequency interval is described by the Power Spectrum (PS) (Wöske, 2021). The PS is represented as the squared signal, therefore, for example, the PS units would be $(\text{m/s}^2)^2$ for the acceleration. Power Spectral Density (PSD) represents how the power of a signal is distributed with frequency. PSD is a normalization of PS, meaning the power in each infinitesimal frequency interval is divided by the width of this interval. PSD of the acceleration would have units $(\text{m/s}^2)^2/\text{Hz}$. Mathematically, PSD are calculated as the Fourier transform of the autocorrelation sequence of the time series (Heinzl et al., 2002). Amplitude Spectrum (AS) and ASD are calculated

as the square root of the PS and PSD, respectively. Therefore for accelerations, AS would have units of the signal itself, i.e. m/s^2 and ASD $(\text{m/s}^2)/\sqrt{\text{Hz}}$. Figure 2.5 summarizes the mathematical transformations between the above-mentioned variables and the signal in the time domain.

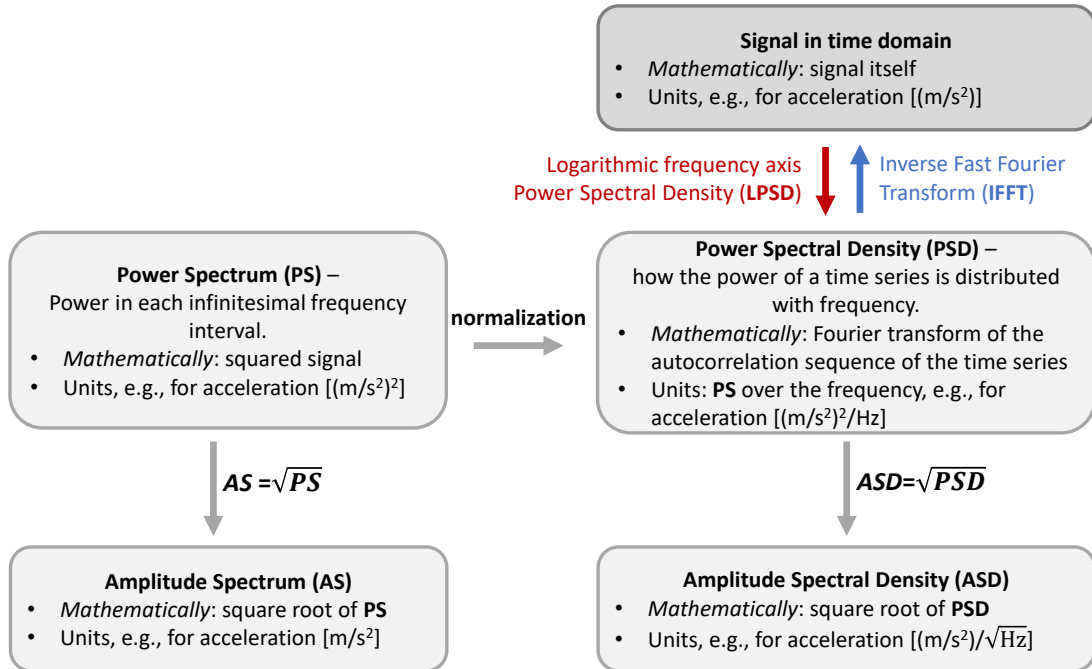


Figure 2.5: Scheme of the mathematical transformations between the different quantities of the discrete Fourier transform and the signals in the time domain (modified from Heinzl et al. (2002) and Wöske (2021))

During this work, signal transformations from the time series domain to PSD and vice versa are widely used. In order to get a PSD from the signal in the time domain, an extension of the well-known Welch’s technique of ‘averaging over modified periodograms’, which is called Logarithmic frequency axis Power Spectral Density (LPSD) is used (Tröbs and Heinzl, 2006). Welch’s Overlapped Segmented Averaging (WOSA) algorithm with segment detrending and variance estimation calculated a modified periodogram for each segment and averaged these estimates to estimate the PSD. According to Heinzl et al. (2002) averaging is applied to reduce the variance of the spectral estimates. A periodogram is a Discrete Fourier Transform (DFT) of a segment of a time series, and ‘modified’ means an application of a time-domain window function. Within the LPSD procedure, an adjustment of the frequency resolution for each Fourier frequency in the estimate is done, while in the WOSA method the same frequency resolution for each Fourier frequency is utilized (Tröbs and Heinzl, 2006).

A dedicated Matlab function called `flpsd` (Reis et al., 2022b) is used in this work for the transformation from the time-domain signal into the PSD. This function used the LPSD method described by Tröbs and Heinzl (2006). In short, mathematically, the utilized procedure can be explained by the following: after the segmentation of the time-domain data into the overlapping segments,

the number of averages $K(j)$ of the Fourier frequency $f(j)$ is described as

$$K(j) = \text{floor} \left(\frac{N - L(j)}{L(j)(1 - \xi)} + 1 \right), \quad (2.17)$$

where $\text{floor}()$ selects the largest integer that is smaller or equal to its argument, N is the total number of the data, $L(j)$ is the number of data in one segment and ξ is fractional segment overlap ($0 \leq \xi \leq 1$). Then the average value of each segment $a(j,k)$, where $k = 0, \dots, K(j) - 1$ is calculated and then subtracted from each segment in order to reduce the spectral leakage. Afterwards, a spectral estimate is calculated with a selected data window and window sequences. Different types of window functions exist (Heinzel et al., 2002) and they act as a weight on the signal in the time domain (Wöske, 2021). For all calculations in this work, a Hanning window was used with a time-domain signal length usually of 31 days and different sample frequencies, for example 1, 2.5 or 5 s, depending on the simulation and scenario. Then the scalar products $A(j,k)$ of the windowed sequences $G(j,k,l)$ with the complex exponential of the appropriate Fourier frequency $f(j)$ is calculated:

$$A(j,k) = \sum_{l=0}^{L(j)-1} G(j,k,l) \exp \left(-2\pi i \frac{m(j)l}{L(j)} \right), \quad (2.18)$$

where l is the data index within one segment, $L(j)$ is the number of data in one segment, $m(j)$ is the frequency index or the bin number. The spectral estimate P of the Fourier frequency $f(j)$ is calculated as

$$P(f(j)) = \frac{C}{K(j)} \sum_{k=0}^{K(j)-1} |A(j,k)|^2, \quad (2.19)$$

where C is the normalization factor, $|A(j,k)|^2$ the squared magnitudes of the complex scalar product.

The comparison of different ASDs curves, representing various instruments' noise budgets, is widely used in this work. Here mostly ASDs of the acceleration with the units $(\text{m/s}^2)/\sqrt{\text{Hz}}$ are considered. When comparing the performance of two different instruments, the one where the ASD curve lies below is considered to have better accuracy.

For back transformations, from the PSD to the time-domain signal, a standard Matlab function `ifft` was used (The MathWorks, 2024b). By implementing this function, the inverse discrete Fourier transform $\mathbf{X} = \text{ifft}(\mathbf{Y})$ was calculated using a fast Fourier transform algorithm. In order to ensure that the output of this function is real, a 'symmetric' option was defined. According to The MathWorks (2024b), the inverse Fourier transform of the signal with length n is described as:

$$X(j) = \frac{1}{n} \sum_{k=1}^n Y(k) W_n^{-(j-1)(k-1)}, \quad (2.20)$$

where $W_n = \exp(-2\pi i/n)$ is one of n roots of unity.

2.4 Least-Squares Adjustment for Spherical Harmonics Estimation

The process of SH estimation from satellite gravimetry observations is called spherical harmonic analysis (Colombo, 1981; Koop, 1993; Wu, 2016). Large-scale and over-determined linear equation systems formed by the observations are solved by the Least-Squares (LS) technique, discussed in detail, e.g., by Wu (2016) in the context of the gravity field recovery software packages of Institute of Geodesy (IfE) that are also applied in this study.

The Gauss-Markov model of a linear equation systems expresses the measurements as a function of unknown parameters:

$$\mathbf{l} + \mathbf{v} = \mathbf{A}\mathbf{x}, \quad (2.21)$$

where \mathbf{l} represents the time-series observation vector [$s \times 1$], \mathbf{v} the observation residuals [$s \times 1$], \mathbf{A} the design matrix [$s \times r$], \mathbf{x} the vector of unknown parameters [$r \times 1$]. Precision and correlation of the measurements are given by the stochastically modeled full Variance/Covariance Matrix (VCM) Σ_u :

$$\Sigma_u = \begin{bmatrix} \sigma_1^2 & \sigma_{12} & \dots & \sigma_{1s} \\ \sigma_{21} & \sigma_2^2 & \dots & \sigma_{2s} \\ \vdots & \vdots & \ddots & \vdots \\ \sigma_{n1} & \sigma_{n2} & \dots & \sigma_s^2 \end{bmatrix}, \quad (2.22)$$

where σ_i^2 is the variance of the i -th element and σ_{ij} is the covariance between the i -th and the j -th measurements. In Niemeier (2008), the estimated solution $\hat{\mathbf{x}}$ that minimizes the sum of squares of the weighted residuals, according to the rule of LS adjustment, is obtained as:

$$\hat{\mathbf{x}} = (\mathbf{A}^T \mathbf{P} \mathbf{A})^{-1} \mathbf{A}^T \mathbf{P} \mathbf{l} = \mathbf{N}^{-1} \mathbf{w}, \quad (2.23)$$

where $\mathbf{P} = \Sigma_u^{-1}$ is the weight matrix (obtained from stochastic modeling), $\mathbf{N} = \mathbf{A}^T \mathbf{P} \mathbf{A}$ the normal matrix and $\mathbf{w} = \mathbf{A}^T \mathbf{P} \mathbf{l}$. Since the observation vector \mathbf{l} enters only \mathbf{w} , the matrix \mathbf{N} that describes the inner geometry of the data distribution is independent from the observations.

After the LS adjustment, the residuals $\hat{\mathbf{v}}$ that are used to assess the quality of the observations can be calculated by

$$\hat{\mathbf{v}} = \mathbf{A}\hat{\mathbf{x}} - \mathbf{l}. \quad (2.24)$$

Also, the posterior variance $\hat{\sigma}_0^2$ of the post-fit residuals $\hat{\mathbf{v}}$, which serves as a measure of the quality of the solution, can be computed from the estimated residuals:

$$\hat{\sigma}_0^2 = \frac{\hat{\mathbf{v}}^T \mathbf{P} \hat{\mathbf{v}}}{s - r} = \frac{\mathbf{l}^T \mathbf{P} \mathbf{l} - \mathbf{w}^T \hat{\mathbf{x}}}{s - r}, \quad (2.25)$$

where s is the number of observations and r the number of parameters.

Knowing the a posterior variance $\hat{\sigma}_0^2$, the VCM of the coefficients $\Sigma_{\hat{\mathbf{x}}\hat{\mathbf{x}}}$ can be calculated:

$$\Sigma_{\hat{\mathbf{x}}\hat{\mathbf{x}}} = \hat{\sigma}_0^2 \mathbf{N}^{-1}. \quad (2.26)$$

As it was mentioned in Wu (2016), post-fit residuals $\hat{\mathbf{v}}$ are very useful because outliers in the observations can be detected and their PSD show the spectral behavior of the measurement error, modeling error, residual signal parts, etc. Also, the square root of the variance or, in other words, diagonal elements of the VCM of the estimated unknown parameters $\Sigma_{\hat{\mathbf{x}}\hat{\mathbf{x}}}$, provide the standard deviation, so called formal errors (Dahle et al., 2019).

2.5 Stochastic Modeling

As it was demonstrated by Cesare (2002), the coloured noise of the gravity gradients has been identified in the GOCE pre-launch phase and further confirmed with real observations (Wu, 2016) due to the drift at the low-frequency domain of the electrostatic accelerometers forming the gradiometer (see Section 3.2 for more details). Also, the errors of the gravity gradients measurements are highly correlated. Therefore, a full VCM of the measurements $\Sigma_{\mathbf{u}}$ must be applied in order to de-correlate and down-weight the observations (Knabe, 2023). This VCM is composed of the biased estimation of the auto-covariance vector \mathbf{r} of the observations, which is calculated from the post-fit residuals (Koch et al., 2010). In contrast to the normal matrix \mathbf{N} that is assembled arc-wisely (in this work one arc is defined as 12 hours, unless otherwise stated), the VCM $\Sigma_{\mathbf{u}}$ is built from the post-fit residuals that consider the whole observation period (1 month in this work), similar to Knabe (2023). Based on Koch et al. (2010), the biased auto-covariance element r_i is estimated from the residual observations \hat{v}_n as

$$r_i = \frac{1}{N} \sum_{n=0}^{N-1-|i|} \hat{v}_n \cdot \hat{v}_{n+i}, \quad (2.27)$$

where N is the length of the observations, i.e. 1 month and $i = [0; N - 1]$. According to Koch et al. (2010), the biased estimator is preferred over the unbiased version because the latter results in large variances for lags i approaching N .

Taking into account that observations separated by equal distances have the same covariance, the assembled VCM $\Sigma_{\mathbf{u}}$ is the symmetric, positive definite Toeplitz (diagonal elements are constant) matrix (Schuh, 1996):

$$\Sigma_{\mathbf{u}} = \begin{bmatrix} r_0 & r_1 & r_2 & \dots & r_{N-1} \\ r_1 & r_0 & r_1 & \dots & r_{N-2} \\ r_2 & r_1 & r_0 & \dots & r_{N-3} \\ \vdots & \vdots & \vdots & \ddots & \vdots \\ r_{N-1} & r_{N-2} & r_{N-3} & \dots & r_0 \end{bmatrix}. \quad (2.28)$$

The assembled VCM matrix can be decomposed by the Cholesky approach into the product of two matrices: \mathbf{F} - lower triangle, the so called de-correlation filter (Wu, 2016) and \mathbf{F}^T - the transpose of \mathbf{F} . This step allows to avoid the storage of the full VCM matrix with dimensions $s \times s$, where s is the number of observations, which is hundreds of millions, and further matrix multiplication in order to get the normal matrix \mathbf{N} . So, the Cholesky decomposition for VCM looks like:

$$\Sigma_{\mathbf{u}} = \mathbf{F}\mathbf{F}^T = \begin{bmatrix} F_{11} & 0 & 0 & \dots & 0 \\ F_{21} & F_{22} & 0 & \dots & 0 \\ F_{31} & F_{32} & F_{33} & \dots & 0 \\ \vdots & \vdots & \vdots & \ddots & \vdots \end{bmatrix} \begin{bmatrix} F_{11} & F_{21} & F_{31} & \dots & \dots \\ 0 & F_{22} & F_{32} & \dots & \dots \\ 0 & 0 & F_{33} & \dots & \dots \\ \vdots & \vdots & \vdots & \ddots & \vdots \end{bmatrix}. \quad (2.29)$$

At the beginning, the normal matrix \mathbf{N} is assembled with a unit weight matrix \mathbf{P} , representing white noise. Then, in further iterations of the stochastic modeling, the normal matrix \mathbf{N} is built with the VCM $\Sigma_{\mathbf{u}}$. Substituting the Cholesky decomposition of the $\Sigma_{\mathbf{u}}$, Equation (2.29), to the normal matrix equation $\mathbf{N} = \mathbf{A}^T \mathbf{P} \mathbf{A}$, instead of the weight matrix \mathbf{P} , gives (Wu, 2016):

$$\mathbf{N} = \hat{\sigma}_0^2 (\mathbf{F}^{-1} \mathbf{A})^T (\mathbf{F}^{-1} \mathbf{A}). \quad (2.30)$$

In general, the stochastic modeling was implemented in gravity field recovery in the same way as it was introduced by Knabe (2023):

1. Assembling the normal matrix \mathbf{N} with unit weight matrix \mathbf{P} ,
2. Deriving SH coefficients from the inversion of the normal matrix,

3. Computing the post-fit residuals $\hat{\mathbf{v}}$,
4. Assembling the VCM $\Sigma_{\mathbf{u}}$ from the biased estimation of the auto-covariance vector \mathbf{r} , that is estimated from the post-fit residuals,
5. Assembling the normal matrix \mathbf{N} using VCM $\Sigma_{\mathbf{u}}$,
6. Deriving final SH coefficients and formal errors by the inversion of the normal matrix.

In this work, parallel computing (Wu, 2016; Knabe, 2023) was applied for the gravity field retrieval in gradiometric scenarios with SH degree/order (d/o) up to 180 due to the large data sets. The idea consists of splitting 1-month observations into 6 equally long segments. Hence, the design matrix \mathbf{A} is divided into blocks. Normal matrix \mathbf{N} and \mathbf{w} are assembled separately for each segment and then summed up to form the complete matrices. For this procedure a `Math Kernel` library is used and the whole Gravity Field Recovery (GFR) process was done in the Leibniz University Computational Cluster (LUIS). Section 4.4 introduces the description of the utilized GFR software.

2.6 Validation of the Retrieved Gravity Field Models

Validation of the retrieved gravity field model is a necessary step to assess the quality of the solutions. Validation can be carried out in the spatial and spectral domains as well as with independent observations, e.g., GPS measurements (Wu, 2016).

In the spatial domain, the validation shows the geographical distribution of the errors. It can be computed as the difference between the reference and recovered gravity field models plotted on a global map, e.g., in terms of geoid height or Equivalent Water Height (EWH).

Taking the difference of the gravitational potentials, represented in a SH series (Equation (2.2)), of the retrieved and reference gravity models, one gets the disturbing potential T as

$$T = \frac{GM}{R} \sum_{n=0}^N \left(\frac{R}{r}\right)^{n+1} \sum_{m=0}^n [\Delta\bar{C}_{nm} \cos m\lambda + \Delta\bar{S}_{nm} \sin m\lambda] \bar{P}_{nm}(\cos\theta), \quad (2.31)$$

where $\Delta\bar{C}_{nm}$ and $\Delta\bar{S}_{nm}$ are the SH coefficient differences w.r.t. the normal gravity field, which is represented by the zonal SH coefficients of degree 0, 2, 4, 6, 8 (Heiskanen and Moritz, 1967).

The geoid height N representation can be calculated as (Torge et al., 2023):

$$N = R \sum_{n=0}^N \left(\frac{R}{r}\right)^{n+1} \sum_{m=0}^n [\Delta\bar{C}_{nm} \cos m\lambda + \Delta\bar{S}_{nm} \sin m\lambda] \bar{P}_{nm}(\cos \theta), \quad (2.32)$$

and EWH amplitudes are calculated by the following equation (Wahr et al., 1998; Schrama et al., 2007; Knabe, 2023):

$$\Delta\text{EWH} = \frac{R\rho_E}{3\rho_w} \sum_{n=0}^N \frac{2n+1}{1+k_n} \times \sum_{m=0}^n [\Delta\bar{C}_{nm} \cos m\lambda + \Delta\bar{S}_{nm} \sin m\lambda] \bar{P}_{nm}(\cos \theta), \quad (2.33)$$

where ρ_E is the Earth's average density, ρ_w the density of water and k_n the Love number of degree n .

In the spectral domain, the validation can be done within one- and two-dimensional error spectra. The formal errors (Dahle et al., 2019) $\sigma_{\bar{C}_{nm}}$ and $\sigma_{\bar{S}_{nm}}$ of the estimated spherical harmonic coefficients are calculated as the square root of the diagonal elements of the VCM of the estimated parameters, calculated by Equation (2.26) (Wu, 2016). Retrieved formal errors or SH coefficient differences can be represented in a triangular two-dimensional error spectrum, formed by degree and order, similar as depicted in Figure 2.1. In this dissertation, a logarithmic scale is used for a better representation of such graphs.

The two-dimensional error spectrum turns into a one-dimensional when the sum of the squares of the error of the SH coefficients at the same degree are calculated. The error degree variance can be calculated from the formal errors $\sigma_{\bar{C}_{nm}}$ and $\sigma_{\bar{S}_{nm}}$ as (Wu, 2016)

$$\sigma_n^2 = \sum_{m=0}^n \left(\sigma_{\bar{C}_{nm}}^2 + \sigma_{\bar{S}_{nm}}^2 \right). \quad (2.34)$$

When the formal errors are not available, they can be replaced by the true errors, which are the coefficient differences between the reference and estimated gravity fields: $\Delta\bar{C}_{nm}$ and $\Delta\bar{S}_{nm}$. In this thesis, the degree Root Mean Square (RMS) in geoid height is calculated from the degree variance σ_n^2 at a specific degree n as

$$\text{RMS}(\text{geoid height}) = \sqrt{\frac{\sigma_n^2}{2n+1}} \times R, \quad (2.35)$$

where R is the radius of the Earth.

2.7 Regularization of Retrieved Gravity Field Solutions

The upcoming Next Generation Gravimetry Mission (NGGM) is supposed to be placed in an inclined orbit with an inclination i between 65° and 70° (Haagmans and Tsaoussi, 2020) (more details about future gravimetry missions is given in Section 3.3). Therefore, near-polar and polar regions with the latitudes higher than $65 - 70^\circ$ will not be covered by such NGGM. This leads to the so-called ‘polar gap’ problem (Sneeuw and Van Gelderen, 1997) when the SH zonal and near-zonal coefficients are distorted and the gravity field retrieval becomes an ill-posed problem (Ditmar et al., 2003; Wu, 2016). An ill-posed problem is one that does not meet one of the three Hadamard criteria: existence of a solution, solution should be unique and it should depend continuously on the parameters or input data (Gockenbach, 2016).

As it was mentioned in Forsberg et al. (2011) and Lu et al. (2020), adding external information or additional measurements, for example, from the near-polar satellite pair or from airborne gravimetry could solve the ill-posedness of the problem. Gravity anomalies, computed from an a priori gravity field model and generating pseudo observations, could also tackle the polar gap problems (Yi, 2012).

Another option of stabilizing the solution is applying a regularization. For retrieving the gravity field from inclined satellite pairs, regularization is necessary to perform the inversion of the normal matrix in order to derive the SH coefficients, otherwise the inversion would crash. Moreover, regularization plays a role as a low-pass filter that suppresses high-frequency errors in a model due to the propagation of the noisy data (Ditmar et al., 2003).

Different regularization techniques exist, but in general, their common target is minimizing the L_2 -norm of the unknown function together with the L_2 -norm of its derivatives (Ditmar et al., 2003). This can also be expressed as minimizing the L_2 -norm of the disturbing potential T on the sphere of radius R , introduced in Equation (2.31). Initially, the regularization concept was developed by Tikhonov (Tikhonov, 1963a,b; Tikhonov and Arsenin, 1977), but many other techniques were applied in satellite gravimetry (Kusche and Mayer-Gürr, 2002; van Lonkhuyzen et al., 2002; Kaula, 2000). According to Metzler and Pail (2005) the Tikhonov regularization method could be of zero-order (when the applied regularization matrix \mathbf{R}_{reg} is the unit one), first-order (when the elements of the regularization matrix are defined as $r_{ij} = \delta_{ij}n(n+1)$) or second-order (when $r_{ij} = \delta_{ij}n^2(n+1)^2$) where n is the spherical harmonic degree.

Regularization is called Kaula, when the elements of \mathbf{R}_{reg} matrix correspond to the inverse Kaula rule (Kaula, 2000), in particular $r_{ij} = \delta_{ij}10^{10}n^4$. Two more Kaula regularization techniques can be mentioned with impact exclusively to spherical harmonic coefficients that are affected by the polar gap problem. Mathematically this can be written as

$$r_{ij} = \begin{cases} 10^{10}n^4, & \text{if } i = j \text{ and } m \leq m_{\text{reg}} \\ 0, & \text{otherwise} \end{cases}, \quad (2.36)$$

where m_{reg} is the maximum order of the spherical harmonic coefficient to which regularization is applied. According to Sneeuw and Van Gelderen (1997)

$$m_{\text{reg}} = \theta n, \quad (2.37)$$

where θ is the opening angle of the polar gap in radians. Metzler and Pail (2005) also mentioned so-called order-dependent Kaula regularization, defined as

$$r_{ij} = \begin{cases} 10^{10}n^4 (m_{\text{reg}} - m)^p, & \text{if } i = j \text{ and } m \leq m_{\text{reg}} \\ 0, & \text{otherwise} \end{cases}, \quad (2.38)$$

where p defines the order-dependent weighting, e.g., linear ($p = 1$), quadratic ($p = 2$), etc. The advantage of such approach consists of avoiding a significant low-pass filtering of the geopotential (Metzler and Pail, 2005).

With applied regularization, Equation (2.23), describing an estimated solution, can be re-written as (modified from Hansen (1999) and Wu (2016)):

$$\hat{\mathbf{x}} = (\mathbf{A}^T \mathbf{P} \mathbf{A} + \alpha \cdot \text{tr}(\mathbf{N}) \mathbf{R}_{\text{reg}})^{-1} \mathbf{A}^T \mathbf{P} \mathbf{l}, \quad (2.39)$$

where α is the regularization parameter and $\text{tr}(\mathbf{N})$ is the trace of the matrix \mathbf{N} . The trace of matrix equals the sum of its eigenvalues ($\lambda_1, \lambda_2, \dots$) and is associated with the largest eigenvalue (λ_{max}) of matrix \mathbf{N} . Multiplying the regularization parameter by the trace of the matrix means defining a cutoff of the eigenvalue spectrum at $\alpha \cdot \lambda_{\text{max}}$. Since eigenvalues are dependent on the normal matrix \mathbf{N} and consequently on the considered data of the specific month, the trace of the matrix was considered in this study as it provides more control and consistency.

Since the data that are used in gravity field recovery simulations includes various noise models, such as accelerometer noise, range instrument noise, etc., the selection of the proper regularization parameter is not a trivial task (Ditmar et al., 2003). Therefore, the L-curve method was applied to find the proper and most optimum regularization parameter α (Hansen, 1999). It is a graph where a solution norm $\|\hat{\mathbf{x}}\|_2$ is plotted w.r.t. the residual norm $\|\mathbf{A}\hat{\mathbf{x}} - \mathbf{l}\|_2$, showing the trade-off between the size of the regularized solution and its fit to the given data (Hansen, 1999). For the Tikhonov regularization method, normally this kind of graphs have an L-shape and therefore this method has its name.

2.8 Combination of Various Retrieved Gravity Field Solutions

In this work a combination of the simulated data acquired by the different measurement techniques (for example, the combination of range accelerations with cross-track gradiometry) or from the various orbits is widely used. Typically the combination is performed at the level of normal equations. Koch and Kusche (2002) introduced a Variance Component Estimation (VCE) approach for combining the data acquired by the different observation techniques. In this regard a summation of the weighted normal equations is done and Equation (2.23) can be represented as following (Knabe, 2023):

$$\hat{\mathbf{x}} = \mathbf{N}^{-1}\mathbf{W} = \left(\frac{1}{\sigma_1^2}\mathbf{N}_1 + \frac{1}{\sigma_2^2}\mathbf{N}_2 \right)^{-1} \left(\frac{1}{\sigma_1^2}\mathbf{w}_1 + \frac{1}{\sigma_2^2}\mathbf{w}_2 \right), \quad (2.40)$$

where σ_1^2, σ_2^2 are the variance components from the two different observation groups, acting here as weighting factors and $\mathbf{N}_1, \mathbf{N}_2$ are the normal matrices of the combined data (first and second). As it was mentioned in Koch and Kusche (2002), the variance components can be estimated iteratively, but in this work a one step iterations were used. The combination was applied for merging the data from the ll-SST and cross-track SGG (Section 6.3.3), from the different orbits of the novel triple satellite formations (Section 6.4.4) and from the satellite constellations of the Bender double pair configuration (Section 6.4.1).

2.9 Multi-step Integrator of Orbital Dynamics Simulator

Different satellite gravimetry mission scenarios were simulated in the MATLAB/Simulink software called Extended High Performance Satellite Dynamics Simulator (XHPS) (Wöske et al., 2016). Section 4.2 represents a more detailed description of XHPS.

In XHPS, a multi-step integrator was implemented to calculate the satellite dynamics, including the effect of the Earth's gravity field, various tidal components, third-body impacts and non-gravitational forces acting on the spacecraft. In XHPS, a system of differential equations is transformed into a system of Ordinary Differential Equations (ODE) which can be solved by one of the three numerical integration methods (upon the user choice): two embedded Runge-Kutta (RK) methods with optional local error control and adapted step size and an Adams-Bashforth-Moulton (ABM) multi-step predictor-corrector method with variable order. Wöske (2021) estimated CPU time and step size over the mean error for ABM and RK schemes and showed the superiority of the ABM integrator compared to the RK methods in terms of accuracy and efficiency. He also demonstrated that the ABM of the 8th order reached a maximal accuracy

for the step sizes that were also considered in this work (2.5 s) and higher orders do not show any advantage. Therefore, the ABM method of 8th order was used. As it was mentioned in Wöske (2021), since it is a multi-step method, the computation of the states at the new time point did not consider just the last known point but as many as the order of the scheme. That is why the number of initial conditions is the same as the order of the integration scheme. These additional conditions are automatically computed using the Dormand–Prince (DoPri87) algorithm (Dormand, 2018) and therefore the first steps are computed with the Dopri87 integrator. The stability of the ABM method solution is a function of the step size and the order of the scheme.

Equation (2.41) represents a system of the first order ODE that is solved by numerical integration within XHPS.

$$\frac{\partial \mathbf{x}}{\partial t} = \dot{\mathbf{x}} = \mathbf{f}(t, \mathbf{x}), \quad (2.41)$$

where \mathbf{x} is the so-called state vector with all variables of the system and \mathbf{f} the right-hand-side vector-valued function (Wöske, 2021).

Multi-step integrators interpolate the backpoints with a polynomial \mathbf{p} , which is evaluated at the desired time t_{n+1} and analytically integrated (Wöske, 2021). As it was demonstrated in Montenbruck et al. (2002) integrating Equation (2.41) from the last known time t_n to the new one t_{n+1} gives:

$$\mathbf{x}(t_{n+1}) = \mathbf{x}(t_n) + \int_{t_n}^{t_{n+1}} \mathbf{f}(t, \mathbf{x}(t)) dt \approx \mathbf{x}(t_n) + \int_{t_n}^{t_{n+1}} \mathbf{p}(t) dt, \quad (2.42)$$

where the polynomial $\mathbf{p}(t)$ approximates $\mathbf{f}(t, \mathbf{x}(t))$.

The ABM, so-called ‘predictor-corrector’, algorithm includes the Adams-Bashforth (AB) and Adams-Moulton (AM) methods. The ‘Prediction’ part (AB) consists in applying of the Newton method to determine a polynomial \mathbf{p} of order $m - 1$ with m known function values. But the approximation of the function $\mathbf{f}(t_{n+1})$ at the unknown time-step t_{n+1} is not accurate enough because it is outside of the known function values. Therefore, the ‘correction’ step (AM) suggests that the value at the unknown step $\mathbf{f}(t_{n+1})$ is also considered for the interpolation polynomial \mathbf{p} (Wöske, 2021). For a more detailed description of the ABM multi-step integration method, the reader is referenced to (Shampine, 1975).

2.10 Implemented Mathematics of the Accelerometer Modeling Environment

This section gives an overview of the mathematical apparatus implemented in the Accelerometer Modeling Environment (ACME) (Kupriyanov et al., 2024b).

A detailed description of the ACME software tool is done in Section 4.3. Here, the basics of the Test Mass (TM) dynamics, including assumptions, are presented.

2.10.1 Test Mass Dynamics - Assumptions and Physical Model

Equations describing the TM dynamics were taken from Kupriyanov et al. (2024b), which in turn were adapted from Theil (2002). For the satellite gravimetry mission utilizing the ll-SST measurement principle, with a single TM located at the Center of the Mass (CoM) of the spacecraft, the equation of motion of the TM in the inertial (I) reference frame looks like:

$$m\ddot{\mathbf{x}}^I = m\mathbf{g}^I(\mathbf{x}^I) + \mathbf{F}_C^I(\mathbf{x}^I, \dot{\mathbf{x}}^I, \mathbf{X}^I, \dot{\mathbf{X}}^I) + \mathbf{F}_{\text{ctrl}}^I, \quad (2.43)$$

where m is the mass of the TM, $\mathbf{x}^I, \dot{\mathbf{x}}^I, \ddot{\mathbf{x}}^I$ are the position, velocity and acceleration vectors of the TM, $\mathbf{X}^I, \dot{\mathbf{X}}^I$ are the position and velocity vectors of the satellite, \mathbf{F}_C^I the coupling force between the TM and the spacecraft, $\mathbf{F}_{\text{ctrl}}^I$ the control force that is applied to the TM from the actuation electrodes to keep the TM centered in the electrode housing. It is important to note, as it was mentioned in Theil (2002) and regardless of the instrument (e.g., electrostatic, optical or magnetic) that is utilized for sensing the TM displacements due to the affected non-gravitational forces, the displacement measurement can not be obtained without applying a force on the TM. Therefore, the coupling term comprises a combination of the force produced by the measurement and other coupling effects between the electrode housing and the TM, for example, residual gas particle collisions, electrostatic or magneto-static actions, internal gravitational effects, etc. Various measures can be applied in order to minimize the coupling effects, for example, magnetic shielding of the accelerometer, substitution of a polarization wire by an ultraviolet radiation charge management system (for more details see Section 3.2), placement of the TM at the CoM of the spacecraft, etc.

For the non drag-compensated mission, Equation (2.43), can be represented in the satellite frame (S) as:

$$m\ddot{\mathbf{x}}^S \approx \mathbf{F}_C^S - \mathbf{F}_{\text{ctrl}}^S. \quad (2.44)$$

This differential equation should account for six degrees of freedom (three linear and three rotational). However, in the ACME version that was utilized in the current research, an assumption is made that the relative displacements and inclinations of the TM are negligibly small and, therefore, all non-linear and cross terms have not to be considered (Kupriyanov et al., 2024b). Nevertheless, the system still can be implicitly represented as six ‘independent’ (given current assumptions) degrees of freedom, taking into account that control forces \mathbf{F}_{ctrl} and torques \mathbf{T}_{ctrl} are proportional to the TM’s position and rotation, respectively:

$$\begin{cases} F_{\text{ctrl}}(x) = b(x) \\ F_{\text{ctrl}}(y) = b(y) \\ F_{\text{ctrl}}(z) = b(z) \\ T_{\text{ctrl}}(\zeta) = \zeta \\ T_{\text{ctrl}}(\theta) = \theta \\ T_{\text{ctrl}}(\phi) = \phi \end{cases}, \quad (2.45)$$

where $b(x,y,z)$ is the displacement of the TM along x, y and z axes, ζ, θ, ϕ are roll, pitch and yaw angles of the TM.

2.10.2 Second-Order Integrator in Test Mass Dynamics

In the simulation procedure that was implemented (for more details, see Chapter 4), accelerometers and gradiometers modeled in ACME were integrated into the satellite dynamics simulator (XHPS) in order to simulate their behavior in an orbiting regime. Therefore, the ‘second-order integrator limited’ Simulink block that was implemented through ACME allows to integrate the differential Equation (2.44) with different solvers according to the user preferences (The MathWorks, 2024a). The aforementioned block is a dynamic system with two continuous states x and dx/dt which solve the second-order initial value problem:

$$\begin{aligned} \frac{d^2x}{dt^2} &= u, \\ \frac{dx}{dt} \Big|_{t=0} &= dx_0, \\ x \Big|_{t=0} &= x_0. \end{aligned} \quad (2.46)$$

Also, a ‘variable step solver’ option was selected within Simulink, as it allows automatically to adjust the step size (The MathWorks, 2024c). For example, when the model states change rapidly, the step size is reduced in order to increase the accuracy and when the model states change slowly, the step size is increased. Moreover, a local error at each time step was computed and compared w.r.t. acceptable error and, in case if the latter one was smaller, then the solver reduces the step size and repeat the procedure.

2.11 Chapter Summary

This chapter gives a detailed overview of the ‘fundamentals’, key terms and the mathematics that are widely used in this thesis. At the beginning of the chapter, the representation of the gravity field in spherical harmonic series is introduced (Section 2.1), then the measurement principles utilized in satellite gravimetry are

presented (Section 2.2). The chapter continues with the introduction to the amplitude spectral density (Section 2.3) and least-squares adjustment procedure in the gravity field recovery software (Section 2.4). Afterwards, it is explained how the stochastic modeling was applied in order to down-weight and de-correlate coloured noise measurements due to the low-frequency drift of the accelerometers (Section 2.5). In Section 2.6, equations of the physical quantities that can be used for the validations of the retrieved gravity field models are introduced. Applied regularization techniques for solving the ‘polar gap’ problem for the inclined orbits are given in Section 2.7. The applied Variance Component estimation approach for combining different types of measurements is presented in Section 2.8. The chapter ends with the description of the multi-step integrator that is used in the orbital dynamics simulator (Section 2.9) and the description of the test mass dynamics, assumptions and physical models of the accelerometer modeling environment (Section 2.10).

3 Past, Current and Future Satellite Gravimetry Missions and Technologies

3.1 Overview of Realised Gravity Missions and LISA-Pathfinder Flight Heritage

The Challenging Minisatellite Payload (**CHAMP**) was a satellite developed by the German Aerospace Center (DLR) and launched in July 2000 from the Russian launch site Plesetsk into an almost circular, near-polar orbit. This mission operated for 10 years and ended in 2010. The mission goals were: improved observations of the static and time-variable components of the gravity field, core and crustal magnetic fields, electric field, atmosphere sounding and GPS altimetry as an experiment (Reigber et al., 2006). The hl-SST measurement principle (see Figure 2.2) was utilized to determine the true orbit of the satellite. Taking into account the atmospheric perturbations, the difference between the true and unperturbed orbits provides the Earth's gravity field (Equation (2.3)). Perturbations caused by non-conservative, or in other words non-gravitational, forces were measured by the electrostatic Space Triaxial Accelerometer for Research Missions (STAR) (see Figure 3.1).

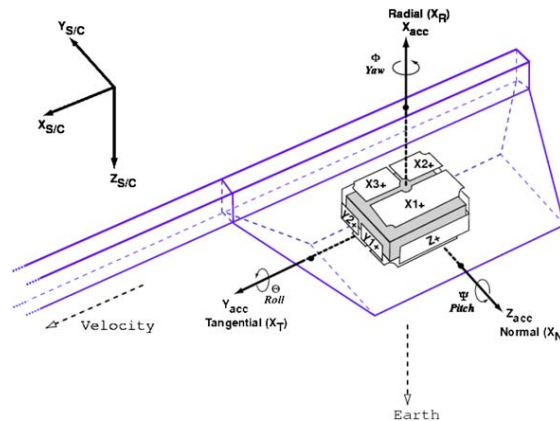


Figure 3.1: STAR accelerometer reference frame with respect to CHAMP satellite frame (Bruinsma et al., 2004)

As a result from the CHAMP mission, the first satellite-only gravity field model EIGEN-1S was determined, which improved the previous gravity models by more than a factor 2 (Reigber et al., 2002). Considering more years of Earth observation with CHAMP, a 10 cm geoid accuracy corresponding to a spatial resolution of 350 km (half wavelength) at the Earth's surface was resolved and a 1 cm geoid accuracy threshold obtained at 1000 km spatially (Reigber et al., 2005).

The Gravity Recovery and Climate Experiment (**GRACE**) was a joint mission of the National Aeronautics and Space Administration (NASA) and DLR launched from Plesetsk in March 2002 and operated till October 2017. The mission goals were: retrieving the static and time-variable components of the gravity field for long to medium wavelengths and atmosphere sounding (Case et al., 2010). GRACE consisted of two identical satellites orbiting in in-line formation within a range $220 \text{ km} \pm 50 \text{ km}$. This mission operated in a LEO, near-polar orbit with the initial altitude of 485 km. In addition to the instruments that were on-board the CHAMP mission, GRACE also had a microwave KBR inter-satellite system (Tapley et al., 2004; Kim and Lee, 2009), since the ll-SST with a high precision was a fundamental measurement of this mission. The connection of the gradient of the gravitational field with the observed range between the satellites was given in Equation (2.4). The contribution to the inter-satellite range from the non-gravitational forces was measured by electrostatic SuperSTAR accelerometers located at the center of mass of each spacecraft (see Figure 2.3). GRACE successfully reached the goals and provided the mm-geoid accuracy at globally high-resolution (up to 350 km) (Dahle et al., 2014). Moreover, the GRACE mission provided valuable measurements of the temporal variations of Earth’s gravity field on the global scale (Rodell et al., 2018).

GRACE-Follow On (**GRACE-FO**) is a successor of the GRACE mission. It was launched in 2018 with a Falcon rocket from the USA and has similar orbital parameters, payload and mission goals as GRACE. However, the major innovation in GRACE-FO was the utilization of the LRI (Sheard et al., 2012) as a technology demonstrator in addition to the KBR range measurement system. Inter-satellite distance observations with a laser interferometer provide measurements with nm level of accuracy (Abich et al., 2019), while the KBR microwave system only achieved the level of a few μm (Müller et al., 2022). A scheme of the inter-satellite laser ranging system that was implemented in GRACE-FO mission is depicted in the Figure 3.2.

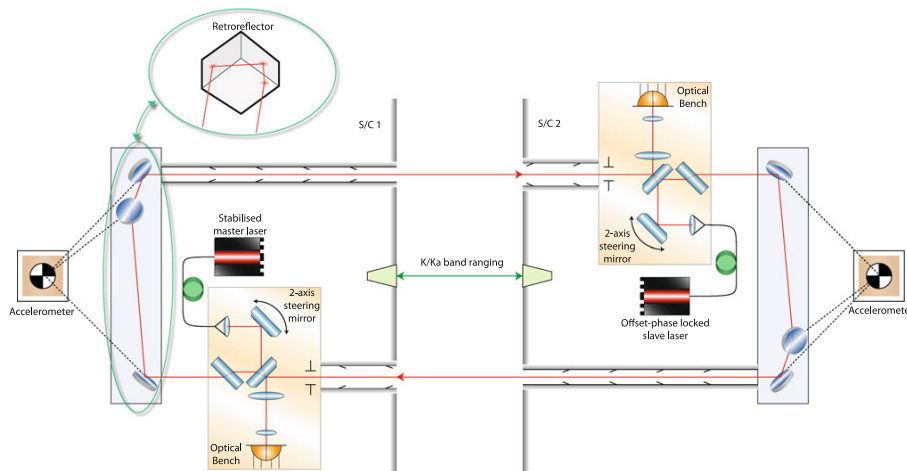


Figure 3.2: Layout of the laser ranging instrument on-board the GRACE-FO satellites (Sheard et al., 2012)

The Gravity Field and Steady-State Ocean Circulation Explorer (**GOCE**) was developed by the European Space Agency (ESA) and launched in March, 2009 (van der Meijde et al., 2015). It was the first mission utilizing the SGG principle. This mission was positioned as first Earth Core Explorer and was launched in a near-circular and sun-synchronous orbit at the initial altitude 255 km and inclination $i = 96.7^\circ$. Such a low altitude was maintained by the drag-free ion-propulsion system (Canuto, 2008). GOCE goal was to determine the geoid with an accuracy of 1 – 2 cm at a spatial resolution of 100 km. For this purpose, the satellite was equipped with a dedicated gradiometer that consisted of six electrostatic accelerometers (3 pairs of 3 axis) oriented orthogonal to each other. The gravitational gradient was determined through the differential mode accelerations (Equation (2.5)). GOCE has provided a geoid with centimeter level of accuracy at the spatial scales of 80 to 100 km (Gruber and Willberg, 2019).

The Laser Interferometer Space Antenna (**LISA-Pathfinder (LPF)**) was developed by ESA and launched in December 2015 from the European spaceport of Kourou to the parking orbit in the vicinity of Lagrange point L_1 (Armano et al., 2015). The main goal of this mission was to demonstrate feasibility of the intra-satellite laser interferometer technologies which will be used in future ESA gravitational wave observatory named LISA (Armano et al., 2018a). For this purposes, LPF carried two heavy (1960 g), compared to those that were used in satellite gravimetry before (e.g., 72 g in GRACE-FO), cubical-shaped test masses with a high precision laser metrology block, forming so-called optical accelerometers. In addition, the LPF spacecraft was equipped with a drag-free control using an ultra-precise propulsion system (Armano et al., 2015). Figure 3.3 from Armano et al. (2019) shows a simplified sketch of the LPF satellite with its major technical components.

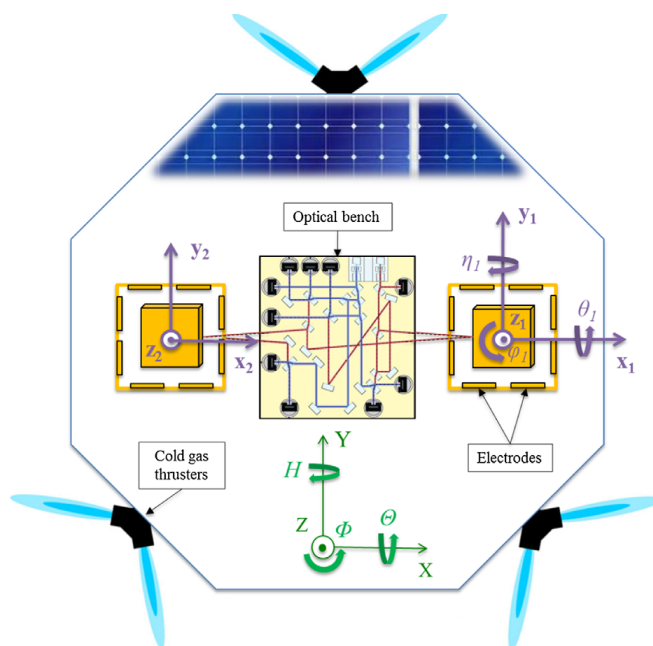


Figure 3.3: Simplified scheme of the LISA-Pathfinder spacecraft (Armano et al., 2019)

Two test masses were put in a nearly perfect gravitational free-fall and the laser interferometer measured the relative position and orientation of one of the test masses with respect to the other one (Armano et al., 2016). The LPF showed very promising results. Among other things, it has demonstrated the benefit of a drag-free system in combination with optical accelerometry (Armano et al., 2019; Wanner, 2019; Bortoluzzi et al., 2021; Miller and Mendes, 2023).

Table 3.1 summarizes information regarding realised LEO satellite gravimetry missions (CHAMP, GRACE, GRACE-FO and GOCE) and LPF. The missions are sorted there by year of the launch and the table includes the actual mission duration, orbital parameters (initial altitude and inclination), major payload instruments, mission goals and main features.

Table 3.1: Orbital parameters, payload and major features of the realised satellite gravimetry missions and LISA-Pathfinder, ordered by launch year (based on Armano et al. (2009, 2016); Audley et al. (2011); Christophe et al. (2015); Dalin et al. (2020))

Mission name	Actual mission duration	Altitude (after launch)	Inclination	Payload	Mission goals	Major features
CHAMP	2000-2010	454 km	87°	<ul style="list-style-type: none"> - 3-D electrostatic accelerometer - GPS receiver (16 channels) - Laser retro-reflector - 2 Star cameras - Magnetometer - Digital ion drift meter 	<ul style="list-style-type: none"> - Gravity field: static & time variable - GPS altimetry (experiment) - Magnetic field: core & crustal field - Electric field - Atmosphere sounding 	<ul style="list-style-type: none"> - Non-gravitational accelerations observation with 3×10^{-9} m/s² accuracy - GPS observations for orbit determination - Atmosphere sounding
GRACE	2002-2017	485 km	89°	<ul style="list-style-type: none"> - 3-D electrostatic accelerometer - GPS receiver (24 channels) - Laser retro-reflector - 2 Star cameras - K-band microwave ranging system 	<ul style="list-style-type: none"> - Gravity field: static & time variable in low frequency domain - Atmosphere sounding 	<ul style="list-style-type: none"> - Non-gravitational accelerations observations with 1×10^{-10} m/s² accuracy - GPS observations for orbit determination - Inter-satellite measurements with μm accuracy
GOCE	2009-2013	255 km	96.5°	<ul style="list-style-type: none"> - Gradiometer incl. 6 electrostatic accelerometers - GPS/GLONASS receiver (12 channels) - Laser retro-reflector - Standard Radiation Environment Monitor - Drag-free control 	<ul style="list-style-type: none"> - Static gravity field - Geoid determination with accuracy of 1-2 cm at resolution of 100 km 	<ul style="list-style-type: none"> - Differential mode accelerations from gradiometer with measurement noise $11 \text{ mE} = 11 \times 10^{-12} \text{ s}^{-2}$ - GPS observations for orbit determination - Drag-free system compensating non-gravitational accelerations
LISA-Pathfinder	2015-2017	Lissajous orbit around L_1		<ul style="list-style-type: none"> - Two 3-D optical accelerometers - High precision laser metrology block - Ultra-precise μN propulsion system - Drag-free control 	<ul style="list-style-type: none"> - Measure deviations from geodesic motion - Demonstrate feasibility of intra-satellite laser interferometry 	<ul style="list-style-type: none"> - Movement of two free-falling test masses with relative acceleration noise with PSD at sub-femto-g level ($5.2 \pm 0.1 \text{ (fm/s}^2\text{)}/\sqrt{\text{Hz}}$) - Ultra-precise drag-free system compensating non-gravitational accelerations
GRACE-FO	2018-present	450 km	89°	<ul style="list-style-type: none"> - 3-D electrostatic accelerometer - GPS receiver (24 channels) - Laser retro-reflector - 3 Star cameras - K-band microwave ranging system - Inter-satellite laser ranging interferometer (LRI) as a technology demonstrator 	<ul style="list-style-type: none"> - Gravity field: time variable - Atmosphere sounding 	<ul style="list-style-type: none"> - Non-gravitational acceleration observation with 1×10^{-10} m/s² accuracy - GPS observations for orbit determination - Inter-satellite measurements by LRI with 40 nm accuracy

3.2 Accelerometers Used in Gravimetry Missions

The use of accelerometers in orbit for gravity field missions started with the German CHAMP mission in 2000. The electrostatic 3-axis Space Triaxial Accelerometer for Research Missions (**STAR**) was on-board CHAMP measuring capacitively three linear and three angular accelerations. In the measurement range of $\pm 10^{-4} \text{ m s}^{-2}$, STAR achieved a resolution of better than $3 \times 10^{-9} \text{ m s}^{-2}$ for the y and z axes, or corresponding to the along-track and cross-track directions (see Figure 3.1). For the x axis (nadir direction), $3 \times 10^{-8} \text{ m s}^{-2}$ was achieved (Touboul et al., 2012). The test mass with a shape of parallelepiped, made from titanium alloy and coated by chromium, has been suspended by six servo-controlled loops according to its six degrees of freedom. In principle, all electrostatic accelerometers utilized the so-called ‘servo-controlled’ concept (Touboul et al., 2012), where the applied electrostatic correction forces keep the test mass motionless in the electrode housing according to the capacitive sensing. In the left part of Figure 3.4, a STAR sensor unit is depicted.

The **SuperSTAR** accelerometer that was utilized in both GRACE and GRACE-FO missions became the successor of the STAR instrument. This quasi-identical sensor, with certain advantages, was able to achieve the $10^{-10} \text{ m s}^{-2}$ level of accuracy (Daras and Pail, 2017). The mechanical core of the SuperSTAR, including the test mass and the plates with the electrodes, is shown in the middle of Figure 3.4.

The satellite gravity gradiometry mission GOCE utilized electrostatic accelerometers called **GRADIO**, which in principle are identical to the STAR and SuperSTAR instruments, but heavier and with a denser proof mass (Touboul et al., 2012). In GRADIO a platinum-rhodium alloy was used, which has more weight (320 g) in the same dimensions rather than the other STAR-class instruments. Heavier proof masses together with larger gaps between the test mass and the surrounding electrode housing enables a measurement precision at the level of $3 \times 10^{-12} \text{ m s}^{-2}$ (Rodrigues et al., 2022) along the high sensitive axis of the gradiometer (Marque et al., 2010; Touboul et al., 2016).

However, all current STAR-class electrostatic accelerometers (STAR, SuperSTAR and GRADIO) have a characteristic feature that also acts as one of the major limiting factors in nowadays satellite gravimetry missions. Figure 3.5 shows a comparison of the ASD of the accelerometers, where a prominent decrease of accuracy at the frequencies below 1 mHz is noticeable. This reflects the so-called ‘drift’ of the electrostatic accelerometers (Frommknecht et al., 2003; van Camp et al., 2021) that is mainly caused by the polarization wire that connects the test mass with the electrode housing and is a significant source of stiffness (Christophe et al., 2015). This polarization wire is needed to remove the accumulated electrical charge that occurs due to bombarding cosmic rays. A significant contribution to this drift is also provided by the thermal instability of the system (Dalin et al., 2020; Maquaire et al., 2023).

The LISA-Pathfinder (LPF) mission was a pioneer of utilizing optical interferom-

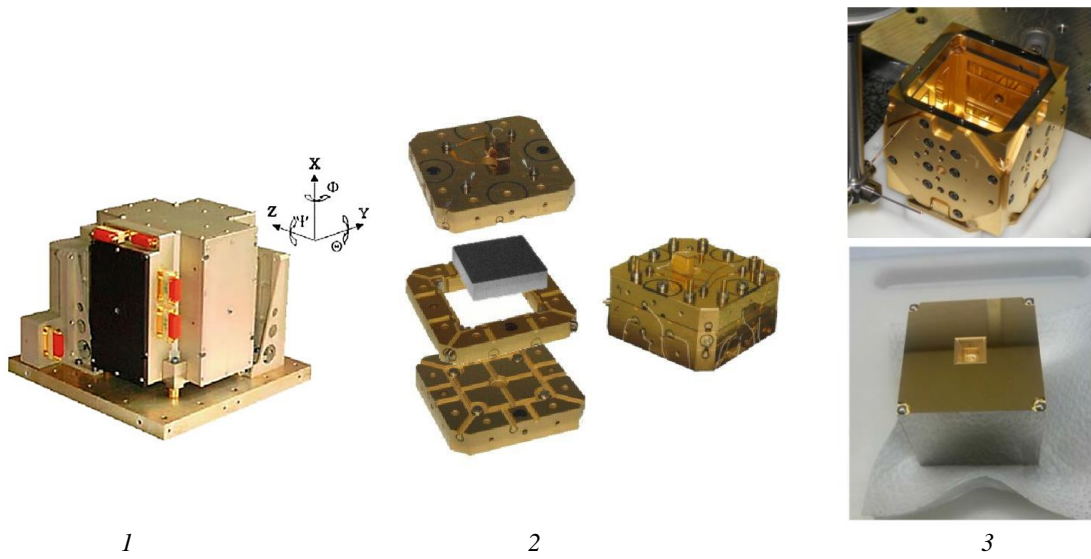


Figure 3.4: State of the art accelerometers. 1 - STAR sensor unit before integration in the CHAMP satellite (Touboul et al., 2012); 2 - SuperSTAR accelerometer mechanical core from GRACE mission (Touboul et al., 2012); 3 - Electrode housing (top) and test mass (bottom) of the LISA-Pathfinder mission (Armano et al., 2015)

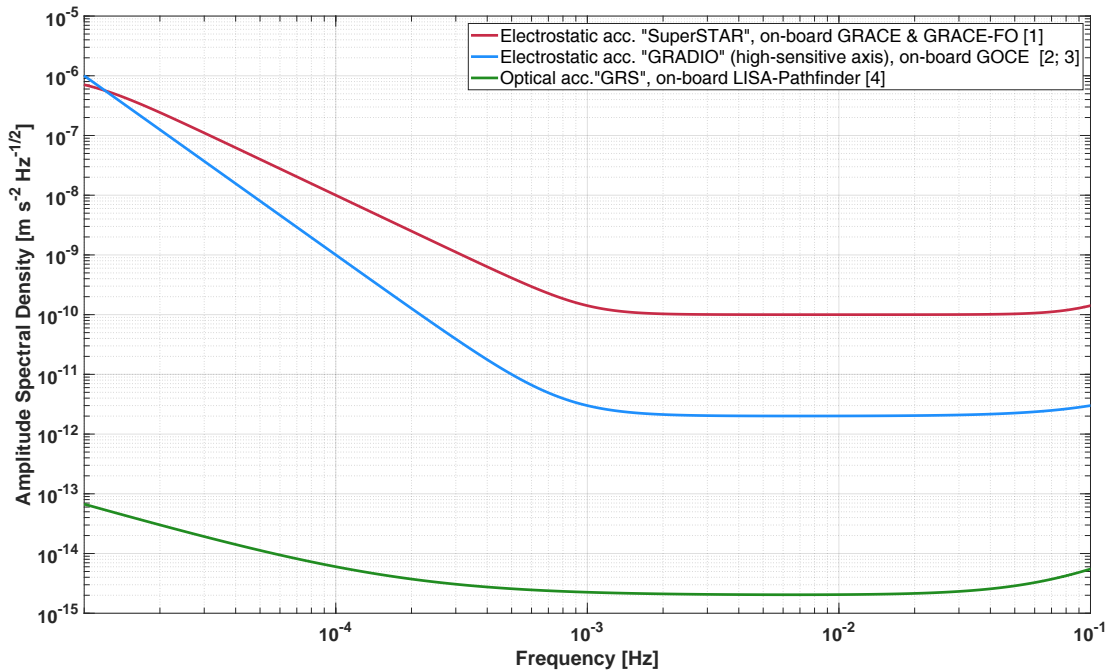


Figure 3.5: Comparison of the ASD sensitivities of current accelerometers. SuperSTAR used in GRACE and GRACE-FO [1] - Daras and Pail (2017); high-sensitive axis of GRADIO from GOCE [2, 3] - Touboul et al. (2016), Marque et al. (2010); GRS from LISA-Pathfinder [4] - Armano et al. (2018a)

etry to readout the test mass displacements. The optical accelerometer of LPF is called Gravitational Reference Sensor (**GRS**) (Armano et al., 2018a). Several novel techniques were used in space in the GRS for the first time. One of the major innovations was the use of an ultraviolet radiation charge management system (Armano et al., 2018b) instead of a polarization wire that was used in previous spaceborne electrostatic accelerometers. The working principle of the wireless charge management system was explained in Sumner et al. (2020) and consists of impinging ultraviolet light on the test mass which excites and expels the extra electrons from the test mass, keeping the electrostatic noise sources at an acceptable level. The utilization of wireless discharging technology allowed to increase the cubical-shaped test mass weight up to 1960 g and the gap between the proof mass and electrode housing. All these innovations, together with the operating LPF in the quiet space environment in the vicinity of the Sun-Earth Lagrange point L_1 , with almost complete absence of non-gravitational disturbing forces, allowed to reach an accuracy at the unprecedented level of $2 \times 10^{-15} \text{ (m/s}^2\text{)}/\sqrt{\text{Hz}}$ for a frequency range approximately from 1 mHz to 30 mHz (Armano et al., 2018a). The amplitude spectral density of the GRS from LISA-Pathfinder is depicted in Figure 3.5 and a photo of the electrode housing with the cubic-shaped test mass on the right side of Figure 3.4.

Table 3.2 summarizes the major design characteristics and performance levels of the STAR-class electrostatic accelerometers (STAR, SuperSTAR and GRADIO) together with the optical inertial sensor GRS from the LISA-Pathfinder mission.

Table 3.2: Summary table of accelerometer performances and design parameters (based on Touboul et al. (1999, 2012); Armano et al. (2018a); Rodrigues et al. (2022))

Space mission	CHAMP (2000-2010)	GRACE (2002-2017) GRACE-FO (2018-now)	GOCE (2009-2013)	LISA-Pathfinder (2015-2017)
Accelerometer name	STAR	SuperSTAR	GRADIO	GRS
Accelerometer type	electrostatic	electrostatic	electrostatic	optical
Charge management system	polarization wire	polarization wire	polarization wire	wireless, LED UV
Measurement bandwidth (Hz)	10^{-4} to 10^{-1}	10^{-4} to 10^{-1}	5×10^{-3} to 10^{-1}	10^{-4} to 10^0
Level of accuracy ($(\text{m/s}^2)/\sqrt{\text{Hz}}$ @ 1 mHz)	3×10^{-9}	$\sim 1 \times 10^{-10}$	3×10^{-12}	2×10^{-15}
Test mass material	Chromium coated Titanium alloy	Chromium coated Titanium alloy	Platinum-rhodium alloy	Gold-platinum alloy
Test mass weight (g)	72	72	320	1960
Test mass dimensions (mm) [x/y/z]	40 / 10 / 40	40 / 10 / 40	40 / 10 / 40	46 / 46 / 46
Gap between the test mass and electrode housing (mm) [x/y/z]	0.075 / 0.06 / 0.075	0.175 / 0.06 / 0.175	0.299 / 0.032 / 0.299	4 / 2.9 / 3.5

3.3 Overview of Upcoming Gravimetry Missions

Mass change was identified by US National Academy of Sciences in the Decadal Survey for Earth Science and Applications as one of the five designated observables that have the highest priority in terms of Earth observations for the

2017-2027 decade (Wiese et al., 2022). For this purpose and in order to have a continuity in the time-series of gravity measurements, a successor of the current GRACE-FO mission called GRACE-Continuity (**GRACE-C**), previously known as Mass change mission, is anticipated. At the time of writing (first half of 2024), GRACE-C successfully passed the Preliminary Design Review (PDR), major steps towards its realization started and the mission is planned to be launched in 2028. According to the press releases, published on 19 March 2024, by Airbus (Airbus, 2024), DLR (DLR, 2024) and Albert Einstein Institute (AEI, 2024), GRACE-C is expected to be built in a German-American partnership and shall substitute the current GRACE-FO mission, utilizing in general the same instruments, technologies and near-polar ($i = 89^\circ$) orbit. According to Haagmans and Tsaoussi (2020), GRACE-C will only use a LRI as an inter-satellite laser ranging instrument.

On the European side, another GRACE-like satellite gravimetry pair called Next Generation Gravimetry Mission (**NGGM**) is planned to be launched in 2031 into an inclined orbit ($i = 65^\circ$ - 70°) with a drag-compensation system. GRACE-C in near-polar orbit and NGGM in an inclined one form the Mass change And Geosciences International Constellation (**MAGIC**). The ESA Council Meeting at Ministerial Level allocated €2.7 billion for Earth science research in November 2022, in particular €120 million for the MAGIC project (ESA, 2022). The MAGIC double pair, so-called Bender (Bender et al., 2008) constellation, shall reach an unprecedented high spatial and temporal resolution of less than one week and provide a significant contribution to emergency and near-real-time (from daily to subweekly) applications (Massotti et al., 2021). In the mission requirement document, the threshold accuracy of 10.1 cm EWH at high spatial resolution 260 km for unfiltered solutions was mentioned. Also, (Daras et al., 2023) demonstrated that the double satellite pair MAGIC formation could significantly lower the detectable earthquake moment magnitude from M 8.8 to M 8.0 compared to weekly solutions of a single-pair configuration.

However, the topic of orbit selection, in particular inclination and altitude for the NGGM (inclined) mission is a complicated problem. It poses a trade-off between reduction of retrieval errors at latitudes that will be covered by both satellite pairs and at high-latitude regions which would be visited only by the single near-polar pair (Heller-Kaikov et al., 2023). In the MAGIC Mission Requirement Document (Haagmans and Tsaoussi, 2020) an inclination between $i = 65 - 70^\circ$ was proposed. Multiple orbit optimization studies for satellite gravimetry were carried out, for example, by Iran Pour et al. (2021); Murböck et al. (2014). Specific double pair constellations were also broadly studied by Iran Pour et al. (2015); Dobsław et al. (2016); Daras and Pail (2017); Hauk and Pail (2018); Dionisio et al. (2018); Srinivasan et al. (2019); Purkhauser et al. (2020); Haagmans et al. (2020); Hauk and Wiese (2020); Massotti et al. (2021); Wiese et al. (2022); Heller-Kaikov et al. (2023); Kupriyanov et al. (2024b).

In this thesis, an inclined orbit for NGGM with an altitude of around 400 km and an inclination $i = 70^\circ$ was considered. According to Heller-Kaikov et al. (2023), these orbital parameters, together with a drag-compensation system, should allow

to get a 5-day repeat subcycle.

As it was already mentioned in Section 1.1, since CAI accelerometers are anticipated to have a high-level resolution performance, using these sensors in ll-SST configuration provide an interesting perspective for measuring the time-variable gravity field (Haagmans et al., 2020). The recently started Cold Atom Rubidium Interferometer in Orbit for Quantum Accelerometry - Pathfinder Mission Preparation (**CARIOQA-PMP**) project, funded by the European Union, has an objective of increasing the technology readiness level and preparing a Quantum Pathfinder mission for space gravimetry by 2030 (Lévêque et al., 2023).

On 9 May 2024, the University of Florida published a press release stating that NASA has selected their proposed Gravitational Reference Advanced Technology Test in Space (**GRATTIS**) mission for a launch around 2027 aboard a SpaceX Falcon 9 rocket (Hinds, 2024). This mission is supposed to demonstrate end-to-end functionality and the accuracy level of the Simplified Gravitational Reference Sensor (SGRS) (ESTO-NASA, 2024). Two identical SGRS are planned to be mounted next to each other at the center of mass of the commercial microsatellite. The mission goal is declared to demonstrate the acceleration noise level of $10^{-11} \text{ (m/s}^2\text{)}/\sqrt{\text{Hz}}$. Within the next years the science team of the University of Florida, together with other institutes and companies, will finalize the sensor technology and integrate it into the spacecraft.

3.4 Novel Electrostatic Accelerometer Concepts

Various studies have been carried out evaluating the performance of anticipated inertial instruments and their concepts, as mentioned in the Introduction. In this section, a more detailed overview of four well-studied, realistic and technically feasible concepts of electrostatic accelerometers for the near future is given.

Fifteen accelerometers developed and built by the French aerospace lab ONERA have been used in space for geodesy and fundamental physics applications (Rodrigues et al., 2022). This manufacturer, which also built electrostatic accelerometers for all previous gravimetry missions, i.e. GRACE, GOCE and GRACE-FO, presented two STAR-class concepts of electrostatic accelerometers with a cubic-shaped test masses, named **CubeSTAR** and **MicroSTAR** (Dalin et al., 2020). A cubic proof mass gives various advantages, in particular enabling the same level of accuracy on all three axes with full performance in orbit (Rodrigues et al., 2022). This is important since with parallelepiped-shaped test masses of the SuperSTAR and GRADIO accelerometers additional geometry adjustments, i.e. gap reduction has to be done. MicroSTAR is supposed to have a cubic proof-mass with a 3 cm side length, while the CubeSTAR has 2 cm, and lower voltages to simplify the electronics and make this sensor compatible for CubeSat missions. Both instruments, CubeSTAR and MicroSTAR, shall sense the non-gravitational accelerations in six degrees of freedom, i.e. three linear and three rotational. It is expected that CubeSTAR will have an analog control of the proof mass, while MicroSTAR a digital one with an option of analog for

lower power consumption (Dalin et al., 2020). CubeSTAR is anticipated to have a similar level of accuracy ($\sim 1 \times 10^{-10} \text{ (m/s}^2\text{)}/\sqrt{\text{Hz}}$ @ 1 mHz with 100 μm gap between test mass and electrode housing) as the SuperSTAR instrument, but in all three axes. MicroSTAR shall reach the GRADIO accelerometer level of performance $\sim 2 \times 10^{-12} \text{ (m/s}^2\text{)}/\sqrt{\text{Hz}}$ @ 1 mHz (Christophe et al., 2018). But for both concepts the mechanical noise of the thin gold wire is a limiting factor (Rodrigues et al., 2022). Mechanical cores as well as physical development models of CubeSTAR and MicroSTAR accelerometers are shown in Figure 3.6. The ASD curve of the MicroSTAR instrument is given in Figure 3.7 where a prominent drift in the low-frequency domain is noticeable.

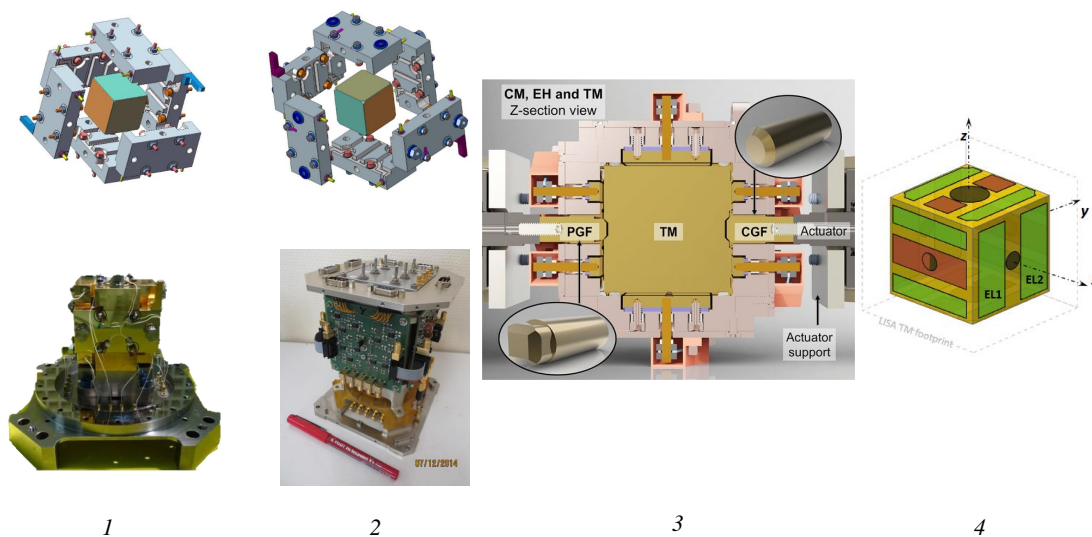


Figure 3.6: Improved accelerometer concepts. 1 - CubeSTAR mechanical core (top) and CubeSTAR prototype under integration (bottom) (Christophe et al., 2019); 2 - MicroSTAR mechanical core (top) and its development model of the Front End electronics (bottom) (Christophe et al., 2015); 3 - Section view of the charge management (CM), electrode housing (EH) and test mass (TM) of the SGRS (Dávila Álvarez et al., 2022); 4 - Scheme of the LISA-GRS test mass for future inter-satellite geodesy missions (Weber et al., 2022)

Dávila Álvarez et al. (2022) developed a novel Simplified Gravitational Reference Sensor (**SGRS**) that could be used in future gravimetry missions. There, a heavy (540 g) cubic-shaped test mass is supposed to have a wireless UV photoemission-based charge management system. Eliminating the polarization wire allowed to have a larger gap between the proof mass and the electrode housing. The SGRS performance has been evaluated in two mission scenarios: at 350 km altitude on a drag-free platform and at 500 km in a non-drag compensated regime. In the latter scenario, a level of accuracy of $\sim 6 \times 10^{-12} \text{ (m/s}^2\text{)}/\sqrt{\text{Hz}}$ is anticipated. Despite the fact that SGRS measures the test mass displacements and rotation capacitively, it is possible, in principle, to utilize optical sensors to determine TM position and attitude.

A scheme of the SGRS, including the charge management system, electrode housing and a test mass, is shown in Figure 3.6 and the ASD curves of both scenarios

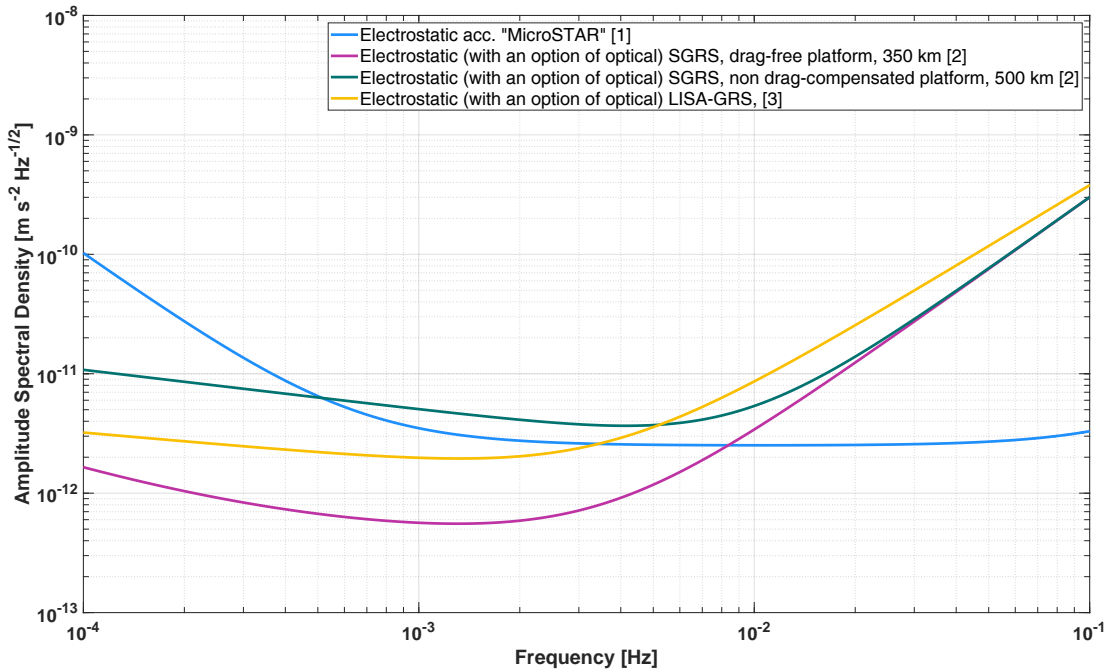


Figure 3.7: Comparison of the ASD sensitivities of improved accelerometer concepts. MicroSTAR [1] - Dalin et al. (2020); SGRS on drag-free and non-drag compensated platforms [2] - Dávila Álvarez et al. (2022); LISA-GRS for future inter-satellite geodesy missions [3] - Weber et al. (2022)

are plotted in Figure 3.7.

Another concept of an inertial instrument is called **LISA-GRS** for future inter-satellite geodesy missions, that was inspired by the performance of optical accelerometry from the LISA-Pathfinder mission, was proposed by Weber et al. (2022). There, an even heavier (790 g), also cubic-shaped (side 34 mm) test mass is capacitively sensed and the UV photoemission wireless charging system is used. Authors are anticipating a residual proof mass acceleration noise at the level of $2 (\text{pm/s}^2)/\text{Hz}^{-1/2}$ at 1 mHz. A sketch of the LISA-GRS test mass is shown in Figure 3.6 and the ASD curve of the anticipated instrument performance in Figure 3.7.

Table 3.3 summarizes the major design characteristics and performance levels of some of the electrostatic accelerometers concepts, i.e. CubeSTAR, MicroSTAR, SGRS and LISA-GRS.

Table 3.3: Summary table of enhanced electrostatic accelerometers concepts, their performances and design parameters (based on Christophe et al. (2018); Dalin et al. (2020); Dávila Álvarez et al. (2022); Weber et al. (2022); Liorzou et al. (2023)). * specific test mass material and gap of the CubeSTAR accelerometer depends on the mission specification (Portier (2024) personal communication); ** estimated from the test mass size given by Dalin et al. (2020) and considering platinum-rhodium material; *** non drag-free platform

Accelerometer name	CubeSTAR*	MicroSTAR	SGRS	LISA-GRS for Future Intersatellite Geodesy Missions
Proposed by	ONERA	ONERA	Dávila Álvarez et al. (2022)	Weber et al. (2022)
Accelerometer type	electrostatic		electrostatic (with an option of optical)	
Charge management system	polarization wire	polarization wire	wireless, LED UV	wireless, LED UV
Level of accuracy ((m/s ²)/√Hz @ 1 mHz)	$\sim 1.5 \times 10^{-10}$	$\sim 3.9 \times 10^{-12}$	$\sim 6 \times 10^{-12}$ ***	$\sim 2 \times 10^{-12}$
Test mass material	Platinum-rhodium alloy	Platinum-rhodium alloy	Gold coated Titanium alloy	Gold-platinum alloy
Test mass weight (g)	65**	218	540	790
Test mass dimensions (mm) [x/y/z]	20/ 20/ 20	30/ 30/ 30	30/ 30/ 30	34/ 34/ 34
Gap between the test mass and electrode housing (mm) [x/y/z]	0.1/ 0.1/ 0.1	0.4/ 0.4/ 0.4	1/ 1/ 1	0.8/ 0.8/ 0.8

3.5 Chapter Summary

This chapter gives an overview of the realized LEO satellite gravimetry missions (CHAMP, GRACE, GOCE, GRACE-FO) and LPF flight heritage (Section 3.1) with the comparison of their accelerometer performances and design parameters (Section 3.2). The chapter ends with an overview of upcoming spaceborne gravimetry missions (Section 3.3) and the discussion of four improved concepts of electrostatic accelerometers and the comparison of their level of accuracy and technical features (Section 3.4).

4 Simulation Procedure and Software Overview

In this chapter, a closed-loop simulation procedure and the basics of the implemented software tools are described. Different software parts and tools were utilized in order to perform satellite dynamics calculations (Section 4.2), simulate novel accelerometers and gradiometers (Section 4.3) and retrieve gravity field models using various sensors in different satellite formations (Section 4.4).

4.1 Closed-loop Simulation Procedure

A Matlab/Simulink software named eXtended High Performance Satellite Dynamics Simulator (XHPS) (Wöske et al., 2016; Wöske, 2021) was utilized to simulate the dynamics of the various spaceborne gravimetry missions, i.e. similar to GRACE and GOCE, as well as novel satellite formations. The XHPS environment conveniently allows also to include ancillary instruments, i.e. a drag compensation system (Knabe et al., 2022). As it is illustrated in the block-scheme diagram of the closed-loop simulation procedure for ll-SST cases in Figure 4.1, calculated coordinates of two spacecraft are given as an input to the GFR software tool Quantum Accelerometry (QACC) (Wu, 2016), which is coded in Fortran and operated at the Leibniz University Computational Cluster, due to the involved high computational demands. For the ll-SST (GRACE-like) simulations, noise-free range accelerations are generated at the satellite positions that are provided from XHPS. Modeling of the various accelerometers and gradiometers is carried out with the tool ACME, (Kupriyanov et al., 2024b). This software tool was designed to work as a standalone or integrated into the satellite simulator XHPS. ACME runs concurrent with XHPS in Simulink. The noise budget of the accelerometers and gradiometers is acquired as ASDs in the frequency domain. Afterwards, the ASDs are transformed into instrument noise time-series. Finally, in QACC the noise-free range accelerations are combined with inertial instruments' and range sensor noise' time-series. After the estimating of the SH parameters of the retrieved gravity field model by least-squares adjustment, the obtained gravity model is compared with the reference one. As a reference gravity field, the European Improved Gravity model of the Earth by New techniques (EIGEN)-6C4 has been taken. This high-resolution global gravity field model up to SH degree and order (d/o) 2190 include: LAGEOS-1/2 satellite laser ranging data to d/o 30, GRACE GPS satellite-to-satellite tracking and K-band range-rate data till d/o 175, GOCE data and terrestrial global anomaly data (Förste et al., 2014).

For GFR from satellite gradiometry missions, the procedure is, in general, similar to ll-SST. The difference is that only a single satellite orbit has to be integrated in XHPS and the noise-free gravity gradients are then combined with the cor-

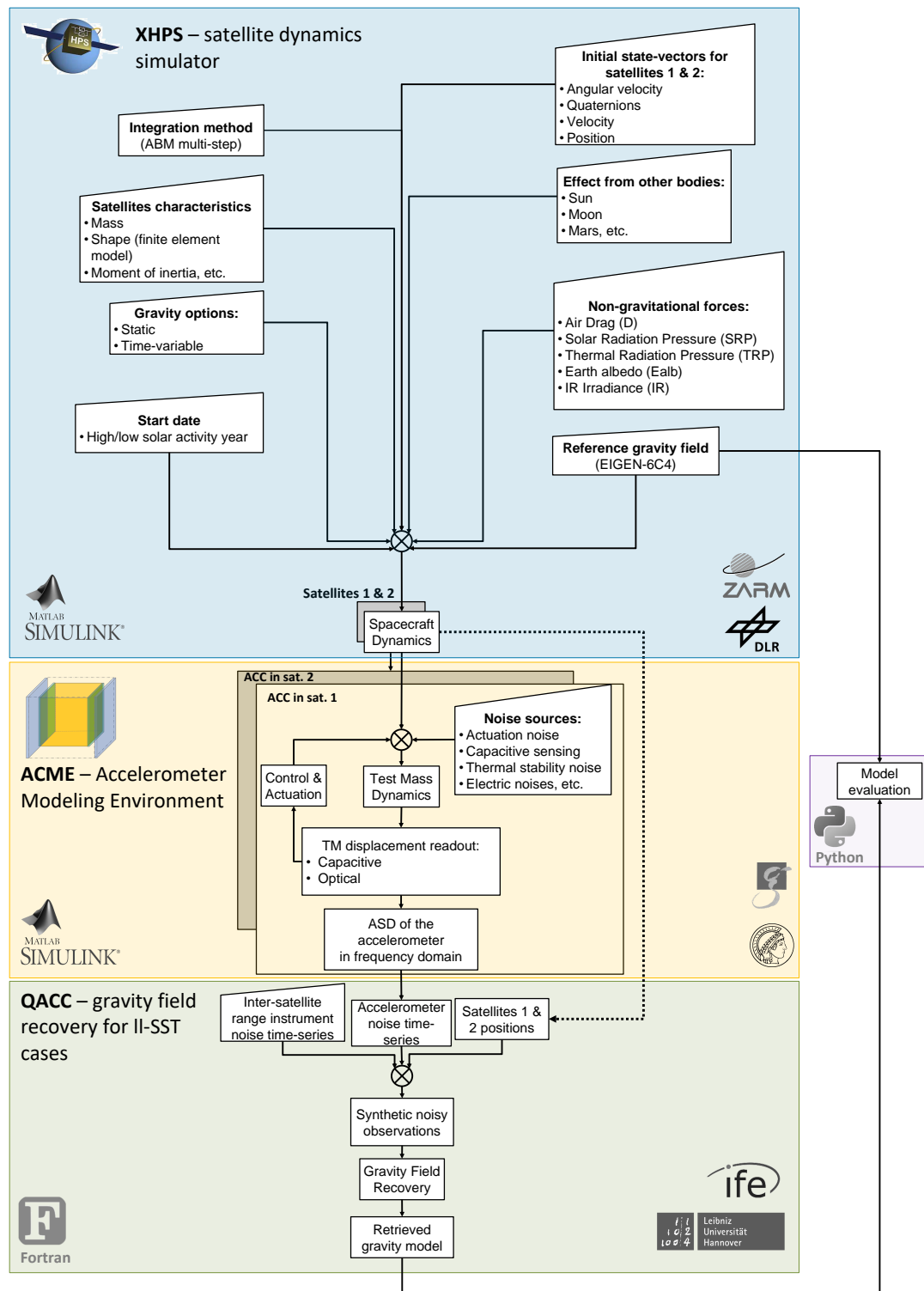


Figure 4.1: Block-scheme diagram of the closed-loop simulation procedure for II-SST simulations

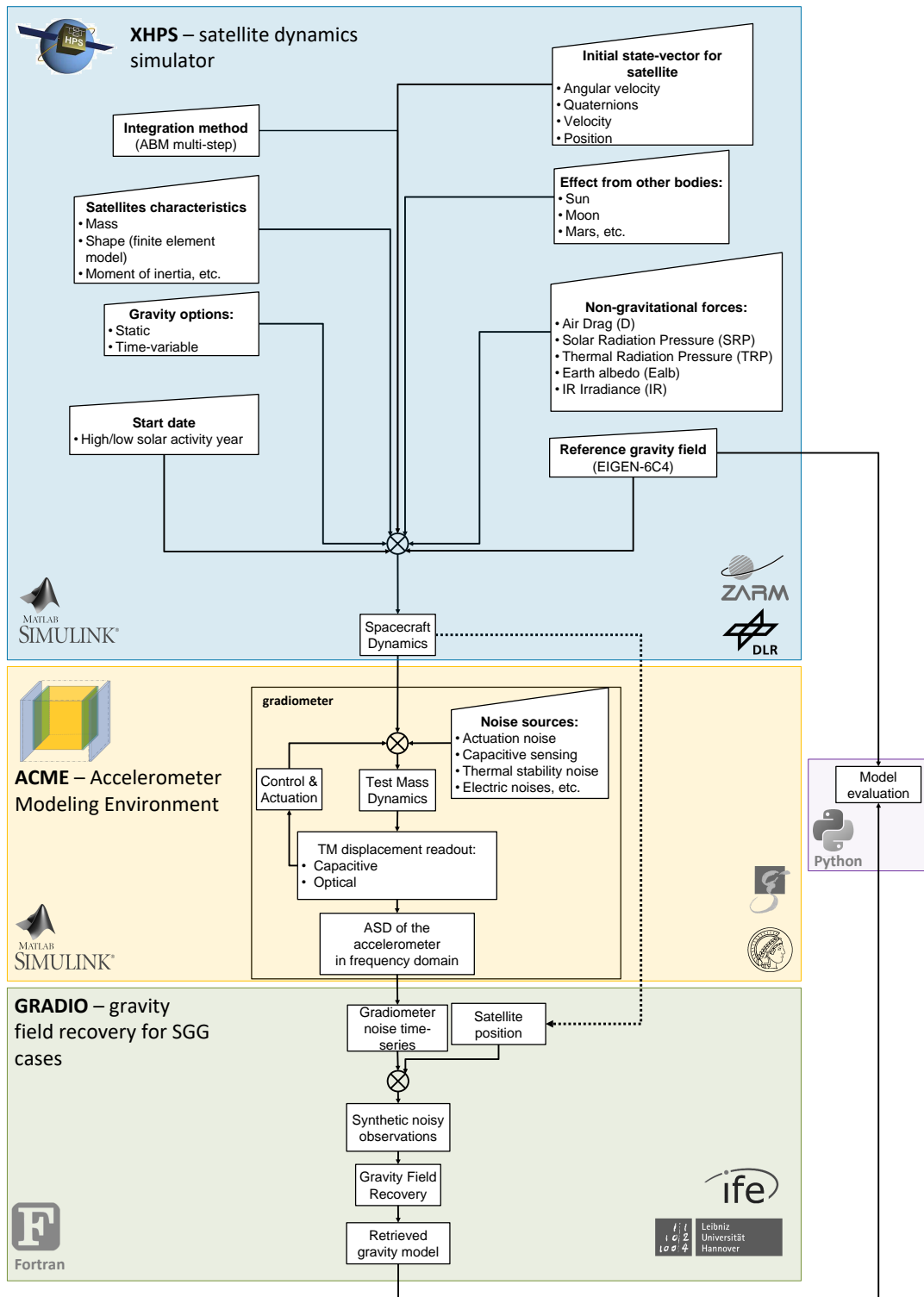


Figure 4.2: Block-scheme diagram of the closed-loop simulation procedure for gradiometry simulations

responding gradiometer noise time-series in the GRADIO GFR software (Wu, 2016). The block diagram of the closed-loop procedure for the SGG case is shown in Figure 4.2.

4.2 Satellites Dynamics Simulator

XHPS was developed by the Center of Applied Space Technology and Micro-gravity (ZARM, Bremen) and the Institute for Satellite Geodesy and Inertial Sensing, German Aerospace Center (DLR, Bremen). This Matlab/Simulink software transforms a system of differential equations into a system of ordinary differential equations and solves it with double precision. Dynamics of single or multiple spacecraft are calculated by applying a multi-step integrator which user can select (Wöske, 2021). For satellite dynamics simulations in this work, an Adams-Bashforth-Moulton predictor-corrector integrator of 8th order was utilized (Section 2.9). Various input parameters can be selected by the user, e.g., the static gravity field with certain maximum degree and order, different time-variable tidal models (ocean, solid Earth, Pole tide) as well as third-body contributions and non-gravitational forces. Also, different spacecraft shapes can be considered in XHPS. In this work, for all simulations (except section with modified spacecraft shapes), a finite element model of the GRACE-like satellite was considered (Wöske et al., 2018). In Subsection 4.2.1, the considered background and environmental models, as well as the non-conservative forces that are crucial in LEO satellites dynamics, are introduced. Subsection 4.2.2 introduces key parameters of the simulated orbits.

4.2.1 Environmental Background Models and Non-gravitational Forces

Accurate orbit propagation of the LEO gravimetry satellites is possible with detailed and high-precision modeling of the perturbations acting on the spacecraft. In reality, precise orbit determination of gravimetry satellites is required for obtaining plausible results (Wöske et al., 2018). In the utilized orbital dynamics simulator XHPS, various background models are possible to be included in the simulations. Table 4.1 summarizes perturbations that were included in the orbital simulations in this study as well as the considered SH degrees and orders (d/o). In particular, the static gravity field EIGEN-6C4 (Förste et al., 2014) was used till d/o 180, for ocean tides, the EOT11a model Savcenko and Bosch (2012) till d/o 120 was selected, and the IERS 2010 (Petit and Luzum, 2013) models for solid Earth tides (till d/o 4) and pole tides (till d/o 180). The analytical DE430 ephemeris model of Folkner et al. (2014) was chosen for calculating the orbit of the spacecraft. Also, solar and lunar impacts were included in the satellite dynamics computations.

Non-conservative, so-called non-gravitational forces affecting the satellites can be caused by five sources in XHPS: Air Drag (D), Solar Radiation Pressure (SRP),

Thermal Radiation Pressure (TRP), Earth albedo (Ealb) and Infrared Irradiance (IR). The considered models of the non-gravitational forces are also listed in the Table 4.1. For example, the calculation of air drag was based on the JB2008 atmosphere density model (Bowman et al., 2008) which, in turn, is correlated with the solar activity. For SRP calculation, a point-like Sun and geometric eclipse options were selected. The satellite's relative velocity computation was based on the Horizontal Wind Model 1993 (Hedin et al., 1996). Earth albedo and infrared irradiance were taken from the hourly Clouds and the Earth's Radiant Energy System (CERES) database and geostationary Top of Atmosphere (ToA) fluxes (Doelling et al., 2013, 2016).

The strengths of the non-gravitational forces depend on multiple factors, such as altitude of the orbit, type of solar activity (high or low), shape and mass of the spacecraft, etc. In all orbit simulations in this study, the mass of a single spacecraft was considered equal to 478 kg, which is close to the GRACE launching weight (NASA, 2002). A finite element model of the GRACE satellite body was used (Wöske et al., 2018) and a constant drag coefficient equal to 2.25 was taken. This value was selected in accordance with the analysis of Wöske et al. (2018). It is in the range of a typical number for a convex-shaped spacecraft (Montenbruck et al., 2002).

Table 4.1: Considered background models in orbital simulations. [1] - Förste et al. (2014); [2] - Savcenko and Bosch (2012); [3] - Petit and Luzum (2013); [4] - Folkner et al. (2014); [5] - Bowman et al. (2008); [6] - Doelling et al. (2013); [7] - Doelling et al. (2016)

Perturbation	Model	Remark
Static gravity field	EIGEN-6C4 [1]	considered till d/o 180
Ocean tides	EOT11a [2]	considered till d/o 120
Solid Earth tides	IERS 2010 [3]	considered till d/o 4
Pole tides	IERS 2010 [3]	considered till d/o 180
Ephemeris model	DE430 [4]	-
Third bodies: - Sun - Moon	-	-
Non-gravitational forces: - Air Drag (D)	JB2008 [5]	-
- Solar Radiation Pressure (SRP)	-	- SRP calculation case: point-like Sun -Eclipse calculation case: geometric eclipse
- Thermal Radiation Pressure (TRP)	-	-
- Earth albedo (Ealb)	Daily CERES and geostationary ToA fluxes [6; 7]	-
- Infrared Irradiance (IR)	Daily CERES and geostationary ToA fluxes [6; 7]	-

In this study, a one-month mission duration in May 2002 was considered. According to the history of the sunspot number, which represents the activity of the entire visible disk of the Sun (NOAA, 2024), provided by the SILSO World Data Center (1954-2024), there was one of the solar maxima (Figure 4.3). A period with high solar activity (when the air-drag and SRP are high) was deliberately chosen to make sure that the parameters for the electrostatic levitation of the TM were sufficient and the accelerometer would not saturate.

Figure 4.4 shows the amplitude spectral density comparison of the affected non-

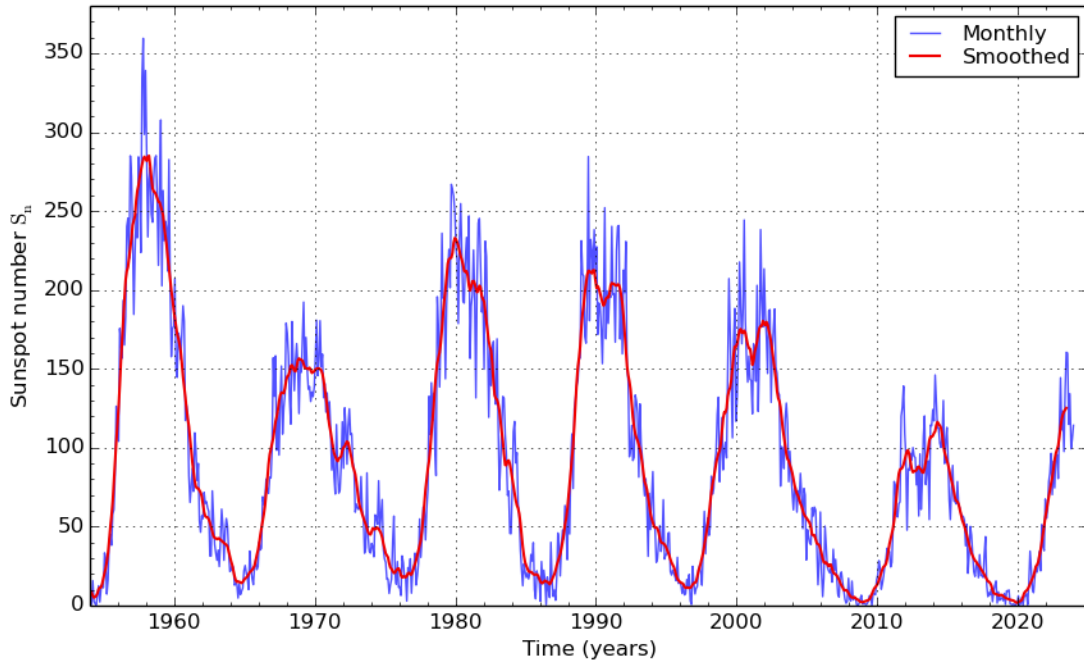


Figure 4.3: Monthly mean (blue) and 13-month smoothed (red) international sunspot number (SILSO World Data Center, 1954-2024)

gravitational accelerations in the altitude 450 km for years with high (May, 2002) and low (May, 2006) solar activities. A one order of magnitude difference can be noticed between the curves.

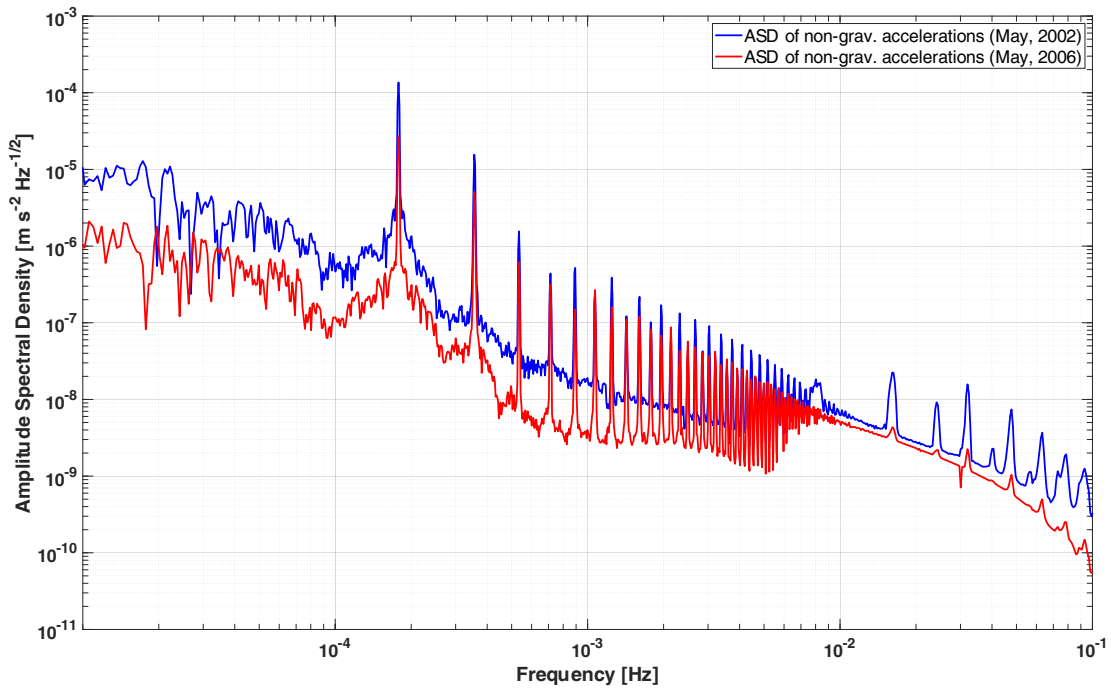


Figure 4.4: Amplitude spectral density of the non-gravitational accelerations for the year with high solar activity (2002) and low solar activity (2006). Orbit parameters: $h = 450$ km, $i = 89^\circ$

Time-series of the non-gravitational accelerations at altitude 450 km are shown for May, 2002 in Figure 4.5. Taking into account the mass of the satellite $M_{\text{sat}} = 478$ kg, dissipative accelerations were calculated in XHPS from the corresponding forces:

$$a_{\text{non-grav}} = \frac{F_{\text{non-grav}}}{M_{\text{sat}}}. \quad (4.1)$$

In along-track (upper graph in Figure 4.5) and cross-track (middle graph) directions, the largest perturbation comes from the D (blue curve). While in nadir direction, SRP, consisting of absorbing or reflecting the photons from the Sun, is dominating. TRP due to the heating of the satellite, Ealb and IR from the Earth's surface have minor effects in comparison to the former ones.

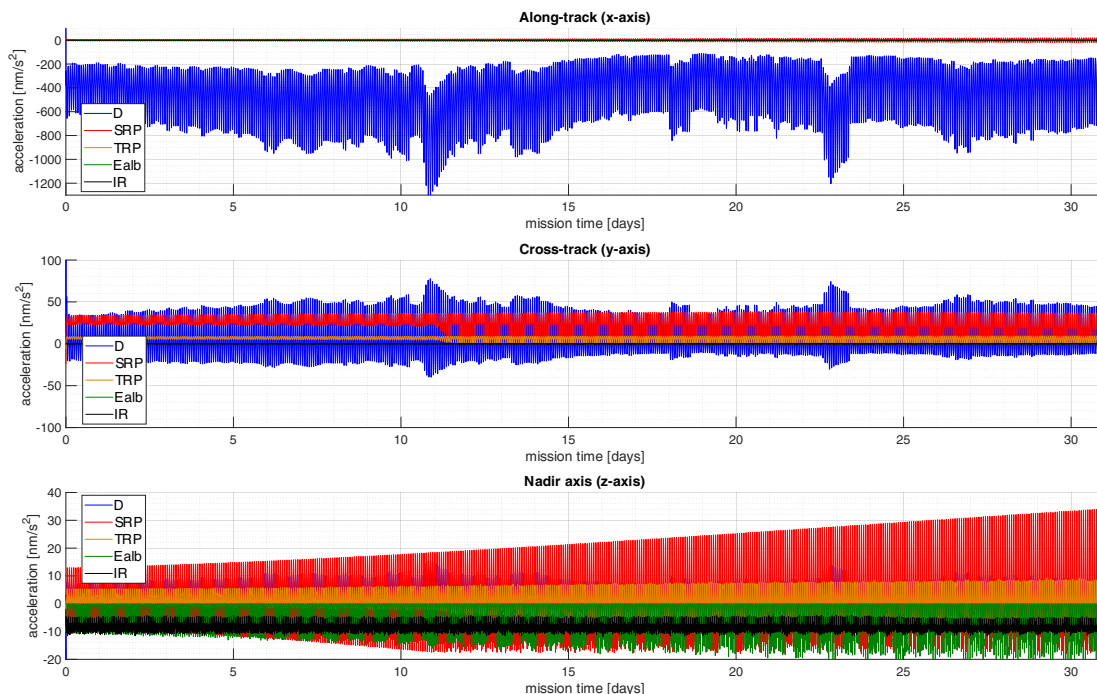


Figure 4.5: Time-series of the non-gravitational accelerations that were considered in the orbit simulator for May, 2002. Orbit parameters: $h = 450$ km, $i = 89^\circ$. Note the different orders of magnitude on the plots.

4.2.2 Description of the Simulated Orbits

Since one focus of this study is to evaluate the performance of the novel accelerometers and gradiometers and also investigate novel satellite formations, different orbits, listed in the Table 4.2, were simulated. Altitudes of the considered orbits vary from 247 km to 478 km according to the type of mission. Inclinations and right ascension of the ascending node angles are also given in the table. Orbits #1 and #4 have parameters according to the MAGIC mission requirement document (Haagmans and Tsaoussi, 2020) that will realize a so-called Bender double

satellite pair constellation. The first orbit (#1) was taken for comparison of the GFR results in the ll-SST case (GRACE-like), and together with orbits #2 and #3, they form novel triple satellite formations. Finally, the lowest orbit #5 was chosen for performing SGG analyses. In all near-polar orbits except the inclined one (#4), an inclination around $i = 90^\circ$ was taken in order to have a small polar gap area. Also, a Line of Sight (LOS) attitude control system was chosen for all scenarios to ensure a precise pointing of the leading and trailing satellites to each other. Orbits #1 to #3 are considered as non-drag compensated, while #4 and #5 are drag-free. There, the effect of all non-gravitational forces was not included in the orbital simulations or, in other words, a perfect drag compensation system was assumed.

Table 4.2: Overview of the orbits utilized in the simulations

orbit index	mean altitude [km]	i [°]	Ω [°]	mean inter-sat. distance [km]	Drag compens.	type of GFR simulation
1	478.48	89.03	203.47	207.55	no	- Near-polar orbit in ll-SST comparison - Near-polar orbit in Bender constellation - Near-polar orbit in novel triple satellite formation
2	478.48	90.03	203.47	207.87	no	- 2 nd orbit in novel triple satellite formation (differ by inclination)
3	478.48	89.03	204.47	207.79	no	- 2 nd orbit for novel triple satellite formation (differ by RAAN)
4	396.55	70.01	203.47	194.79	yes	- Inclined orbit in Bender constellation
5	247.35	89.03	203.47	203.96	yes	- Near-polar orbit in SGG comparison - Near-polar orbit for combination ll-SST + SGG

4.3 Inertial Sensor Modeling Environment

Electrostatic and optical accelerometers and gradiometers with the parameters based on the GRS from the LISA-Pathfinder mission were modeled in Matlab/Simulink software, called ACME (Kupriyanov et al., 2024b). This toolbox was mainly developed by the Max Planck Institute for Gravitational Physics at Albert Einstein Institute (Reis et al., 2022a), in a collaborative project of the SFB 1464 Relativistic and Quantum-based Geodesy (TerraQ). The author of this thesis also contributed in testing, debugging and integrating of ACME in the satellite dynamic models in XHPS software. This section gives an overview of the techniques, physical models and approaches that were incorporated in SGRS instruments in ACME, that replicate processes of real instruments. Corresponding assumptions are also mentioned.

4.3.1 Accelerometers Modeling

In general, accelerometers can be divided into three groups according to their measurement techniques: electrostatic, optical and CAI (Chapter 1). The first two are able to be simulated in ACME. Electrostatic and optical inertial sensors measure a control signal voltage which corresponds to the actuation force applied to the TM in order to keep it at the nominal position in the non-drag free or

accelerometer regime. More precisely, this force ensures that the TM remains centered within the EH (Kupriyanov et al., 2024b). In case of electrostatic sensors, this voltage is caused by a discrepancy between capacitance on a pair of electrodes around the TM due to its movement. An acting acceleration can be inferred from the control voltage by applying the appropriate transfer function. For a capacitive sensing, electrodes are mounted on the walls of the EH, and the TM is made from conductive material, e.g., gold-platinum alloy, to form a capacitor with the electrodes at each side. Plane parallel capacitors were considered in ACME in order to model equations of capacitive detector electronics and actuation from Josselin et al. (1999). Figure 4.6 shows an illustration of the simplified one-degree-of-freedom accelerometer. In this figure, actuation and sensing electrodes on the walls of the EH cage have a size equal to the full area of one face of the EH. And the hatched green sides of the TM surfaces, together with the nearby electrodes, form the capacitors.

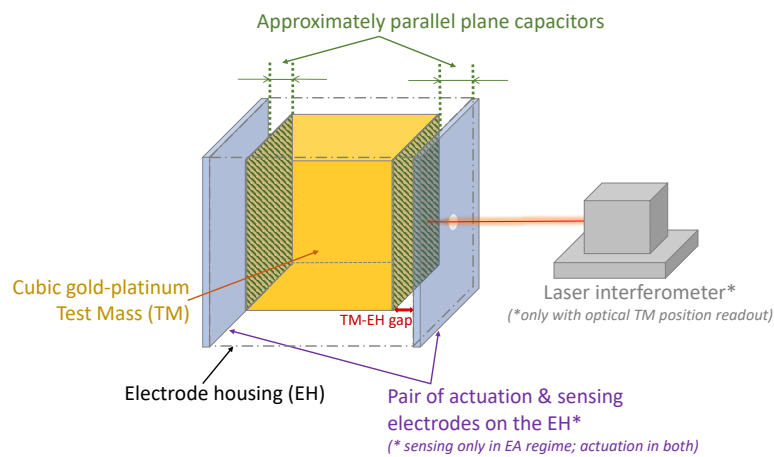


Figure 4.6: Illustration of a one-degree-of-freedom accelerometer model (Kupriyanov et al., 2024b)

ACME was designed in a way that the user can define the quantity and orientation of the actuation and sensing electrodes. For example, Figure 4.7 shows a six-degrees-of-freedom accelerometer model, with six pairs of actuation and sensing electrodes oriented in a way that allows to sense three linear and three rotational displacements. Note that for clarity, the injection electrodes driven with a 100 kHz AC bias voltage that are used for shifting the capacitive measurement to a high frequency (Dávila Álvarez et al., 2022) are not shown here. Also, the window for the ultraviolet TM discharge system, the caging mechanism and the valve for outgassing are not drawn here.

For an optical readout of the proof mass displacement, one surface of the TM acts as a mirror, except the cases of shadow sensors (Zoellner et al., 2017). In general, the TM displacement can be readout by optical interferometry, e.g., Michelson or Mach-Zehnder interferometers or by an optical lever. Figure 4.8 demonstrates a simplified scheme of the Michelson interferometer (on the left) and of the quadrant-photodiode type optical lever (on the right). In the first case, the displacement of the proof mass will cause a difference in the interference

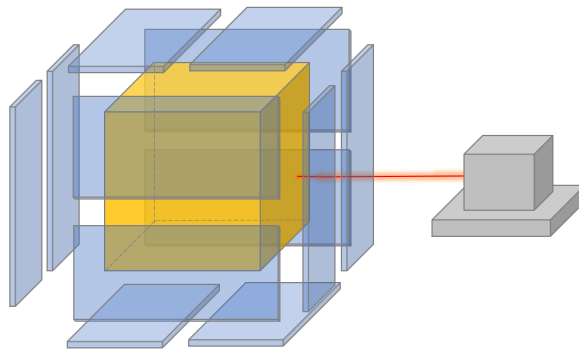


Figure 4.7: Illustration of a six-degrees-of-freedom accelerometer model

pattern (Heinzl et al., 2003) and in the second case, a change of the position of incidence of the beam onto a quadrant photodiode (Huarcaya et al., 2020).

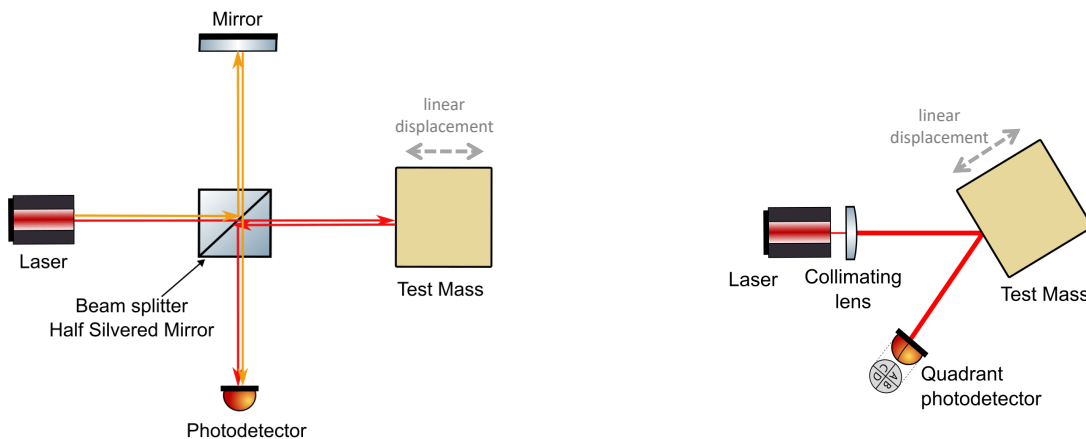


Figure 4.8: Different techniques (optics) to readout a one-degree-of-freedom test mass displacement. *Left*: Scheme of the Michelson interferometer; *Right*: Conventional photodiode-type optical lever with a single frequency laser (modified from Shimizu et al. (2017)). Optic schemes were drawn with publicly available Component Library (A. Franzen, AEI, Hannover, 2021)

Actuation of the TM is achieved by means of electrostatic levitation. A 100 kHz 5 V AC injection voltage (U_{inj}), mentioned earlier, is electrostatically coupled to the TM, producing polarized voltage (U_p) (Mance, 2012), which was considered in SGRS derived in ACME equal to 0.5 V. The polarized voltage on the TM was maintained via capacitive injection. Considering no displacement of the TM from its nominal position, an equation describing the control force from a single electrode will look like (Josselin et al., 1999; Kupriyanov et al., 2024b):

$$\mathbf{F}_{ctrl}(U) = \frac{2\varepsilon A}{d^2} U_p U_{act} \hat{\mathbf{n}}, \quad (4.2)$$

where A is the area of each electrode, U_{act} the actuation voltage, d the gap between the TM and the walls of the housing, ε the dielectric constant of vacuum and $\hat{\mathbf{n}}$

is the normal vector to the electrode.

Figure 4.9 illustrates a generalized block diagram of a one-degree-of-freedom SGRS modeled in ACME. This closed-loop procedure is similar to those that were introduced by Speake and Andrews (1997), Touboul et al. (1999), Frommknecht et al. (2003). As an input, non-gravitational forces modeled in XHPS are given. Under these forces, the TM is displaced. The proof mass dynamics is represented by a double integrator. After implementing the corresponding sensing electronics, a correction voltage through the PID controller and amplifier is sent back to adjust the TM position and keep it levitating. Also, multiple instrument noise sources were considered in SGRS modeling, in particular: thermal, actuation, capacitive sensing, various electrostatic, etc. (Kupriyanov et al., 2024b).

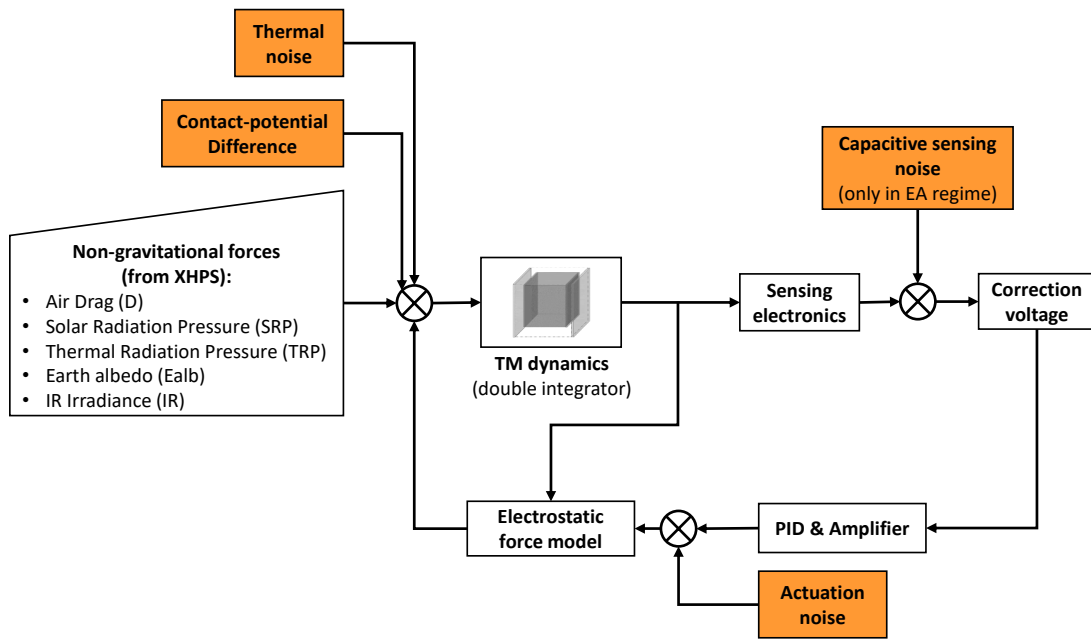


Figure 4.9: Generalized and simplified one-degree-of-freedom accelerometer block diagram

ASD curves of the SGRS noise sources are shown in Figure 4.10. Actuation noise (black dashed line) is related to the stable voltage reference for the actuation electrodes (Mance, 2012). For actuation noise modeling, 10 V of the reference voltage with a $0.6 \text{ ppm}/\sqrt{\text{Hz}}$ voltage reference stability are considered. The latter one is assumed as over the last decade, the integrated circuit technology has improved in comparison to Halloin et al. (2013). Capacitive sensing and the electrostatic noise level (green and orange dashed curve) depend on the characteristics of the involved electronics (Kupriyanov et al., 2024b). The dominant noise sources there could be a thermal noise of the sensing bridge (Mance, 2012) or the voltage noise of the charge amplifiers (Lotters et al., 1999; Dávila Álvarez et al., 2022). The thermal stability noise level (yellow dashed curve) depends on the Brownian motion of the residual gas molecules inside the EH and on the differential pressure due to unbalanced radiation on different sides of the housing (Carbone et al., 2007). For SGRS derived in ACME the thermal stability in

the low frequency domain was considered similar to the MicroSTAR electrostatic accelerometer (Christophe et al., 2018; Dalin et al., 2020), introduced in Section 3.4. The sensing noise of a laser interferometric readout is disregarded here at first approximation due to a low level (Dávila Álvarez et al., 2022). Additionally, the non-gravitational forces act on the TM through the spacecraft-TM coupling (Josselin et al., 1999). Considering all above-mentioned noise sources, one can notice that the difference between the electrostatic and optical SGRS is given only at high frequencies (> 10 mHz).

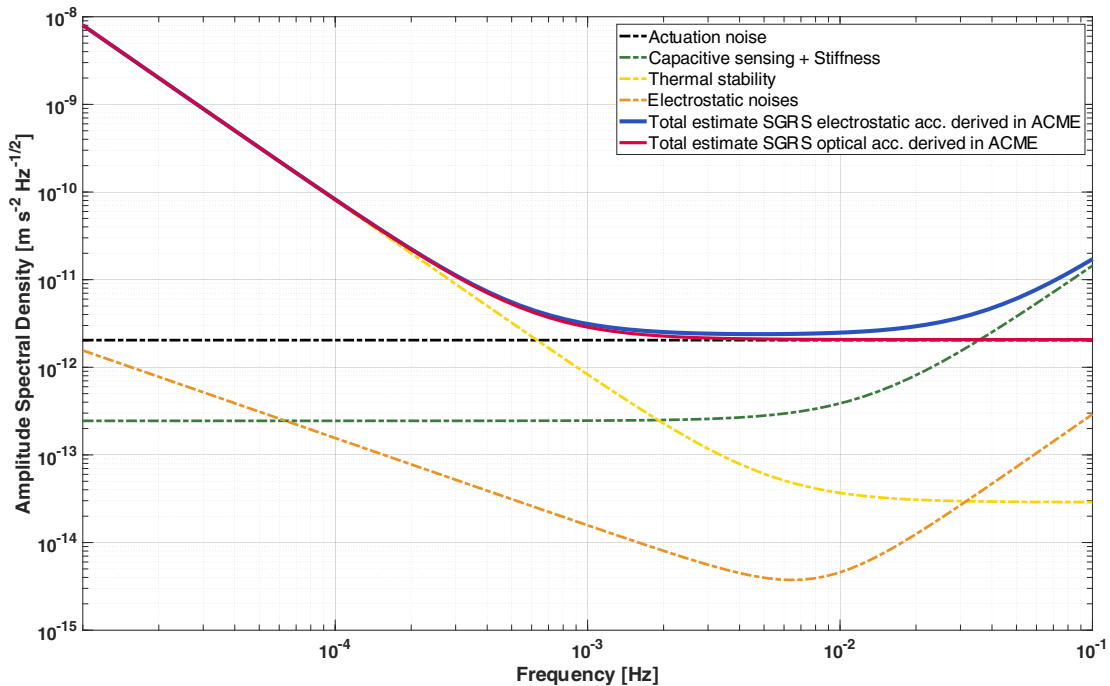


Figure 4.10: ASD of the noise budget of the modeled SGRS (both electrostatic and optical) in ACME

A parametrization of the modeled SGRS electrostatic accelerometer w.r.t. weight of the TM and the gap size between the TM and the electrode housing was set up. Changed parameter values are: TM weight between 0.02 kg and 6.89 kg and a separation from the walls of the housing between 1 mm and 4 mm. ASDs with the changed parameter values are shown in Figure 4.11. From the graph, it is visible that accelerometers with a heavier TM perform better, however, the larger gap between the TM and surrounding electrode housing (EH) makes sensing more difficult and, as a consequence, decreases the accuracy. Therefore, for gravity field recovery analysis in this work, SGRS with a TM side of 40 mm and a TM-EH gap of 1 mm has been selected as the optimum one for trade-off between the sensors' volume and anticipated resolution.

Main characteristics of the SGRS derived in ACME (both electrostatic and optical) are summarized in Table 4.3. Inertial sensors with these parameters are considered in gravity field recovery simulations and compared with other accelerometers.

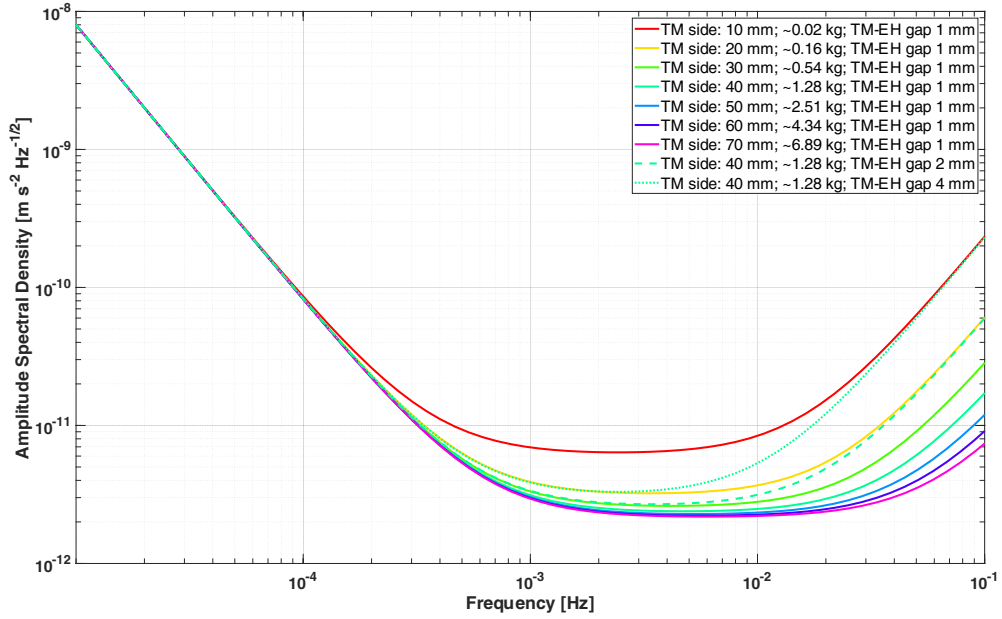


Figure 4.11: ASDs of the SGRS electrostatic accelerometers with changed parameter values

Table 4.3: Key characteristics of the SGRS developed in ACME and utilized further in gravity field recovery. Parameters are based on Carbone et al. (2007), Mance (2012), Halloin et al. (2013), Dalin et al. (2020), Dávila Álvarez et al. (2022) and Reis et al. (2023)

	SGRS electrostatic acc. derived in ACME	SGRS optical acc. derived in ACME
General information		
Accelerometer type	electrostatic	optical
Charge management system	wireless, LED UV or Mercury lamp	
Measurement bandwidth (Hz)	10^{-4} to 10^{-1}	
Level of accuracy ((m/s^2)/ $\sqrt{\text{Hz}}$ @ 1 mHz)	$\sim 3 \times 10^{-12}$	
TM material	Gold-platinum alloy	
TM density (kg/m^3)	20099	
TM weight (g)	1286	
TM dimensions (mm) [x/y/z]	40 / 40 / 40	
TM-EH gap (mm) [x/y/z]	1 / 1 / 1	
Actuation noise		
Reference voltage (V)	10	
Reference voltage stability (ppm/ $\sqrt{\text{Hz}}$)	0.6	
Thermal stability		
Thermal stability @ low frequencies	similar to MicroSTAR	
Pressure (Pa)	10^{-5}	
Temperature (K)	293	
Capacitive sensing + Stiffness		
Capacitance between electrode and TM (pF)	~ 1	—
Differential capacitance (F)	10^{-18}	
AC frequency (kHz)	100	
Injection voltage (V)	5	
Polarized voltage (V)	0.5	
Electrostatic noises		
Impedance amplifier noise ($\text{nV}/\sqrt{\text{Hz}}$)	51	—

4.3.2 Gradiometer Modeling

A pair of accelerometers form a gradiometer. SGG measurement principles are based on differential mode accelerations which were introduced in Subsection 2.2.3. As it was mentioned in Section 3, a three-axis gradiometer on-board the GOCE mission was the key instrument that carried out spaceborne measurements of the gravity gradients. Six electrostatic STAR-class accelerometers named ‘GRADIO’, which have colored noise in the low-frequency domain, were used in the GOCE gradiometer (Section 3.2). On the other hand, after promising results of ‘GRS’ inertial sensors in LPF that utilized optical interferometry to read out the TM displacements, multiple studies have been carried out evaluating the performance of simplified GRS on LEO (Chapter 1). The ACME toolbox allows to model not only single accelerometers, but also a combination of them. For example, Figure 4.12 shows a one degree of freedom optical gradiometer consisting of two SGRS. In contrast to the optical metrology system of LPF, where the position of one TM was measured relative to the other, here, the displacement of each TM is sensed independently by the laser interferometer. Since both TMs are not located at the Center of the Mass (CoM) of the spacecraft, additional terms have to be taken into account in the calculation of the observed gravity gradient (Section 2.2.3).

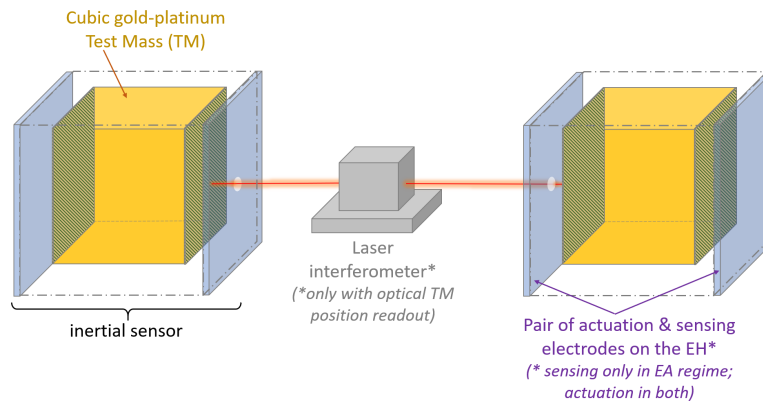


Figure 4.12: Illustration of 1 degree of freedom optical gradiometer model (Kupriyanov et al., 2024b)

4.4 Gravity Field Recovery Software

Two software tools, named QACC and GRADIO (Wu, 2016), were utilized for carrying out gravity field recovery computations from ll-SST and SGG measurements. In this section, approaches connecting the orbital kinematic quantities with the gravity accelerations (first derivatives of V) and gravity gradients (second derivatives of V) are described.

4.4.1 Gravity Field Retrieval for ll-SST Scenarios

Various approaches are utilized to connect the primary observables of ll-SST missions, range rates, to the gravity disturbance or gravity gradient. Globally, these approaches can be divided into several groups, e.g., space-wise, time-wise, direct, tensor invariants, etc. Wu (2016) formulated three major aspects in which these approaches differ. First is how the observation equations are set up; second, how is the colored noise of the observations treated, and the last one, which numerical strategy is applied to derive the SH coefficients. The QACC software applies the approximate solution of the acceleration approach (Weigelt, 2017) that belongs to the time-wise group of methods. This approach is carried out in two steps. Firstly, the observations are collected along the orbit at the measurement positions and afterwards connected to the gradients of the gravitational potential (∇V). Secondly, the system is solved by least-squares adjustment and SH coefficients of the retrieved gravity field model are determined.

The equation describing the functional model for ll-SST observations, that was implemented in the QACC toolbox, reads (Knabe, 2023):

$$\ddot{\rho} = \ddot{\mathbf{x}}_{AB} \cdot \mathbf{e}_{AB}^a + \dot{\mathbf{x}}_{AB} \cdot \dot{\mathbf{e}}_{AB}^a. \quad (4.3)$$

This expression is a re-arranged version of Equation (2.4). Taking into account Newton's second law, the relation connecting the relative acceleration vector with the relative gradient of the gravitational field $\ddot{\mathbf{x}}_{AB} = \nabla V_{AB}$, and $\dot{\mathbf{x}}_{AB} \cdot \dot{\mathbf{e}}_{AB}^a = (\dot{\mathbf{x}}_{AB} \cdot \dot{\mathbf{x}}_{AB} - \dot{\rho}^2)/\rho$, where $\dot{\mathbf{e}}_{AB}^a$ is the time-derivative of the unit vector along LOS between the two spacecraft.

It is important to note here, that a second 'centrifugal' term $\dot{\mathbf{x}}_{AB} \cdot \dot{\mathbf{e}}_{AB}^a$ of Equation (4.3) was neglected in QACC. The reason for ignoring this term is its independence from the acceleration measurements (Knabe, 2023), while one focus of this study is to evaluate improvements from the novel sensors w.r.t. state-of-the-art technologies. However, omitting this term brings the calculations in QACC from a full kinematic approach to the force level, where the effect of the non-gravitational forces are implicitly considered through the positions of the satellites. The omitted term was estimated to be less than $4.3 \times 10^{-9} \text{ m/s}^2$ for a satellite pair at an altitude $h = 400 \text{ km}$, separated by $\rho = 220 \text{ km}$ and with a relative range rate in LOS $\dot{\rho} \approx 0.5 \text{ m/s}$.

4.4.2 Gravity Field Retrieval for Cross-track Gradiometry

In the gravity field recovery software for SGG, called GRADIO, a time-wise approach was implemented (Wu, 2016). In this method, observed gravity gradients are treated as time-series measurements along the satellite orbit provided from XHPS. This makes the observations highly correlated. Therefore, certain filtering has to be applied to de-correlate the observations (Siemes, 2008; Pail, 2010; Wu, 2016). In GRADIO, a stochastic modeling, based on the variance covariance matrix, was applied for down-weighting and de-correlating the measurements.

This matrix is built iteratively by the biased estimation of the auto-covariance vector, computed from the post-fit residuals (Section 2.5). This procedure allows to avoid introducing external a priori information.

The functional model for SGG simulations is given by (Knabe, 2023):

$$V_{ij} = V_{ij}^0 + \sum_{n=2}^N \sum_{m=0}^N \mathbf{A}_{\hat{x}_{nm}} \hat{\mathbf{x}}_{nm}, \quad (4.4)$$

where V_{ij} are the point-wise measured gravity gradients in the GRF $i, j \in \{x, y, z\}$ (c.f. Equation (2.13)), V_{ij}^0 are the initial gradients from the normal gravity field model, $\mathbf{A}_{\hat{x}_{nm}}$ the design matrix elements including base function transformations from Local North-Oriented Reference Frame to GRF and $\hat{\mathbf{x}}_{nm} = \{\overline{C}_{nm}, \overline{S}_{nm}\}$ the vector of the estimated parameters (Wu, 2016).

4.5 Chapter Summary

The chapter starts with the closed-loop simulation procedure implemented for ll-SST (Subsection 4.1) and SGG measurements (Subsection 4.2). Also, the considered background models in orbit calculation in XHPS as well as the description of the simulated orbits were introduced in Section 4.2. Section 4.3 gives an overview of the physics and major considerations that were implemented for accelerometer and gradiometer modeling in ACME. Finally, in Section 4.4, the approaches and functional models are described that are used in the gravity field recovery software tools QACC and GRADIO.

5 Amplitude Spectral Densities of the Investigated Instruments

This chapter gives an overview of the performance of the inertial sensors (Section 5.1) and inter-satellite ranging instruments (Section 5.2) that are used in the GFR simulations (Chapter 6). The graphs are plotted as the ASD curves, that are mathematically introduced in Section 2.3 and the ASDs are used to build a corresponding noise time-series (Section 4.1).

5.1 Errors of the Inertial Sensors

Electrostatic Accelerometers (EA), that have already been used in gravimetry missions, i.e. SuperSTAR and GRADIO, were introduced in Section 3.2. Accelerometer concept descriptions, i.e. the electrostatic SGRS from Dávila Álvarez et al. (2022) and MicroSTAR EA, were given in Section 3.4. Here, ASD curves of the mentioned inertial instruments as well as other sensors that are used in GFR are presented. Figure 5.1 shows the noise of the various inertial sensors in terms of ASD.

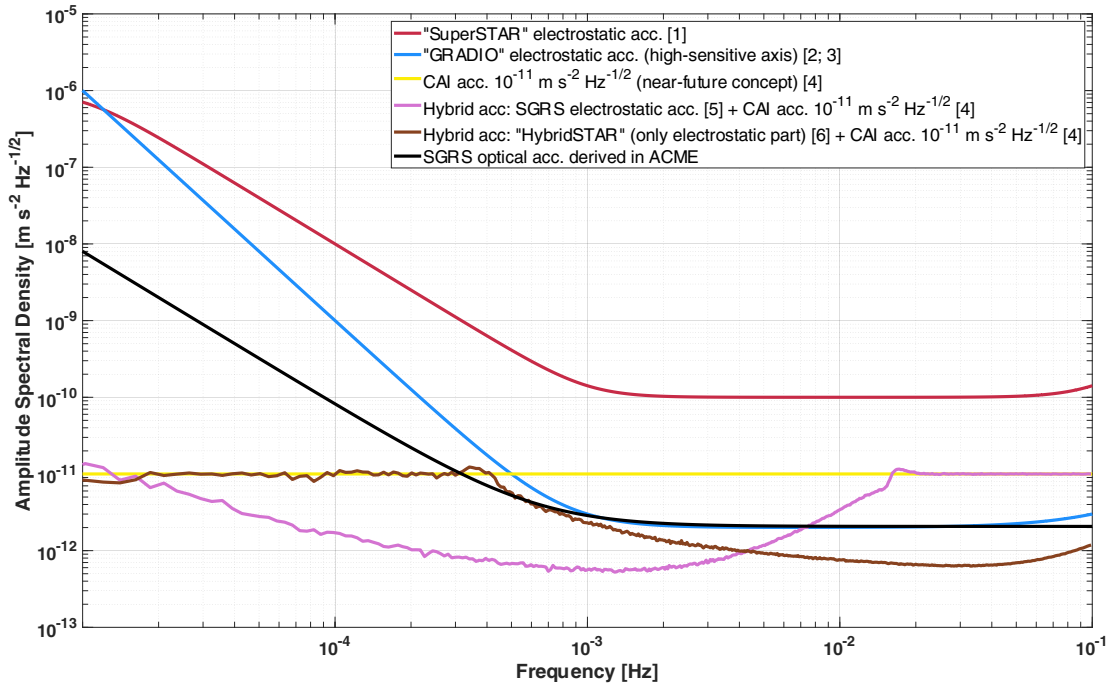


Figure 5.1: Comparison of the ASD sensitivities of accelerometers that are used in gravity field recovery analysis in this work. [1] Daras and Pail (2017); [2] Touboul et al. (2016); [3] Marque et al. (2010); [4] HosseiniArani et al. (2024); [5] Dávila Álvarez et al. (2022); [6] Dalin et al. (2020)

The ASD of the SuperSTAR EA (red curve), which has a limited sensitivity in the low frequency domain (below 1 mHz) is described as (Daras and Pail, 2017)

$$S^{1/2}(f) = 10^{-10} \frac{\text{m s}^{-2}}{\sqrt{\text{Hz}}} \times \sqrt{\frac{\left(\frac{1 \text{ mHz}}{f}\right)^4}{\left(\frac{10 \text{ } \mu\text{Hz}}{f}\right)^4 + 1} + 1 + \left(\frac{f}{0.1 \text{ Hz}}\right)^4}. \quad (5.1)$$

For the high-sensitive axis of the GOCE gradiometer, formed by GRADIO EA (blue curve), in the measurement bandwidth a specification performance level was considered (c.f. Fig. 8 of Marque et al., 2010). In the low frequency domain a thermal stability, achieved in flight, were taken (c.f. Fig. 7 of Touboul et al., 2016):

$$S^{1/2}(f) = 10^{-12} \frac{\text{m s}^{-2}}{\sqrt{\text{Hz}}} \times \left(\left(\frac{0.001}{f}\right)^3 + \left(\frac{f}{0.1}\right)^2 + 2 \right). \quad (5.2)$$

The noise of the CAI accelerometer, that is used in GFR simulations both as a standalone sensor and hybridized one with other EA, is assumed as white noise at the level of $10^{-11} (\text{m/s}^2)/\sqrt{\text{Hz}}$ in one degree of freedom (yellow curve). This order of magnitude corresponds to the near-future CAI accelerometer concept and can be described by the following key parameters: number of atoms 1×10^6 , laser waist 20 mm, atomic temperature 10 pK and interrogation time 10 s (HosseiniArani et al., 2024). Barrett et al. (2019) demonstrated that achieving the same level of accuracy in all three axes for CAI inertial sensor is quite challenging.

Two hybrid inertial sensors are considered in GFR analysis. The first one (pink curve) combines a SGRS EA on a drag-compensated platform from Dávila Álvarez et al. (2022) with the above-mentioned CAI ACC. The ASD of a SGRS in a drag-free regime, including the contribution of the capacitive sensing at high frequencies (c.f. Fig. 13 of Dávila Álvarez et al., 2022), is

$$S^{1/2}(f) = 10^{-10} (\text{m/s}^2)/\sqrt{\text{Hz}} \times \left[3 \times 10^2 \left(\frac{f}{1 \text{ Hz}}\right)^2 + 4 \times 10^{-3} \sqrt{1 + \frac{700 \text{ } \mu\text{Hz}}{f} + \left(\frac{300 \text{ } \mu\text{Hz}}{f}\right)^2} \right]. \quad (5.3)$$

Hybridization was done in the frequency domain. To the sensitivity ASD of the SGRS EA a low-pass filter at 11 mHz was applied, while to the ASD of the CAI accelerometer, a high-pass filter at 17 mHz. Figure 5.2 shows the ASD curves of the accelerometers that are combined together with the cut-off frequencies. Here, the low- and high-pass filters were applied at different frequencies in order to have a smooth transition between the ASDs.

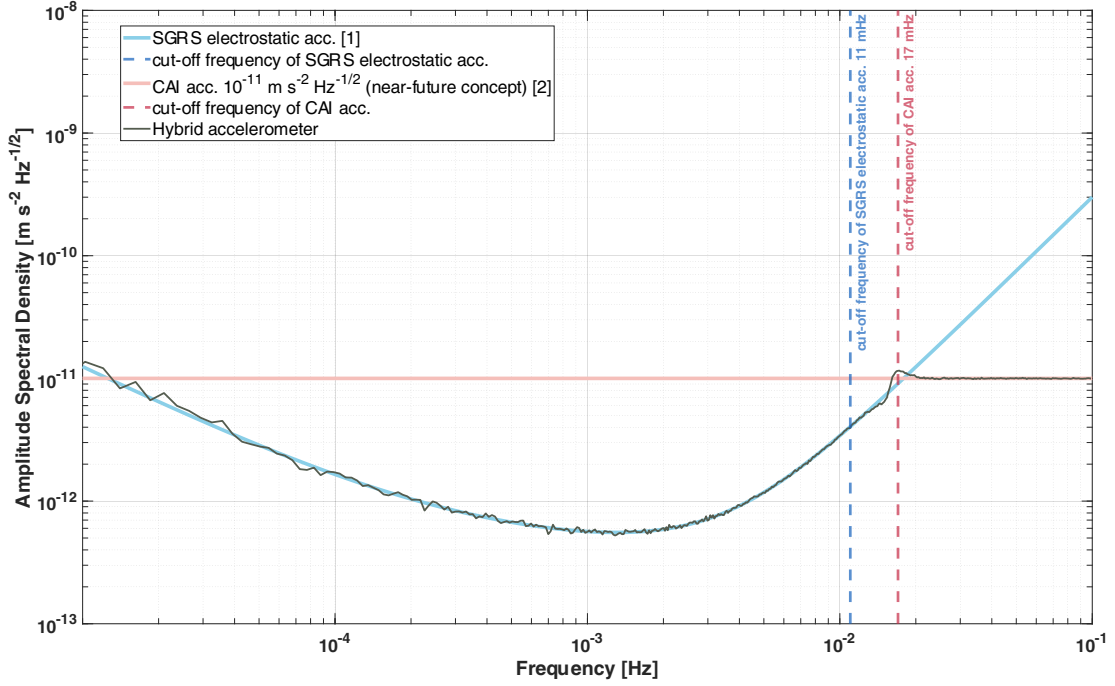


Figure 5.2: ASD sensitivities of the accelerometers that are used for hybridization including cut-off frequencies. [1] Dávila Álvarez et al. (2022); [2] HosseiniArani et al. (2024)

Another hybrid accelerometer (brown curve in Figure 5.1) consists of an electrostatic part of a HybridSTAR accelerometer (Dalin et al., 2020) and also a CAI ACC with white noise at the level of $10^{-11} \text{ (m/s}^2\text{)}/\sqrt{\text{Hz}}$. Only one cut-off frequency (0.35 mHz) was used for both low- and high-pass filters in hybridization. The ASD equation of the HybridSTAR (electrostatic part) is

$$S^{1/2}(f) = 10^{-11} \text{ (m/s}^2\text{)}/\sqrt{\text{Hz}} \times \left[2.4 \times 10^{-2} \times \frac{1}{f^{0.25}} + 10^{-7} \frac{1}{f^2} + 8f^2 \right]. \quad (5.4)$$

Finally, the ASD equation of the SGRS optical accelerometer derived in ACME with the following parameters: TM side = 40 mm, $m = 1.286 \text{ kg}$, TM-EH gap = 1 mm, which were selected in Section 4.3, is described as

$$S^{1/2}(f) = 10^{-12} \text{ (m/s}^2\text{)}/\sqrt{\text{Hz}} \times \left[2.0695 + 8 \times 10^{-7} \frac{1}{f^2} \right]. \quad (5.5)$$

In order to get this ASD equation, a typical spectrum of non-gravitational accelerations at the altitude $h = 478 \text{ km}$ of the year with high solar activity (2002) was given as input to ACME. The corresponding ASD equation was fitted to the frequency response of the linearized SGRS model.

5.1.1 Filtering of Accelerometer Colored Noise at Low Frequencies

When generating a noise time-series of the inertial sensors, e.g., the electrostatic SuperSTAR, GRADIO as well as the SGRS optical accelerometer derived in ACME, a dominating low-frequency component occurs. For example, for the SGRS optical accelerometer, it is around $10^{-10} \text{ (m/s}^2\text{)}/\sqrt{\text{Hz}}$ at 10^{-4} Hz and for GRADIO and SuperSTAR inertial sensors, it is even higher (see Figure 5.3). Therefore, in this study, this problem was minimized by applying a minimum-order finite impulse response high-pass filter at 0.5 mHz to the inertial sensors with colored noise. This is a certain simplification that was considered, as in reality one can not distinguish between the noise and the signal of the instrument. The cutoff frequency value was selected from the trade-off of minimizing the degradation of the filtered solution at applied stochastic modeling on the one hand, and keeping the reference noise ASD at high frequencies, on the other. A minor degradation of the high-pass filtered solution in the applied stochastic modeling occurs in the GRADIO gravity field recovery software due to the non-optimized numerical approach of stochastic modeling that was used there and which is planned to be improved in future. Figure 5.3 shows the ASDs of the high-pass filtered noise time-series of the inertial sensors with colored noise at low frequencies, as well as the ASDs of the reference models. High-pass filtered noise time-series of SGRS optical, SuperSTAR and GRADIO accelerometers were used in the gravity field simulations of this study.

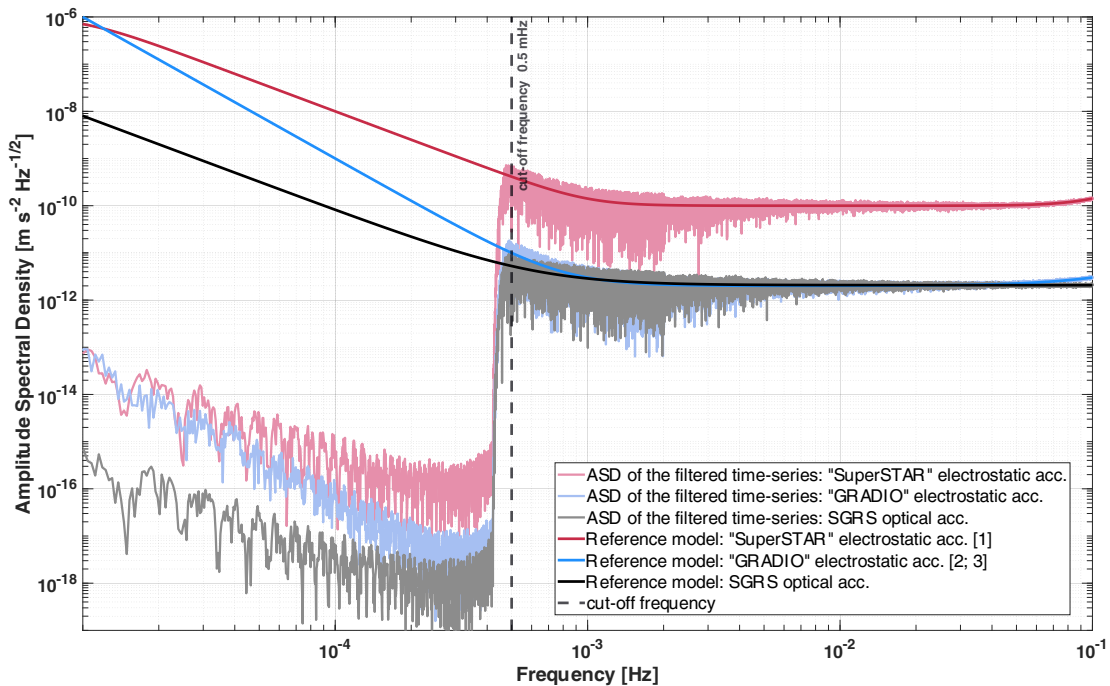


Figure 5.3: ASD sensitivities of high-pass filtered accelerometers that are used in gravity field recovery simulations. [1] Daras and Pail (2017); [2] Touboul et al. (2016); [3] Marque et al. (2010)

5.2 Errors of the Inter-satellite Ranging Instruments

The ASDs of the inter-satellite ranging instrument errors that are used in the gravity field recovery simulations in this work are plotted in Figure 5.4.

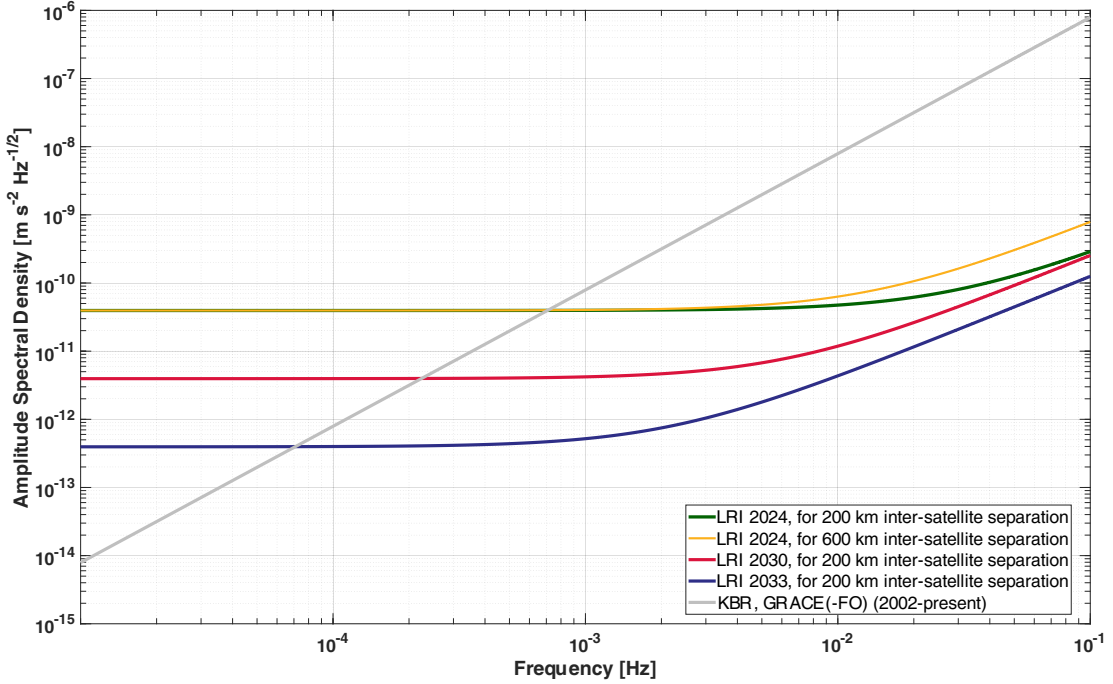


Figure 5.4: Comparison of the ASDs of the inter-satellite LRI (Kupriyanov et al., 2024b) and KBR Frommknecht et al. (2006) measurement errors that are used in the gravity field recovery analysis in this work.

The ASD of the KBR instrument error, depicted as grey curve, can be described as (Frommknecht et al., 2006)

$$S^{1/2}(f) = (2\pi f)^2 \cdot 2 \times 10^{-6} \frac{\text{m s}^{-2}}{\sqrt{\text{Hz}}}. \quad (5.6)$$

The ASD of the LRI for the present-day GRACE-FO mission was assumed as (Kupriyanov et al., 2024b)

$$S^{1/2}(f) = \left[\frac{L}{1 \text{ m}} \cdot 10^{-15} \sqrt{\frac{1 \text{ Hz}}{f}} + 10^{-12} \left(\frac{1 \text{ Hz}}{f} \right)^2 \right] \times (2\pi f)^2 \frac{\text{m s}^{-2}}{\sqrt{\text{Hz}}}, \quad (5.7)$$

where L is the inter-satellite distance for which values of 200 km (green curve) and 600 km (yellow curve) are used in the simulations. The cavity intrinsic thermal noise (Francis et al., 2015) is accounted for by the first term in the bracket, which is proportional to L . Low-frequency thermal stability of the cavity is approximated by the second term in the bracket.

Analogously, the ASD of the anticipated behavior of the inter-satellite LRI error in future GRACE-like missions in 2030 (red curve) is considered as

$$S^{1/2}(f) = \left[\frac{L}{1 \text{ m}} \cdot 10^{-15} \sqrt{\frac{1 \text{ Hz}}{f}} + 10^{-13} \left(\frac{1 \text{ Hz}}{f} \right)^2 \right] \times (2\pi f)^2 \frac{\text{m s}^{-2}}{\sqrt{\text{Hz}}}. \quad (5.8)$$

The LRI error in GRACE-like missions beyond 2033 (blue curve) is estimated as

$$S^{1/2}(f) = \left[\frac{L}{1 \text{ m}} \cdot 5 \times 10^{-16} \sqrt{\frac{1 \text{ Hz}}{f}} + 10^{-14} \left(\frac{1 \text{ Hz}}{f} \right)^2 \right] \times (2\pi f)^2 \frac{\text{m s}^{-2}}{\sqrt{\text{Hz}}}. \quad (5.9)$$

5.3 Chapter Summary

This chapter introduces the ASD equations of the inertial sensors and inter-satellite range measurement errors that are used in gravity field recovery simulations. Corresponding graphs show the relative comparison of the error ASDs for different instruments to evaluate sensor sensitivities w.r.t. each other.

6 Gravity Field Recovery Results from Simulations

This chapter presents the results from the various GFR simulations. GFR is done in order to assess and quantify the improvements from the novel inertial sensors, various satellite formations and the combination of different measurement principles. Evaluation of the recovered gravity fields is done by computing the difference to a reference gravity field model (EIGEN-6C4). Therefore, the analysis is carried out on the level of the residuals that are obtained by adding various stochastic error sources, mostly instrument errors (Chapter 5). GFR results are given in both spatial and spectral domain, as introduced in Section 2.6. Section 6.1 demonstrates the impact of the stochastic modeling for the accelerometers and gradiometers with their colored noise behavior (brown $\sim 1/f^2$ and pink $\sim 1/f$) at low frequencies as well as the difference in solutions' convergence to the white noise instruments. The comparison of the retrieved gravity models from the optical accelerometers w.r.t other inertial instrument concepts in ll-SST measurement configuration (GRACE-like) is discussed in Section 6.2.1. Although the focus of this study is instruments' evaluation and performance comparison, where the effect of the time-variable background models and associated errors are not considered in gravity field retrieval, Section 6.2.2 presents GFR from the ll-SST with time-variable background modeling errors. Section 6.2.3 shows the GFR results from the closed-loop ll-SST simulations with the modified satellite shapes, i.e. with extended solar arrays, in order to meet the power requirements of additional novel sensors, that might be implemented in the future gravimetry missions. In Section 6.3.1, retrieved gravity field models from the cross-track gradiometers are presented, followed by the discussion of the common mode gain uncertainty in the gradiometry case (Subsection 6.3.2). Residuals in the spatial and spectral domains from the combination of ll-SST and cross-track gradiometry are shown in the Section 6.3.3. Section 6.4.1 demonstrates GFR results obtained by a double pair 'Bender' constellation, including the discussion of the scale factor study for the residual drag in ll-SST case (Subsection 6.4.2). Investigation of different regularization techniques, including L-curve analysis for the standalone inclined satellite pair, is discussed in Section 6.4.3. Finally, the chapter ends up with a Section 6.4.4, introducing the GFR results obtained from the two novel triple satellite formations.

6.1 Impact of Stochastic Modeling

Stochastic modeling, introduced in Section 2.5, is applied to the observations in GFR for down-weighting and de-correlating purposes. In GFR, stochastic modeling is usually implemented iteratively in order to retrieve a series of solution approximations until convergence. Luthcke et al. (2013) explained the advantage

of such approach, where the signal-to-noise ratio increases with each iteration. Iterative down-weighting strategies are widely used for GFR from GOCE gravity gradient observations (Klees et al., 2000; Pail and Plank, 2002; Baur and Grafarend, 2006; Arnold et al., 2023). Also, iterative methods are applied to down-weight the outliers from GRACE results (Loomis et al., 2019; Darbeheshti et al., 2020; Mayer-Gürr et al., 2021).

6.1.1 Colored Noise at Low Frequencies

6.1.1.1 II-SST case

Figure 6.1 shows the converging behavior of the retrieved solutions due to application of the stochastic modeling as degree RMS, plotted as geoid height (Equation (2.35)). Although stochastic modeling itself is not applied iteratively, certain weights are optimized in successive steps. This result is obtained by applying the II-SST measurement principle for the the near-polar orbit #1 (Table (4.2)), using the SuperSTAR EA (Equation (5.1)) as inertial sensor, without high-pass filtering for demonstration purposes, and LRI 2024 (Equation (5.7)) as inter-satellite ranging instrument. Since the SuperSTAR EA has a brown noise ($\sim 1/f^2$) at frequencies below 1 mHz (Figure (5.1)), a prompt de-correlation effect on the SH coefficient differences can be observed for the true errors (solid lines) and the formal errors (dashed lines). The degree RMS curves of the true errors and formal errors converged after the 3rd iteration of weights adaptation. Therefore, it is sufficient to apply only 3 successive steps. Moreover, a certain smoothing of the true error curves is obtained when applying stochastic modeling.

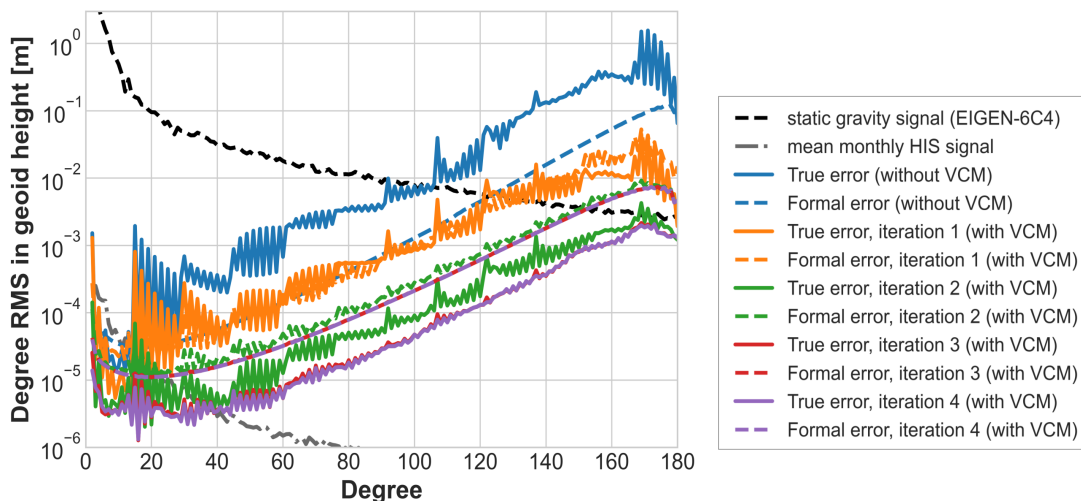


Figure 6.1: Impact of the stochastic modeling, where the weights are optimised iteratively, in II-SST with colored (brown) noise. Solid lines are degree RMS of the coefficient differences (true errors) between recovered and EIGEN-6C4 gravity field models in geoid height (m); Dashed lines are standard deviations of the estimated unknown parameters (formal errors); Orbit: #1 (Table 4.2), $h = 478.48$ km; Instruments: SuperSTAR EA and LRI 2024

Figure 6.2 shows the results of the stochastic modeling, where the weights are optimised step-by-step, as global maps of the residuals (retrieved gravity field w.r.t. EIGEN-6C4) on the left and as two-dimensional SH error spectra of true and formal errors on the right. The same order of magnitude of the spatial residuals, plotted in equivalent water height, are used in all global maps for a more explicit difference. In general, the North-South striping effect, that occur due to the orbit resonance effects (Kvas et al., 2019), sub-Nyquist artifacts due to latitudinal oversampling of the low-frequency gravitational signal (Peidou and Pagiatakis, 2020) and drift of the electrostatic accelerometer, typical for GRACE solutions, can be reduced at a certain level with the novel instruments. Also, for convenience SH error spectra are plotted in logarithmic scale. A difference between the true and formal error spectra in the case without stochastic modeling (on the top) is quite noticeable, while after application of the down-weighting procedure, both spectra are consistent (on the bottom).

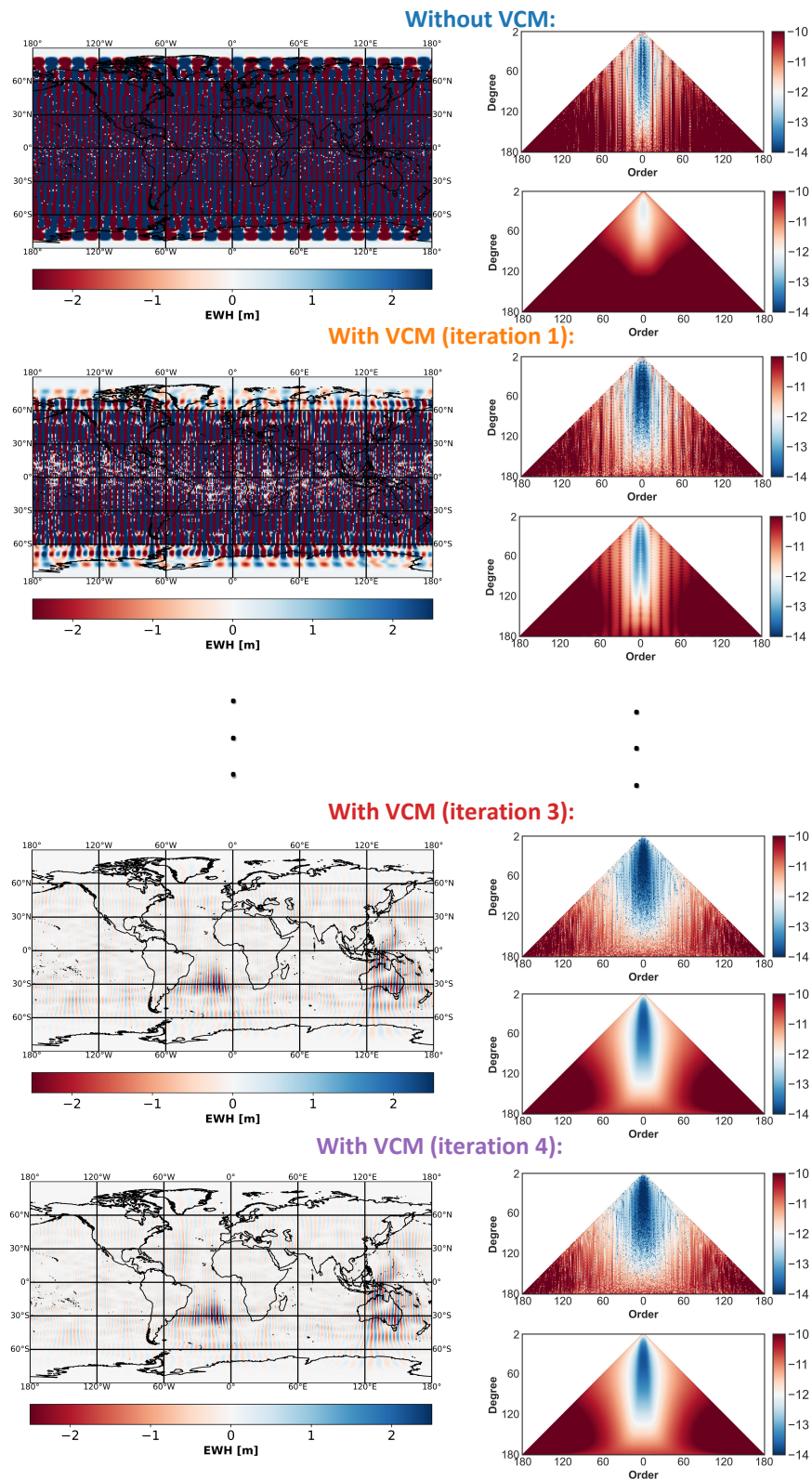


Figure 6.2: Impact of the stochastic modeling, where the weights are optimised iteratively, in ll-SST with colored (brown) noise. Global maps with the residuals in EWH (left), SH error spectra of the true errors and formal errors (right); Orbit: #1 (Table 4.2), $h = 478.48$ km; Instruments: SuperSTAR EA and LRI 2024. Colorbar of the global maps limited to ± 2.5 m EWH.

6.1.1.2 SGG case

For the demonstration the impact of the stochastic modeling, where the weights are progressively optimized in successive steps, in the SGG case with colored noise (pink $\sim 1/f$ at frequencies below 1 mHz), the required specification level for the GRADIO electrostatic accelerometer (c.f. Fig. 8 of Marquet et al. (2010) and c.f. Fig. 7 of Touboul et al. (2016)) is considered without high-pass filtering. The ASD equation is

$$S^{1/2}(f) = 2 \times 10^{-12} \text{ (m/s}^2\text{)/}\sqrt{\text{Hz}} \times \sqrt{\left(\frac{1 \text{ mHz}}{f}\right)^2 + 1 + \left(\frac{f}{0.1 \text{ Hz}}\right)^4}. \quad (6.1)$$

Figure 6.3 shows the convergence behavior of the retrieved solutions due to application of the stochastic modeling in SGG as degree RMS, plotted as geoid height (Equation (2.35)). These results are calculated for the near-polar orbit #5 (Table (4.2)) using the high-sensitive cross-track component V_{yy} of the GOCE gradiometer (Equation (6.1)). The retrieved curves of the true (solid lines) and formal (dashed lines) errors show a fast convergence. The true errors and formal errors converged after the 2nd iteration. However, for consistency in GFR comparison and in combination with other solutions, 3 iterations of de-correlation filter are used in this work.

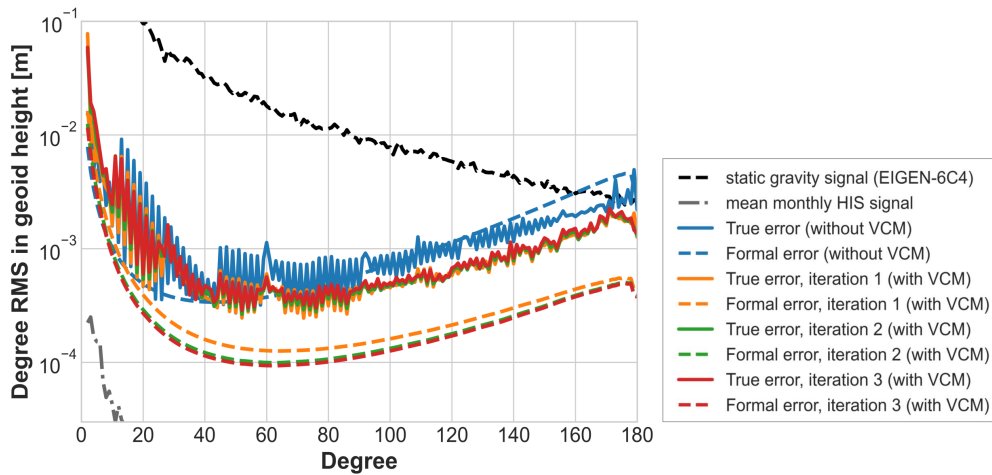


Figure 6.3: Impact of the stochastic modeling, where the weights are optimised iteratively, in SGG with colored (pink) noise. Solid lines are true errors and dashed lines are formal errors; Orbit: #5 (Table 4.2), $h = 247.35$ km; Instruments: Specification level of the high-sensitive, cross-track axis of the GOCE gradiometer.

Figure 6.4 shows the validation of the retrieved gravity fields for the gradiometry case, before and after applying the down-weighting procedure, in the spatial domain as residuals w.r.t. the reference gravity field EIGEN-6C4 (left), and in the spectral domain as true and formal errors (right). SH error spectra of true and formal errors show good consistency when stochastic modeling is applied.

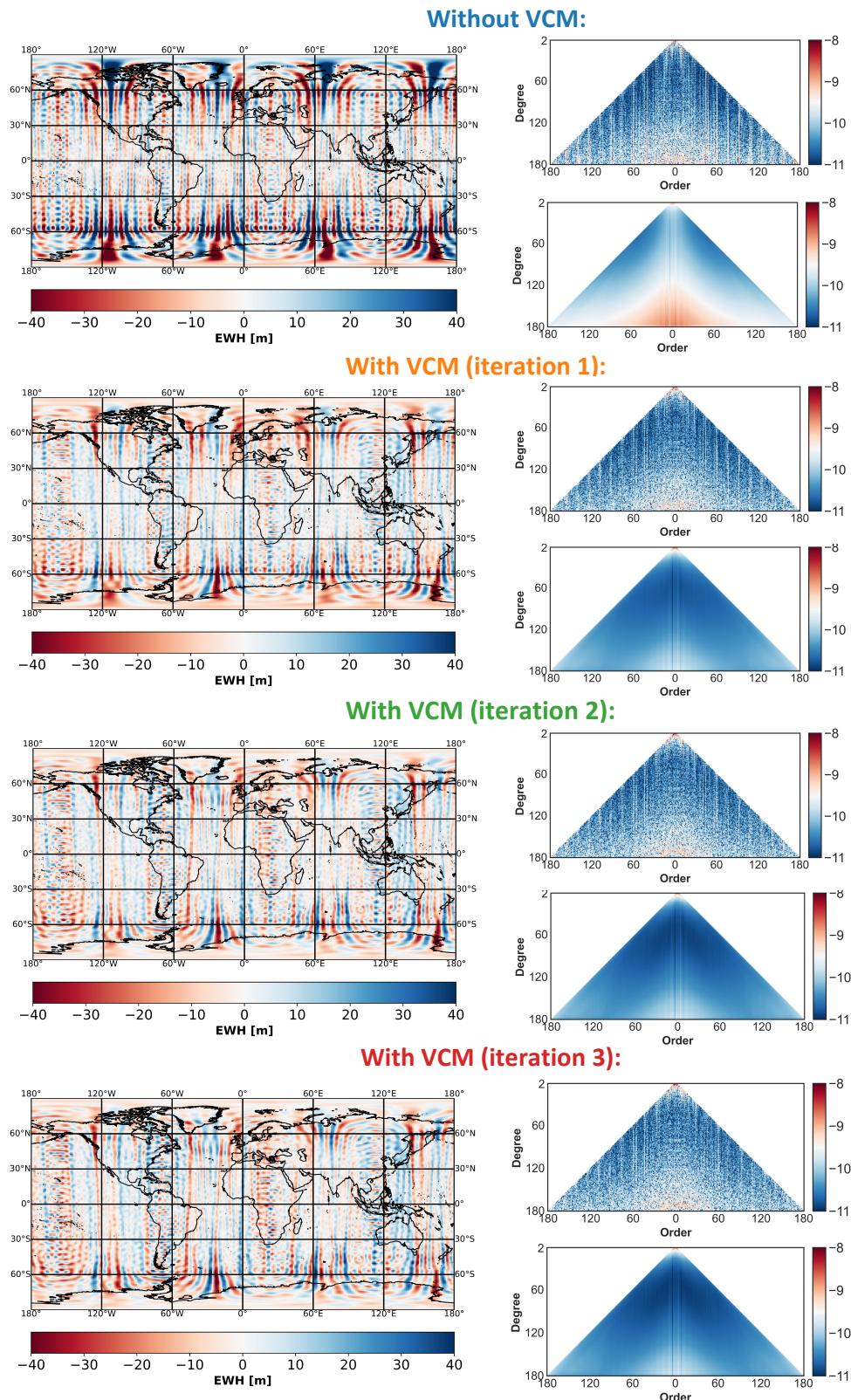


Figure 6.4: Impact of the stochastic modeling, where the weights are optimised iteratively, in SGG with colored (pink) noise. Global maps with the residuals in EWH (left), SH error spectra of the true errors and formal errors (right); Orbit: #5 (Table 4.2), $h = 247.35$ km; Instruments: high-sensitive cross-track axis of the GOCE gradiometer. Colorbar of the global maps limited to ± 40 m EWH.

6.1.2 White Noise at Low Frequencies

6.1.2.1 ll-SST case

Figure 6.5 shows the convergence behavior of the retrieved solutions as degree RMS, plotted in geoid height (Equation (2.35)), due to application of the stochastic modeling, where the weights are refined incrementally in each step, in the ll-SST case assuming white noise behavior of the inertial instrument. These results are calculated for the near-polar orbit #1 (Table (4.2)), using a CAI accelerometer with white noise at the level of $10^{-11} \text{ (m/s}^2\text{)}/\sqrt{\text{Hz}}$ as the inertial sensor and LRI 2030 (Equation (5.8)) as the inter-satellite ranging instrument. Due to the white noise behavior of the accelerometer, true and formal errors already converged from the 1st iteration with applied stochastic modeling. Likewise to the previously mentioned SGG-case with colored noise, for consistency in GFR comparison and in combination with other solutions, 3 iterations of de-correlation filter are used for ll-SST scenarios with white noise accelerometers as well.

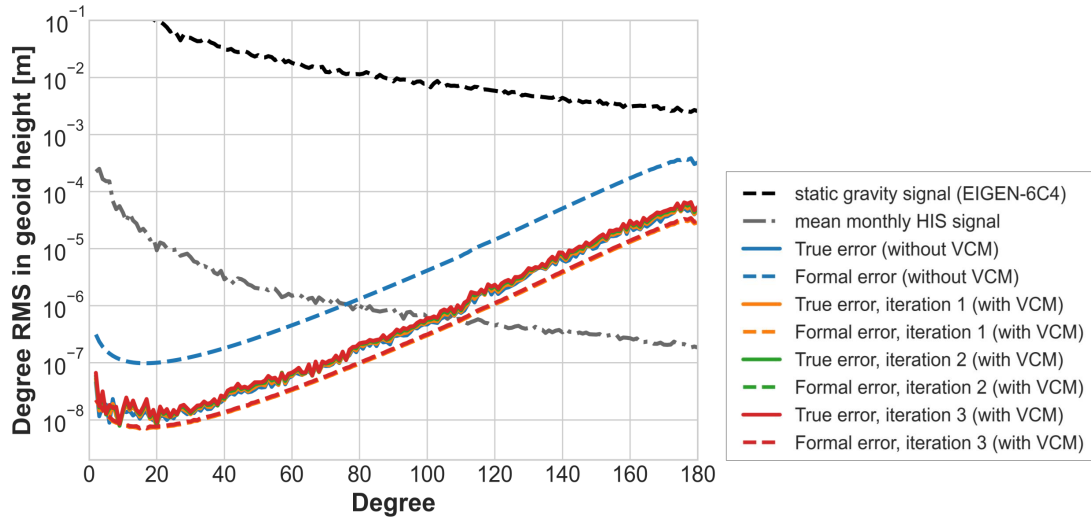


Figure 6.5: Impact of the stochastic modeling, where the weights are optimised iteratively, in ll-SST with white noise. Solid lines are degree RMS of the coefficient differences (true errors) between recovered and EIGEN-6C4 gravity field models in geoid height (m); Dashed lines are standard deviations of the estimated unknown parameters (formal errors); Orbit: #1 (Table 4.2), $h = 478.48 \text{ km}$; Instruments: CAI $10^{-11} \text{ (m/s}^2\text{)}/\sqrt{\text{Hz}}$ and LRI 2030.

Figure 6.6 shows the results of applied stochastic modeling for the ll-SST case using a white noise CAI accelerometer. The global maps of the residuals (retrieved gravity field w.r.t. EIGEN-6C4) are on the left, and two-dimensional SH error spectra of true and formal errors are on the right. It is obvious that, starting from the 1st iteration of the de-correlation filter, the true and formal error spectra are identical to the ones from the following steps.

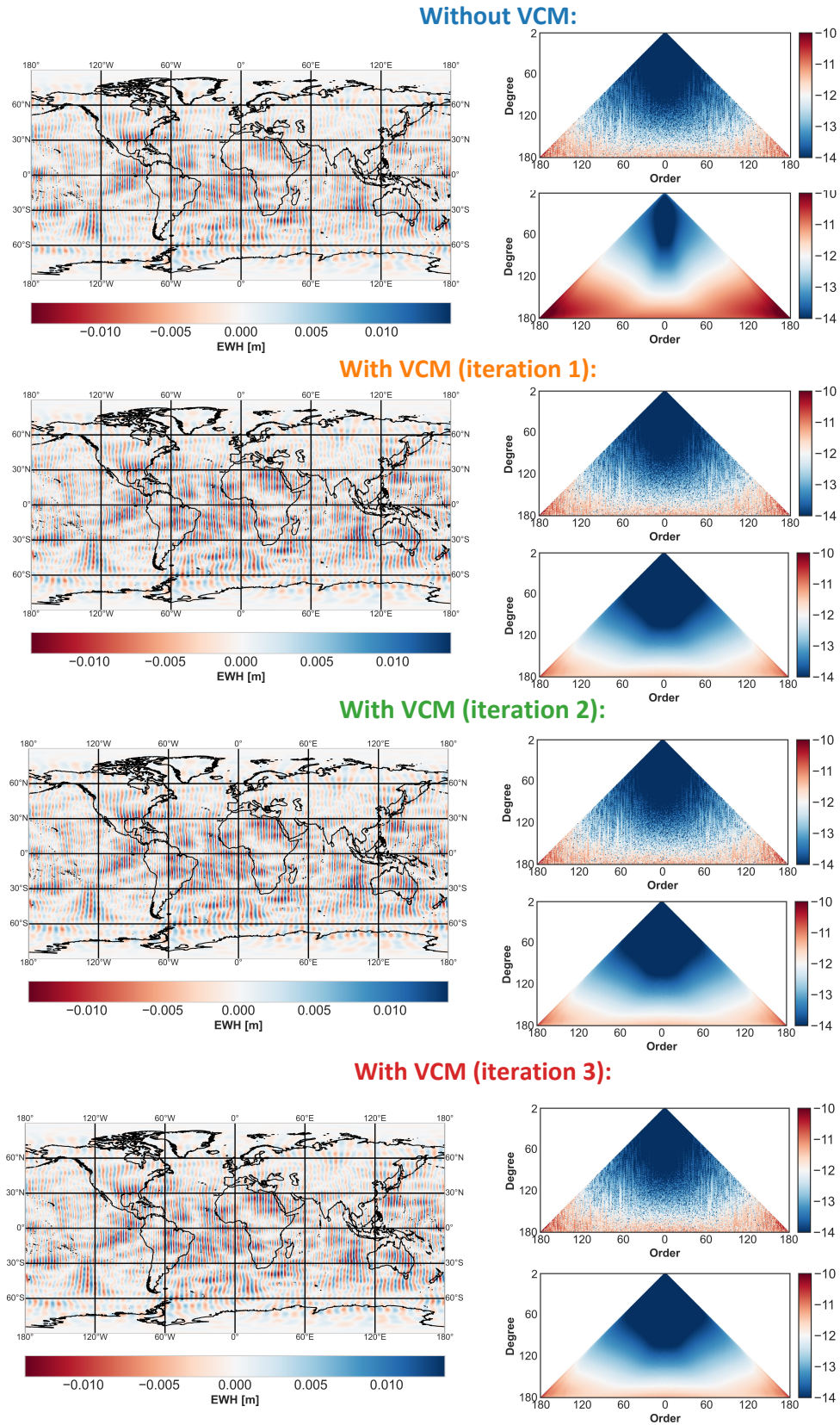


Figure 6.6: Impact of the stochastic modeling, where the weights are optimised iteratively, in ll-SST with white noise. Global maps with the residuals in EWH (left), SH error spectra of the true errors and formal errors (right); Orbit: #1 (Table 4.2), $h = 478.48$ km; Instruments: CAI 10^{-11} (m/s²)/ $\sqrt{\text{Hz}}$ and LRI 2030. Colorbar of the global maps limited to ± 0.015 m = ± 15 mm EWH.

6.1.2.2 SGG case

With application of the stochastic modeling, where the weights are progressively optimized in successive steps, the retrieved GFR solutions in the SGG case using a white noise gradiometer converged also quite fast. Figure 6.7 shows the degree RMS in geoid height (Equation (2.35)) of the true (solid lines) and formal (dashed lines) errors, obtained for the near-polar orbit #5 (Table (4.2)) using a CAI gradiometer with white noise at the level of $10 \text{ mE}/\sqrt{\text{Hz}}$ and a CAI gyroscope, with a performance achieved in the lab, demonstrated by Savoie et al. (2018). A white-noise level close to $10^{-8} \text{ rad s}^{-1}$ in terms of angular velocity was considered for the CAI gyroscope. True and especially the formal errors converged after the 2nd iteration. However, for consistency in GFR comparison and in combination with other solutions, 3 iterations of the de-correlation filter are used for SGG with white noise gradiometers.

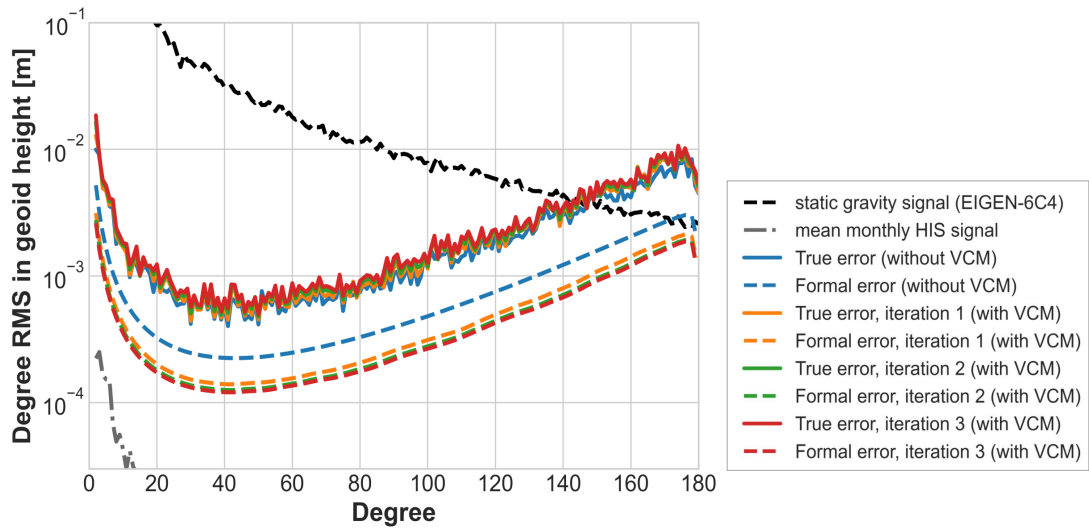


Figure 6.7: Impact of the stochastic modeling, where the weights are optimised iteratively, in SGG with white noise. Solid lines are degree RMS of the coefficient differences (true errors) between recovered and EIGEN-6C4 gravity field models in geoid height (m); Dashed lines are standard deviations of the estimated unknown parameters (formal errors); Orbit: #5 (Table 4.2), $h = 247.35 \text{ km}$; Instruments: CAI $10 \text{ mE}/\sqrt{\text{Hz}}$ gradiometer and CAI gyroscope.

The spatial distribution of the residuals between recovered and reference gravity field (EIGEN-6C4) as well as SH error spectra of the true and formal errors, applying a down-weighting procedure in the SGG case with a white noise gradiometer, are shown in the Figure 6.8. The SH error spectra of the true and formal errors are consistent by applying stochastic modeling.

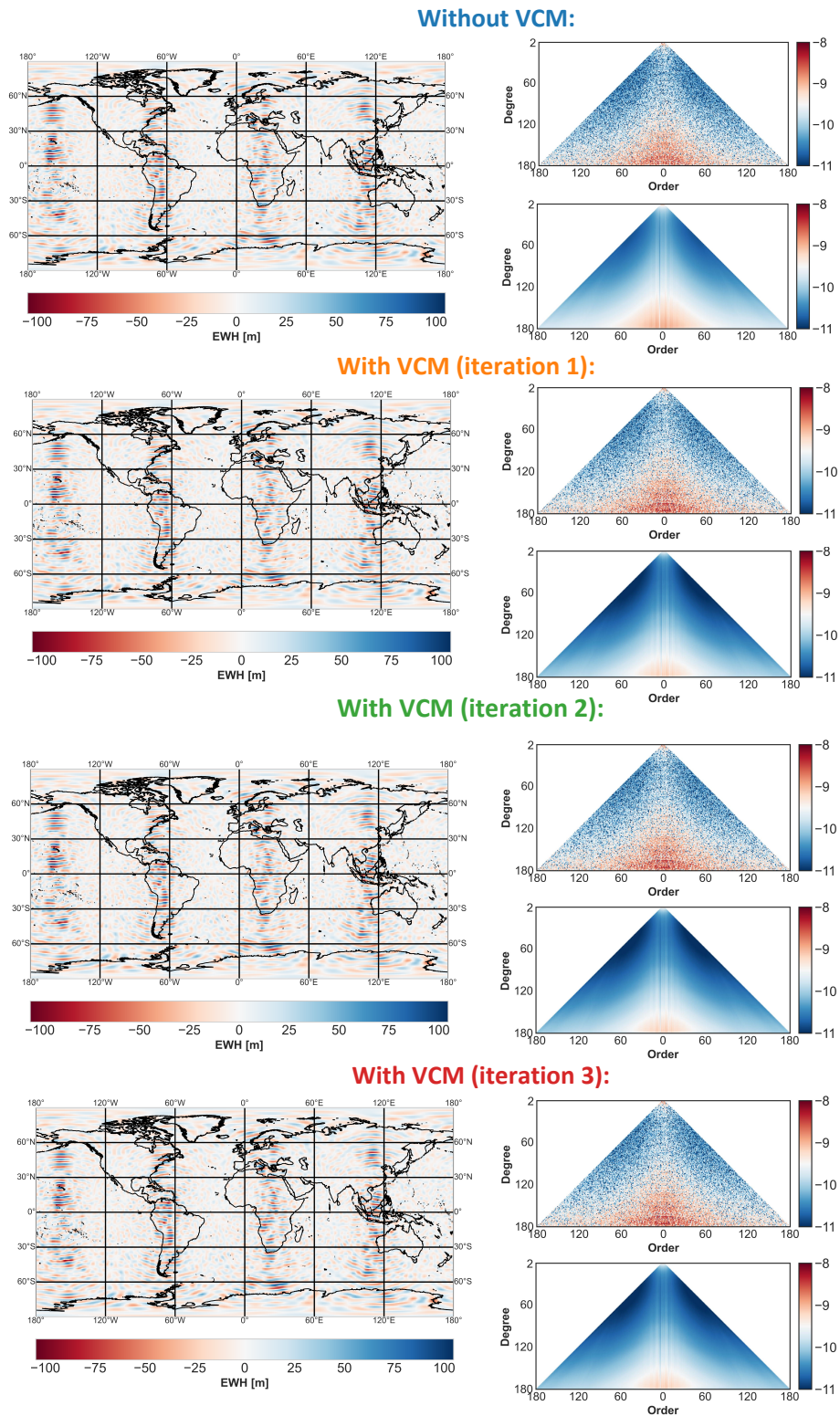


Figure 6.8: Impact of the stochastic modeling, where the weights are optimised iteratively, in SGG with white noise. Global maps with the residuals in EWH (left), SH error spectra of the true errors and formal errors (right); Orbit: #5 (Table 4.2), $h = 247.35$ km; Instruments: CAI $10 \text{ mE}/\sqrt{\text{Hz}}$ gradiometer and CAI gyroscope. Colorbar of the global maps limited to ± 100 m EWH.

6.2 low-low Satellite-to-Satellite Tracking

6.2.1 Performance of Accelerometers and Range Instruments

This section presents the retrieved gravity field models from ll-SST type of missions using different inertial sensors and inter-satellite range measurement instruments. For all cases, a near-polar non-drag compensated orbit #1 (Table 4.2) with altitude $h = 478.48$ km was considered. A one-month mission duration in May, 2002, which corresponds to a year with high solar activity (Section 4.2.1), was selected for orbit and GFR simulations. The effect of the background models (which addressed in Section 6.2.2) was not included in GFR, since we focus on the instruments' comparison. ASD sensitivity curves and equations of the corresponding accelerometers used here have been introduced in Section 5.1, while the measurement errors of the inter-satellite instruments in Section 5.2. For the inertial sensors with colored noise behavior in the low-frequency domain, e.g., the 'SuperSTAR' and SGRS optical accelerometer, a high-pass filter was applied.

Figure 6.9 shows the degree RMS in geoid height (Equation (2.35)) of the true errors retrieved from the ll-SST simulations with different instruments.

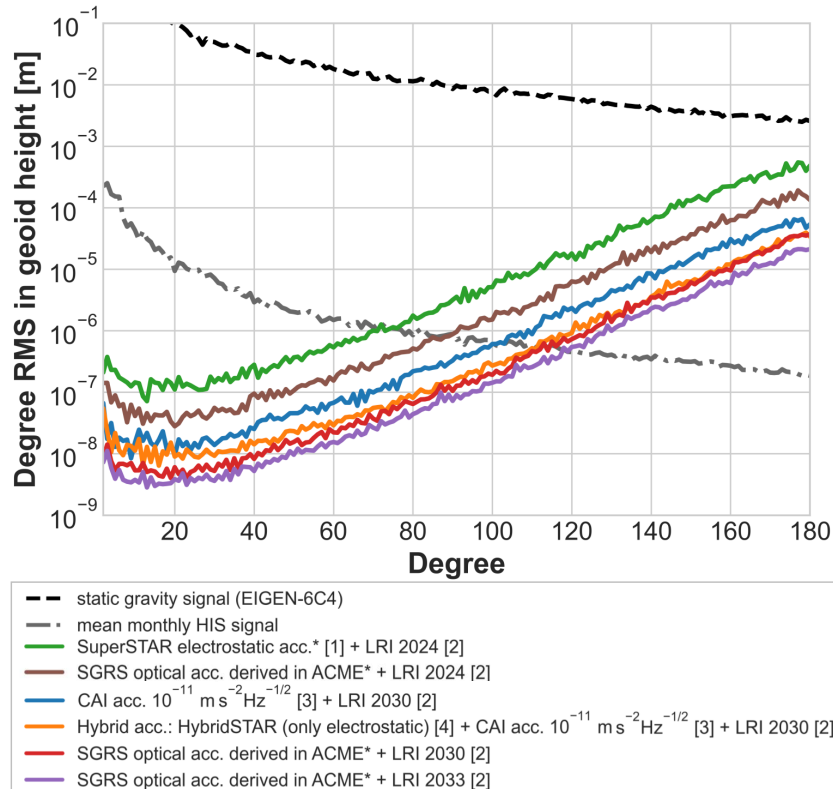


Figure 6.9: Degree RMS of the spherical harmonic coefficient differences (true errors) between recovered and EIGEN-6C4 gravity field models in geoid height (m) from ll-SST simulations; Orbit: #1 (Table 4.2), $h = 478.48$ km. * applied high-pass filter. [1] Daras and Pail (2017); [2] Kupriyanov et al. (2024b); [3] HosseiniArani et al. (2024); [4] Dalin et al. (2020).

In all cases, stochastic modeling have been applied with weights progressively optimized over three successive steps. The green curve represents the GRACE-FO mission with a SuperSTAR electrostatic accelerometer (Daras and Pail, 2017) and the level of errors of the current LRI 2024 with 200 km inter-satellite separation (Kupriyanov et al., 2024b). The mean monthly Hydrology, Ice, and Solid Earth (HIS) signal (Dobslaw et al., 2015), depicted as a grey dashed line, indicates the potential resolution of the time-variable signal. This represents an ideal scenario in which temporal aliasing is sufficiently accounted for, and the instruments' high performance is fully utilized. By the mentioned instruments the mean monthly HIS signal can be resolved up to degree 70. The brown curve corresponds to the case of the SGRS optical accelerometer derived in ACME and the same LRI. The blue and orange curves represent the CAI (HosseiniArani et al., 2024) and hybrid accelerometers (Dalin et al., 2020) with the anticipated level of accuracy of LRI 2030. Finally, the red and purple curves show the residuals in the spectral domain for the SGRS optical accelerometer with LRI 2030 and LRI 2033. It is clear that the combination of a high-pass filtered optical SGRS from ACME with LRI 2033 (purple curve) outperforms other inertial sensors. In favorable conditions, when the temporal aliasing does not play a role, potentially the time-variable gravity field can be determined with such instruments up to degree 120. Comparing the green and the brown curves, one can notice a prominent improvement by substituting a state-of-the-art electrostatic accelerometer (SuperSTAR) by an optical one. On the other hand, the inclusion of the anticipated performance of LRI 2033 instead of 2030 does not reduce the residuals dramatically, achieving a $\sim 5 \times 10^{-9}$ m level in geoid height (see red and purple curves).

Figure 6.10 shows the global maps with the spatial distribution of the unitless spherical harmonic residuals of the recovered gravity model w.r.t. the reference EIGEN-6C4, plotted in terms of EWH. The same limits of the colorbar of the spatial residuals, equal to ± 5 mm of EWH, are used in all global maps for easier comparison. By moving from the global map **I**, which corresponds to a GRACE-FO scenario, towards **VI**, representing the combination of the SGRS optical accelerometer from ACME with LRI 2033, the order of magnitude of the residuals reduces and patterns transform certain regular to more multi-directional ones. In other words, with advanced sensors, spatial residuals are more isotropically distributed, rather than uniformly in North-South direction with state-of-the-art electrostatic accelerometers.

Corresponding spherical harmonic error spectra of the coefficient differences of the above-mentioned scenarios in logarithmic scale are shown in Figure 6.11. The larger absolute values, depicted in dark blue in the colorbar, represent a smaller relative error of the SH coefficients. Therefore, spectra **V** and **VI**, for example, have more zonal and tesseral SH coefficients that are closer to the reference gravity field, compared to spectrum **I**. In general, all spectra are consistent with the degree RMS curves (Figure 6.9) and global maps of the residuals (Figure 6.10), showing that advanced instruments outperform state-of-the-art sensors.

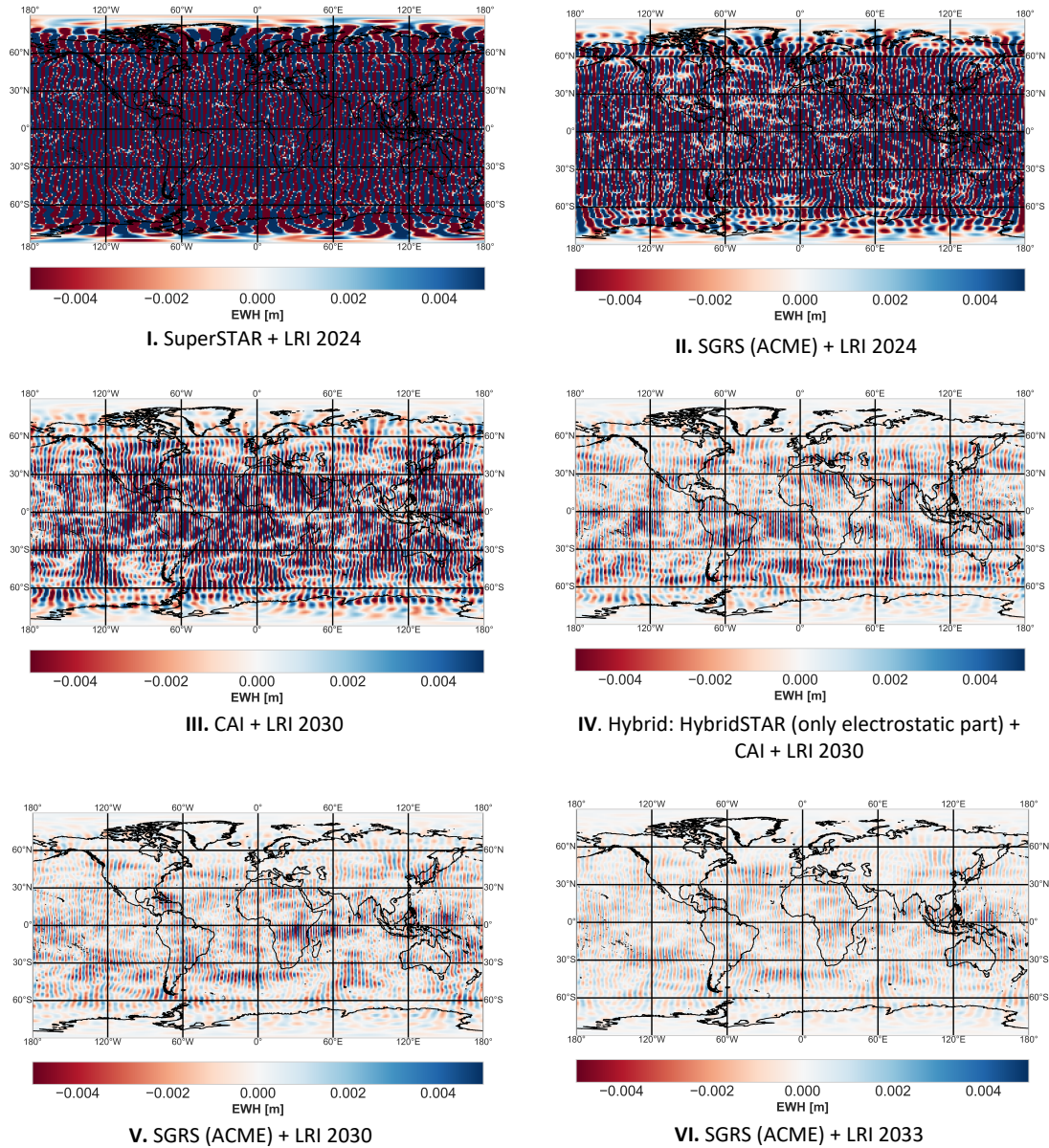


Figure 6.10: Spatial distribution of the residuals of the recovered gravity models w.r.t. EIGEN-6C4, plotted on global maps in EWH from ll-SST simulations; Orbit: #1 (Table 4.2), $h = 478.48$ km; Considered inertial sensors and inter-satellite range measurement instruments are given below each graph. Colorbar limited to ± 0.005 m = ± 5 mm EWH.

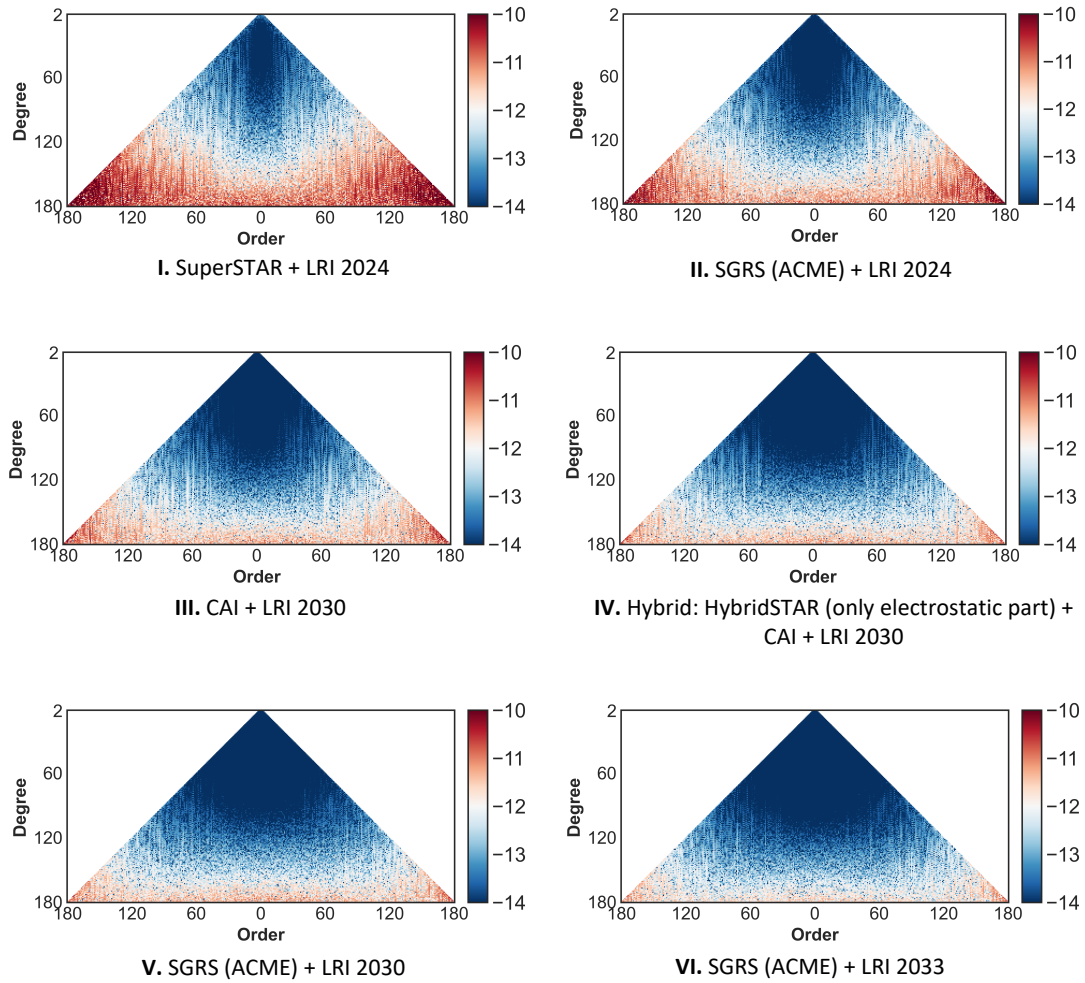


Figure 6.11: Spherical harmonic error spectra of the coefficient differences (true errors) of the recovered gravity models w.r.t. EIGEN-6C4, from Il-SST simulations; Orbit: #1 (Table 4.2), $h = 478.48$ km; Considered inertial sensors and inter-satellite range measurement instruments are given below each graph.

6.2.2 II-SST Simulations with Time-variable Background Modeling Errors

Tidal and non-tidal time-variable background models are not considered in this study since the main focus lies in the instruments' evaluation and performance comparison (see closed-loop procedures in Section 4.1). However, one should keep in mind that mass redistributions with short periods in the atmosphere and oceans can not be properly resolved by the monthly sampling provided by GRACE and GRACE-FO missions (Dobslaw et al., 2016). This leads to temporal aliasing phenomena, when the spurious signals occur in the gravity field model (Dobslaw et al., 2017). Also, a so-called vertical signal separation problem is given. Satellite gravimetry, as any gravimetric measurement technique, is affected by the lack of sensitivity for distinguishing mass changes at, above, or beyond the Earth's surface due to substantially diminished harmonic upward continuation (Dobslaw et al., 2017). Water mass changes happening with low frequencies, e.g., in the continental ice-sheets (Ciraci et al., 2020) or sub-surface aquifers (Kvas et al., 2024), can be inferred from GRACE(-FO) with a spatial resolution of mm-geoid height down to 350 kilometers (Dahle et al., 2014).

An a priori time-variable background model called Atmosphere and Ocean De-Aliasing Level-1B (AOD1B) provided by Deutsches GeoForschungsZentrum (GFZ) is normally used in the gravity recovery procedure to assist the vertical separation problem and reduce temporal aliasing (Dobslaw et al., 2017). In Shihora et al. (2022) it was mentioned that the atmospheric component of AOD1B is based on analysis and forecast data of the operational weather prediction model, provided at 3-hourly time-steps by the European Centre for Medium-Range Weather Forecasts (ECMWF). In order to represent only non-tidal mass variations, three major components are empirically estimated and subtracted. These constituents are surface pressure anomalies, upper density anomalies and ocean bottom pressure (Shihora et al., 2023). The ocean component is based on unconstrained simulations with the Max-Planck-Institute for Meteorology Ocean Model (MPIOM). AOD1B models are provided in terms of Stokes coefficients. For gravity field recovery in this study, monthly averaged products, calculated as a mean of the daily products for May 2002, were used. In this work the errors of the AOD1B product were considered either as the difference between monthly averaged releases 6 (RL6) (Dobslaw et al., 2017) and 7 (RL7) (Shihora et al., 2022) or as recently available AOe07 (Shihora et al., 2024), interpolated to each time step. Comparing RL6 with RL7, the latter one incorporates the effects of the self attraction and solid Earth deformation. Also, an updated estimation and subtraction of atmospherically induced tidal signals enhanced the representation of the bathymetry and atmospheric forcing near Antarctica (Shihora et al., 2022). AOe07 error time-series are considered as an estimation of the residual uncertainties in the AOD1B RL07 model and complemented by a new spatial error variance-covariance matrix (Shihora et al., 2024).

For simulating the error of the tidal time-variable background models, the difference between monthly averaged EOT11a (Savcenko and Bosch, 2012) and

FES2014b (Lyard et al., 2021) was considered. The first one is based on an empirical analysis of long time-series data from satellite altimetry, acquired from multiple missions, and refinements in hydrodynamic modeling (Savcenko and Bosch, 2012). The finite element solution model (FES2014b) also includes hydrodynamic modeling and provides three components: tide elevations, currents and loading. FES2014 was produced by Noveltis, Legos and CLS and distributed by Aviso+, with support from CNES (Aviso+, 2024).

Ocean-tide models were converted to spherical harmonic coefficients by routines provided by Mayer-Gürr et al. (2012, 2021) using a software named Gravity Recovery Object Oriented Programming System (GROOPS) developed by the Institute of Geodesy from the Technical University of Graz. According to the software description, corrections to the Stokes coefficients of a spherical harmonics expansion represented the gravitational effect of ocean and atmospheric tides including loading effects.

Figure 6.12 shows the time-variable background modeling errors, as the difference of the monthly averaged AOD RL7 and RL6, ocean tides EOT11a and FES2014b and interpolated from 6-hourly series to each time step (5 s) AOe07, in terms of ASD. It is evident that, by reaching an order of magnitude of $10^{-8} \text{ (m/s}^2\text{)}/\sqrt{\text{Hz}}$ around 1 mHz, these modeling errors dominate over the noise of the inertial and range measurement instruments, discussed in Chapter 5.

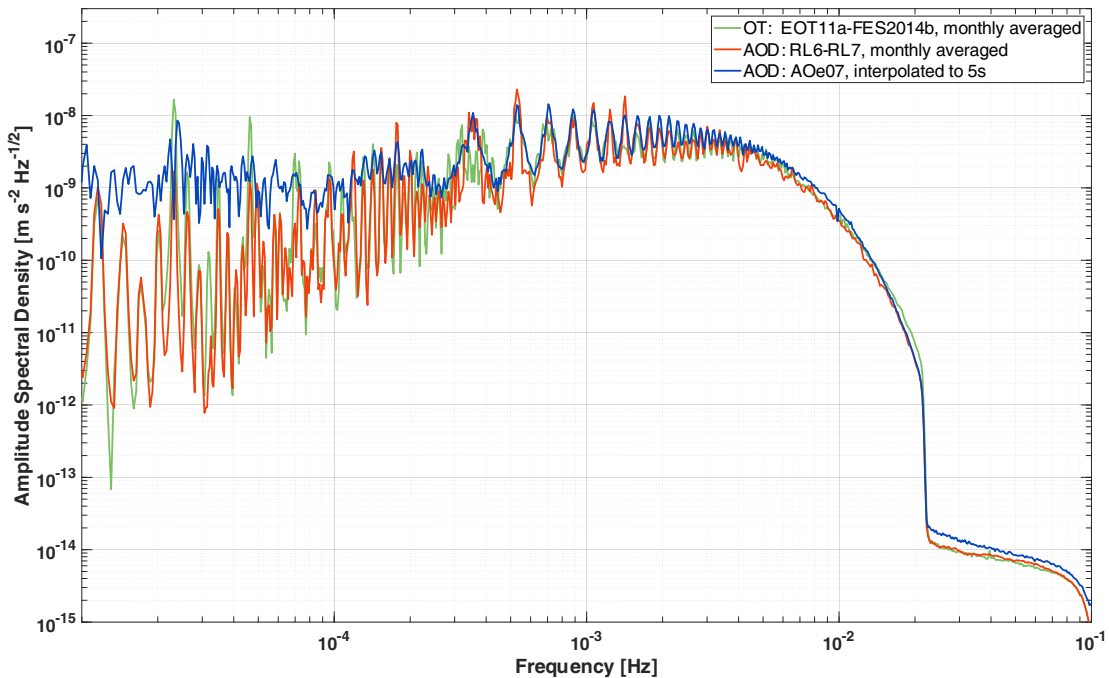


Figure 6.12: ASD of the difference of the monthly averaged AOD RL7 and RL6, ocean-tide difference of the EOT11a and FES2014b and interpolated AOe07, representing the time-variable background modeling errors, considered in gravity field recovery simulation.

In order to demonstrate the impact of background modeling errors on the retrieved gravity field models, four different simulations were carried out. In par-

particular: two instrument noise-free cases and two instrument configurations from the previous Section 6.2.1: CAI accelerometer $10^{-11} \text{ (m/s}^2\text{)}/\sqrt{\text{Hz}}$ with LRI 2030 and a high-pass filtered SGRS optical accelerometer, derived in ACME with the same LRI. Degree RMS of the spherical harmonic coefficient differences from all scenarios are shown in Figure 6.13. In all cases the difference between monthly averaged EOT11a and FES2014b was considered. There is no difference almost up to degree 80 among the scenarios with the monthly averaged AOD (orange, green and blue curves). The instrument noise-free simulation with AOD AOe07, interpolated to each time step (red curve), demonstrates even larger residuals. Therefore, it can be concluded that a monthly averaged approximation of the AOD might be not sufficient, or in other words, provides a too optimistic estimation of the modeling errors. In contrast, interpolating to each time step offers a more accurate representation because the associated error is calculated and assigned at each epoch during generation of the synthetic observations. In general, all cases confirm the dominating behavior of the time-variable background modeling errors over the inertial and range measurement instruments. A certain difference among the CAI accelerometer with LRI 2030 (orange curve), SGRS optical accelerometer with the same LRI (green curve) and an instrument noise-free case (blue curve) is noticed only at higher degrees.

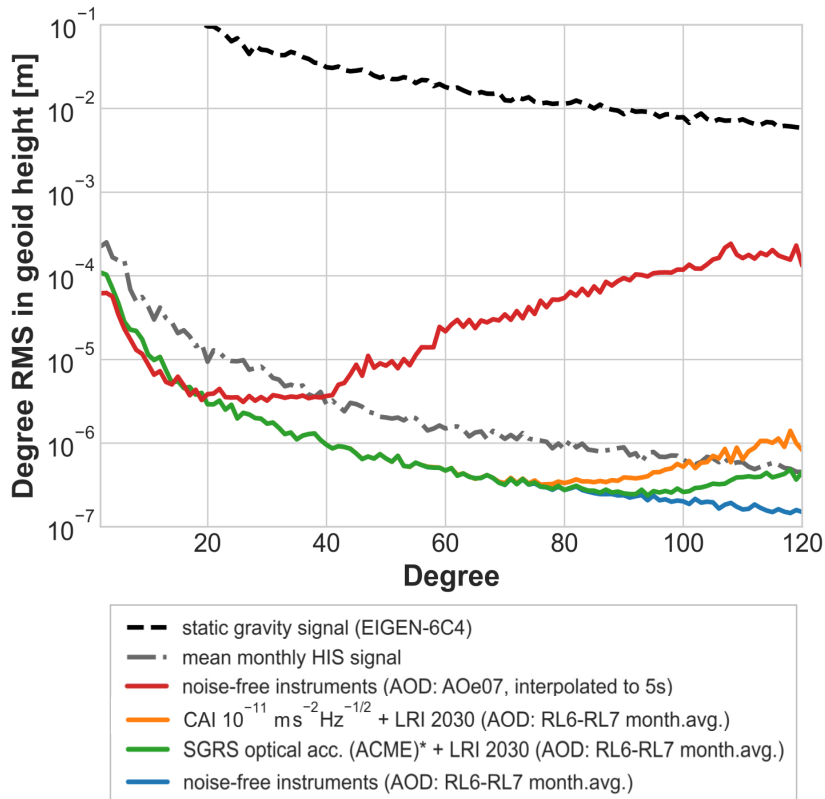


Figure 6.13: Degree RMS of the spherical harmonic coefficient differences (true errors) between recovered and EIGEN-6C4 gravity field models in geoid height (m) from ll-SST simulations including time-variable background modeling errors; Orbit: #1 (Table 4.2), $h = 478.48 \text{ km}$. * applied high-pass filter.

Figure 6.14 shows the global maps, as well as the spherical harmonic error spectra of the residuals for the corresponding cases. For clarity, the same orders of magnitude, equal to ± 5 cm of EWH, are used in all global maps. Since the residuals in the spectral domain for the case with the AOD interpolated to each time interval (red curve in Figure 6.13) were the largest, the discrepancies in the spatial domain in this simulation are also the biggest among the considered scenarios. In addition to the large order of magnitude differences, the corresponding graph (top left in Figure 6.14) shows a prominent North-South striping behavior. Despite of the general similarity of the other three graphs, certain differences can be noticed on closer look. The CAI accelerometer $10^{-11} \text{ (m/s}^2\text{)}/\sqrt{\text{Hz}}$ with LRI 2030 shows the worst performance among the cases with the difference of the monthly averaged AOD RL6 and RL7 and a particular striping behavior is observed. In general, the pattern of the spatial distribution of the residuals from the SGRS optical accelerometer with LRI 2030 is similar to the instrument noise-free case (bottom row).

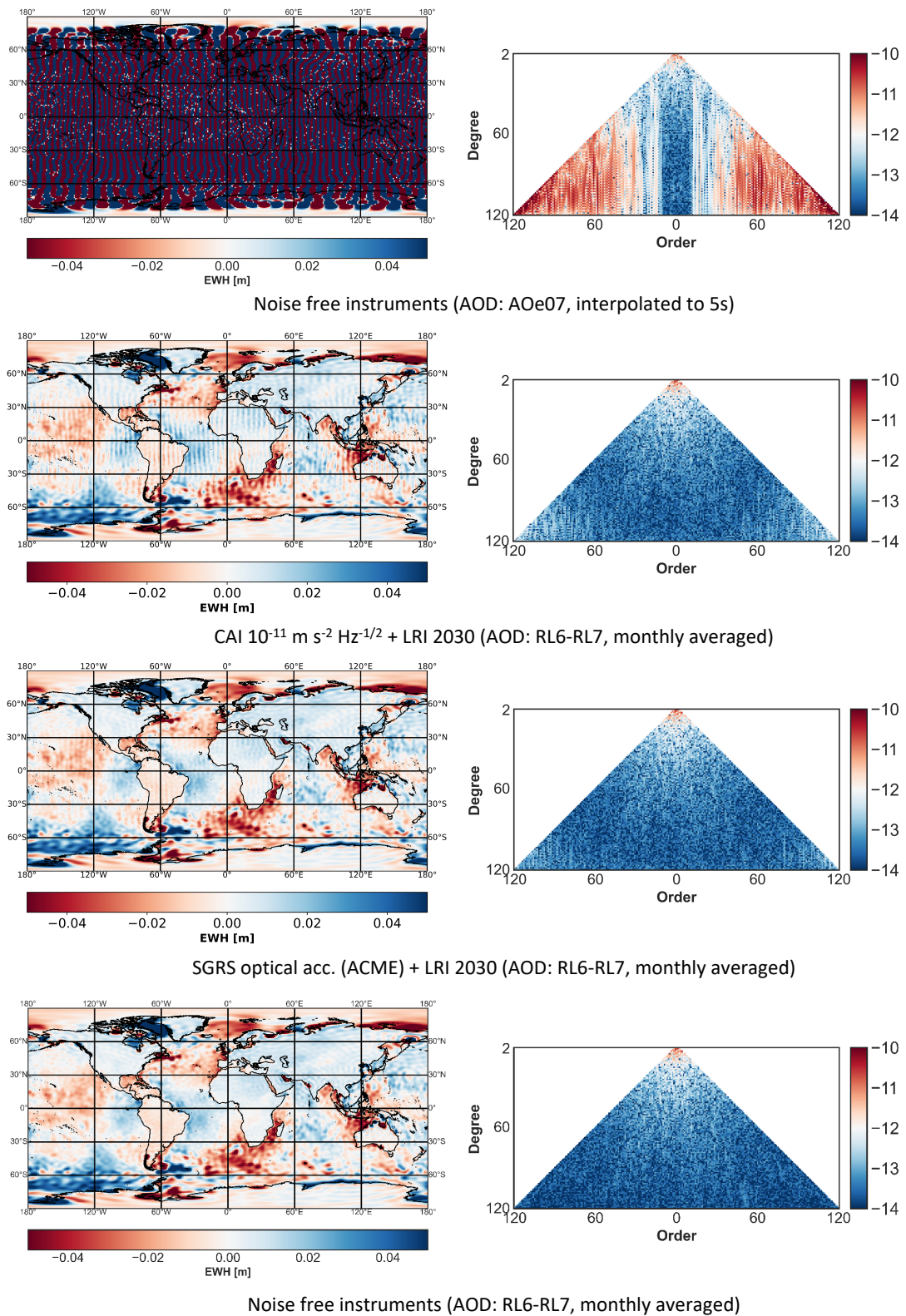


Figure 6.14: Spatial distribution (on the left) and spherical harmonic error spectra (on the right) of the residuals from ll-SST simulations including time-variable background modeling errors; Orbit: #1 (Table 4.2), $h = 478.48 \text{ km}$. Considered inertial sensors and inter-satellite range measurement instruments are given below each graph. Colorbar of the global maps limited to $\pm 0.05 \text{ m} = \pm 5 \text{ cm}$ EWH.

6.2.3 II-SST Simulations with Modified Satellites Shapes

Three critical factors, i.e. Size, Weight and Power, forming a so-called SWaP concept, have to be considered in designing and implementing new concepts and techniques. Originated from defense industry, where SWaP requirements are crucial, for example in weapon systems, unmanned aerial vehicles (Jones and Gross, 2014), etc., this concept also spread to the aerospace sector. SWaP is a key consideration in the design for all types of orbiters, from cubesats (Kingsbury et al., 2017) to large satellites, e.g., GNSS (Gramling et al., 2024). Reduction of size and weight of the satellite can dramatically save launch expenses, while minimizing power consumption can extend the lifespan of the missions, especially when power supply is limited. In satellite gravimetry missions, the weight of the spacecraft is also one of multiple constraints that have to be complied in future (Dionisio et al., 2018). Since II-SST requires two satellites, a dual-launch configuration system, similar as it was used in the GRACE and GRACE-FO missions, has to be utilized. Dionisio et al. (2018) and Haagmans et al. (2020) considered the Vega-C rocket as a launch vehicle with a 2250 kg maximum launch mass. That means it can lift off both satellites, each of 1000 kg, and a 250 kg satellite dispenser. Moreover, the geometrical dimensions of the rocket fairing also constrain the maximum size of the satellites. On the other hand, the authors mentioned that, for successful gravimetry missions, the orbit altitude should be low (<400 km), while the mission lifetime long enough to cover a full solar cycle (11 years). On the instruments' level, ultrasensitive inertial sensors perform better on a drag-compensated platform, as it was shown for SGRS by Dávila Álvarez et al. (2022). Inter-satellite laser interferometers also require an accurate enough pointing to maintain the range measurements. Therefore, an advanced attitude and orbit control system including eight ion thrusters and three magnetic torquers for maintaining the satellite's orientation as well as a large ion thruster for compensating air drag were considered by Dionisio et al. (2018). Such an electric propulsion system is estimated to have a high power demand (~ 1 kW), which might be enlarged by novel inertial sensors. Deployable solar panels might be an optimum option as they could acquire enough power for all consumer devices, also within unfavorable solar illumination conditions due to the non sun-synchronous orbits, and do not significantly increase the satellite dimensions and mass. However, extended solar arrays increase the satellite's cross-sectorial area, enlarging the impact of the atmospheric drag and solar radiation pressure. If these solar arrays are not perfectly rigid, they may vibrate, leading to unwanted perturbations and accelerations.

A joint study of the three institutions Leibniz University Hannover, Max Planck Institute for Gravitational Physics (IGP) and German Aerospace Center (DLR) within the TerraQ collaborative project has been carried out in order to evaluate the effect of the modified GRACE-like satellite shapes in terms of gravity field recovery. Preliminary results of this study will be published in a joint paper (Leipner et al. (2025), under revision).

Closed-loop simulations, similar to those that were introduced in Section 4.1, were carried out. Here also finite element models of the satellites with modified shapes

and changing performance of the optical accelerometer modeled in ACME SGRS were considered. Figure 6.15 shows a graphic rendition of the satellite shapes that were studied. **I** - is a ‘standard’ GRACE(-FO) satellite shape (JPL-NASA, 2024) and the modified ones with the solar array mounted on top and bottom are shown in **II** and **III**, respectively. According to Kornfeld et al. (2019), for the ‘standard’ GRACE(-FO) satellite shape, the top panel provides 350 W, while each of the two side panels more than 510 W in the worst-case scenario. Therefore in total, solar arrays of the ‘standard’ spacecraft shape produce around 1.37 kW, while within the modified shapes this quantity could be potentially increased up to around 2 kW (Leipner et al., 2025).

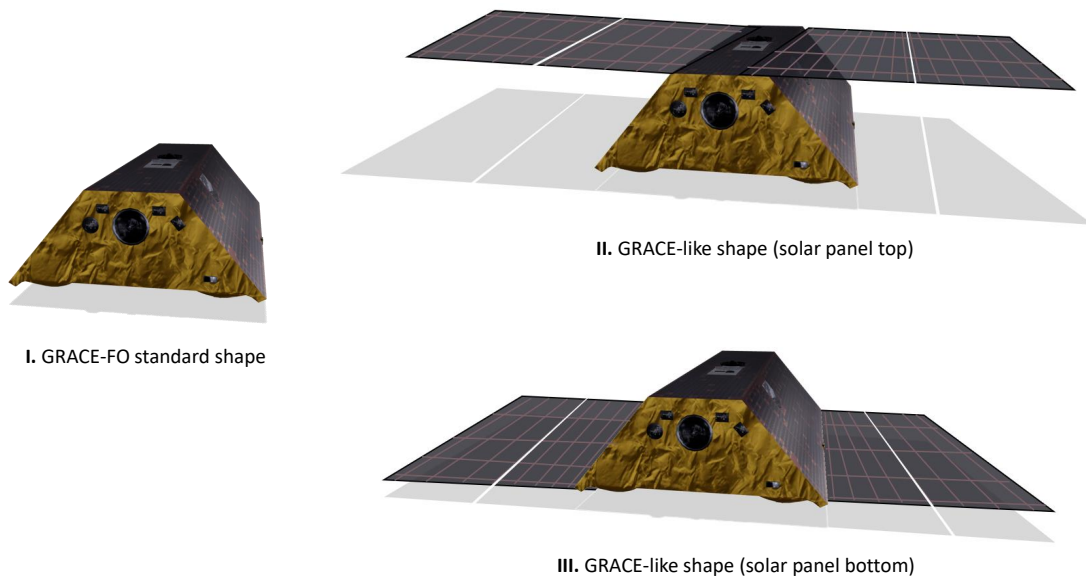


Figure 6.15: 3D graphic rendition of the studied satellite shapes. **I** - GRACE-FO 3D model JPL-NASA (2024); **II** - GRACE-like satellite with solar panels on top; **III** - GRACE-like satellite with solar panels at bottom (**I**, **II** modified based on JPL-NASA (2024)).

As the first step of the closed-loop procedure, orbit simulations in XHPS, described in Section 4.2, were carried out. In addition to the different finite element models of the spacecraft, various drag coefficients (C_D) were used in the satellite dynamics simulator. For the standard GRACE-FO satellite shape, a drag coefficient equal to 2.25 was considered, which is in the range of a typical number for a convex-shaped spacecraft (Montenbruck et al., 2002; Wöske et al., 2018). For the modified satellite shapes, a drag coefficient equal to 4.5 was assumed as a worst case scenario in order to adequately represent the enlarged surface area in the direction of the drag. This number, which is twice larger than for the ‘standard’ spacecraft shape, was considered also in accordance with the drag coefficient estimates in Mehta et al. (2017). Also, a non-drag compensated regime was considered in the orbit simulations. Figure 6.16 shows an orbit decay during the simulated one month mission time span of the standard GRACE-FO satellite (blue curve) and two satellites with extended solar panels (red and orange curves). A similar altitude decay of both satellites with modified shapes are due

to the same area of the solar arrays and identical drag coefficients. From the orbit simulations, a total altitude difference of around 4 km can be observed after 31 days.

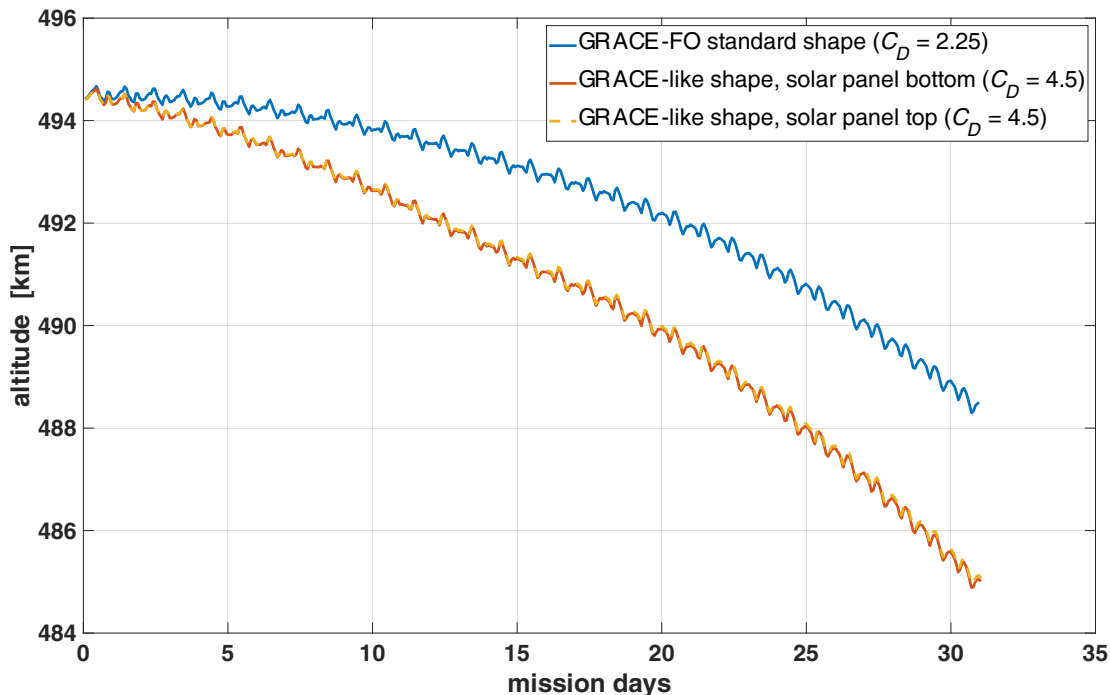


Figure 6.16: Decay of the maximum orbit altitude per revolution of the standard GRACE-FO and two shape-modified spacecraft during the simulated one month mission time span (modified from Leipner et al. (2025)).

As it was already mentioned, a different level of accuracy of the SGRS optical accelerometer modeled in ACME was considered in this study w.r.t. various satellite shapes. Figure 6.17 shows ASD sensitivities of the modeled SGRS optical accelerometer for the standard GRACE-FO shape with a cross-sectorial area of 1.16 m^2 (black curve) and for the orbiters with extended solar panels and a cross-sectorial area of 1.47 m^2 (blue curve). Josselin et al. (1999) showed that non-gravitational forces impact the TM through its coupling to the spacecraft. Therefore, various cross-sectorial areas of the satellite would cause a different level of the actuation noise, introduced in Section 4.3. This, in turn, would lead to a certain discrepancy between the ASD curves above 1 mHz (Leipner et al., 2025). Similar to the other studies, high-pass filtering was also applied at 0.5 mHz in order to minimize the effect of the low-frequency components. It is clear that in the high-frequency domain the errors of the inter-satellite LRI dominate over the SGRS noise.

Figure 6.18 shows a degree RMS of the spherical harmonic coefficient differences, plotted in geoid height, for the closed-loop simulations with the different satellite shapes w.r.t. the time-variable HIS signal. The blue curve represents the residuals from the standard shape case and the two modified ones are shown with orange and green curves. First of all, it can be noticed that there is no degradation of the science output due to more complicated satellite shapes. So, they can be used for

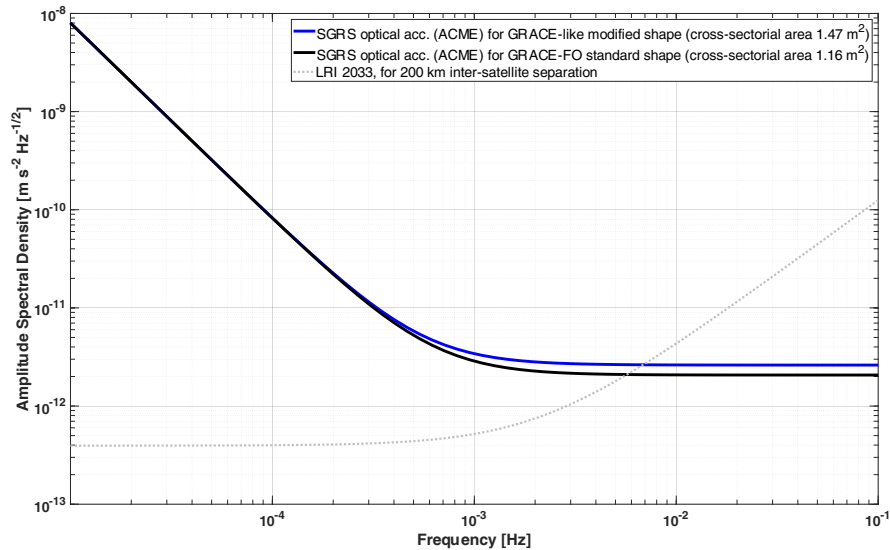


Figure 6.17: Comparison of the ASD sensitivities of the modeled SGRS optical accelerometers on-board of the satellite with standard GRACE-FO shape (black curve) and modified ones (blue curve). Measurement error of the inter-satellite LRI anticipated in 2033 for the satellites separated by 200km is shown as grey dotted line (Leipner et al., 2025).

gravity field recovery achieving similar performance as the standard GRACE-FO shape. However, it is important to note here that multiple simplifications and assumptions were considered in this evaluation in various steps, e.g. neglecting of the ‘centrifugal’ term in QACC software (Equation (4.3)), omitting propellant consumption and orbit maneuvering, assuming a rigid body of the spacecraft, etc. The convergence of the curves of the modified cases can be explained by their identical orbit decay and the same level of the modeled SGRS performance. Therefore, it can be concluded that a non-drag compensated regime, leading to the faster orbit decay of the satellites with extended solar arrays, is a relevant factor in the retrieved gravity field models. In essence, the difference in GFR between the standard and modified cases is mainly caused by the orbit effects. In general, an important point to consider in this simulation is that modified spacecraft shapes provide a trade-off between the duration of the mission life-time and achieved accuracy of retrieved gravity models. On the one hand, smaller residuals between the recovered and reference gravity models can be achieved, but on the other hand, a prolongation of the mission time-frame would require a higher supply of the propellant.

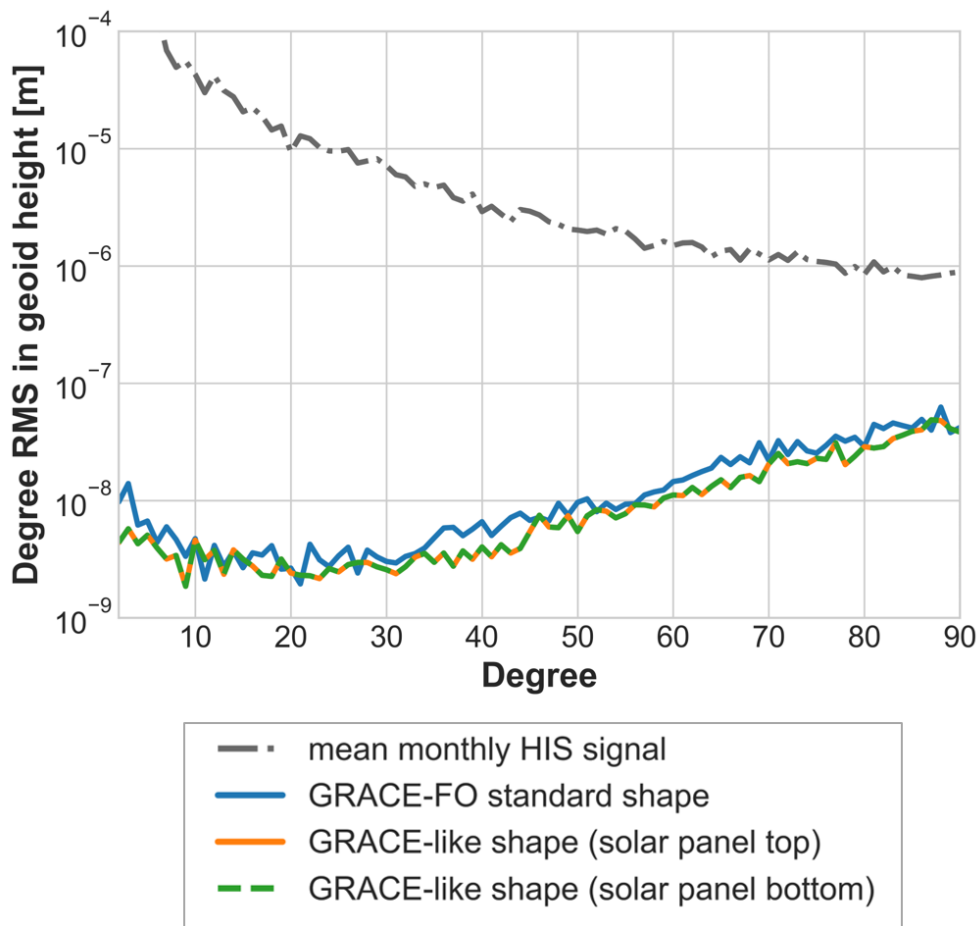


Figure 6.18: Degree RMS of the spherical harmonic coefficient differences (true errors) between recovered and EIGEN-6C4 gravity field models in geoid height (m) from 11-SST simulations with different satellite shapes (based on Leipner et al. (2025)).

6.3 Cross-track Satellite Gravity Gradiometry

In Sections 6.1.1 and 6.2.1 it was shown that the North-South striping behavior in GRACE-like ll-SST solutions is a common problem that occurs due to multiple factors, i.e. orbit resonance effects (Kvas et al., 2019), sub-Nyquist artifacts resulting from the oversampling of the Earth’s low-frequency gravitational signal (Peidou and Pagiatakis, 2020) and measurement errors. On the other hand, a cross-track gradiometer could provide useful measurements in East-West direction. Therefore, the idea of combining along-track ll-SST with cross-track SGG, introduced in Section 6.3.3, also appears promising in terms of redundancy or ‘backup’ of inertial sensors in case of any failure or technical problem of one of them. In Section 6.3.1, a performance comparison of the standalone single-axis gradiometers that are placed in cross-track direction is shown. Such instruments could be a component of the above-mentioned combination with ll-SST by placing them on-board a GRACE-like satellite. An important factor is that an optical gradiometer has higher technology readiness level, due to the flight heritage of the GRS sensor on-board LISA-Pathfinder mission (Section 3.2), than a CAI instrument. Therefore, an optical gradiometer, modeled in ACME, is considered for the combination with ll-SST.

6.3.1 Cross-track SGG Instruments

SGG is sensitive to different wavelengths of the gravity field signal, compared to ll-SST type of measurements, as it was discussed in Sections 2.2.2, 2.2.3 and 3.1. Therefore, it is crucial to evaluate the performance of gradiometers, formed by novel inertial sensors, and compare it w.r.t. GOCE’s high-sensitive axis gradiometer - the only realised SGG mission up to now. Angular rates of the satellite about the cross-track axis ω_y are much larger than about the along-track (ω_x) and nadir (ω_z) axes (Stummer, 2012). Therefore, in this study modeled gradiometers were arranged in the cross-track direction, measuring the V_{yy} gravity gradient component (Equation (2.9)) with a baseline length $L_y = 0.5$ m. A near-polar, drag-compensated orbit (#5 in Table 4.2) with a mean altitude of 247.35 km was used in the SGG simulations.

Figure 6.19 shows the degree RMS in geoid height (Equation (2.35)) of the true errors retrieved from the cross-track SGG simulations with different instruments. In all cases, stochastic modeling have been applied with weights systematically refined through three consecutive steps. Since the gradiometer measurements are not sensitive to detect the time-variable gravity field signals, e.g. HIS, all curves are located far over the mean monthly HIS signal (gray dashed line). The red curve corresponds to the high-pass filtered high-sensitive axis of the GOCE electrostatic gradiometer (Equation (5.2)). The purple curve belongs to the gradiometer formed by a pair of modeled SGRS optical accelerometers in ACME. Here, a high-pass filter was also applied in order to minimize the effect of the low-frequency components. Both curves (red and purple) show a similar performance, especially at high degrees. However, the latter one performs slightly

better than the GOCE instrument in the degrees below 80. The other three curves represent results based on CAI $10 \text{ mE}/\sqrt{\text{Hz}}$ and two hybrid gradiometers, formed by a pair of hybrid accelerometers, introduced in Section 5.1. There the effect of the CAI gyroscope, with a white-noise level close to $10^{-8} \text{ rad s}^{-1}$ in terms of angular velocity, which corresponds to an interrogation time of 10 s, was also considered (Savoie et al., 2018). Gyroscopes are required to correct the rotation of the gradiometer axis in the cross-track direction. However, the CAI gyroscope with this level of accuracy does not significantly affect the GFR results. In general, up to a degree of roughly 20, both hybrid gradiometers and those formed by the optical SGRS show identical performance. The residuals from a hybrid gradiometer that consists of the electrostatic SGRS of Dávila Álvarez et al. (2022) and CAI (HosseiniArani et al., 2024) accelerometers are larger (orange curve). This hybrid gradiometer is able to resolve the static gravity signal EIGEN-6C4 only up to degree 140, similar as the CAI $10 \text{ mE}/\sqrt{\text{Hz}}$ standalone gradiometer, formed by a pair of inertial sensors introduced by HosseiniArani et al. (2024). The green curve, that consists of a hybrid gradiometer formed by the electrostatic part of the HybridSTAR sensor (Dalin et al., 2020) and the CAI accelerometers (HosseiniArani et al., 2024), shows the best performance among the considered instruments.

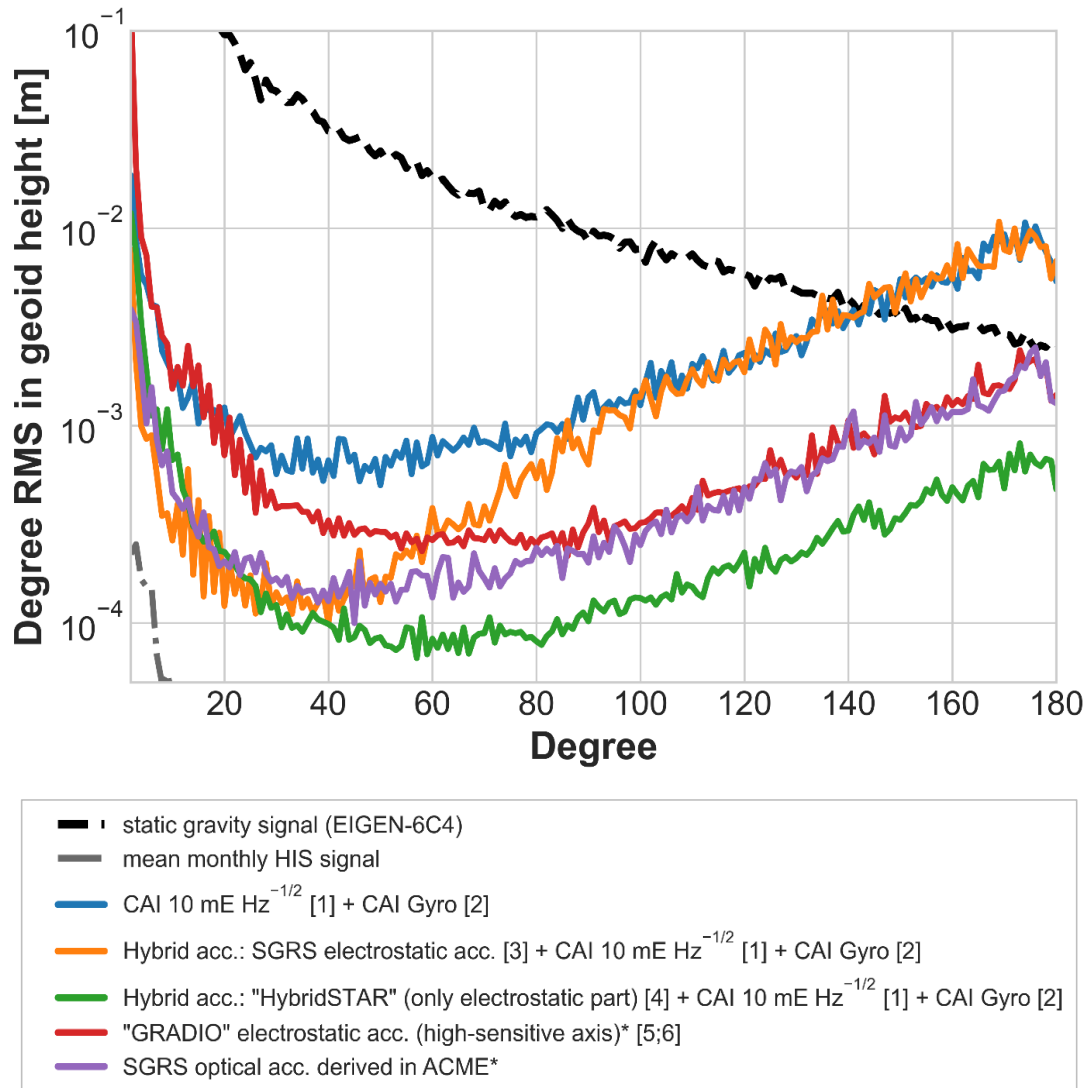


Figure 6.19: Degree RMS of the spherical harmonic coefficient differences (true errors) between recovered and EIGEN-6C4 gravity field models in geoid height (m) from cross-track SGG simulations; Orbit: #5 (Table 4.2), $h = 247.35$ km; * applied high-pass filter. [1] HosseiniArani et al. (2024); [2] Savoie et al. (2018); [3] Dávila Álvarez et al. (2022); [4] Dalin et al. (2020); [5] Marque et al. (2010); [6] Touboul et al. (2016).

6 Gravity Field Recovery Results from Simulations

The global maps with the spatial distribution of the unitless spherical harmonic residuals of the recovered gravity model w.r.t. the reference EIGEN-6C4, from the above-mentioned gradiometer missions are shown in the Figure 6.20. The same order of magnitude of the spatial residuals, equal to ± 30 m of EWH, are used in all global maps for a more explicit comparison. On some maps, especially in **I** and **II**, the residuals are grouped in wide stripes along the longitudinal direction, which can be explained by the relatively poor performance of the single-axis gradiometers in these cases and certain orbit resonance effects of the simulated near-polar orbit. The smallest residuals can be observed in the maps **III** and **V**, which correlates with the results shown in Figure 6.19.

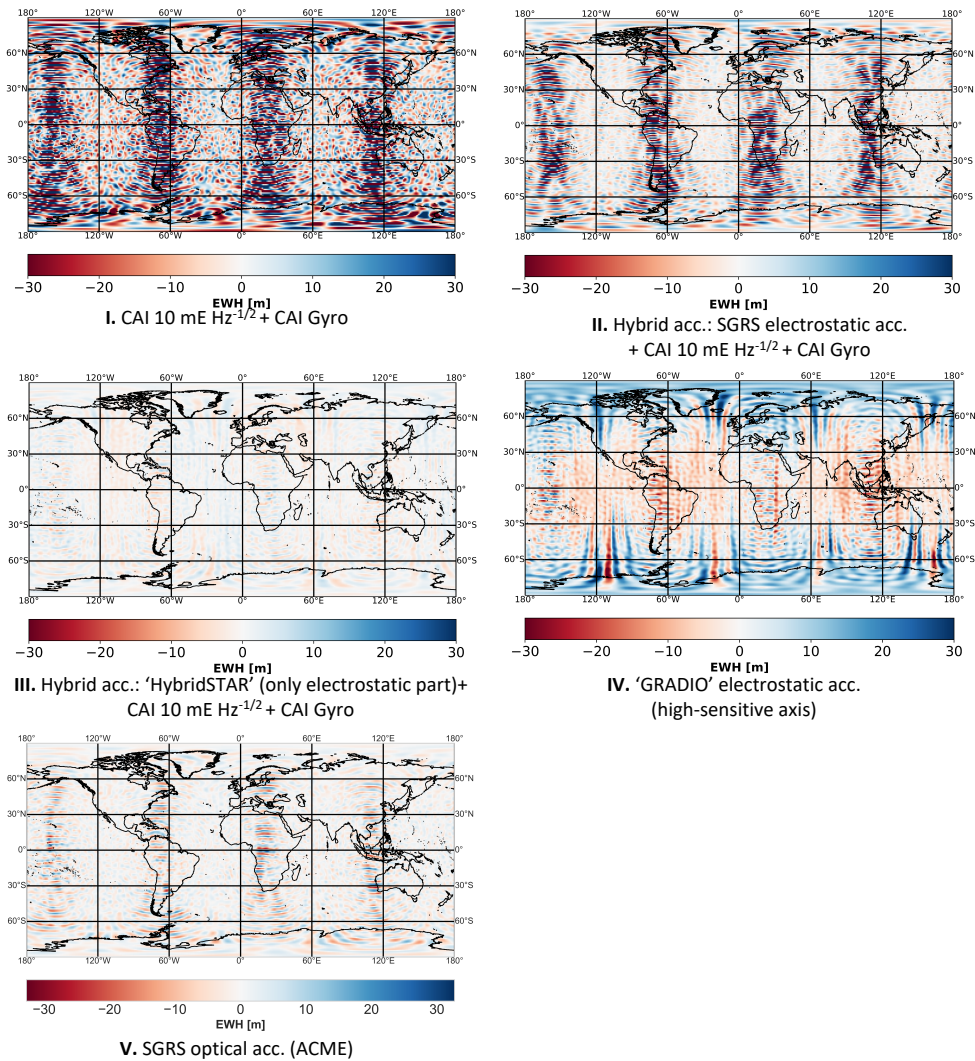


Figure 6.20: Spatial distribution of the residuals of the recovered gravity models w.r.t. EIGEN-6C4, plotted on the global maps in EWH from cross-track SGG simulations; Orbit: #5 (Table 4.2), $h = 247.35$ km; Considered inertial sensors that formed the gradiometers are given below each graph. Colorbar limited to ± 30 m EWH.

Spherical harmonic error spectra of the coefficient differences between the recovered and reference gravity field models from the cross-track SGG simulations are

shown in Figure 6.21 in logarithmic scale. In general, these graphs are consistent w.r.t. the previously shown degree RMS curves (Figure 6.19) or global maps with the residuals (Figure 6.20). The largest residuals of the zonal and tesseral spherical harmonic coefficients are given (in red color) in graphs **I** and **II**. The cases **III** and **V** show the smallest residuals, corresponding to the blue color.

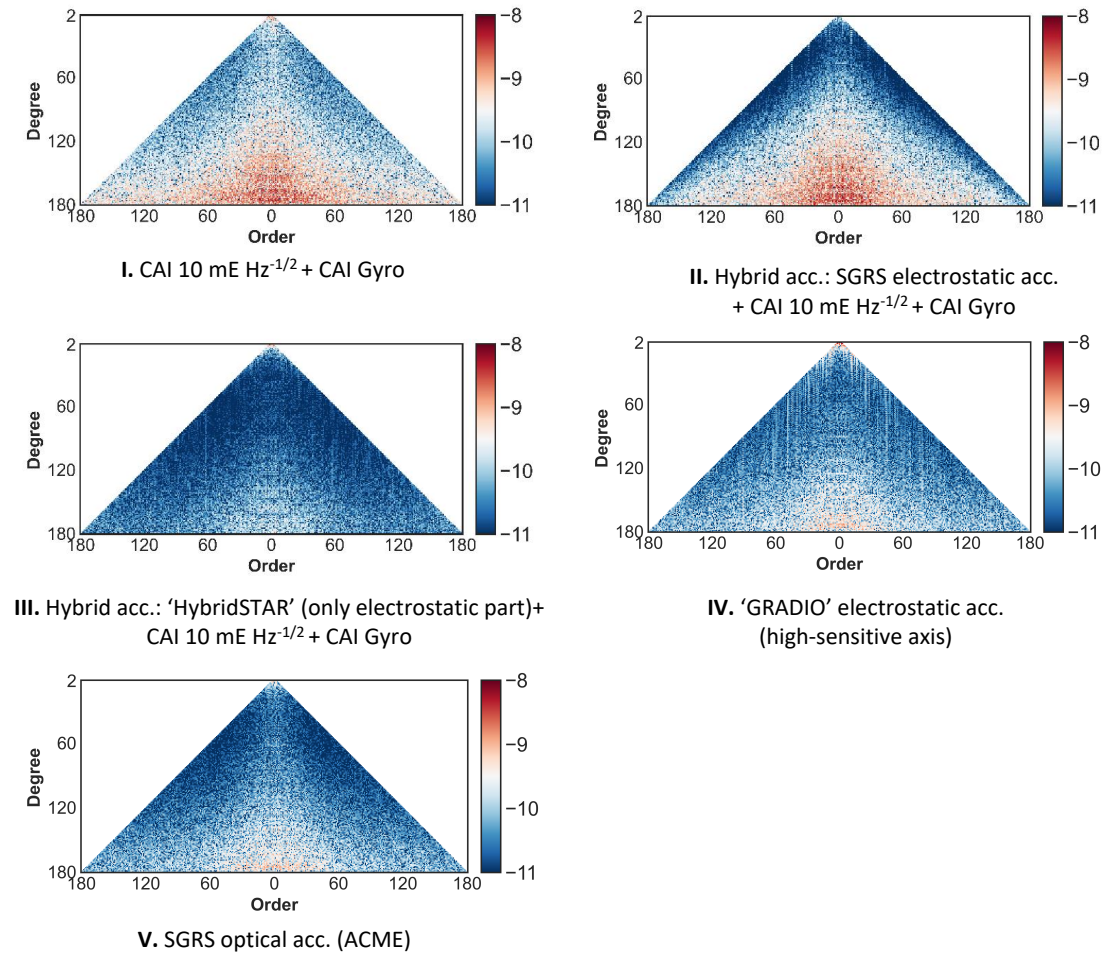


Figure 6.21: Spherical harmonic error spectra of the coefficient differences (true errors) of the recovered gravity models w.r.t. EIGEN-6C4, from cross-track SGG simulations; Orbit: #5 (Table 4.2), $h = 247.35$ km; Considered inertial sensors that formed the gradiometers are given below each graph.

6.3.2 Study of the Common Mode Gain Uncertainty in the SGG case

Gravity gradients, derived from differential mode accelerations (Equation (2.5)), are obtained from an ideal gradiometer. In reality estimated gravity gradients, for example, in cross-track direction, can be introduced as

$$V_{est,yy} = \alpha \left(\frac{a_2 - a_5}{L_y} \right) + \beta \left(\frac{a_2 + a_5}{L_y} \right), \quad (6.2)$$

where, following the notation of Equation (2.9), a_2 and a_5 are the acceleration measurements of accelerometers 2 and 5, L_y is the gradiometer baseline, α is the differential mode gain and β is the common mode gain. In ideal case, $\alpha = 1$ and $\beta = 0$. However, imperfections of the gradiometer instrument, e.g., rotational misalignments of the accelerometers, scale factor errors, non-perpendicular accelerometer axes, etc., cause a failure of the common mode rejection (Koop et al., 2001; Stummer et al., 2012; Douch et al., 2018). Therefore, a small fraction of common mode accelerations leaks to measured differential mode accelerations. The effect of the common mode rejection can be reduced by a proper calibration method (Stummer, 2012). Different gradiometer calibration approaches exist using various sensors and data, e.g., accelerometers and star sensors (Siemes et al., 2012), precise orbit determination (Visser, 2009; Visser and van den IJssel, 2016), hl-SST, terrestrial and global gravity data (Bouman et al., 2004) and using only star sensor data (Rispen and Bouman, 2009). It is important to mention that common mode accelerations represent the sum of non-gravitational forces acting on the spacecraft and feed to the satellite's drag-free control system (Sneeuw et al., 2001). Knabe (2023) estimated the common mode gain uncertainty for a GOCE-like altitude from the calibration procedure tested within the simulated XHPS data in the range of 2×10^{-5} to 3×10^{-7} . Sechi et al. (2011) showed that an amplitude spectral density of the residual linear acceleration is at the level of $2 \times 10^{-9} \text{ (m/s}^2\text{)}/\sqrt{\text{Hz}}$ for the drag-free and attitude control of the GOCE satellite (Romanazzo et al., 2011). Considering the above-mentioned terms, an equation describing the ASD of the total gradiometer error ($\text{ASD}_{\text{gradio, total}}$) is

$$\text{ASD}_{\text{gradio, total}} = \text{ASD}_{\text{gradio}} + \beta \times \text{ASD}_{\text{residual acc.}}, \quad (6.3)$$

where $\text{ASD}_{\text{gradio}}$ is the ASD of gradiometer noise, β is the common mode gain and $\text{ASD}_{\text{residual acc.}}$ is the ASD of the residual linear acceleration. Figure 6.22 shows ASD curves of the common mode gain uncertainty values, taken from Knabe (2023), multiplied by the ASD of the residual linear acceleration (Sechi et al., 2011), assumed as white noise. For comparison, an ASD of the gradiometer formed by SGRS optical accelerometers derived in ACME is also shown. The latter ASD (black curve) lies far above the other two ASDs. Therefore, the impact of the common mode gain uncertainty, multiplied by the residual drag acceleration, is negligibly small and can be neglected in gravity field recovery simulations from SGG.

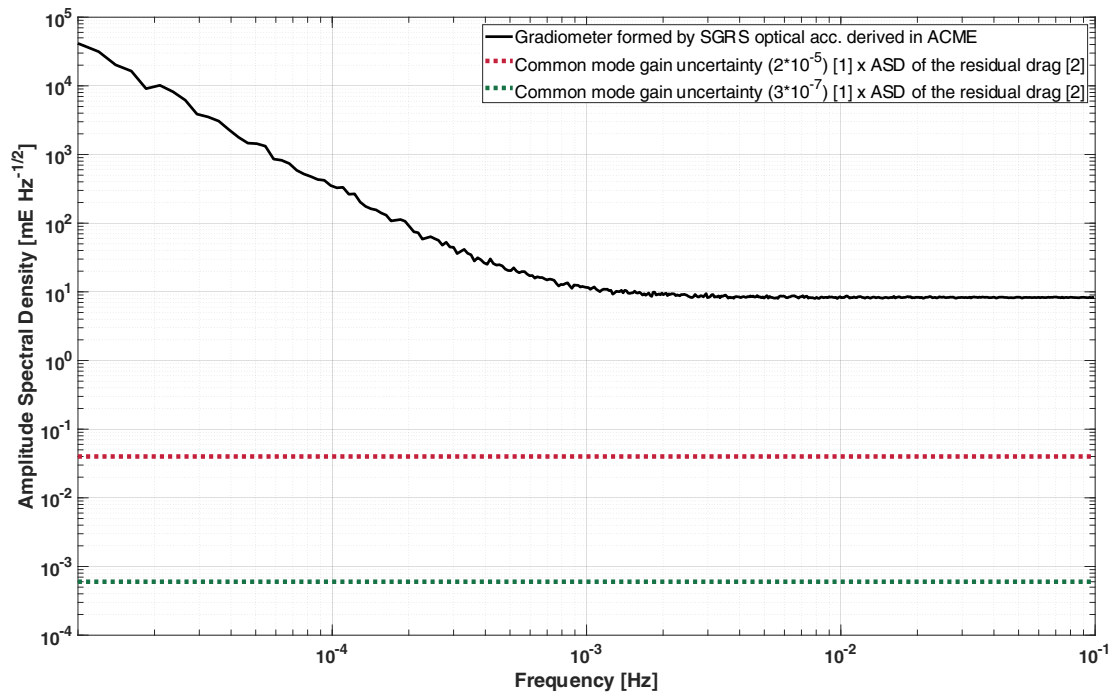


Figure 6.22: ASD curves of two cases of the common mode gain uncertainty for a GOCE-like orbit ($h=250 \text{ km}$), multiplied by the residual drag ASD. Also, the ASD sensitivity of the gradiometer formed by a pair of SGRS optical accelerometers derived in ACME is shown. [1] Knabe (2023); [2] Sechi et al. (2011)

6.3.3 Combination of ll-SST and Cross-track SGG

An elegant idea of placing a cross-track gradiometer in a ll-SST mission could potentially solve multiple issues. In particular, this instrument configuration could benefit from the advantages of the ll-SST and SGG measurement techniques, that are sensitive to different spatio-temporal parts of the gravity signal (Purkhauser and Pail, 2020). Cross-track gravity gradient measurements introduce valuable information in East-West direction that could reduce the North-South striping behavior, which is typical for GRACE-like solutions. Finally, the inclusion of additional inertial sensors could provide redundancy, ensuring functionality in case of any failure or unexpected measurement noise, as it was the case in GRACE-FO about one month after the launch (Landerer et al., 2020). As a consequence, placing supplementary inertial sensors might avoid the necessity of accelerometer data transplantation (Bandikova et al., 2019) or the missing data recovery, for example, by high-precision environment modeling (Huckfeldt et al., 2024).

The scheme of the combination of the ll-SST and cross-track SGG measurement principles is shown in the Figure 6.23 (Kupriyanov et al., 2024b). The idea is to place a state-of-the-art electrostatic SuperSTAR accelerometer in the center of mass of each orbiter with a KBR inter-satellite range measurement instrument in between. In the cross-track direction an enhanced gradiometer, formed by a pair of optical SGRS, modeled in ACME, with a 10 times better performance w.r.t. inertial sensor, given by the ASD Equation (5.5) is used. For this simulation, a near-polar, drag-compensated orbit (#5 in Table 4.2) was used with a mean altitude of 247.35 km. All colored noise sensors were high-pass filtered.

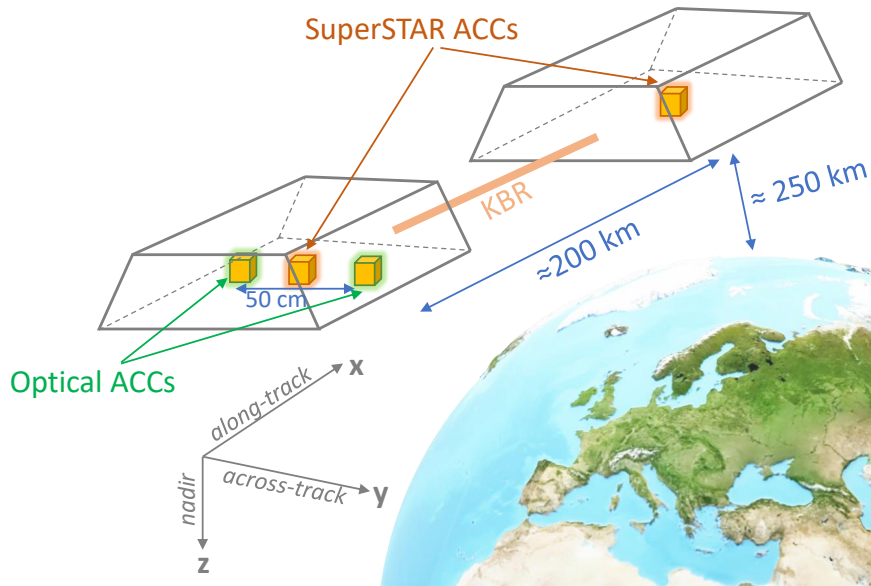


Figure 6.23: Scheme of the combination of ll-SST and cross-track SGG in a possible future gravimetry mission (Kupriyanov et al., 2024b).

Figure 6.24 shows the degree RMS in geoid height (Equation (2.35)) of the true errors retrieved from the cross-track SGG (blue curve), ll-SST (orange curve) and their combination (green curve). For the combination of retrieved gravity solutions, here empirical weighting values (0.01 for ll-SST and 2 for SGG) were utilized, instead of computed variance components (Equation (2.40)). This was done in order to maximize the level of accuracy of the combined solution. However, despite of the utilization of an enhanced optical gradiometer, there is still a large difference in the residuals between the ll-SST and SGG curves. The difference of more than two orders of magnitude originates from the application of the stochastic modeling, when then true errors in the ll-SST case are reducing significantly with each step (see Subsection 6.1.1). This makes it quite challenging to benefit from combining these two measurement principles. Therefore, the green curve is almost identical to the orange one. However, as it was shown in Kupriyanov et al. (2024b) (see Figure A.1 in the appendix) and Knabe (2023), with only one iteration of stochastic modeling and non high-pass filtered instruments, it is possible to get an improvement in the combined case w.r.t. standalone ll-SST or SGG.

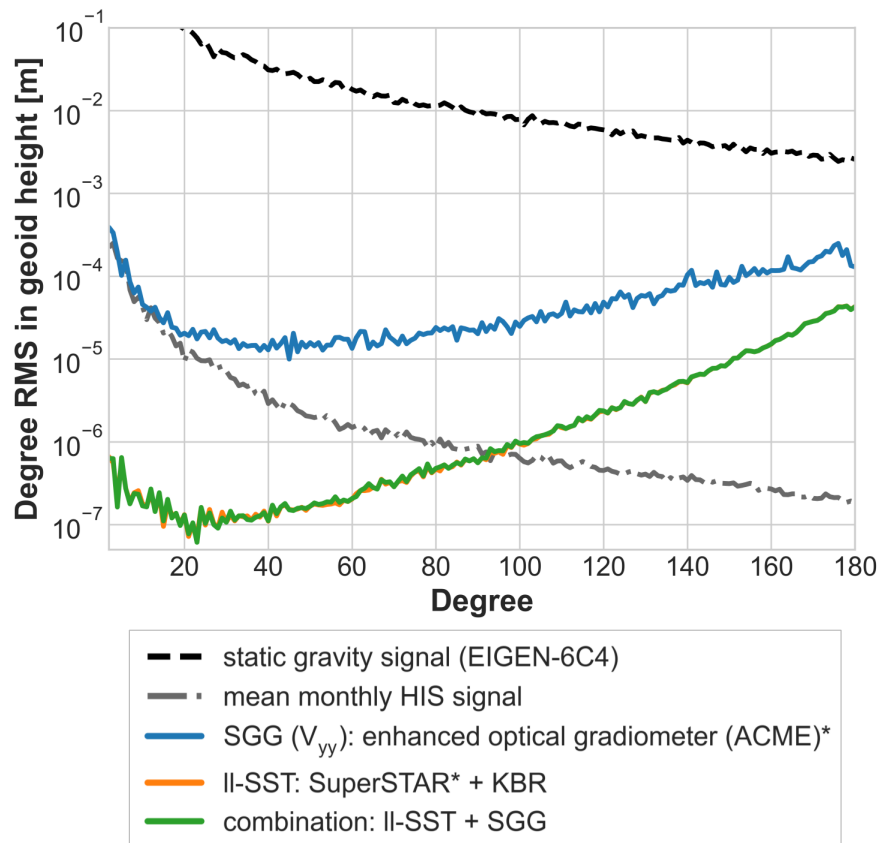


Figure 6.24: Degree RMS of the spherical harmonic coefficient differences (true errors) between recovered and EIGEN-6C4 gravity field models in geoid height (m) from ll-SST, cross-track SGG and their combination; Orbit: #5 (Table 4.2), $h = 247.35$ km; * applied high-pass filter.

Figure 6.25 shows the global maps, as well as the spherical harmonic error spectra

6 Gravity Field Recovery Results from Simulations

of the residuals for ll-SST, cross-track SGG and their combination. The global maps are plotted with the same orders of magnitude equal to ± 3 cm EWH. The residuals in both, spatial and spectral domains from the ll-SST and combined cases barely differ from each other.

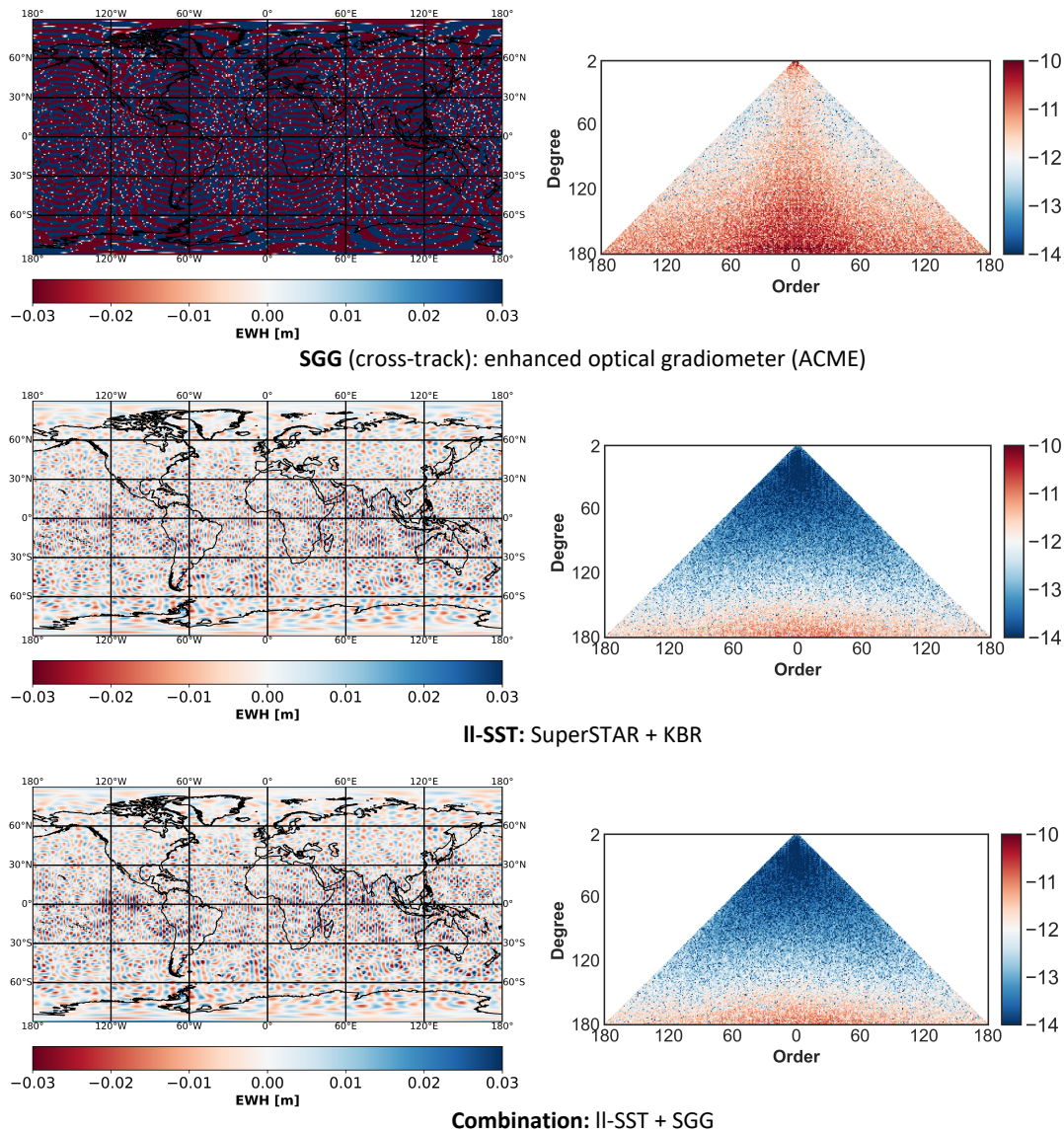


Figure 6.25: Spatial distribution (on the left) and spherical harmonic error spectra (on the right) of the residuals from ll-SST, cross-track SGG and their combination; Orbit: #5 (Table 4.2), $h = 247.35$ km; Measurement principles, considered accelerometers and gradiometers are given below each graph. Colorbar of the global maps limited to ± 0.03 m = ± 3 cm EWH.

6.4 Triple and Quadruple Satellite Formations

6.4.1 Double Satellite Pair ‘Bender’ Constellation

The upcoming GRACE-C mission in a near-polar orbit and the NGGM in an inclined orbit shall form the double-pair MAGIC. As it was mentioned in Section 3.3, it is anticipated that this Bender constellation of two satellite pairs will dramatically improve the spatio-temporal resolution of the recovered gravity field model. Such a new observation geometry will allow to determine smaller gravity signals, e.g. from smaller river basins, as well as improve the resolvability of high-frequency mass transport phenomena (Daras et al., 2023). Since the revisit time will be reduced, short-term gravity field measurements can be used in early warning services (Heller-Kaikov et al., 2023). As it was shown by multiple studies, the performance of the MAGIC mission strongly depends on the orbit parameters, especially of the inclined orbit. In order to maintain short-term repeat subcycles of a few days, it is planned to utilize a drag-compensated platform in the inclined orbit (Haagmans and Tsaoussi, 2020).

For the evaluation of the impact of the novel sensors for a Bender constellation, a non-drag compensated, near-polar orbit (#1 in Table 4.2) and a drag-free, inclined one (#4 in Table 4.2) were considered. A high-pass filtered SGRS optical accelerometer modeled in ACME with the anticipated level of the accuracy of LRI 2030 were assumed in both satellite pairs. Stochastic modeling have been applied in each case with weights progressively optimized over three successive steps. And the combination of the retrieved gravity field solutions was done at the level of normal equations, where the computed variance components act as a weighting factors (Equation (2.40)).

Figure 6.26 shows the degree RMS in geoid height (on the left) and the corresponding degree medians (on the right) of the true errors obtained from the ll-SST simulations for the near-polar (blue curve), the inclined orbit (orange line) and their combination (green curve). Residuals in the spectral domain are plotted w.r.t. the static gravity signal EIGEN-6C4 (black dashed line) and the mean monthly HIS signal (grey dashed dotted line). The combined case can reduce the residuals, improving the retrieved model by almost 1 order of magnitude at all degrees w.r.t. the standalone near-polar. However, it is important to note that while the degree RMS is valid for all orbit configurations, the standalone inclined pair lacks full global coverage, particularly over polar regions, and therefore does not offer a globally representative error characterization—reflected in the elevated RMS values across all degrees (orange curve in the left graph). These RMS values should be interpreted only as an indication of relative sensitivity over the regions actually observed by the inclined pair. This coverage-related limitation is addressed in Section 2.7, where different regularization techniques of the inclined solution are presented. On the other hand, the degree median (right graph) provides a more robust metric in the case of the inclined orbit, as it suppresses the influence of large outliers associated with non-observed zonal and near-zonal SH coefficients due to the polar gap. In the subsequent investigation of the regularization techniques for standalone incline solution (Section 6.4.3), GFR results are

shown in both metrics for full comparison.

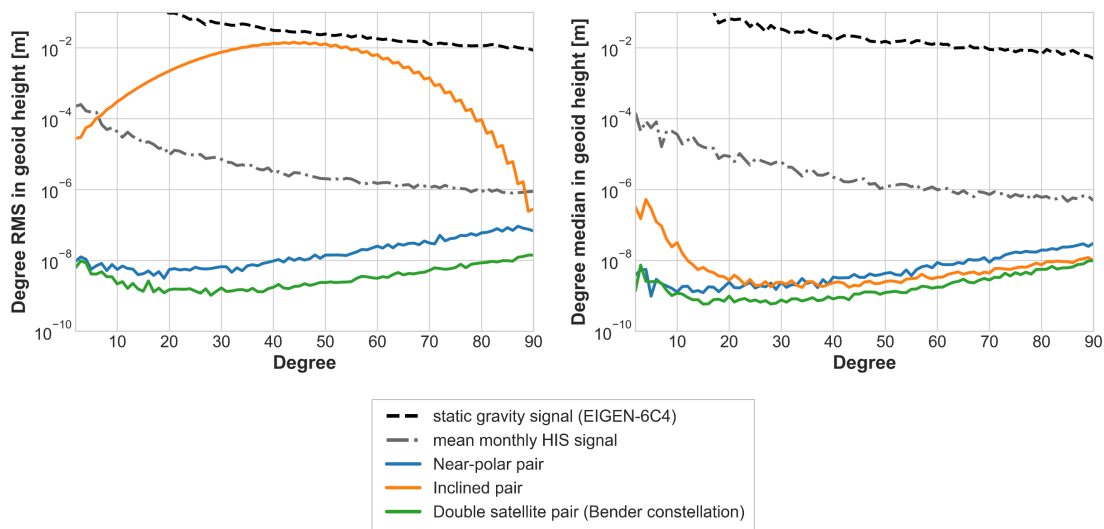


Figure 6.26: One-dimensional error spectrum of the spherical harmonic coefficient differences (true errors) between recovered and EIGEN-6C4 gravity field models in geoid height (m) from the near-polar, inclined orbit and their combination. *Left*: degree RMS; *Right*: degree median values; Orbits: #1 and #4 (Table 4.2); $h_1 = 478.48$ km, $i_1 = 89.03^\circ$; $h_4 = 396.55$ km, $i_4 = 70.01^\circ$.

The spatial distribution of the residuals and spherical harmonic error spectra from the near-polar, inclined orbit and combined case are shown in Figure 6.27. For clarity, the same orders of magnitude, equal to ± 0.5 mm of EWH, are used in all global maps. The global map of the residuals from the inclined orbit is plotted only in the range of $\pm 63^\circ$ of latitude, since in the near-polar and polar regions there are large outliers, due to non-coverage of those areas by the inclined satellite pair. A characteristic feature of the spherical harmonic error spectrum from the inclined satellite pair is the wedge of the poorly determined zonal and near-zonal coefficients due to the polar gap problem. This is clearly visible in the corresponding graph in Figure 6.27. By closer examination of this wedge, a specific expanding-narrowing shape can be noticed along the degree axis. At spherical harmonic degrees less than 40-45, the amount of poorly determined coefficients (depicted in red) is increasing faster than the well-observed tesseral and sectorial coefficients (shown in blue color). At degrees above 50, the wedge, due to the polar gap, gets stabilized. In other words, the number of properly observed spherical harmonic coefficients per degree is increasing more noticeably than the amount of poorly-determined coefficients. This can be noticed especially around degrees 80-90. And this specific feature of the wedge explains the parabolic shape of the degree RMS curve from the inclined orbit (orange line) in Figure 6.26.

Regarding the pattern of the spatial residuals, they are more evenly distributed in the combined case than in the near-polar case. Measurements from the inclined pair reduce the North-South striping behavior without any filtering and post-processing.

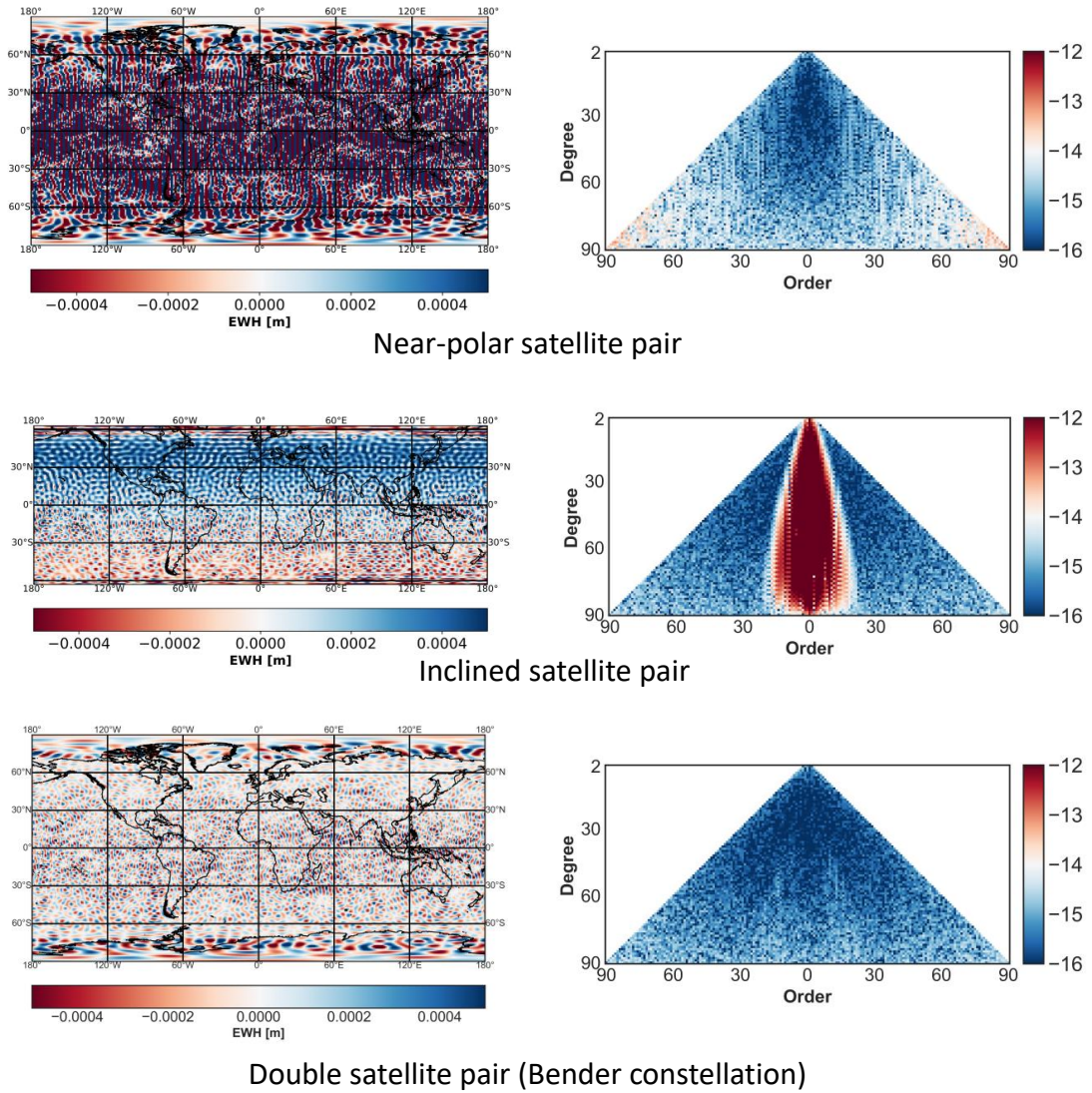


Figure 6.27: Spatial distribution (on the left) and spherical harmonic error spectra (on the right) of the residuals from ll-SST on the near-polar, inclined orbit and their combination; Orbits: #1 and #4 (Table 4.2); $h_1 = 478.48$ km, $i_1 = 89.03^\circ$; $h_4 = 396.55$ km, $i_4 = 70.01^\circ$. Colorbar of the global maps limited to ± 0.0005 m = ± 0.5 mm EWH.

6.4.2 Scale Factor Study for Residual Drag in II-SST Case

The upcoming NGGM mission is supposed to operate in a drag-free regime in an inclined orbit (Massotti et al., 2021). Accelerometers in this case will measure only non-compensated residual non-gravitational accelerations that are dominated by air drag (Abrykosov et al., 2019). This residual drag occurs due to the inability of the satellite's thrusters to generate a small enough compensation thrust. In general, accelerometer calibration is a complicated task, where one has to consider the effects from the onboard environment on the inertial sensor, and it depends on the context of data usage (Klinger and Mayer-Gürr, 2016). Different accelerometer calibration approaches exist, e.g., by non-gravitational force modeling (Klinger and Mayer-Gürr, 2016; Wöske et al., 2018), by replacing unrealistic accelerations because of thruster firing by model-based responses (Behzadpour et al., 2021), by precise orbit determination processes (Zhang et al., 2023).

Oberndorfer (2000) introduced a measurement model of the accelerometer as

$$\Gamma_a = \mathbf{K}_{0,A} + \mathbf{K}_{1,A}\gamma_A + \mathbf{K}_{lm,A}\gamma_A + \mathbf{K}_{2,A}\gamma_A\gamma_A + noise, \quad (6.4)$$

where Γ_a is the measured acceleration, $\mathbf{K}_{0,A}$ bias, $\mathbf{K}_{1,A}$ linear scale factor, γ_A acceleration of the test mass, $\mathbf{K}_{lm,A}$ coupling and misorientation matrix, $\mathbf{K}_{2,A}$ quadratic factor and *noise* is the measurement noise. Here, among the measurement noise, we also consider a linear scale factor and neglect the coupling and misorientation of the accelerometer axes, quadratic factor and bias. For the GRACE and GOCE missions, scale factor knowledge was considered equal to 1 %, while for the e^2 -motion concept for a future gravimetry mission it was assumed at the level of 0.2 % (NGGM-D Team et al., 2014). Abrykosov et al. (2019) mentioned 10^{-2} or 1 % scale factor knowledge for electrostatic accelerometers. In more recent studies, Zahzam et al. (2022) gave a scale factor knowledge of 2×10^{-3} for electrostatic and 10^{-5} or 0.001 % for hybrid inertial sensors. For standalone CAI accelerometers, 10^{-9} scale factor knowledge was given by Knabe (2023).

In this scale factor study, we consider an equation describing the ASD of the total accelerometer error ($ASD_{ACC., total}$) as

$$ASD_{ACC., total} = ASD_{ACC} + sf \times ASD_{residual acc.}, \quad (6.5)$$

where ASD_{ACC} is the ASD of accelerometer noise, sf is the scale factor knowledge and $ASD_{residual acc.}$ is the ASD of the residual linear acceleration. The latter one was considered as white noise at the level of $5 \times 10^{-9} \text{ (m/s}^2\text{)}/\sqrt{\text{Hz}}$, which corresponds to NGGM with an inclined orbit at $h = 400 \text{ km}$ (Massotti et al., 2021). Multiplication of the residual drag with the scale factor shows an incomplete compensation of the non-conservative accelerations that contribute to the accelerometer performance (Abrykosov et al., 2019). Figure 6.28 shows ASD curves of the different scale factors multiplied by the ASD of the residual linear acceleration. Three scale factor uncertainties, constant over the observation period, were

considered: 1 % pessimistic, 0.1 % realistic and 0.01 % optimistic cases. For comparison, an ASD of the SGRS optical accelerometer derived in ACME and ASD curves of inter-satellite LRI measurement errors are shown. The impact from the ‘pessimistic’ scale factor (red curve) causes a certain noise increase in the range of ~ 0.13 mHz – 10 mHz when considering an optical inertial sensor with LRI 2024 (grey solid line). The impact from the ‘realistic’ scale factor (green curve) gives a small noise increase in the vicinity of 1 mHz considering an optical accelerometer with LRI 2030 (grey dashed line). Since the ASD of the ‘optimistic’ scale factor, multiplied by the residual drag (yellow line), lies below the ASD of the SGRS, it only dominates over the ASD of LRI 2033 (grey dotted line) at low frequencies.

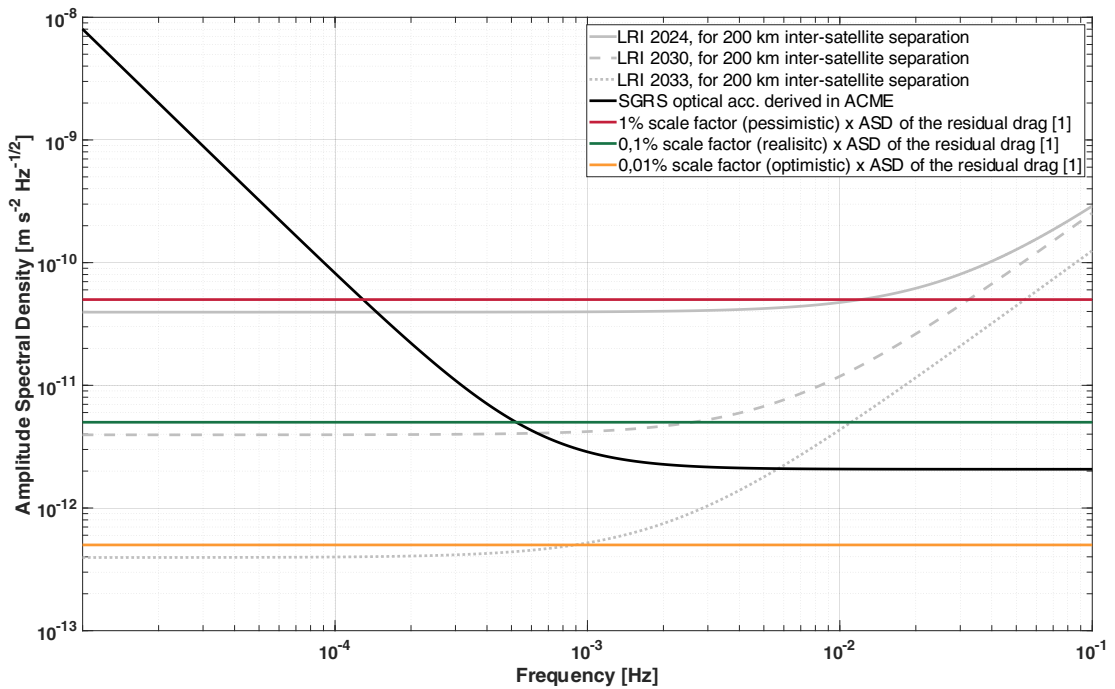


Figure 6.28: Comparison of the ASD curves of three cases of scale factor errors for NGGM in the inclined orbit ($h=400$ km), multiplied by the residual drag ASD. Also, the ASD sensitivity of the SGRS optical accelerometer derived in ACME and ASDs of the inter-satellite LRI measurement errors are shown. [1] Massotti et al. (2021).

6.4.3 Investigation of the Regularization Techniques for ll-SST at the Standalone Inclined Orbit

The upcoming GRACE-C mission in a near-polar orbit is planned to be launched a few years earlier than NGGM. Therefore, it may happen that after the decommissioning of GRACE-C at its end-of-life and in case of not replacing it by a new polar pair in time, NGGM in the inclined orbit could be the only operational ll-SST gravimetry mission. As a consequence, it is important to evaluate the performance of that satellite pair as a standalone mission by means of GFR simulations and taking into account the polar gap problem.

Here and in the Section A.2 of the appendix, results of GFR simulations with different regularization techniques for the ll-SST at the standalone inclined orbit are shown. A drag-compensated orbit with inclination 70.01° and the mean altitude 396.55 km (#4 in Table 4.2) was used. The necessity of regularization for the inclined orbit, as well as six considered techniques, were introduced in Section 2.7. Here a non-filtered SGRS optical accelerometer, modeled in ACME, with LRI 2030 was considered in all cases. High-pass filtering was not applied to the inertial sensor, as it removes both, signal and noise components, and acts by itself as a kind of regularization. A similar effect would have a co-estimation of additional parameters that could minimize the impact of the accelerometer's drift in the low-frequency range. Therefore, for a more explicit difference, a non-filtered inertial sensor was considered. Also, stochastic modeling was not applied, here.

Figure 6.29 (on top) shows the degree RMS in geoid height (Equation (2.35)) of the true errors retrieved from inclined ll-SST simulations with Tikhonov 0 order regularization. The corresponding L-curve is shown on the bottom of the figure. A set of regularization parameters $\alpha = 10^{-12}, 10^{-14}, \dots, 10^{-20}$ has been investigated. Each dot on the L-curve graph has the same color as the corresponding curve on the upper figure. A regularization parameter $\alpha = 10^{-16}$ (red point on the bottom graph of Figure 6.29) seems to minimize both L_2 -norms of the solution (ordinate axis) and residual (abscissa axis) in the best possible way. Degree median values of the Tikhonov 0 order regularization are shown in Figure A.2 in the appendix.

On top of Figure A.3 in the appendix, degree RMS in geoid height of the true errors retrieved from inclined ll-SST simulations with Tikhonov 1st order regularization are shown. Here, the same set of regularization parameters $\alpha = 10^{-12}, 10^{-14}, \dots, 10^{-20}$ was considered. According to the corresponding L-curve and zoomed fragment there (at the bottom of Figure A.3), $\alpha = 10^{-17}$ (purple point) reduces both L_2 norms as much as possible. From the upper graph it is noticeable how the oscillatory behavior of the curves are increasing by moving towards smaller regularization parameters. Figure A.4 in the appendix presents the degree median values obtained using 1st order Tikhonov regularization.

The results of applied Tikhonov 2nd order regularization for the standalone satellite pair in the inclined orbit are shown in Figure A.5 in the appendix. The degree RMS in geoid height of the spherical harmonic coefficient differences are shown

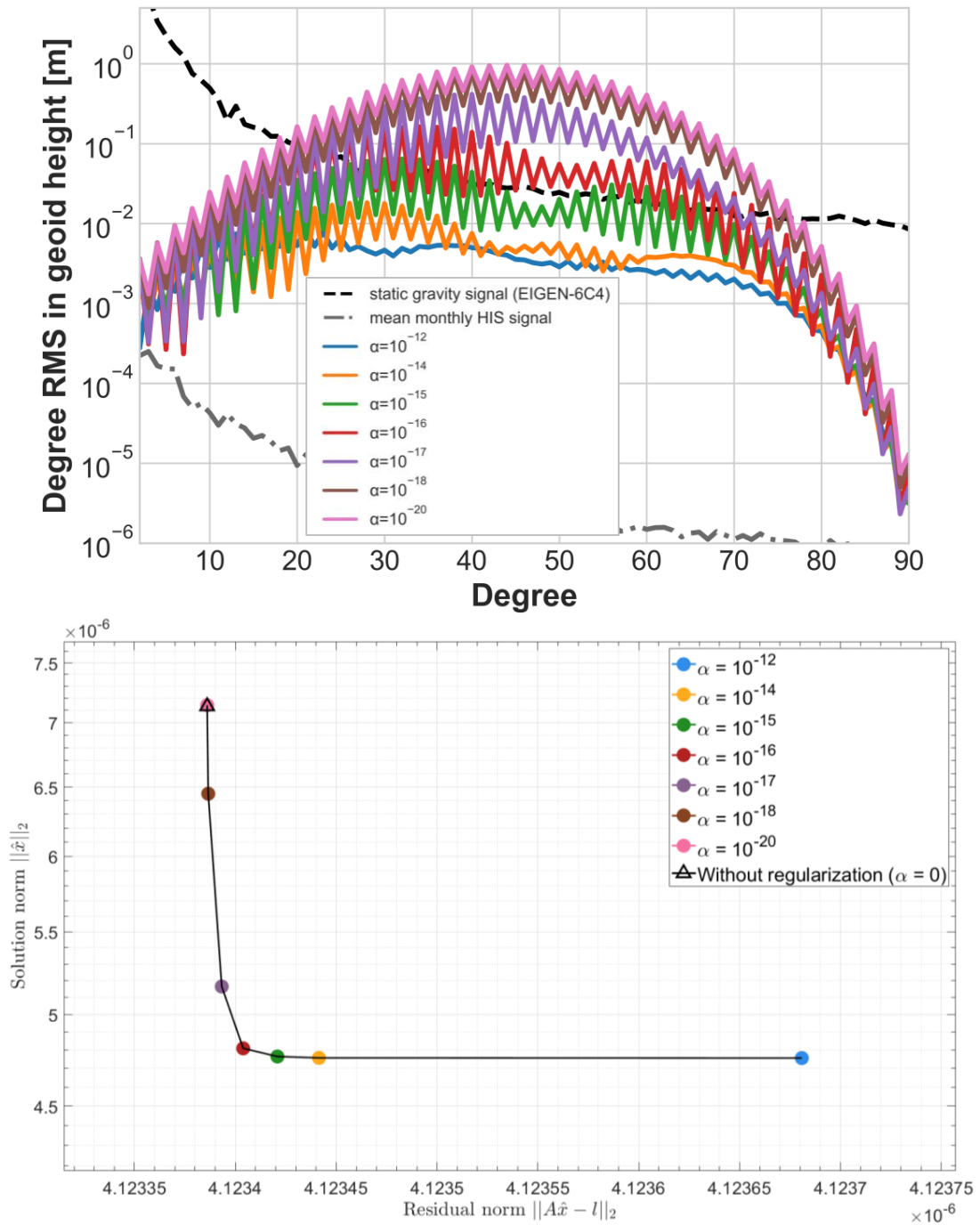


Figure 6.29: *Top*: Degree RMS of the spherical harmonic coefficient differences (true errors) between recovered and EIGEN-6C4 gravity field models in geoid height (m) from inclined 11-SST simulations with Tikhonov 0 order regularization; *Bottom*: Corresponding L-curve for the regularized solutions. Considered regularization parameters are given in the legend. Orbit: #4 (Table 4.2), $h = 396.55$ km.

on the top and the corresponding L-curve at the bottom. The same set of regularization parameters as in the previous two cases has been investigated. From the zoomed fragment of the L-curve, it is visible that a solution with $\alpha = 10^{-18}$ (brown point) minimizes optimally both solution $\|\hat{\mathbf{x}}\|_2$ and residual $\|\mathbf{A}\hat{\mathbf{x}} - \mathbf{l}\|_2$ norms. Degree median values of the Tikhonov 2nd order regularization are shown in Figure A.6 in the appendix.

Regularization of standalone ll-SST in the inclined orbit using the Kaula method is shown in Figure 6.30. Here regularization parameters $\alpha = 10^{-25}, 10^{-27}, \dots, 10^{-33}$ were analyzed. According to the L-curve, the regularization parameter $\alpha = 10^{-29}$ (red point) seems to be the optimum one. In the graph with degree RMS curves, one can notice an increasing oscillatory behavior of the curves with smaller regularization parameters. Figure A.7 in the appendix presents the degree median values obtained using Kaula regularization.

Degree RMS of the true errors, plotted in geoid height, and the corresponding L-curve of the solutions regularized by Kaula including the polar gap (Equation (2.36)) are shown in the Figure A.8 in the appendix. The upper graph is characterized by the oscillatory behavior with all regularization parameters. According to the bottom graph, a regularized solution with $\alpha = 10^{-29}$ (red point) optimally reduces both L_2 -norms. Corresponding Figure A.9 in the appendix shows the degree median values obtained using Kaula including the polar gap regularization.

Finally, results of the Kaula order-dependent regularization (Equation (2.38)) with a set of regularized parameters $\alpha = 10^{-27}, 10^{-29}, \dots, 10^{-35}$ are shown in Figure A.10 in the appendix. According to the L-curve graph, the solution with $\alpha = 10^{-32}$ (purple point) optimally minimizes both L_2 -norms. Curves on the degree RMS graph (on top of Figure A.10) are characterized by an oscillating behavior. Degree median values of the Kaula order-dependent regularization are shown in Figure A.11 in the appendix.

Figure 6.31 shows degree RMS of the spherical harmonic coefficient differences obtained from the non-regularized (blue curve) and regularized by six different methods. All regularized solutions were plotted with an optimal α , discussed above. Besides the non-regularized case, the solution with Tikhonov 0 order (orange curve), Kaula including polar gap (red curve) and Kaula order-dependent weighting (pink curve) intersect the static gravity field signal (black dashed curve). The error spectra of the residuals from the three other cases, Tikhonov 1st order (purple curve), 2nd order (brown curve) and Kaula (green curve), are located beyond the EIGEN-6C4 signal. Note that the residuals in the spectral domain from Tikhonov 2nd order and Kaula regularization are very close to each other, which correlates with Metzler and Pail (2005). Corresponding degree median values of the non-regularized and various regularized methods are shown in Figure A.12 in the appendix. It should also be highlighted that the demonstrated regularized solutions are only valid for particular orbit settings, i.e. drag-free orbit #4 (Table 4.2). With other orbit parameters, e.g., for inclination or altitude, the results would differ.

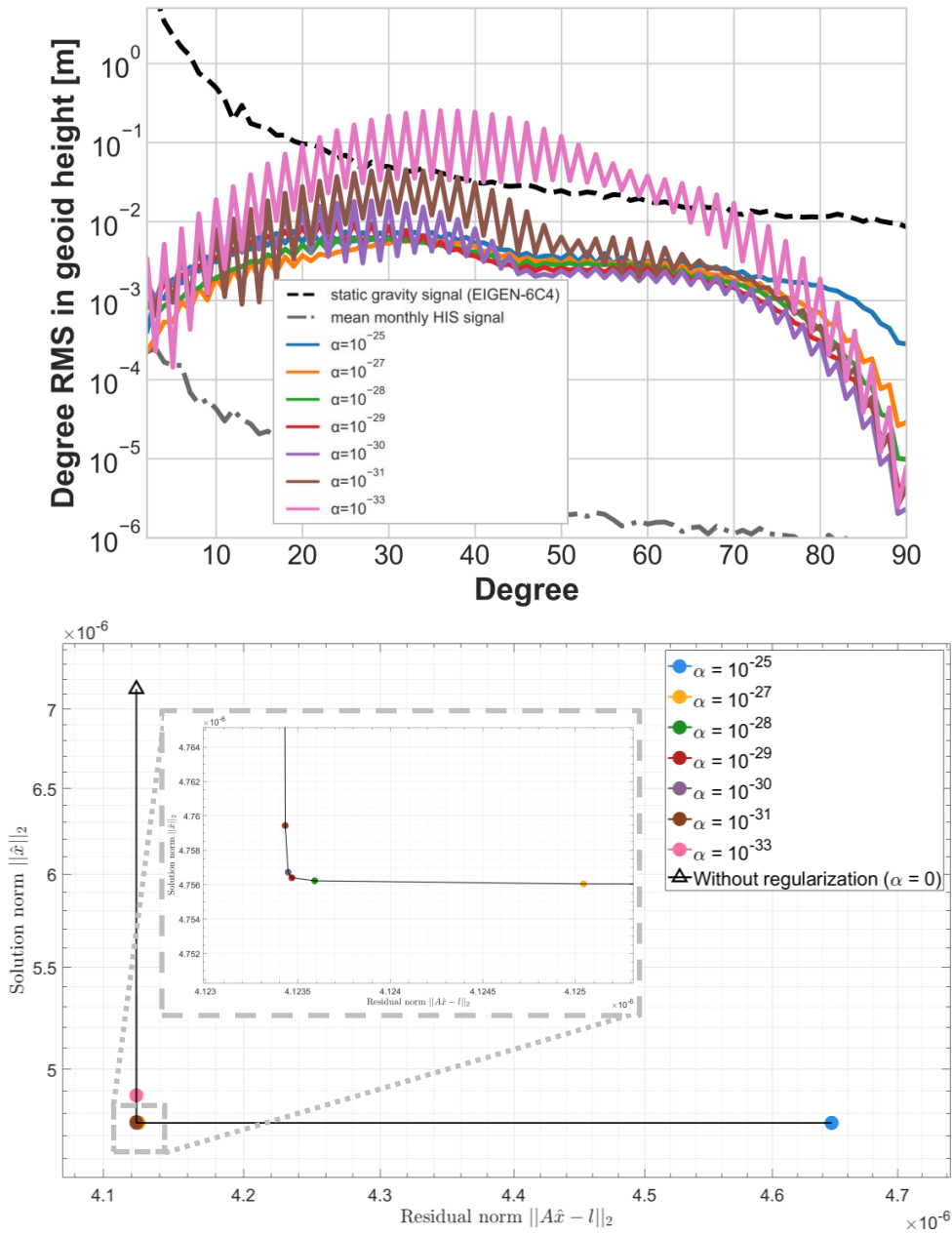


Figure 6.30: *Top*: Degree RMS of the spherical harmonic coefficient differences (true errors) between recovered and EIGEN-6C4 gravity field models in geoid height (m) from inclined II-SST simulations with Kaula regularization; *Bottom*: Corresponding L-curve for the regularized solutions. Considered regularization parameters are given in the legend. Orbit: #4 (Table 4.2), $h = 396.55$ km.

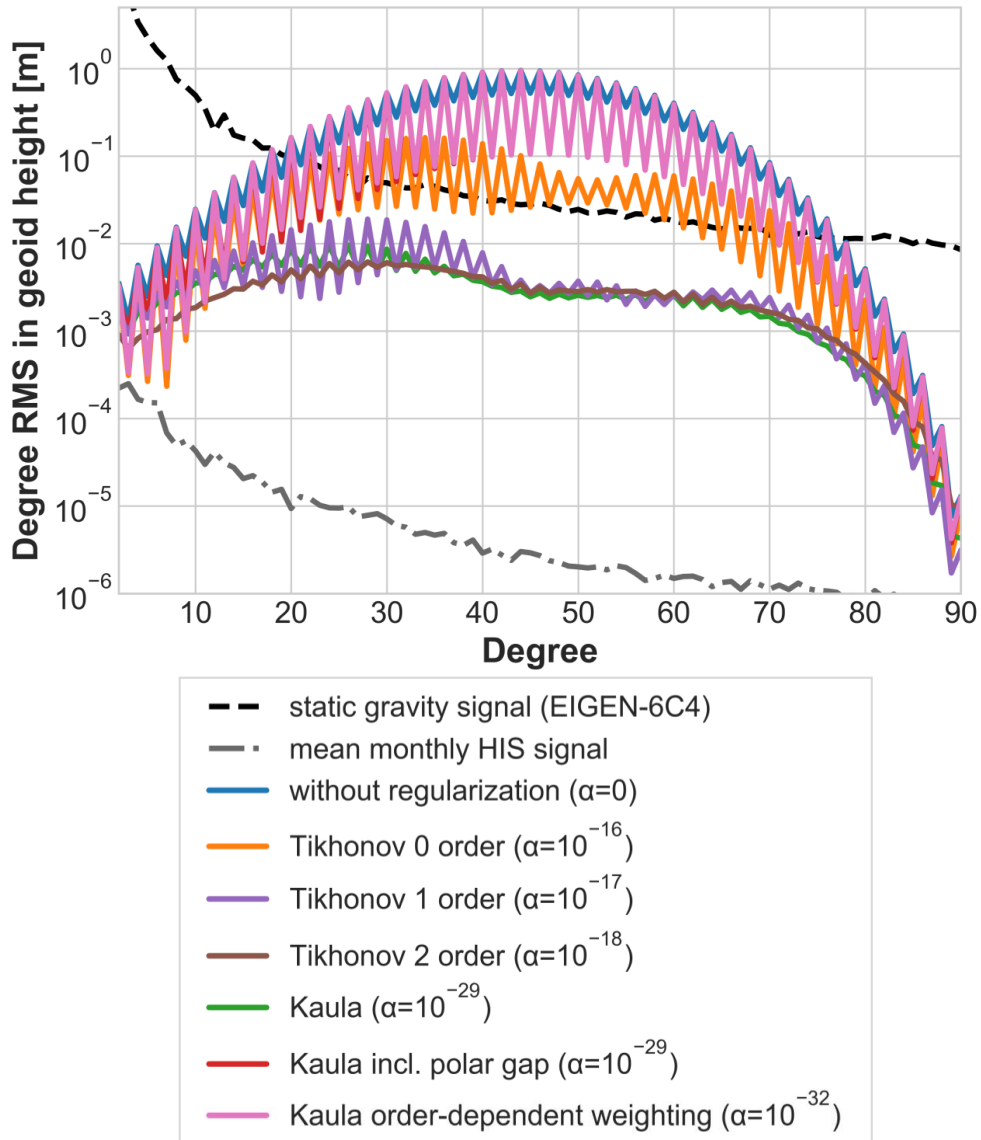


Figure 6.31: Degree RMS of the spherical harmonic coefficient differences (true errors) between recovered and EIGEN-6C4 gravity field models in geoid height (m) for the inclined II-SST simulations, regularized by different methods; Orbit: #4 (Table 4.2), $h = 396.55$ km.

6.4.4 Novel Triple Satellite Formations

Gravity products from GRACE and GRACE-FO missions have a conceptual problem causing North-South striping, which has been noted by many authors (Wouters et al., 2014; Humphrey et al., 2023; Kupriyanov et al., 2024b). The source of such longitudinal stripes could be orbit resonance effects (Kvas et al., 2019), sub-Nyquist artifacts originated from the oversampling of the Earth’s low-frequency gravitational signal of the geoid along the parallels of latitude (Peidou and Pagiatakis, 2020) and measurement errors. Striping effect can be reduced at a certain level by using novel inertial sensors, as it was demonstrated in Section 6.2.1. Another option for improving the multi-directionality of the recovered data could be adding measurements oriented not in the North-South direction. For example, a double satellite pair ‘Bender’ constellation could dramatically improve the pattern of the spatial residuals as it was shown in Section 6.4.1.

Multiple studies were previously carried out evaluating alternative mission architectures for future satellite gravimetry (Wiese et al., 2009; Reubelt et al., 2010; Elsaka et al., 2014, 2015). In this study two new triple satellite formations are evaluated via closed-loop simulations. The key idea, in order to minimize the consistent North-South striping effect, is to add a third satellite in addition to the in-line GRACE-like formation and provide ll-SST measurements in the East-West direction. A third satellite can be placed in an orbit which differs by a certain angle w.r.t. the in-line formation. This difference could be either by a change in right ascension of the ascending node angle (Ω) or of inclination (i). Selection of the orbit parameters for the second orbit is a non-trivial task as the desired satellite configuration should satisfy a certain trade-off. On the one hand, the best sensitivity in terms of GFR can be reached for large inter-satellite distances (Reubelt et al., 2010). On the other, the level of accuracy of the inter-satellite LRI is degrading w.r.t. enlarging the distance (Elsaka et al., 2014). Therefore, considered orbit parameters should be optimal both, in terms of geodetic performance and technical realization.

In this section, the GFR results obtained from the two novel triple satellite formations are shown. Considered assumptions, anticipated advantages as well as technical challenges are also being discussed.

6.4.4.1 Orbits Differ by Right Ascension of the Ascending Node

A scheme of the first triple satellite formation, where the orbits differ by a right ascension of the ascending node (Ω), is shown in Figure 6.32. The orbit for the third satellite, depicted as C in the graph, differs only by $\Delta\Omega = 1^\circ$. Such a variation produces a 120 km separation between the orbits at the equator. Since Ω does not impact the secular variations, such a formation is stable. This means that the inter-satellite distance between the orbiters B and C at the equator is not increasing during the time. The two orbits intersect at the poles, making such formation similar, to some extent, to the Pendulum constellation, evaluated by Elsaka et al. (2014). The key difference is that in the proposed triple formation, the line-of-sight between the satellites B and C is always aligned along the

parallels. Regarding the in-line formation, a ‘standard’ GRACE-like satellite pair is considered, separated by about 200 km. All three satellites are assumed to be placed in near-polar, non drag-compensated orbits with the same altitude around 500 km (#1 and #3 in Table 4.2).

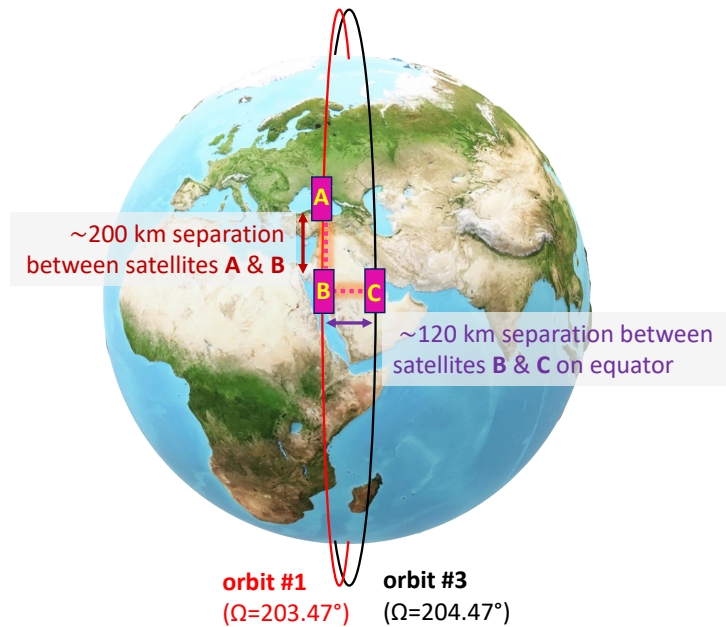


Figure 6.32: Scheme of the combination of the in-line and cross-track formation differing by the right ascension of the ascending node; Orbits: #1 and #3 (Table 4.2); $h_1 = h_3 = 478.48$ km, $\Omega_1 = 203.47^\circ$; $\Omega_3 = 204.47^\circ$ (based on Kupriyanov et al. (2024a)).

Figure 6.33 shows the degree RMS in geoid height (Equation (2.35)) of the true errors retrieved from the ll-SST measurements in the in-line (blue curve), cross-track (orange curve) formation and their combination (green curve). Residuals in the spectral domain are plotted w.r.t. the static gravity signal EIGEN-6C4 (black dashed line) and a mean monthly HIS signal (grey dashed dotted line). Stochastic modeling, where the weights are optimised step-by-step in three iterations, was applied for the in-line (satellites A and B) and cross-track measurements (satellites B and C). The combined solution was acquired at the level of normal equations, where the computed variance components act as weighting factors (Equation (2.40)). It was considered that each satellite is equipped with an SGRS optical accelerometer derived in ACME, where the noise component was high-pass filtered. However, taking into account the current level of pointing accuracies of the GRACE-like satellites, i.e. 2.5 mrad in roll axis and 250 μ rad in pitch and yaw (Goswami et al., 2021), different inter-satellite ranging instruments were assumed in the in-line and cross-track formations (similar to Kupriyanov et al. (2024a)). In the in-line case, the anticipated level of accuracy of LRI 2033 was used, while in the cross-track measurements the LRI 2024. This was done in order to take into account a certain degradation of the laser beam steering mechanism due to increased tilt-to-length noise and the coupling caused by satellites pointing variations (Wegener et al., 2020). According to Figure 6.33 the in-line formation has

a better performance than the cross-track, potentially resolving the time-variable signal up to degree 120, while the latter one only up to degree 90 if evaluated separately.

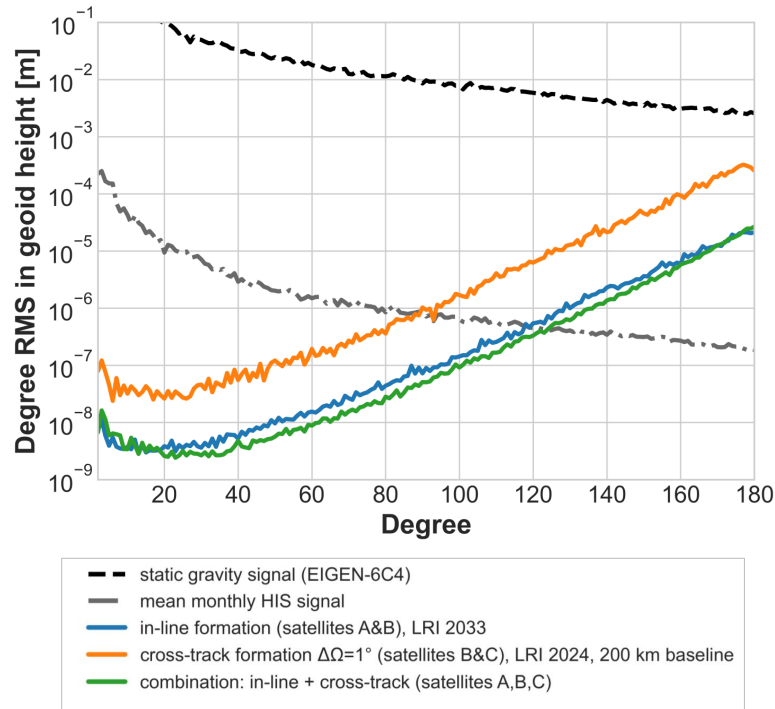


Figure 6.33: Degree RMS of the spherical harmonic coefficient differences (true errors) between recovered and EIGEN-6C4 gravity field models in geoid height (m) from 11-SST for the in-line, cross-track formation (differs by Ω) and their combination; Orbits: #1 and #3 (Table 4.2); $h_1 = h_3 = 478.48$ km, $\Omega_1 = 203.47^\circ$; $\Omega_3 = 204.47^\circ$ (based on Kupriyanov et al. (2024a)).

Figure 6.34 shows the spatial distribution of the residuals and spherical harmonic error spectra from the in-line, cross-track formations and their combination. Similar as before, the global maps are plotted with the same orders of magnitude, equal here to ± 2.5 mm EWH. From the bottom figure, it is evident that the pattern of the spatial residuals in the merged case are more homogeneous, rather than from the standalone in-line case in the top figure.

However, it is important to highlight that the cross-track range measurements in this formation are technically challenging for current inter-satellite LRI systems. The reason is the high relative range-rates between the orbiters B and C (up to several dozen m/s), while the current feasible range-rate for heterodyne lasers that are used on-board GRACE-FO is ± 10 m/s (Sheard et al., 2012; Elsaka et al., 2014). Therefore, in order to maintain measurements with such high relative range-rates, certain developments have to be done, extending the dynamic range of the LRI.

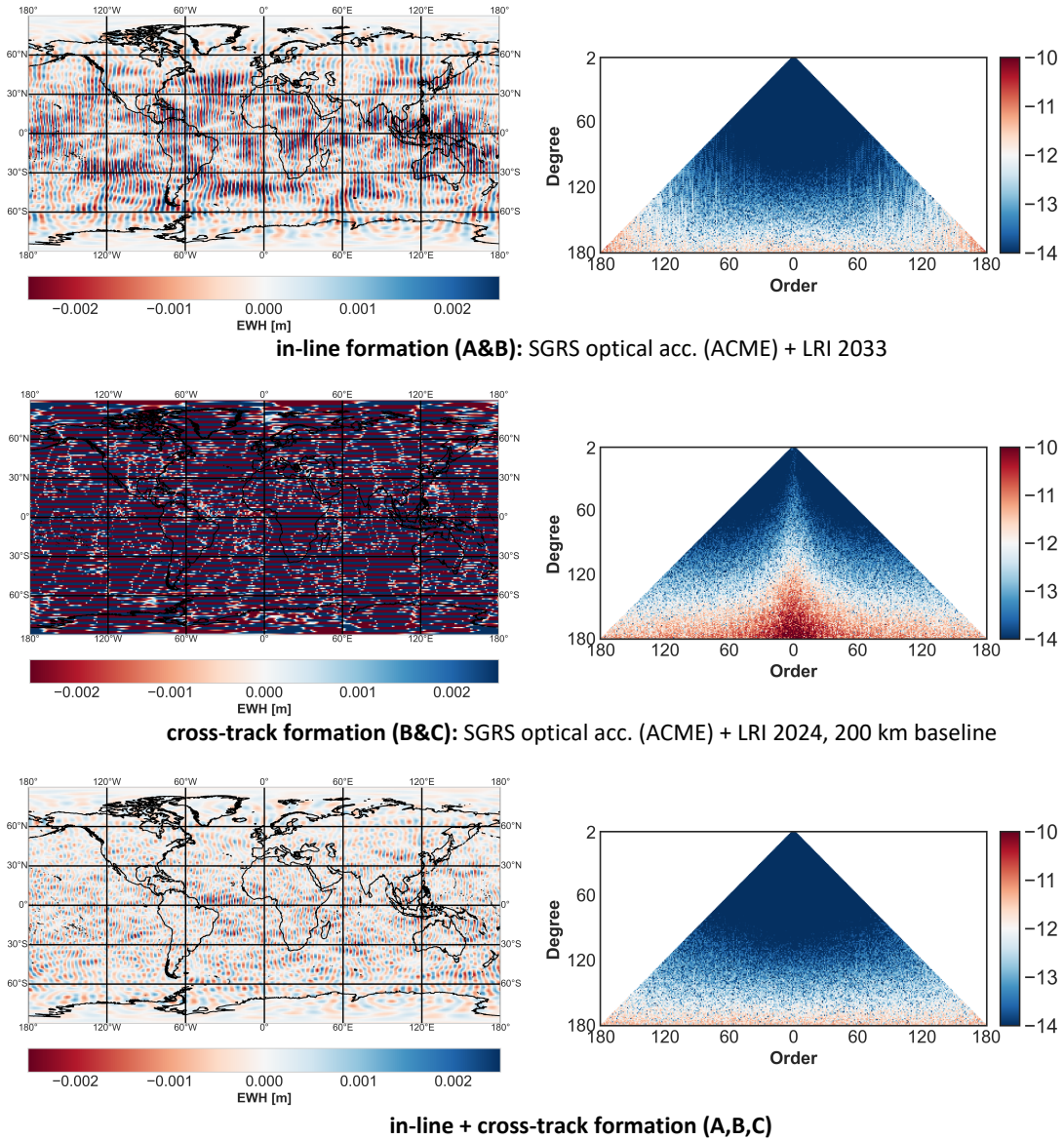


Figure 6.34: Spatial distribution (on the left) and spherical harmonic error spectra (on the right) of the residuals from ll-SST for the in-line, cross-track formation (differs by Ω) and their combination; Orbits: #1 and #3 (Table 4.2); $h_1 = h_3 = 478.48$ km, $\Omega_1 = 203.47^\circ$; $\Omega_3 = 204.47^\circ$ (based on Kupriyanov et al. (2024a)). Colorbar of the global maps limited to ± 0.0025 m = ± 2.5 mm EWH.

6.4.4.2 Orbits Differ by Inclination

The scheme of the second triple satellite formation, where the orbits differ by inclination (i), is shown in Figure 6.35. Here the second orbit differs by $\Delta i = 1^\circ$. With this configuration the orbits are as far apart as possible in the polar regions. Due to the secular perturbations of the right ascension of the ascending node ($\dot{\Omega}$), a stable formation is not guaranteed (Elsaka, 2012; Bloßfeld et al., 2014). Constantly changing $\dot{\Omega}$ leads to the situation that the orbital planes are counter-rotating w.r.t. each other. This implies that the distance between the satellites B and C is permanently increasing. From the orbit simulations performed in XHPS, it was found that after one month the orbital planes are drifted away from each other by 400 km in the near equatorial area, from 120 to 520 km. Here, non-drag compensated, near-polar orbits #1 and #2 from the Table 4.2 were considered.

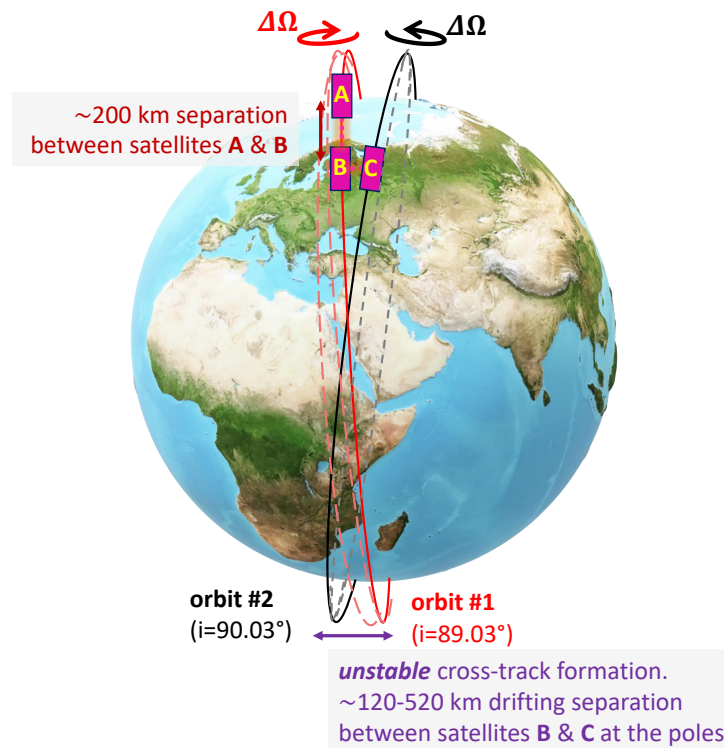


Figure 6.35: Scheme of the combination of the in-line and cross-track formation differing by the inclination; Orbits: #1 and #2 (Table 4.2); $h_1 = h_2 = 478.48$ km, $i_1 = 89.03^\circ$; $i_2 = 90.03^\circ$ (based on Kupriyanov et al. (2024a)).

In this formation, similar to the other one, an SGRS optical accelerometer modeled in ACME with high-pass filtered noise was assumed on-board all spacecraft. Similarly, different levels of accuracy for the inter-satellite LRI have been assumed in the along- and cross-track directions. For the in-line formation, an LRI 2033 was used, while for the perpendicular range measurements, a LRI 2024 with $L = 600$ km baseline was considered (Equation (5.7) and yellow curve in Figure 5.4). Again, stochastic modeling, where the weights are optimised step-by-step in three iterations, was applied for the in-line and cross-track measurements.

Identically the combination was done at the level of normal equations, based on computed variance components. Degree RMS of the true errors from each formation individually and their combination are shown in Figure 6.36. Residuals from the in-line formation are indicated by the blue curve, the cross-track by the orange and the combined case by the green line. In general, the graph looks identical to Figure 6.33, with the only difference that here residuals from the cross-track formation are a bit larger. Therefore, the time-variable background HIS signal can potentially be resolved only up to degree 80.

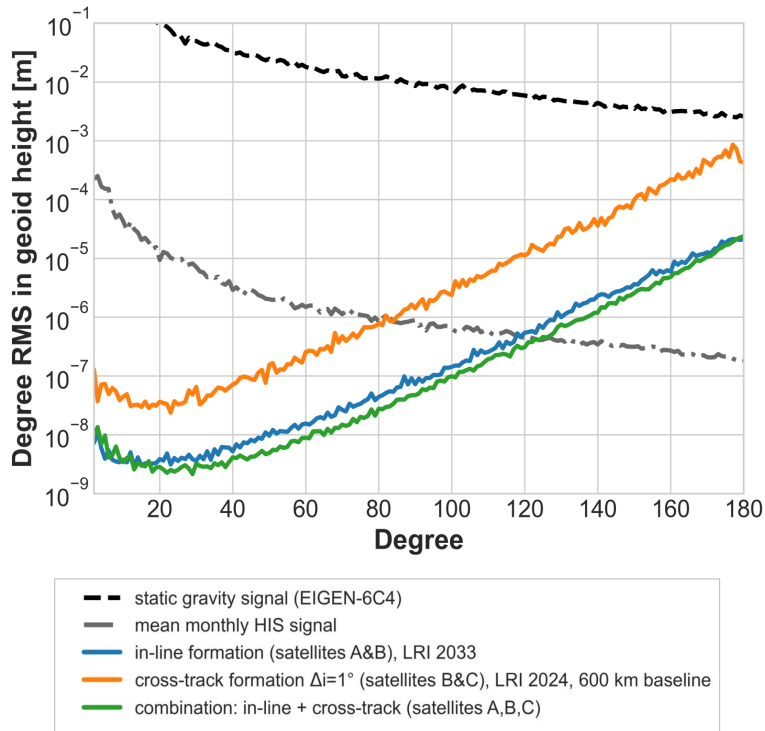


Figure 6.36: Degree RMS of the spherical harmonic coefficient differences (true errors) between recovered and EIGEN-6C4 gravity field models in geoid height (m) from ll-SST for the in-line, cross-track formation (differs by i) and their combination; Orbits: #1 and #2 (Table 4.2); $h_1 = h_2 = 478.48$ km, $i_1 = 89.03^\circ$; $i_2 = 90.03^\circ$.

The spatial distribution of the residuals and spherical harmonic error spectra from this satellite formation, depicted in Figure 6.37, also look very similar to the other constellation (Figure (6.34)). Here the same order of magnitude, equal to ± 2.5 mm EWH, is used in the global maps.

However, the satellite formation which differs by inclination is even more technically challenging compared to the one differing by right ascension of the ascending node. In addition to the orbit planes that are drifting away from each other, the relative range-rates between the satellite B and C are up to several hundred m/s. Without a certain orbit maintenance that might reduce the drifting of the orbit planes, such constellation is extremely challenging to implement.

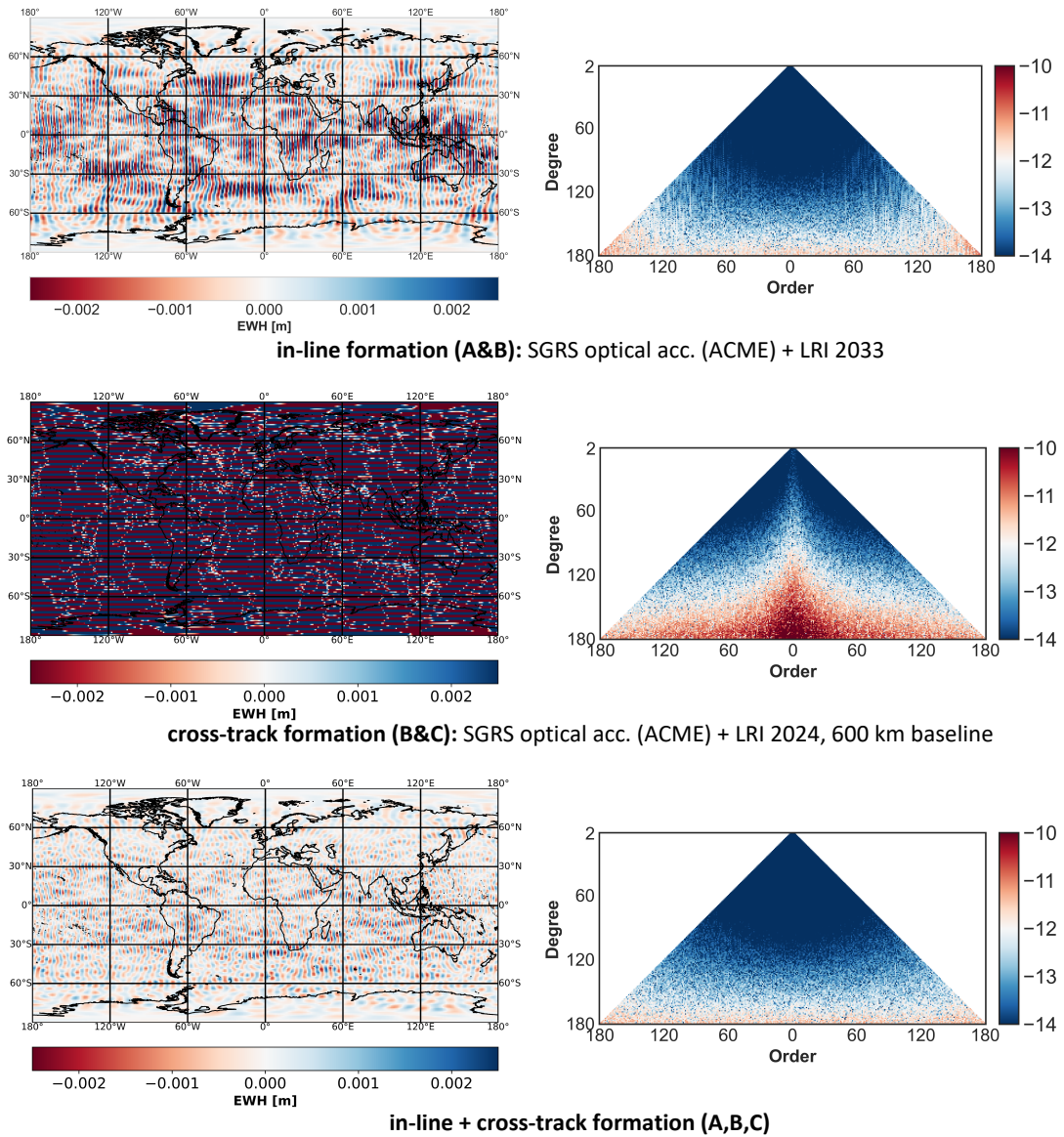


Figure 6.37: Spatial distribution (on the left) and spherical harmonic error spectra (on the right) of the residuals from ll-SST for the in-line, cross-track (differs by i) and their combination; Orbits: #1 and #2 (Table 4.2); $h_1 = h_2 = 478.48$ km, $i_1 = 89.03^\circ$; $i_2 = 90.03^\circ$. Colorbar of the global maps limited to ± 0.0025 m = ± 2.5 mm EWH.

Figure 6.38 shows the comparison of the degree RMS of the true errors from the standalone in-line satellite pair (blue curve), triple satellite formations differing by Ω (green line) and differing by inclination (orange line). Generally speaking, gravity field models retrieved from both novel constellations show a similar level of accuracy. Moreover, they both outperform the standalone formation at degrees starting from 20.

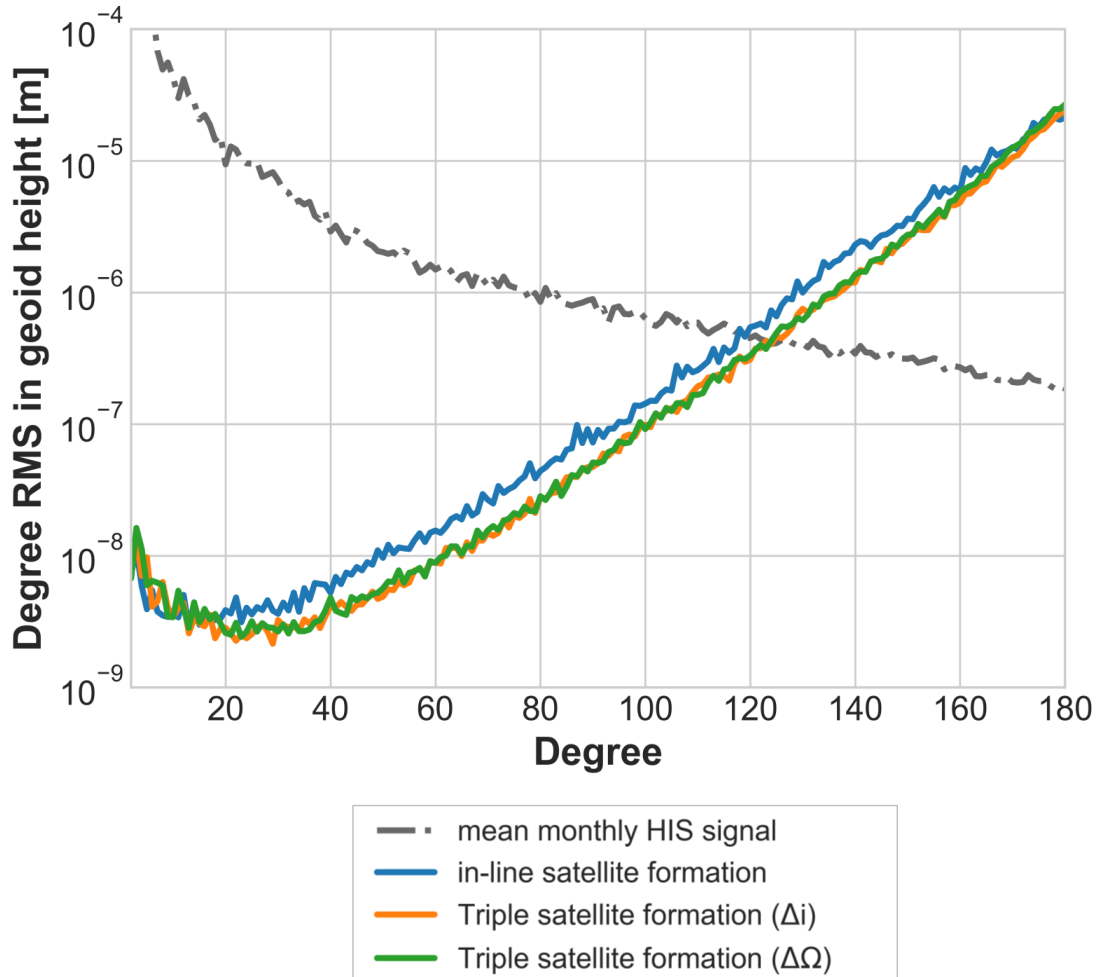


Figure 6.38: Degree RMS of the spherical harmonic coefficient differences (true errors) between recovered and EIGEN-6C4 gravity field models in geoid height (m) from ll-SST for the in-line, triple satellite formation (Δi) and ($\Delta \Omega$); Orbits: #1, #2 and #3 (Table 4.2); based on Kupriyanov et al. (2024a).

6.5 Chapter Summary

This chapter provides a full-fledged, comprehensive evaluation of the performance of the novel sensors on-board current and possible future gravimetry missions. Starting from the nuances of numerical simulation, i.e. impact of stochastic modeling (Section 6.1), a section follows on the assessment of capabilities of the inertial sensors with different measurement principles, e.g., SGRS optical, electrostatic, CAI, hybrid accelerometers in ll-SST formation (Section 6.2.1). It continues by the GFR simulations including time-variable background modeling errors (Section 6.2.2) and GRACE-like satellites with extended solar panels that might be relevant in future (Section 6.2.3). GFR analysis also includes the performance evaluation of the cross-track gradiometers, formed by the different accelerometers (Section 6.3.1), including the study of the common mode gain uncertainty due to the imperfections of the instrument (Section 6.3.2). Results of the combination of the ll-SST and cross-track SGG measurement techniques are shown in Section 6.3.3. In Section 6.4.1 GFR results from the double pair ‘Bender’ constellation with the orbit parameters that the MAGIC mission is supposed to utilize are shown. Also, since the NGGM placed in an inclined orbit will be in a drag-free regime, a scale factor study for the residual drag in ll-SST is discussed in Subsection 6.4.2. Recovered models from the regularized and non-regularized standalone inclined satellite pair are presented in Section 6.4.3. There, the effect of six different regularization techniques is shown and compared w.r.t. each other. The chapter ends with a Section 6.4.4, where the GFR from two novel triple satellite formations are discussed as well as technical challenges that would occur in their realization.

7 Conclusions and Outlook

Satellite gravimetry provides critical data on mass change phenomena and its effects on Earth's systems, but there is an urgent need for new sensors and measurement concepts to meet the scientific community's increasing demand for more accurate spatio-temporal information. This study focuses on the performance evaluation of novel accelerometers with interferometric optical TM displacement readout and satellite formation flights.

The study aimed to address the research questions formulated in Section 1.2. This work is built upon three essential pillars:

1. Adaptation of optical accelerometry technology, pioneered by the LISA Pathfinder mission, for satellite gravimetry missions in LEO. For this part an ACME software tool was developed. Also, forward modeling in XHPS consisting of detailed background models are carried out;
2. Backward modeling, i.e. evaluation and comparison of the performance, in terms of GFR, of the proposed SGRS optical accelerometer (and a gradiometer formed by a pair of corresponding inertial sensors) with other instruments based on different technologies (e.g., CAI, electrostatic, hybrid) using comprehensive closed-loop procedures;
3. Investigation (also in terms of GFR) of novel measurement principles, such as satellite formations or combinations of different techniques, that could potentially improve the quality of future gravity models.

The GRS from the LISA-Pathfinder mission was operated in a 'quiet' environment at Lagrange point L_1 , but in order to study the GRS in LEO with strong non-conservative forces, the satellite dynamics simulator XHPS together with the ACME toolbox were used. Orbit simulations include time-variable background models up to high degrees and consider various non-gravitational forces. A period of high solar activity (May, 2002), characterized by increased air drag and solar radiation pressure, was used as worst case in order to ensure that the parameters for the electrostatic levitation of the TM were adequate and that the accelerometer would maintain controllability. Five different orbits were used in this study for various scenarios. Three of them were non-drag compensated and two consider a perfect drag compensation regime. Regarding the inertial sensor development, a SGRS modeled in ACME was considered to have an identical wireless charge management system similar to the GRS from LISA-Pathfinder. A one-degree-of-freedom accelerometer was used, taking into account multiple error sources. The noise budget of the SGRS was obtained in the frequency domain, taking into account the non-gravitational accelerations acting in corresponding orbits, simulated in the XHPS software. Also, the impact of changed parameter values, e.g., TM mass and the gap between the TM and electrode housing, was evaluated. Dependencies that have been identified during the parameterization,

e.g., an accelerometer with a heavier TM performs better, correlate with studies of other groups. In general, consistent orbit simulations with inertial sensor modeling demonstrated the capability of the adaptation of the optical accelerometry technology for gravimetry missions in LEO, where the environment has a strong effect, e.g. deceleration up to 1300 nm/s^2 in along-track direction at an altitude of 450 km.

Errors of the inertial sensors and inter-satellite ranging instruments that were investigated in terms of GFR simulations are discussed. Accelerometers with a colored noise or ‘drift’ at low frequencies needed a bias co-estimation. This holds for the state-of-the-art electrostatic sensors, for example, SuperSTAR, GRADIO, as well as for the modeled SGRS optical accelerometer. This effect was minimized by applying a minimum-order finite impulse response high-pass filter to the corresponding noise part. However, this is an optimistic approximation, since in reality one can not filter out only the noise part alone.

Comparison of the performance of the simulated SGRS optical accelerometer with other types of inertial sensors, i.e. state-of-the-art CAI and hybrid (electrostatic+CAI), were carried out in terms of GFR for the non-drag compensated ll-SST configuration. GFR simulations with a one month mission time span, demonstrate that the SGRS optical accelerometer outperforms standalone CAI and hybrid inertial sensors. Evaluation in the spatial domain shows that the North-South striping was significantly reduced by utilizing novel instruments w.r.t. the current SuperSTAR sensor and minimize the residuals up to $\pm 5 \text{ mm}$ EWH.

From the comparison of the ASD of the total noise budget of the simulated SGRS with the measurement error of the inter-satellite LRI in high frequencies (above 10 mHz), it can be concluded that future limitations in GFR might be driven more by the performance of the inter-satellite ranging instrument rather than the inertial sensor.

In almost all GFR simulations, the low-frequency part of the SGRS was high-pass filtered. The non-filtered SGRS was considered at the investigation of the impact of stochastic modeling and the study of the different regularization techniques for the inclined orbit, which will be relevant if the near-polar pair would be decommissioned earlier. Here, non-filtered cases were evaluated in order to show more explicitly the effect of the low-frequency part since the high-pass filtering acts by itself as a kind of regularization.

Research confirms that time-variable background modeling and associated aliasing errors significantly impact on current satellite gravimetry missions, overshadowing the advantages offered by novel inertial and range measurement sensors. These errors persist as a limiting factor, complicating efforts to fully leverage the enhanced precision and accuracy of modern sensor technology and to compare instruments effectively.

A possible effect of the satellites with extended solar panels on the recovered gravity models was studied, as these modified shapes of orbiters might be used in

future due to the anticipated increased power consumption of on-board systems. Only a slight difference in the retrieved gravity models from the standard and modified shapes was obtained. Taking into account certain assumptions and simplifications in satellite dynamics, inertial sensor modeling and gravity field recovery, this discrepancy was mostly due to the orbital effects. In principle, there was no degradation of the science output due to more complex spacecraft shapes.

Performance evaluation of the novel sensors was done not only in ll-SST formations, but also considering cross-track gradiometry. It was shown that modeled optical gradiometers show a certain improvement w.r.t high-sensitive axis of the GOCE gradiometer. However, a hybrid gradiometer consisting of an electrostatic part of the HybridSTAR and a CAI of $10 \text{ mE}/\sqrt{\text{Hz}}$ gave the best performance among the considered instruments. To conclude for the second research question, it can be stated that modeled optical accelerometers together with LRI 2033 outperform other inertial sensors in a ll-SST configuration. In the SGG case, an instrument, formed by a pair of SGRS, shows slightly better performance than the high-sensitive axis of the GOCE gradiometer.

The potential combination of ll-SST and cross-track SGG measurement techniques was one of the topics addressed in the third research question, i.e. the investigation of novel satellite formations and combinations. The studied fusions do not provide a valuable benefit. Despite considering a gradiometer, formed by a pair of enhanced optical SGRS, it is quite challenging to obtain any improvement in the combined solution. This result correlates with the outcomes of other research groups. However, this concept could benefit in terms of redundancy of the inertial sensors in case of failure or any other technical issues with one of them. Also within this research question, GFR from a Bender constellation was studied with the orbit parameters of the upcoming MAGIC mission where a SGRS on-board of all four satellites was modeled. As expected, this combined solution drastically improved the quality of the recovered gravity field w.r.t. the standalone near-polar pair, with the added benefit of using optical accelerometers, which further enhanced performance compared to recent electrostatic inertial sensors. Finally, two novel triple satellite formations were investigated to reduce the North-South striping behavior and improve the spatio-temporal quality of the recovered gravity model. A reduced performance of the inter-satellite LRI in the cross-track axis was taken into account in order to consider the less accurate level of the pointing accuracy. Combined solutions from both satellite formations showed a certain improvement w.r.t. the retrieved model from the standalone in-line satellite pair. Spatial residuals from both formations were reduced down to $\pm 2.5 \text{ mm EWH}$ with a good homogeneity of the data. However, extremely high relative range rates between the satellites in the cross-track direction make such measurements quite challenging for current LRI systems. Moreover, in order to measure the cross-track range changes at higher rates, significant modifications of the satellite bus, LRI beam steering mechanism, etc. are needed.

Outlook

Further research can be continued in multiple aspects. At the inertial sensor level, the research can be extended by considering more realistic error budgets. In particular, further development is required for the thermal stability noise level that is the dominant error-source of the modeled accelerometer in the low frequency range. In the current work, it was considered similar to the MicroSTAR inertial sensor of ONERA. But there is a certain potential for enhancement. Moreover, some valuable information regarding the noise level at the low frequencies could probably be expected from the anticipated launch of a SGRS electrostatic accelerometer from a scientific group of the University of Florida that is planned in the upcoming years. Since some of the upcoming gravimetry missions would utilize a drag-compensated regime, a quantification of the performance of the modeled accelerometers and thruster systems on such platforms would be a logical continuation of the work. Also, hybrid accelerometers show promising potential, particularly in the low-frequency domain, where they exhibit a white noise behavior. As these advancements could significantly enhance the precision in various applications, it is essential to further study and optimize their performance in future research to fully exploit their capabilities.

Orbit simulations and their effect on the retrieved gravity field quality possess significant potential for continuing research. For example, investigation of the simulated double-pair orbit scenarios according to the duration of the repeat sub-cycles, altitude, inclination, stability or instability of the orbit formations w.r.t. each other, etc., could provide valuable information for future satellite gravimetry missions. Results can be evaluated by selecting optimal orbit characteristics for short-term (e.g., 3-5 days) gravity field measurements that can be used, for example, in near-real-time early warning services of flooding. Novel triple satellite formations that were introduced in this work could be further studied in detail, for example, considering active drag-reduction or attitude control techniques that could reduce undesirable high relative range-rates and Doppler shifts between the satellite in the cross-track direction. Also, recent lifetime predictions for the GRACE-FO mission suggest it could potentially remain operational into the 2030s, coinciding with the planned launches of GRACE-C and NGGM. This highlights the importance of exploring GFR from more intricate satellite constellations, including configurations with two near-polar pairs and one inclined pair, complemented by measurements from Chinese gravimetry missions.

In general, the inclusion of the insufficient time-variable background modelling would bring the simulations closer to reality. As background models and associated error sources are one of the major limiting factors in current satellite gravimetry, it is of utmost importance to consider them properly in simulations.

The impact of satellites with modified shapes, in particular with extended solar arrays, on the recovered gravity field quality warrants further investigation as well. For example, it would be beneficial to evaluate and compare the performance of the attitude control system for both the standard and modified GRACE spacecraft shapes. This analysis could consider factors such as power production

and consumption estimates, potential reductions in pointing accuracy due to star camera shadowing by enlarged solar panels, impact of vibrations caused by the structural flexibility of the solar arrays, etc.

A promising theme for further research is gravity field recovery with auxiliary sensors and technologies. For example, angular velocity sensing obtained by the differential wavefront measurements of either the orientation of the accelerometer test mass w.r.t. satellite platform or from the inter-satellite laser interferometer. Also, the combination with alternative sensors, e.g., optical clocks, could be investigated. Preliminary studies have shown a certain potential of supplementing the gravity field recovery by this measurement technique.

In addition, in the era of the ‘space renaissance’ when a large number of satellites are planned to be launched in the next decade, a promising avenue of exploration could be the utilization of these extensive constellations in LEO for geodesy applications. Some examples of constellations, which implementation has already begun or is expected to start in the coming years, are: the Starlink mega constellation, designed primarily to provide global internet coverage, could also be used for opportunistic navigation, complementing GNSS satellites in terms of timing and positioning services (Kassas et al., 2021). The IRIS² (Infrastructure for Resilience, Interconnectivity, and Security by Satellite) European Union program will use a multi-orbital satellite constellation in LEO, Medium Earth Orbit (MEO) and Geostationary Orbit (GEO). By 2027 the constellation is expected to include up to 170 LEO satellites providing global coverage, low latency, and high bandwidth for secure communications (Latvian Space Office, 2024). Another European constellation is Low Earth Orbit Positioning Navigation and Timing (LEO-PNT). It is a satellite constellation designed to evaluate the use of novel signals and frequency bands to achieve outstanding resilience and precision in navigation. According to the press release from 18 of March 2024 (European Space Agency, 2024), a complete demonstration constellation shall be in orbit before 2027. The above-mentioned satellite constellations could utilize the hL-SST measurement principle to provide the low-frequency part, i.e. the large-scale structures of the gravity signal (de Teixeira da Encarnacao, 2015). Such measurements would only be sensitive to low spherical harmonic degrees, but with unprecedented spatial distribution this data could be valuable for certain applications, for instance, in temporal de-aliasing of the mass redistributions with short periods occurring in the atmosphere and oceans. Corresponding numerical modeling demonstrated that the aliasing effect on the low-degree part of the Bender constellation can be substantially reduced by combining it with the Starlink-like constellation (Liu et al., 2024).

A Appendix

A.1 Combination of ll-SST and Cross-track SGG

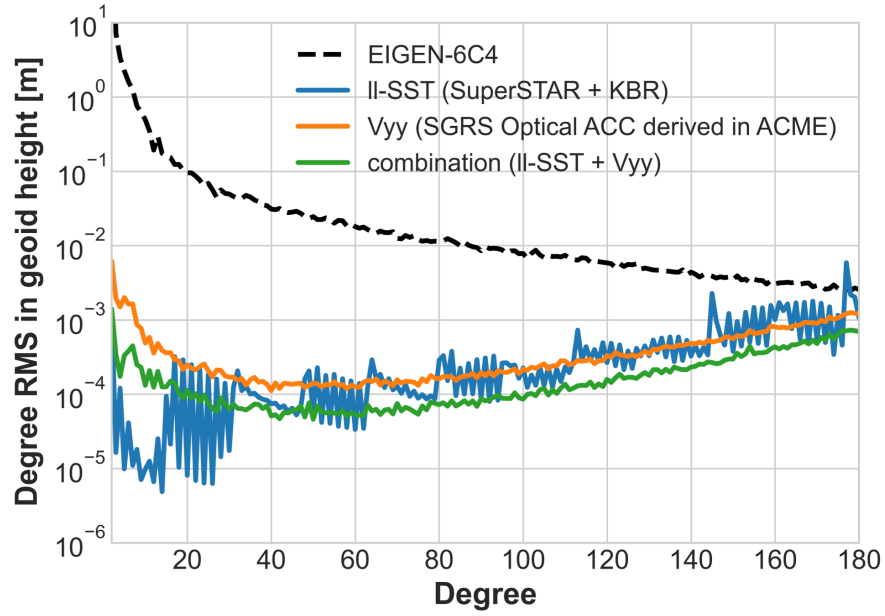


Figure A.1: Degree RMS of the spherical harmonic coefficient differences (true errors) between recovered and EIGEN-6C4 gravity field models in geoid height (m) from ll-SST, cross-track SGG and their combination; Orbit: $h \approx 250$ km; Note: applied stochastic modeling with weights optimised through one consecutive step. Also, a high-pass filter has not been implemented (Kupriyanov et al., 2024b).

A.2 Regularization Techniques for II-SST at the Standalone Inclined Orbit

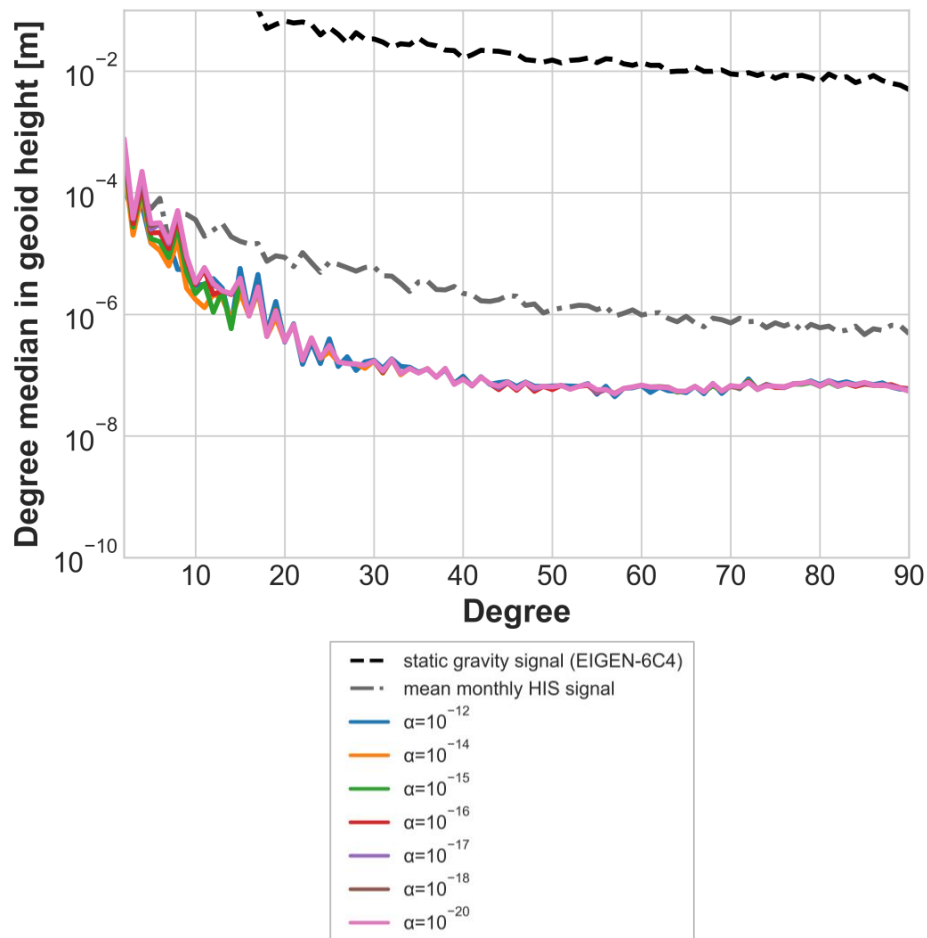


Figure A.2: Degree median values of the spherical harmonic coefficient differences (true errors) between recovered and EIGEN-6C4 gravity field models in geoid height (m) from inclined II-SST simulations with Tikhonov 0 order regularization. Considered regularization parameters are given in the legend. Orbit: #4 (Table 4.2), $h = 396.55$ km.

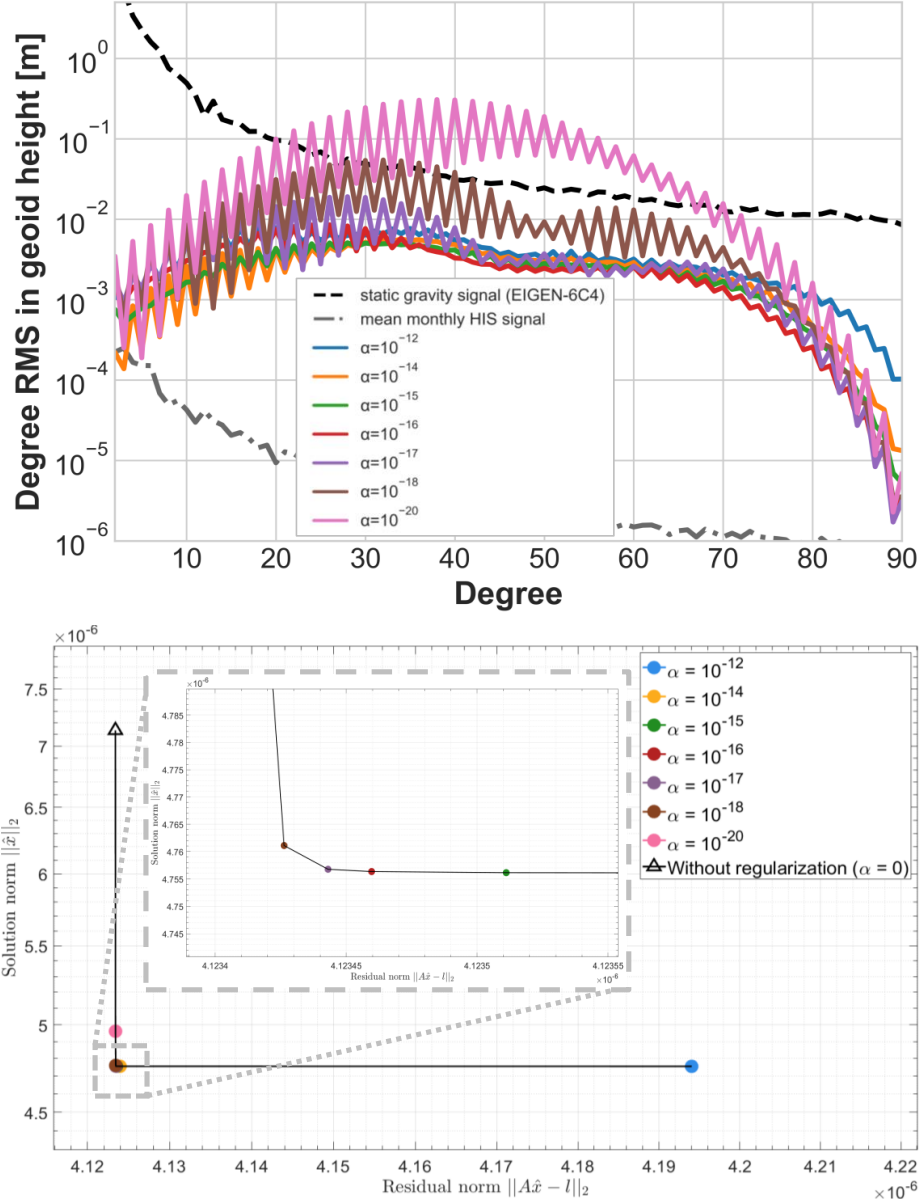


Figure A.3: *Top*: Degree RMS of the spherical harmonic coefficient differences (true errors) between recovered and EIGEN-6C4 gravity field models in geoid height (m) from inclined *ll*-SST simulations with Tikhonov 1st order regularization; *Bottom*: Corresponding L-curve for the regularized solutions. Considered regularization parameters are given in the legend. Orbit: #4 (Table 4.2), $h = 396.55$ km.

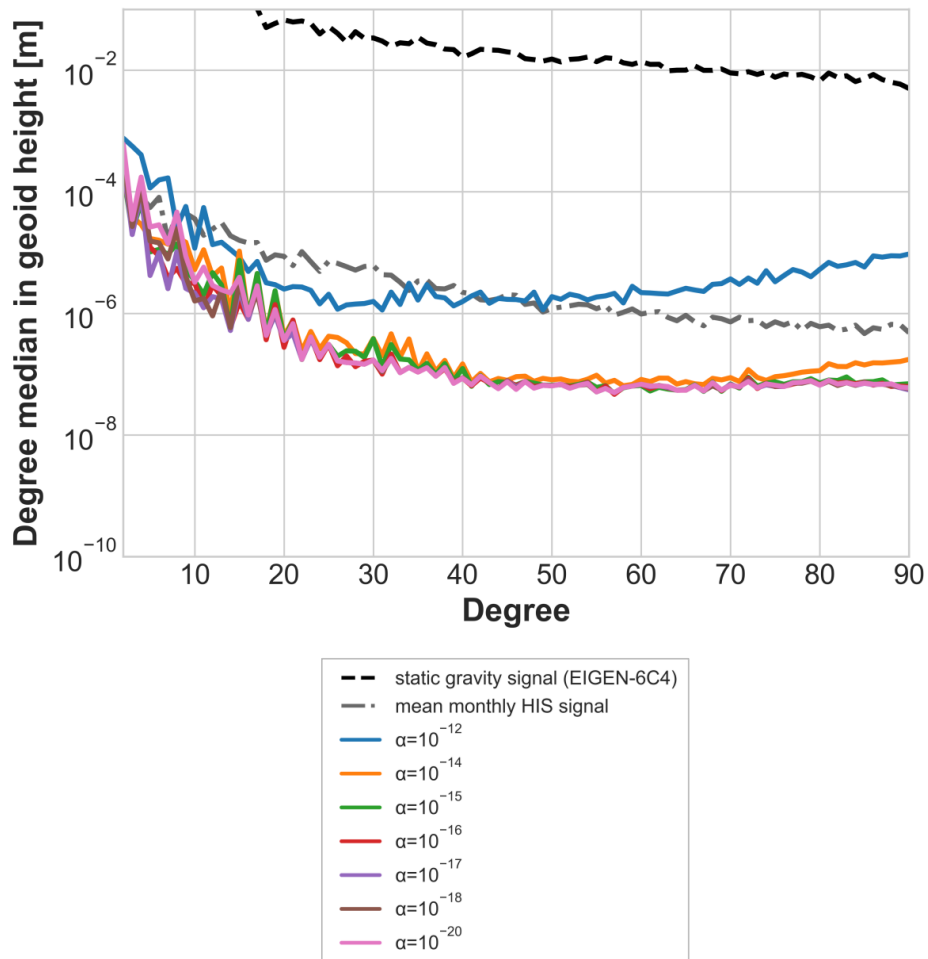


Figure A.4: Degree median values of the spherical harmonic coefficient differences (true errors) between recovered and EIGEN-6C4 gravity field models in geoid height (m) from inclined II-SST simulations with Tikhonov 1st order regularization. Considered regularization parameters are given in the legend. Orbit: #4 (Table 4.2), $h = 396.55$ km.

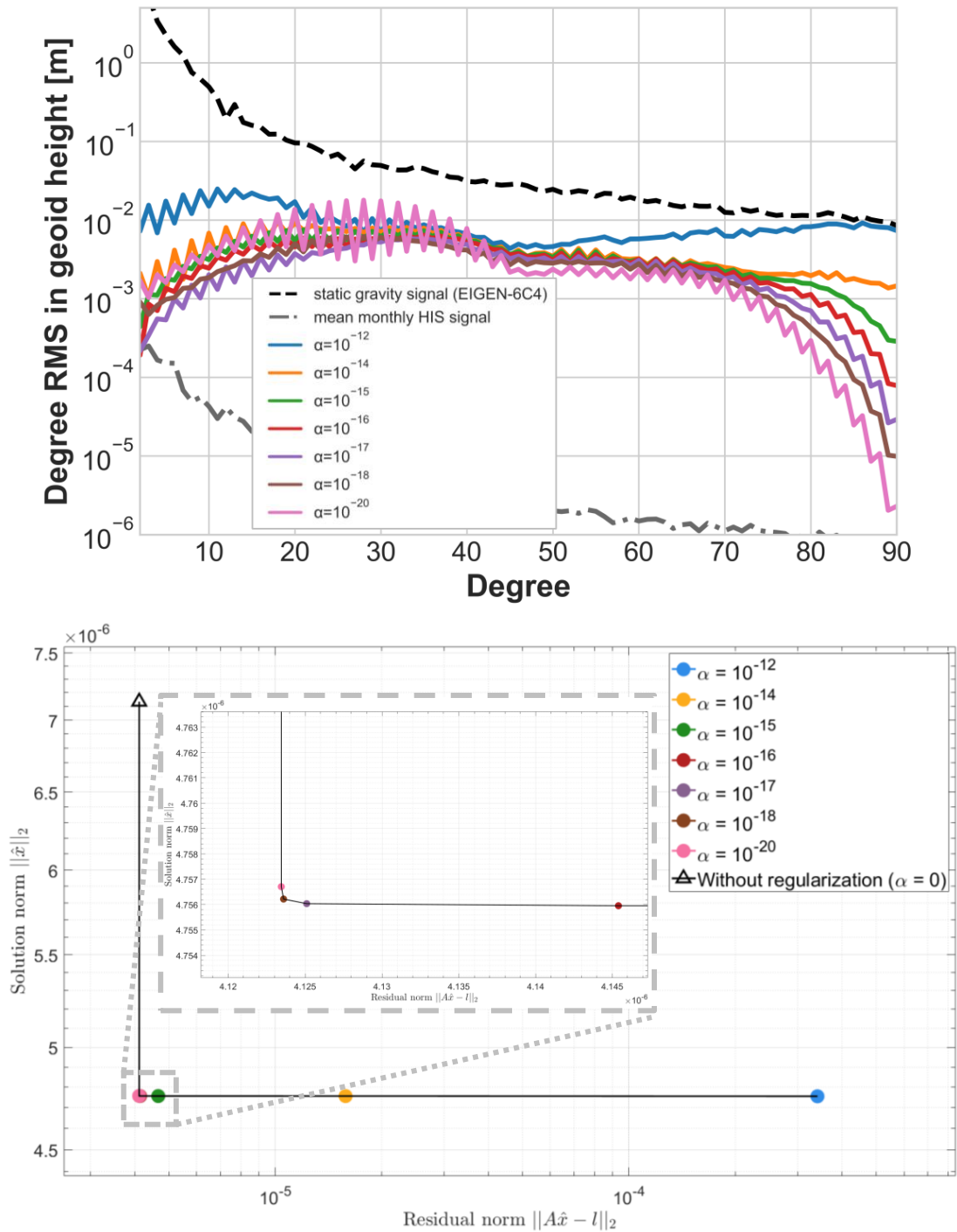


Figure A.5: *Top*: Degree RMS of the spherical harmonic coefficient differences (true errors) between recovered and EIGEN-6C4 gravity field models in geoid height (m) from inclined *ll*-SST simulations with Tikhonov 2nd order regularization; *Bottom*: Corresponding L-curve for the regularized solutions. Considered regularization parameters are given in the legend. Orbit: #4 (Table 4.2), $h = 396.55$ km.

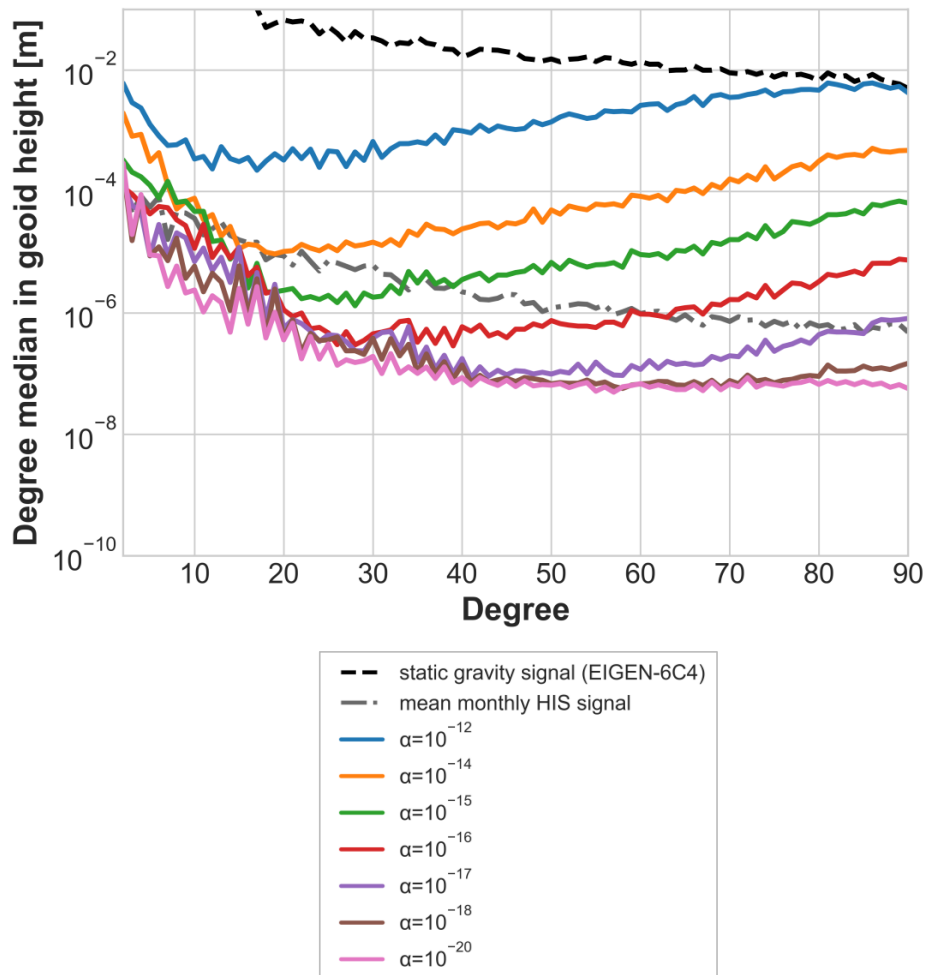


Figure A.6: Degree median values of the spherical harmonic coefficient differences (true errors) between recovered and EIGEN-6C4 gravity field models in geoid height (m) from inclined II-SST simulations with Tikhonov 2nd order regularization. Considered regularization parameters are given in the legend. Orbit: #4 (Table 4.2), $h = 396.55$ km.

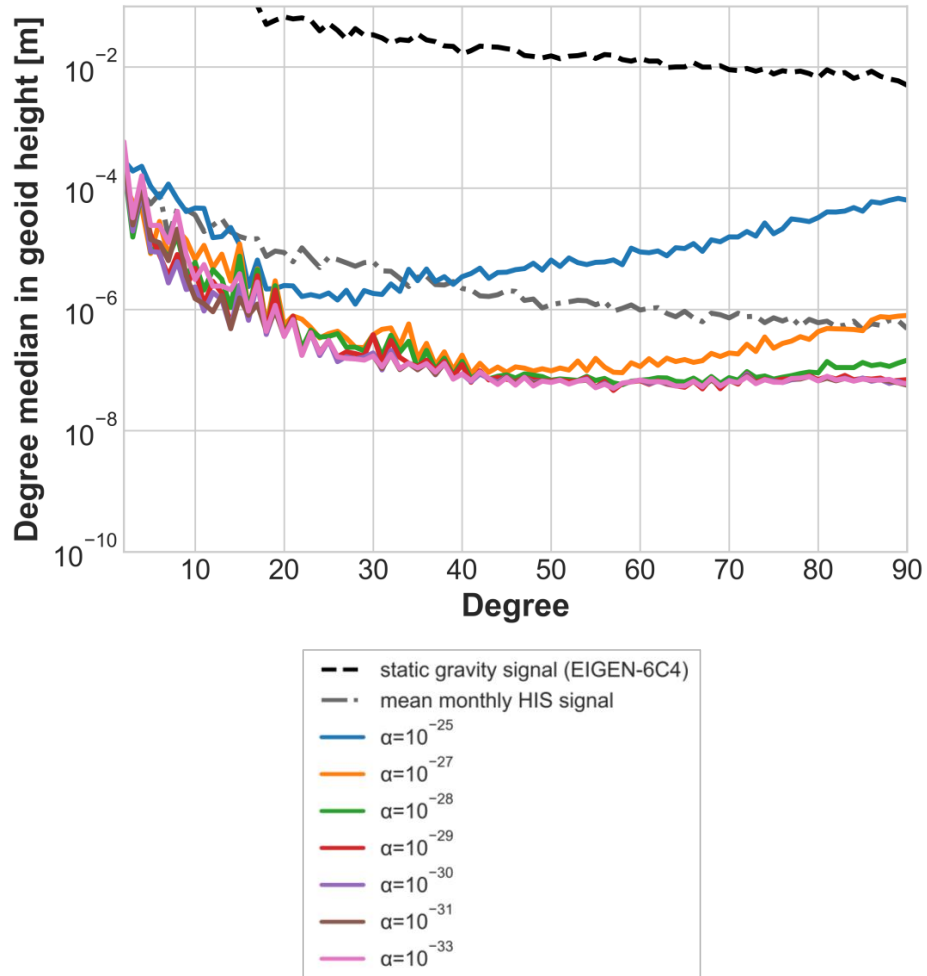


Figure A.7: Degree median values of the spherical harmonic coefficient differences (true errors) between recovered and EIGEN-6C4 gravity field models in geoid height (m) from inclined *ll*-SST simulations with Kaula regularization. Considered regularization parameters are given in the legend. Orbit: #4 (Table 4.2), $h = 396.55$ km.

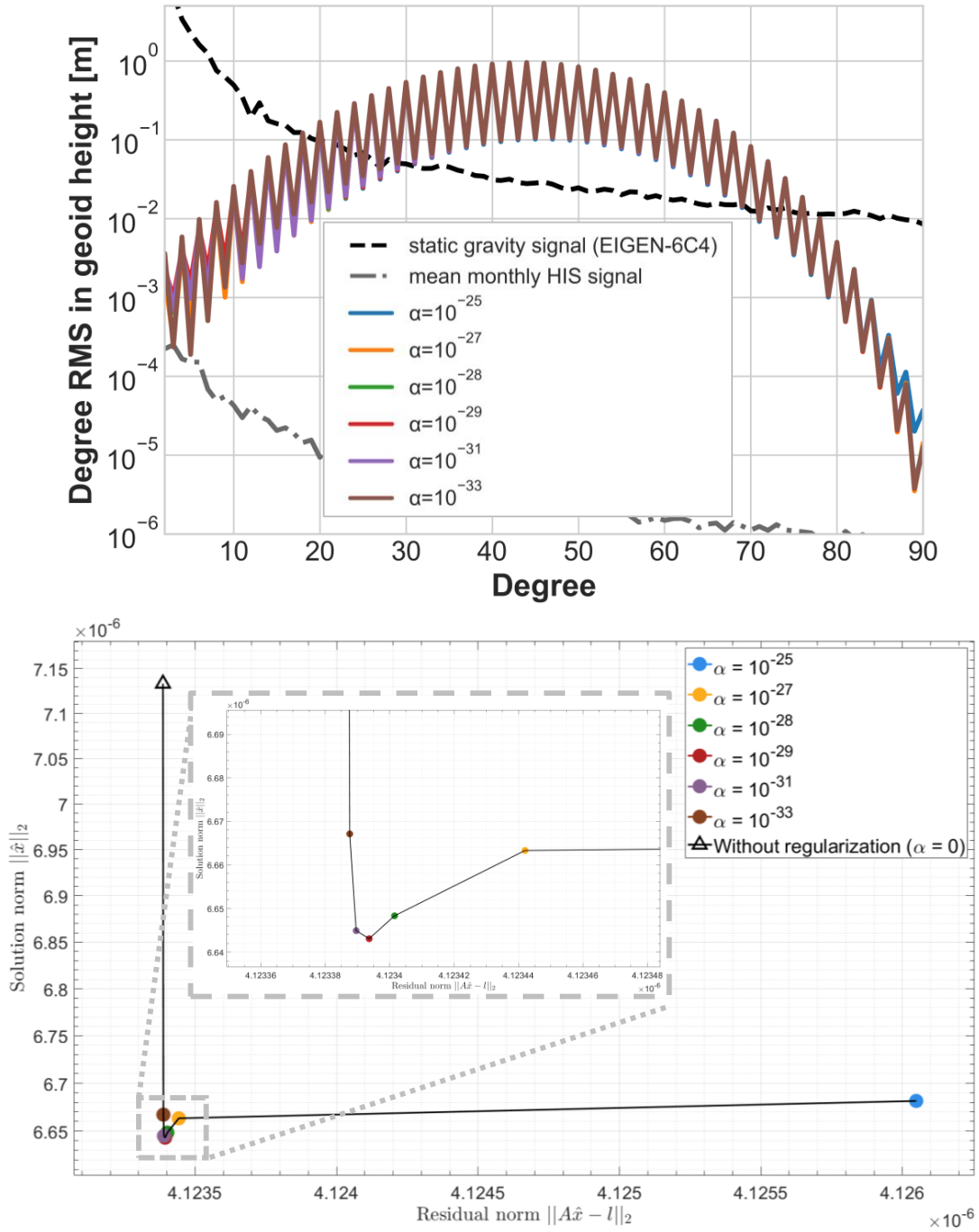


Figure A.8: *Top*: Degree RMS of the spherical harmonic coefficient differences (true errors) between recovered and EIGEN-6C4 gravity field models in geoid height (m) from inclined II-SST simulations with Kaula incl. the polar gap regularization; *Bottom*: Corresponding L-curve for the regularized solutions. Considered regularization parameters are given in the legend. Orbit: #4 (Table 4.2), $h = 396.55$ km.

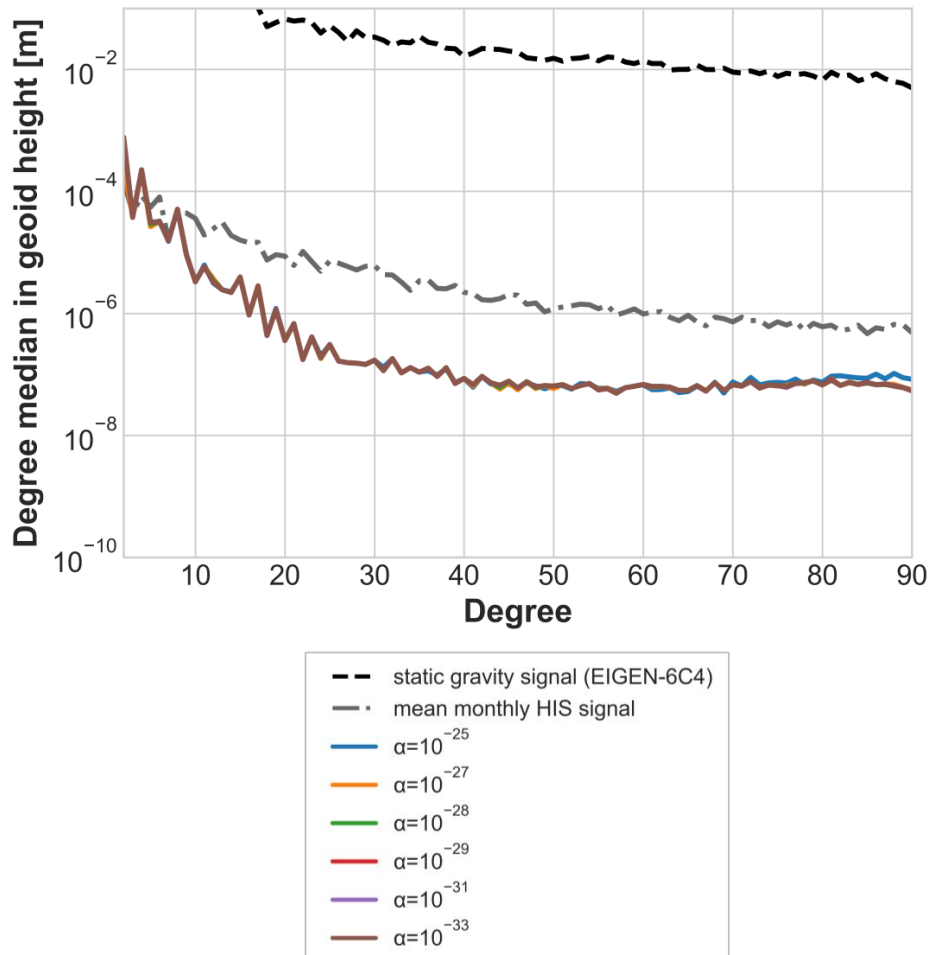


Figure A.9: Degree median values of the spherical harmonic coefficient differences (true errors) between recovered and EIGEN-6C4 gravity field models in geoid height (m) from inclined *ll*-SST simulations with Kaula incl. the polar gap regularization. Considered regularization parameters are given in the legend. Orbit: #4 (Table 4.2), $h = 396.55$ km.

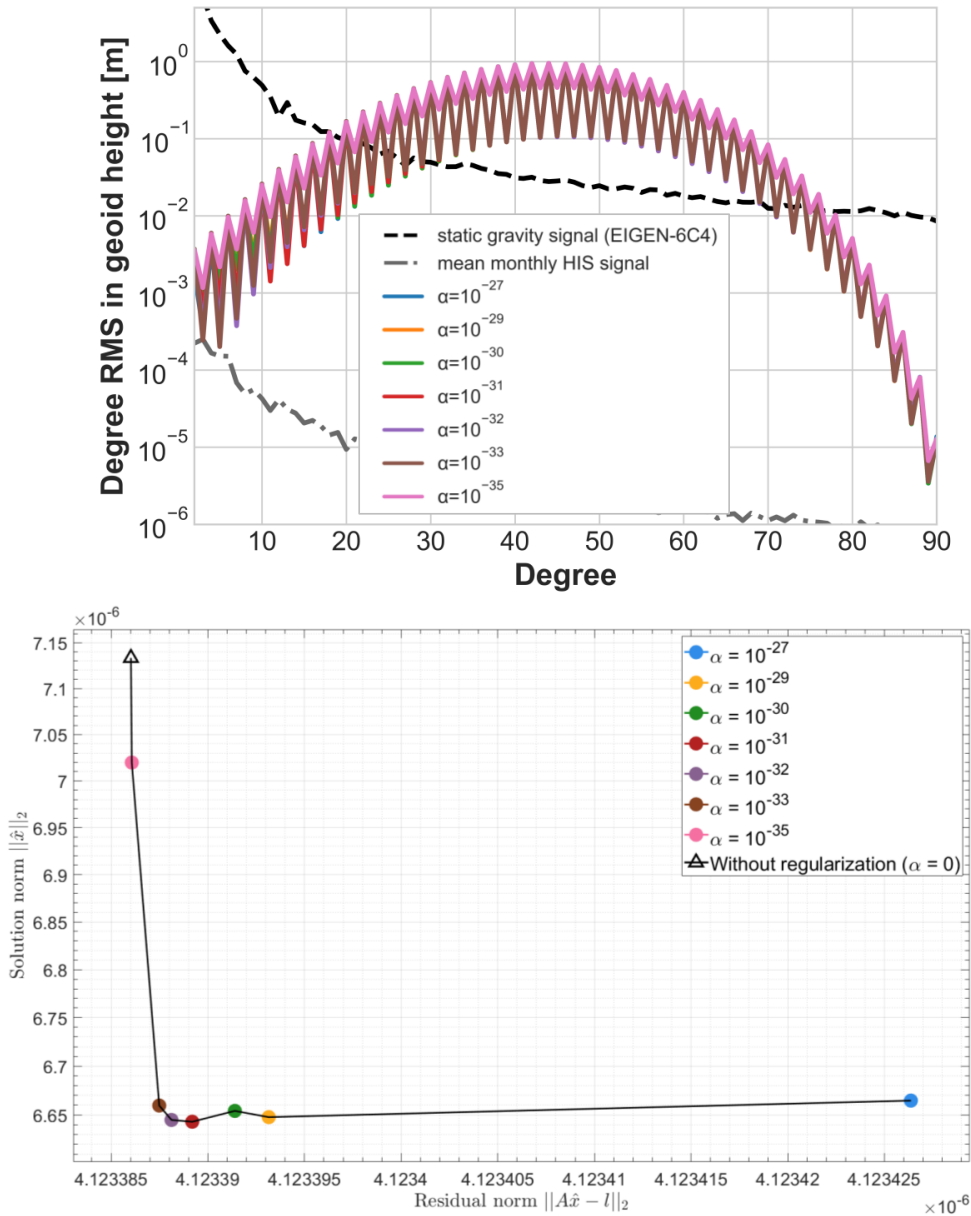


Figure A.10: *Top*: Degree RMS of the spherical harmonic coefficient differences (true errors) between recovered and EIGEN-6C4 gravity field models in geoid height (m) from inclined 11-SST simulations with Kaula order-dependent regularization; *Bottom*: Corresponding L-curve for the regularized solutions. Considered regularization parameters are given in the legend. Orbit: #4 (Table 4.2), $h = 396.55$ km.

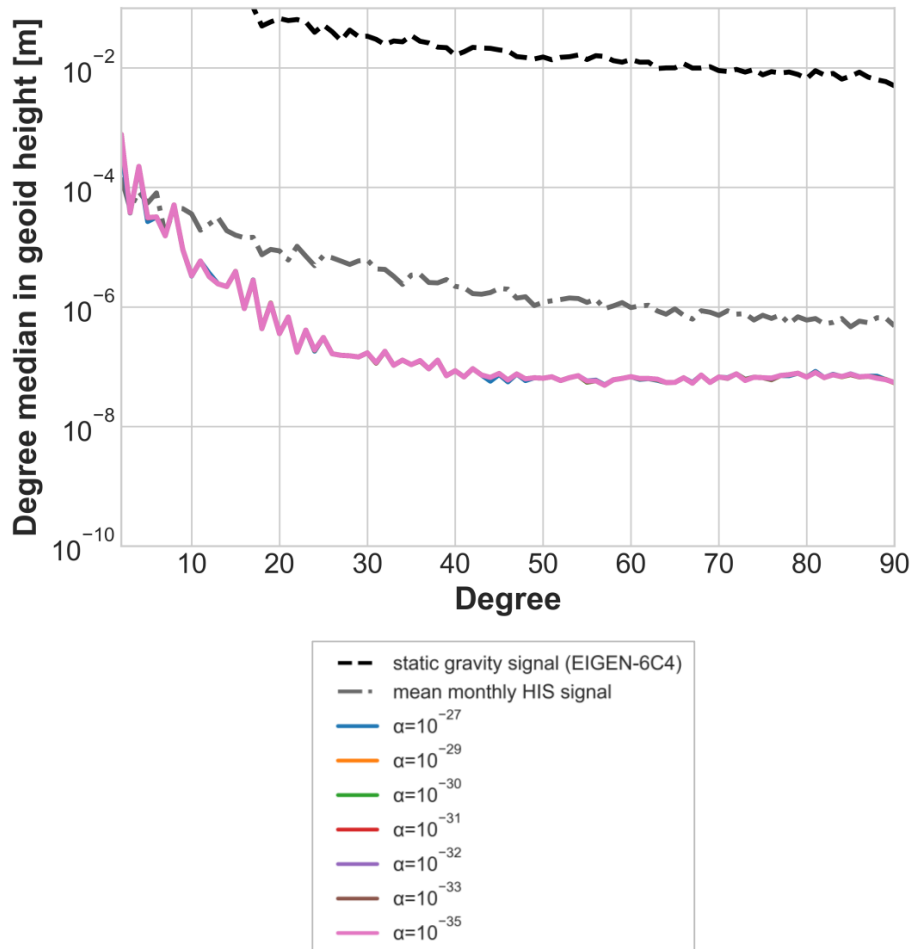


Figure A.11: Degree median values of the spherical harmonic coefficient differences (true errors) between recovered and EIGEN-6C4 gravity field models in geoid height (m) from inclined *ll*-SST simulations with Kaula order-dependent regularization. Considered regularization parameters are given in the legend. Orbit: #4 (Table 4.2), $h = 396.55$ km.

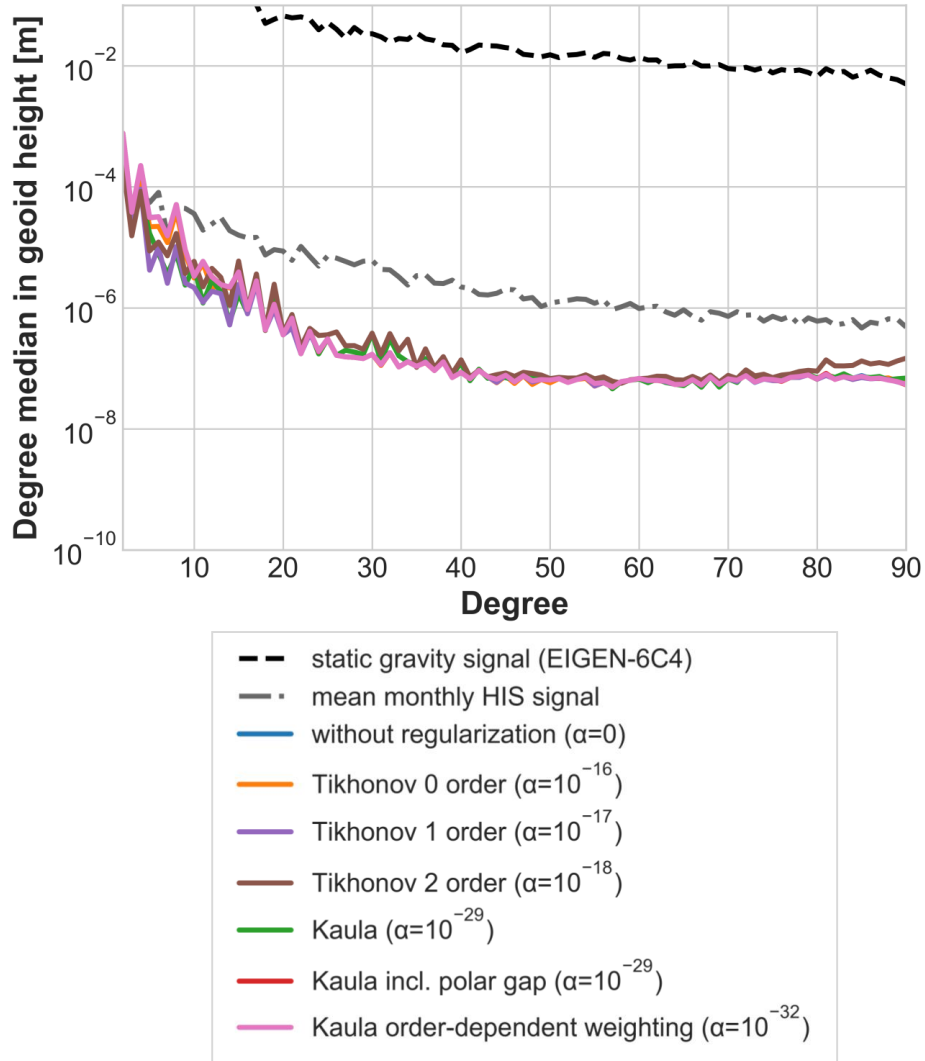


Figure A.12: Degree median values of the spherical harmonic coefficient differences (true errors) between recovered and EIGEN-6C4 gravity field models in geoid height (m) for the inclined ll-SST simulations, regularized by different methods; Orbit: #4 (Table 4.2), $h = 396.55$ km.

List of Figures

2.1	Surface spherical harmonics representation	6
2.2	Measurement concepts applied in satellite gravimetry	7
2.3	Measurement principle of the ll-SST for a GRACE-like mission . .	8
2.4	Extended Meissl scheme	12
2.5	Scheme of the mathematical transformations between the different quantities of the discrete Fourier transform	13
3.1	STAR accelerometer reference frame with respect to CHAMP satellite frame	27
3.2	Layout of the LRI on-board the GRACE-FO satellites	28
3.3	Simplified scheme of the LISA-Pathfinder spacecraft	29
3.4	State of the art accelerometers	33
3.5	Comparison of the ASD sensitivities of current accelerometers . .	33
3.6	Improved accelerometer concepts	37
3.7	Comparison of the ASD sensitivities of improved accelerometer concepts	38
4.1	Block-scheme diagram of the closed-loop simulation procedure for ll-SST	42
4.2	Block-scheme diagram of the closed-loop simulation procedure for SGG	43
4.3	International sunspot number	46
4.4	ASD of the the non-gravitational accelerations for the year with high and low solar activites	46
4.5	Time-series of the non-gravitational acceleration	47
4.6	Illustration of a one-degree-of-freedom accelerometer model	49
4.7	Illustration of a six-degrees-of-freedom accelerometer model	50
4.8	Scheme of the different techniques to readout the test mass displacement	50
4.9	Generalized accelerometer block diagram	51
4.10	ASD of the noise budget of the modeled SGRS	52
4.11	ASDs of the SGRS EAs with changed parameter values	53
4.12	Illustration of 1 degree of freedom optical gradiometer model . . .	54
5.1	Comparison of the ASD sensitivities of accelerometers that are used in this work.	57
5.2	ASD sensitivities of the accelerometers that are used for hybridization	59
5.3	ASD sensitivities of high-pass filtered accelerometers that are used in gravity field recovery simulations.	60
5.4	Comparison of the ASDs of the inter-satellite LRI and KBR range measurement errors that are used in this work.	61

6.1	Impact of the stochastic modeling in ll-SST with colored (brown) noise; Degree RMS graph	64
6.2	Impact of the stochastic modeling in ll-SST with colored (brown) noise; Global maps with the residuals and SH error spectra	66
6.3	Impact of the stochastic modeling in SGG with colored (pink) noise; Degree RMS graph	67
6.4	Impact of the stochastic modeling in SGG with colored (pink) noise; Global maps with the residuals and SH error spectra	68
6.5	Impact of the stochastic modeling in ll-SST with white noise; Degree RMS graph	69
6.6	Impact of the stochastic modeling in ll-SST with white noise; Global maps with the residuals and SH error spectra	70
6.7	Impact of the stochastic modeling in SGG with white noise; Degree RMS graph	71
6.8	Impact of the stochastic modeling in SGG with white noise; Global maps with the residuals and SH error spectra	72
6.9	Degree RMS of the spherical harmonic coefficient differences (true errors) between recovered and EIGEN-6C4 gravity field models in geoid height (m) from ll-SST simulations	73
6.10	Spatial distribution of the residuals of the recovered gravity models w.r.t. EIGEN-6C4, plotted on global maps in EWH from ll-SST simulations	75
6.11	Spherical harmonic error spectra of the coefficient differences (true errors) of the recovered gravity models w.r.t. EIGEN-6C4, from ll-SST simulations	76
6.12	ASD of the difference of the monthly averaged AOD RL7 and RL6, ocean-tide difference of the EOT11a and FES2014b and interpolated AOe07	78
6.13	Degree RMS of the spherical harmonic coefficient differences (true errors) between recovered and EIGEN-6C4 gravity field models in geoid height (m) from ll-SST simulations including time-variable background modeling errors	79
6.14	Spatial distribution (on the left) and spherical harmonic error spectra (on the right) of the residuals from ll-SST simulations including time-variable background modeling error	81
6.15	3D graphic rendition of the studied satellite shapes.	83
6.16	Decay of the maximum orbit altitude per revolution of the standard GRACE-FO and two modified spacecraft shapes during the simulated one month mission time span.	84
6.17	Comparison of the ASD sensitivities of the modeled SGRS optical accelerometers on-board of the satellite with standard GRACE-FO shape and modified ones.	85
6.18	Degree RMS of the spherical harmonic coefficient differences (true errors) between recovered and EIGEN-6C4 gravity field models in geoid height (m) from ll-SST simulations with different satellite shapes.	86

6.19	Degree RMS of the spherical harmonic coefficient differences (true errors) between recovered and EIGEN-6C4 gravity field models in geoid height (m) from cross-track SGG simulations	89
6.20	Spatial distribution of the residuals of the recovered gravity models w.r.t. EIGEN-6C4, plotted on the global maps in EWH from cross-track SGG simulations	90
6.21	Spherical harmonic error spectra of the coefficient differences (true errors) of the recovered gravity models w.r.t. EIGEN-6C4, from cross-track SGG simulations	91
6.22	ASD curves of two cases of the common mode gain uncertainty for a GOCE-like orbit (h=250 km), multiplied by the residual drag ASD	93
6.23	Scheme of the combination of ll-SST and cross-track SGG in a possible future gravimetry mission	94
6.24	Degree RMS of the spherical harmonic coefficient differences (true errors) between recovered and EIGEN-6C4 gravity field models in geoid height (m) from ll-SST, cross-track SGG and their combination	95
6.25	Spatial distribution (on the left) and spherical harmonic error spectra (on the right) of the residuals from ll-SST, cross-track SGG and their combination	96
6.26	Degree RMS and degree median values of the spherical harmonic coefficient differences (true errors) between recovered and EIGEN-6C4 gravity field models in geoid height (m) from the near-polar, inclined orbit and their combination	98
6.27	Spatial distribution (on the left) and spherical harmonic error spectra (on the right) of the residuals from ll-SST on the near-polar, inclined orbit and their combination	99
6.28	Comparison of the ASD curves of three cases of scale factor errors for NGGM	101
6.29	Top: Degree RMS of the true errors between recovered and EIGEN-6C4 gravity field models in geoid height from inclined ll-SST simulations with Tikhonov 0 order regularization; Bottom: Corresponding L-curve for the regularized solutions.	103
6.30	Top: Degree RMS of the true errors between recovered and EIGEN-6C4 gravity field models in geoid height from inclined ll-SST simulations with Kaula regularization; Bottom: Corresponding L-curve for the regularized solutions.	105
6.31	Degree RMS of the spherical harmonic coefficient differences (true errors) between recovered and EIGEN-6C4 gravity field models in geoid height (m) for the inclined ll-SST simulations, regularized by different methods	106
6.32	Scheme of the combination of the in-line and cross-track formation differing by the right ascension of the ascending node	108
6.33	Degree RMS of the spherical harmonic coefficient differences (true errors) between recovered and EIGEN-6C4 gravity field models in geoid height (m) from ll-SST for the in-line, cross-track formation (differs by Ω) and their combination	109

6.34	Spatial distribution (on the left) and spherical harmonic error spectra (on the right) of the residuals from ll-SST for the in-line, cross-track (differs by Ω) formation and their combination	110
6.35	Scheme of the combination of the in-line and cross-track formation differing by the inclination	111
6.36	Degree RMS of the spherical harmonic coefficient differences (true errors) between recovered and EIGEN-6C4 gravity field models in geoid height (m) from ll-SST for the in-line, cross-track formation (differs by i) and their combination	112
6.37	Spatial distribution (on the left) and spherical harmonic error spectra (on the right) of the residuals from ll-SST for the in-line, cross-track (differs by i) and their combination;	113
6.38	Degree RMS of the spherical harmonic coefficient differences (true errors) between recovered and EIGEN-6C4 gravity field models in geoid height (m) from ll-SST for the in-line, triple satellite formation (Δi) and ($\Delta \Omega$)	114
A.1	Degree RMS of the spherical harmonic coefficient differences (true errors) between recovered and EIGEN-6C4 gravity field models in geoid height (m) from ll-SST, cross-track SGG and their combination	123
A.2	Degree median values of the spherical harmonic coefficient differences (true errors) between recovered and EIGEN-6C4 gravity field models in geoid height (m) from inclined ll-SST simulations with Tikhonov 0 order regularization.	124
A.3	Top: Degree RMS of the true errors between recovered and EIGEN-6C4 gravity field models in geoid height from inclined ll-SST simulations with Tikhonov 1st order regularization; Bottom: Corresponding L-curve for the regularized solutions.	125
A.4	Degree median values of the spherical harmonic coefficient differences (true errors) between recovered and EIGEN-6C4 gravity field models in geoid height (m) from inclined ll-SST simulations with Tikhonov 1 st order regularization.	126
A.5	Top: Degree RMS of the true errors between recovered and EIGEN-6C4 gravity field models in geoid height from inclined ll-SST simulations with Tikhonov 2 nd order regularization; Bottom: Corresponding L-curve for the regularized solutions.	127
A.6	Degree median values of the spherical harmonic coefficient differences (true errors) between recovered and EIGEN-6C4 gravity field models in geoid height (m) from inclined ll-SST simulations with Tikhonov 2 nd order regularization.	128
A.7	Degree median values of the spherical harmonic coefficient differences (true errors) between recovered and EIGEN-6C4 gravity field models in geoid height (m) from inclined ll-SST simulations with Kaula regularization.	129

A.8	Top: Degree RMS of the true errors between recovered and EIGEN-6C4 gravity field models in geoid height from inclined ll-SST simulations with Kaula incl. the polar gap regularization; Bottom: Corresponding L-curve for the regularized solutions.	130
A.9	Degree median values of the spherical harmonic coefficient differences (true errors) between recovered and EIGEN-6C4 gravity field models in geoid height (m) from inclined ll-SST simulations with Kaula incl. the polar gap regularization.	131
A.10	Top: Degree RMS of the true errors between recovered and EIGEN-6C4 gravity field models in geoid height from inclined ll-SST simulations with Kaula order-dependent regularization; Bottom: Corresponding L-curve for the regularized solutions.	132
A.11	Degree median values of the spherical harmonic coefficient differences (true errors) between recovered and EIGEN-6C4 gravity field models in geoid height (m) from inclined ll-SST simulations with Kaula order-dependent regularization.	133
A.12	Degree median values of the spherical harmonic coefficient differences (true errors) between recovered and EIGEN-6C4 gravity field models in geoid height (m) for the inclined ll-SST simulations, regularized by different methods.	134

List of Tables

3.1	Overview of realised satellite gravimetry missions	31
3.2	Summary table of state-of-the-art accelerometers	34
3.3	Summary table of enhanced electrostatic accelerometers concepts	39
4.1	Considered background models in orbit simulations	45
4.2	Overview of the orbits utilized in the simulations	48
4.3	Key characteristics of the SGRS developed in ACME	53

Acronyms

AB Adams-Bashforth

ABM Adams-Bashforth-Moulton

AC Alternating Current

ACC(s) Accelerometer(s)

ACME Accelerometer Modeling Environment

AM Adams-Moulton

AOD Atmosphere and Ocean De-Aliasing

AS Amplitude Spectrum

ASD Amplitude Spectral Density

CAI Cold Atom Interferometry

CHAMP Challenging Minisatellite Payload

CoM Center of the Mass

D Air Drag

DFT Discrete Fourier Transform

DLR Deutsches Zentrum für Luft- und Raumfahrt (German Aerospace Center)

EA Electrostatic Accelerometer

Ealb Earth albedo

EH Electrode Housing

EIGEN European Improved Gravity model of the Earth by New techniques

EOT Empirical Ocean Tide model

ESA European Space Agency

EWH Equivalent Water Height

GFR Gravity Field Recovery

GNSS Global Navigation Satellite System

GOCE Gravity field and Ocean Circulation Explorer

GPS Global Positioning System

GRACE Gravity Recovery and Climate Experiment

GRACE-C Gravity Recovery and Climate Experiment-Continuing

- GRACE-FO** Gravity Recovery and Climate Experiment-Follow On
- GRF** Gradiometer Reference Frame
- GRS** Gravitational Reference Sensor
- HIS** Hydrology, Ice and Solid Earth
- hl-SST** high-low Satellite-to-Satellite Tracking
- IR** Infrared Irradiance
- KBR** K-band Ranging
- LEO** Low Earth Orbit
- LISA** Laser Interferometer Space Antenna
- ll-SST** low-low Satellite-to-Satellite Tracking
- LOS** Line of Sight
- LPF** LISA-Pathfinder
- LPSD** Logarithmic frequency axis Power Spectral Density
- LRI** Laser Ranging Interferometer
- LS** Least-Squares
- NASA** National Aeronautics and Space Administration
- NGGM** Next Generation Gravimetry Mission
- MAGIC** Mass change And Geosciences International Constellation
- ONERA** Office National d'Etudes et de Recherches Aérospatiales (French Aerospace Lab)
- ODE** Ordinary Differential Equations
- PS** Power Spectrum
- PSD** Power Spectral Density
- QACC** Quantum Accelerometry
- RK** Runge Kutta
- RL** Release
- RMS** Root Mean Square
- SGG** Satellite Gravity Gradiometry
- SGRS** Simplified Gravitational Reference Sensor
- SH** Spherical Harmonic
- STAR** Space Triaxial Accelerometer for Research Missions

SRP Solar Radiation Pressure

SWaP Size, Weight and Power

TerraQ Relativistic and Quantum-based Geodesy

TM Test Mass

VCM Variance Covariance Matrix

WOSA Welch's Overlapped Segmented Averaging

XHPS Extended High Performance Satellite Dynamics Simulator

Acknowledgments

I sincerely thank all those who made this PhD research possible. Also, I would like to extend special gratitude to the following people who have helped me undertake this study:

- Prof. Dr.-Ing. habil. Jürgen Müller, for the trust he placed in me by accepting my application to join this research. He provided me an incredible opportunity to be part of an advanced and international scientific community. Working at the Institut für Erdmessung (IfE) under his leadership, I appreciated his attentiveness, care for each employee, and helpfulness. It has been a great honor to be part of Prof. Müller's team. I am immensely grateful for the time as well as invaluable experience and knowledge he gave me.
- Prof. Dr.-Ing. Nico Sneeuw and PD Dr.-Ing. Hamza Alkhatib, for their time and effort as referees of this dissertation.
- Dr.-Ing. Manuel Schilling, my co-supervisor for guiding me throughout my PhD research and investing significant time and effort. I also appreciate his valuable comments and corrections on all my papers, posters, and presentations.
- Prof. Dr. Matthias Weigelt, for his willingness to always help and explain everything in detail. I am also appreciative of his meaningful comments on our joint article with DLR.
- Dr. Vitali Müller, for sharing precious knowledge about laser interferometry and organizing regular meetings within the TerraQ B01 project and the Quantum Frontiers 'Space Laser Gravimetry' topical group.
- Prof. Dr. Meike List, for suggesting the organization of a joint study (LUH, DLR, AEI) and for providing important ideas that greatly enhanced our research, which became the foundation for our joint paper.
- Arthur Reis, for his significant help with coding, collaboration on software development and integration as well as valuable contributions to our joint papers. I am likewise thankful for our joint leisure activities that provided a good mental support.
- Dr.-Ing. Annike Knabe, Dr. Alireza HosseiniArani, Dr. Mohsen Romeshkani and Nina Fletling, my colleagues at IfE, for their immense help and support, insightful discussions, and contributions to our collaborative research.
- Andreas Leipner, for carrying out multiple simulations for our joint paper and providing valuable ideas that significantly contributed to our work.
- Britta Michaela Frankel, Dr.-Ing. Raúl Villanueva Granados and Dr. Mona Weyrauch, TerraQ administrators and coordinators at IfE, for their indis-

pensable work in managing finances, including travel costs to the conferences, organizing general assemblies, writing proposals, facilitating TerraQ evaluation and coordinating other social events.

This work was carried out as part of the joint collaborative initiative *Relativistic and Quantum-based Geodesy ‘TerraQ’* (SFB-1464), specifically within the project B01, *New Measurement Concepts with Laser Interferometers*. Additionally, this research was conducted under the umbrella of the *Quantum Frontiers cluster of excellence* (EXC-2123). I acknowledge the funding by:

- Deutsche Forschungsgemeinschaft (DFG) – TerraQ (Project-ID 434617780 – SFB 1464)
- German Excellence Strategy – Quantum Frontiers (Project-ID 390837967 – EXC 2123)

Last but not least, I cannot describe all the words of gratitude to my family, my parents and my wife for their endless support and faith in me.

Bibliography

- K. Abdelmohsen, M. Sultan, H. Save, A. Z. Abotalib, and E. Yan. What can the GRACE seasonal cycle tell us about lake-aquifer interactions? *Earth-Science Reviews*, 211:103392, 2020. doi:10.1016/j.earscirev.2020.103392.
- K. Abich, A. Abramovici, B. Amparan, A. Baatzsch, B. B. Okihiro, D. C. Barr, M. P. Bize, C. Bogan, C. Braxmaier, M. J. Burke, et al. In-orbit performance of the GRACE Follow-On laser ranging interferometer. *Physical review letters*, 123(3):031101, 2019. doi:10.1103/PhysRevLett.123.031101.
- P. Abrykosov, R. Pail, T. Gruber, N. Zahzam, A. Bresson, E. Hardy, B. Christophe, Y. Bidel, O. Carraz, and C. Siemes. Impact of a novel hybrid accelerometer on satellite gravimetry performance. *Advances in Space Research*, 63(10):3235–3248, 2019. doi:10.1016/j.asr.2019.01.034.
- AEI. Successful German-US environmental mission to be continued with GRACE-C, 2024. URL <https://www.aei.mpg.de/1130150/erfolgreiche-deutsch-amerikanische-umweltmission-wird-mit-grace-c-fortgesetzt>. Last accessed: 05.04.2024.
- Airbus. Airbus continues to collaborate with NASA to monitor climate change from Space, 2024. URL <https://www.airbus.com/en/newsroom/press-releases/2024-03-airbus-continues-to-collaborate-with-nasa-to-monitor-climate-change>. Last accessed: 05.04.2024.
- I. Alonso, C. Alpigiani, B. Altschul, H. Araújo, G. Arduini, J. Arlt, L. Badurina, A. Balaž, S. Bandarupally, B. C. Barish, et al. Cold atoms in space: community workshop summary and proposed road-map. *EPJ Quantum Technology*, 9(1): 1–55, 2022. doi:10.1140/epjqt/s40507-022-00147-w.
- D. F. Argus, W. R. Peltier, G. Blewitt, and C. Kreemer. The viscosity of the top third of the lower mantle estimated using GPS, GRACE, and relative sea level measurements of glacial isostatic adjustment. *Journal of Geophysical Research: Solid Earth*, 126(5), 2021. doi:10.1029/2020JB021537.
- M. Armano, M. Benedetti, J. Bogenstahl, D. Bortoluzzi, P. Bosetti, N. Brandt, A. Cavalleri, G. Ciani, I. Cristofolini, A. Cruise, et al. LISA Pathfinder: the experiment and the route to LISA. *Classical and Quantum Gravity*, 26(9): 094001, 2009. doi:10.1088/0264-9381/26/9/094001.
- M. Armano, H. Audley, G. Auger, J. Baird, P. Binetruy, M. Born, D. Bortoluzzi, N. Brandt, A. Bursi, M. Caleno, et al. The LISA Pathfinder mission. In *Journal of Physics: Conference Series*, volume 610, page 012005. IOP Publishing, 2015. doi:10.1088/1742-6596/610/1/012005.
- M. Armano, H. Audley, G. Auger, J. T. Baird, M. Bassan, P. Binetruy, M. Born, D. Bortoluzzi, N. Brandt, M. Caleno, et al. Sub-femto-g free fall for space-based

- gravitational wave observatories: LISA Pathfinder results. *Physical review letters*, 116(23):231101, 2016. doi:10.1103/PhysRevLett.116.231101.
- M. Armano, H. Audley, J. Baird, P. Binetruy, M. Born, D. Bortoluzzi, E. Castelli, A. Cavalleri, A. Cesarini, A. Cruise, et al. Beyond the required LISA free-fall performance: new LISA Pathfinder results down to 20 mHz. *Physical review letters*, 120(6):061101, 2018a. doi:10.1103/PhysRevLett.120.061101.
- M. Armano, H. Audley, J. Baird, P. Binetruy, M. Born, D. Bortoluzzi, E. Castelli, A. Cavalleri, A. Cesarini, A. M. Cruise, K. Danzmann, et al. Precision charge control for isolated free-falling test masses: LISA Pathfinder results. *Physical Review D*, 98(6), 2018b. ISSN 2470-0010. doi:10.1103/PhysRevD.98.062001.
- M. Armano, H. Audley, J. Baird, P. Binetruy, M. Born, D. Bortoluzzi, E. Castelli, A. Cavalleri, A. Cesarini, A. Cruise, et al. LISA Pathfinder platform stability and drag-free performance. *Physical Review D*, 99(8):082001, 2019. doi:10.1103/PhysRevD.99.082001.
- M. Armano, H. Audley, J. Baird, P. Binetruy, M. Born, D. Bortoluzzi, N. Brandt, E. Castelli, A. Cavalleri, A. Cesarini, et al. Sensor Noise in LISA Pathfinder: In-Flight Performance of the Optical Test Mass Readout. *Physical Review Letters*, 126(13), 2021. ISSN 0031-9007. doi:10.1103/PhysRevLett.126.131103.
- D. Arnold, T. Grombein, L. Schreiter, V. Sterken, and A. Jäggi. Reprocessed precise science orbits and gravity field recovery for the entire GOCE mission. *Journal of geodesy*, 97(7):67, 2023. doi:10.1007/s00190-023-01752-y.
- A. Asoka and V. Mishra. Anthropogenic and climate contributions on the changes in terrestrial water storage in India. *Journal of Geophysical Research: Atmospheres*, 125(10), 2020. ISSN 2169-897X. doi:10.1029/2020JD032470.
- H. Audley, K. Danzmann, A. G. Marin, G. Heinzel, A. Monsky, M. Nofrarias, F. Steier, D. Gerardi, R. Gerndt, G. Hechenblaikner, et al. The LISA Pathfinder interferometry—hardware and system testing. *Classical and Quantum Gravity*, 28(9):094003, 2011. doi:10.1088/0264-9381/28/9/094003.
- Aviso+. FES (Finite Element Solution)- Global tide, 2024. URL <https://www.aviso.altimetry.fr/en/data/products/auxiliary-products/global-tide-fes.html>. Last accessed: 05.06.2024.
- T. Bandikova, C. McCullough, G. L. Kruizinga, H. Save, and B. Christophe. GRACE accelerometer data transplant. *Advances in Space Research*, 64(3): 623–644, 2019. doi:10.1016/j.asr.2019.05.021.
- A. Barnoud, J. Pfeffer, A. Cazenave, R. Fraudeau, V. Rousseau, and M. Ablain. Revisiting the global mean ocean mass budget over 2005–2020. *Ocean Science*, 19(2):321–334, 2023. doi:10.5194/os-19-321-2023.
- B. Barrett, P. Cheiney, B. Battelier, F. Napolitano, and P. Bouyer. Multidimensional atom optics and interferometry. *Physical Review Letters*, 122(4):043604, 2019. doi:10.1103/PhysRevLett.122.043604.

- O. Baur and E. W. Grafarend. High-performance GOCE gravity field recovery from gravity gradient tensor invariants and kinematic orbit information. *Observation of the earth system from space*, pages 239–253, 2006. doi:10.1007/3-540-29522-4_17.
- S. Behzadpour, T. Mayer-Gürr, and S. Krauss. GRACE Follow-On accelerometer data recovery. *Journal of Geophysical Research: Solid Earth*, 126(5): e2020JB021297, 2021. doi:10.1029/2020JB021297.
- P. L. Bender, J. L. Hall, J. Ye, et al. Satellite-satellite laser links for future gravity missions. *Space Science Reviews*, 108:377–384, 2003. doi:10.1023/A:1026195913558.
- P. L. Bender, D. N. Wiese, and R. S. Nerem. A possible dual-GRACE mission with 90 degree and 63 degree inclination orbits. In *Proceedings of the 3rd International Symposium on Formation Flying, Missions and Technologies. European Space Agency Symposium Proceedings, SP-654 jILA Pub*, volume 8161, pages 1665–1669, 2008.
- M. Bloßfeld, M. Gerstl, U. Hugentobler, D. Angermann, and H. Müller. Systematic effects in LOD from SLR observations. *Advances in Space Research*, 54(6): 1049–1063, 2014. doi:10.1016/j.asr.2014.06.009.
- D. Bortoluzzi, D. Vignotto, A. Zambotti, M. Armano, H. Audley, J. Baird, P. Binetruy, M. Born, E. Castelli, A. Cavalleri, et al. In-flight testing of the injection of the LISA Pathfinder test mass into a geodesic. *Advances in Space Research*, 67(1):504–520, 2021. doi:10.1016/j.asr.2020.09.009.
- D. Boulanger, B. Christophe, M. Rodrigues, F. Liorzou, V. Lebat, M. Dalin, and P.-A. Huynh. Future electrostatic accelerometer without polarization wire. European Geosciences Union, 2020.
- J. Bouman, R. Koop, C. Tscherning, and P. Visser. Calibration of GOCE SGG data using high–low SST, terrestrial gravity data and global gravity field models. *Journal of Geodesy*, 78:124–137, 2004. doi:10.1007/s00190-004-0382-5.
- B. Bowman, W. K. Tobiska, F. Marcos, C. Huang, C. Lin, and W. Burke. A new empirical thermospheric density model JB2008 using new solar and geomagnetic indices. In *AIAA/AAS astrodynamics specialist conference and exhibit*, page 6438, 2008. doi:10.2514/6.2008-6438.
- S. Bruinsma, D. Tamagnan, and R. Biancale. Atmospheric densities derived from CHAMP/STAR accelerometer observations. *Planetary and Space Science*, 52(4):297–312, 2004. ISSN 00320633. doi:10.1016/j.pss.2003.11.004.
- S. L. Bruinsma, C. Förste, O. Abrikosov, J.-M. Lemoine, J.-C. Marty, S. Mulet, M.-H. Rio, and S. Bonvalot. ESA’s satellite-only gravity field model via the direct approach based on all GOCE data. *Geophysical Research Letters*, 41(21):7508–7514, 2014. ISSN 0094-8276. doi:10.1002/2014GL062045.
- E. Canuto. Drag-free and attitude control for the GOCE satellite. *Automatica*, 44(7):1766–1780, 2008. doi:10.1016/j.automatica.2007.11.023.

- L. Carbone, A. Cavalleri, G. Ciani, R. Dolesi, M. Hueller, D. Tombolato, S. Vitale, and W. J. Weber. Thermal gradient-induced forces on geodesic reference masses for LISA. *Physical Review D*, 76(10):102003, 2007. doi:10.1103/PhysRevD.76.102003.
- K. Case, G. Kruizinga, and S. Wu. GRACE level 1B data product user handbook. *JPL Publication D-22027*, 2010.
- S. Cesare. Performance requirements and budgets for the gradiometric mission. *Technical Note*, 4, 2002.
- J. Chen, B. Tapley, C. Wilson, A. Cazenave, K.-W. Seo, and J.-S. Kim. Global ocean mass change from GRACE and GRACE Follow-On and altimeter and Argo measurements. *Geophysical Research Letters*, 47(22), 2020. ISSN 0094-8276. doi:10.1029/2020GL090656.
- J. Chen, A. Cazenave, C. Dahle, W. Llovel, I. Panet, J. Pfeffer, and L. Moreira. Applications and challenges of GRACE and GRACE Follow-On satellite gravimetry. *Surveys in Geophysics*, 43(1):305–345, 2022. ISSN 0169-3298. doi:10.1007/s10712-021-09685-x.
- B. Christophe, D. Boulanger, B. Foulon, P.-A. Huynh, V. Lebat, F. Liorzou, and E. Perrot. A new generation of ultra-sensitive electrostatic accelerometers for GRACE Follow-On and towards the next generation gravity missions. *Acta Astronautica*, 117:1–7, Dec 2015. ISSN 00945765. doi:10.1016/j.actaastro.2015.06.021.
- B. Christophe, B. Foulon, F. Liorzou, V. Lebat, D. Boulanger, P.-A. Huynh, N. Zahzam, Y. Bidel, and A. Bresson. Status of development of the future accelerometers for next generation gravity missions. In *International Symposium on Advancing Geodesy in a Changing World: Proceedings of the IAG Scientific Assembly, Kobe, Japan, July 30–August 4, 2017*, pages 85–89. Springer, 2018. doi:10.1007/1345_2018_42.
- B. Christophe, F. Liorzou, V. Lebat, D. Boulanger, M. Dalin, E. Hardy, N. Zahzam, A. Bresson, and Y. Bidel. ONERA accelerometers for future gravity mission. In *AGU Fall Meeting Abstracts*, volume 2019, pages G51B–0594, 2019.
- E. Ciraci, I. Velicogna, and S. Swenson. Continuity of the mass loss of the world’s glaciers and ice caps from the GRACE and GRACE Follow-On missions. *Geophysical Research Letters*, 47(9), 2020. ISSN 0094-8276. doi:10.1029/2019GL086926.
- O. L. Colombo. *Numerical methods for harmonic analysis on the sphere*. Department of Geodetic Science, The Ohio State University, 1981. ISBN 978 90 6132 230 6.
- C. Dahle, F. Flechtner, C. Gruber, D. König, R. König, G. Michalak, and K.-H. Neumayer. GFZ RL05: an improved time-series of monthly GRACE gravity field solutions. In *Observation of the System Earth from Space-CHAMP*,

- GRACE, GOCE and future missions: GEOTECHNOLOGIEN Science Report No. 20*, pages 29–39. Springer, 2014. doi:10.1007/978-3-642-32135-1_4.
- C. Dahle, M. Murböck, F. Flechtner, H. Dobslaw, G. Michalak, K. Neumayer, O. Abrykosov, A. Reinhold, R. König, R. Sulzbach, and C. Förste. The GFZ GRACE RL06 Monthly Gravity Field Time Series: Processing Details and Quality Assessment. *Remote Sensing*, 11(18):2116, 2019. doi:10.3390/rs11182116.
- M. Dalin, V. Lebat, D. Boulanger, F. Liorzou, B. Christophe, M. Rodrigues, and P.-A. Huynh. ONERA accelerometers for future gravity mission. In *EGU General Assembly Conference Abstracts*, page 5721, 2020. doi:10.5194/egusphere-egu2020-5721.
- I. Daras and R. Pail. Treatment of temporal aliasing effects in the context of next generation satellite gravimetry missions. *Journal of Geophysical Research: Solid Earth*, 122(9):7343–7362, 2017. doi:10.1002/2017JB014250.
- I. Daras, G. March, R. Pail, C. Hughes, C. Braitenberg, A. Güntner, A. Eicker, B. Wouters, B. Heller-Kaikov, T. Pivetta, and A. Pastorutti. Mass-change And Geosciences International Constellation (MAGIC) expected impact on science and applications. *Geophysical Journal International*, 236(3):1288–1308, 2023. doi:10.1093/gji/ggad472.
- N. Darbeheshti, F. Wöske, M. Weigelt, H. Wu, and C. McCullough. Comparison of Spacewise and Timewise Methods for GRACE Gravity Field Recovery. *Geodetic Time Series Analysis in Earth Sciences*, pages 279–315, 2020. doi:10.1007/978-3-030-21718-1_10.
- A. Dávila Álvarez, A. Knudtson, U. Patel, J. Gleason, H. Hollis, J. Sanjuan, N. Doughty, G. McDaniel, J. Lee, J. Leitch, et al. A simplified gravitational reference sensor for satellite geodesy. *Journal of Geodesy*, 96(10):70, 2022. doi:10.1007/s00190-022-01659-0.
- J. G. de Teixeira da Encarnacao. Next-generation satellite gravimetry for measuring mass transport in the Earth system. PhD thesis, 2015. doi:10.4233/uuid:d0c61fd2-804b-4827-ae8a-e0e93d282a56.
- S. Dionisio, A. Anselmi, L. Bonino, S. Cesare, L. Massotti, and P. Silvestrin. The “Next Generation Gravity Mission”: challenges and consolidation of the system concepts and technological innovations. In *2018 SpaceOps Conference*, page 2495, 2018.
- P. Ditmar, J. Kusche, and R. Klees. Computation of spherical harmonic coefficients from gravity gradiometry data to be acquired by the GOCE satellite: regularization issues. *Journal of Geodesy*, 77:465–477, 2003. doi:10.1007/s00190-003-0349-y.
- DLR. GRACE-C – German-US-American environmental mission has been extended, 2024. URL <https://www.dlr.de/en/latest/news/2024/grace-c->

- german-us-american-environmental-mission-has-been-extended. Last accessed: 05.04.2024.
- H. Dobsław, I. Bergmann-Wolf, R. Dill, E. Forootan, V. Klemann, J. Kusche, and I. Sasgen. The updated ESA Earth System Model for future gravity mission simulation studies. *Journal of Geodesy*, 89:505–513, 2015. doi:10.1007/s00190-014-0787-8.
- H. Dobsław, I. Bergmann-Wolf, E. Forootan, C. Dahle, T. Mayer-Gürr, J. Kusche, and F. Flechtner. Modeling of present-day atmosphere and ocean non-tidal de-aliasing errors for future gravity mission simulations. *Journal of geodesy*, 90:423–436, 2016. doi:10.1007/s00190-015-0884-3.
- H. Dobsław, I. Bergmann-Wolf, R. Dill, L. Poropat, M. Thomas, C. Dahle, S. Esselborn, R. König, and F. Flechtner. A new high-resolution model of non-tidal atmosphere and ocean mass variability for de-aliasing of satellite gravity observations: AOD1B RL06. *Geophysical Journal International*, 211(1):263–269, 2017. ISSN 0956-540X. doi:10.1093/gji/ggx302.
- D. R. Doelling, N. G. Loeb, D. F. Keyes, M. L. Nordeen, D. Morstad, C. Nguyen, B. A. Wielicki, D. F. Young, and M. Sun. Geostationary enhanced temporal interpolation for CERES flux products. *Journal of Atmospheric and Oceanic Technology*, 30(6):1072–1090, 2013. doi:10.1175/JTECH-D-12-00136.1.
- D. R. Doelling, M. Sun, M. L. Nordeen, C. O. Haney, D. F. Keyes, P. E. Mlynarczyk, et al. Advances in geostationary-derived longwave fluxes for the ceres synoptic (syn1deg) product. *Journal of Atmospheric and Oceanic Technology*, 33(3):503–521, 2016. doi:10.1175/JTECH-D-15-0147.1.
- J. R. Dormand. *Numerical methods for differential equations: a computational approach*. CRC press, 2018. doi:10.1201/9781351075107.
- K. Douch, H. Wu, C. Schubert, J. Müller, and F. P. dos Santos. Simulation-based evaluation of a cold atom interferometry gradiometer concept for gravity field recovery. *Advances in Space Research*, 61(5):1307–1323, 2018. doi:10.1016/j.asr.2017.12.005.
- A. Eicker, L. Jensen, V. Wöhnke, H. Dobsław, A. Kvas, T. Mayer-Gürr, and R. Dill. Daily GRACE satellite data evaluate short-term hydro-meteorological fluxes from global atmospheric reanalyses. *Scientific Reports*, 10(1):4504, 2020. doi:10.1038/s41598-020-61166-0.
- B. Elsaka. *Simulated Satellite Formation Flights for Detecting the Temporal Variations of the Earth’s Gravity Field*. PhD thesis, Technical University of Munich, 2012.
- B. Elsaka, J.-C. Raimondo, P. Brieden, T. Reubelt, J. Kusche, F. Flechtner, S. Iran Pour, N. Sneeuw, and J. Müller. Comparing seven candidate mission configurations for temporal gravity field retrieval through full-scale numerical simulation. *Journal of geodesy*, 88:31–43, 2014. doi:10.1007/s00190-013-0665-9.

- B. Elsaka, K. H. Ilk, and A. Alothman. Mitigation of oceanic tidal aliasing errors in space and time simultaneously using different repeat sub-satellite tracks from pendulum-type gravimetric mission candidate. *Acta geophysica*, 63:301–318, 2015. doi:10.2478/s11600-014-0251-4.
- ESA. Ministers back ESA’s bold ambitions for space with record 17% rise, 2022. URL https://www.esa.int/About_Us/Corporate_news/Ministers_back_ESA_s_bold_ambitions_for_space_with_record_17_rise. Last accessed: 26.11.2023.
- ESTO-NASA. Project Selections for InVEST-23, 2024. URL <https://esto.nasa.gov/project-selections-for-invest-23/>. Last accessed: 13.06.2024.
- European Space Agency. ESA Kicks Off Two New Navigation Missions, 2024. URL https://www.esa.int/Applications/Satellite_navigation/ESA_kicks_off_two_new_navigation_missions. Last accessed: 2024-09-05.
- F. Flechtner, C. Reigber, R. Rummel, and G. Balmino. Satellite gravimetry: a review of its realization. *Surveys in Geophysics*, 42(5):1029–1074, 2021. ISSN 0169-3298. doi:10.1007/s10712-021-09658-0.
- F. M. Flechtner, T. Gruber, A. Güntner, M. Manda, M. Rothacher, T. Schöne, and J. Wickert. *System Earth via geodetic-geophysical space techniques*. Springer Berlin Heidelberg, Berlin, Heidelberg, 2010. ISBN 978-3-642-10227-1. doi:10.1007/978-3-642-10228-8.
- W. M. Folkner, J. G. Williams, D. H. Boggs, R. S. Park, and P. Kuchynka. The planetary and lunar ephemerides DE430 and DE431. *Interplanetary Network Progress Report*, 196(1):42–196, 2014.
- R. Forsberg, A. V. Olesen, H. Yidiz, and C. Tscherning. Polar gravity fields from GOCE and airborne gravity. In *4th International GOCE User Workshop*. European Space Agency, 2011. ISBN 978-92-9092-260-5.
- C. Förste, S. L. Bruinsma, O. Abrikosov, J.-M. Lemoine, J. Marty, F. Flechtner, G. Balmino, F. Barthelmes, and R. Biancale. EIGEN-6C4 The latest combined global gravity field model including GOCE data up to degree and order 2190 of GFZ Potsdam and GRGS Toulouse. *GFZ Data Services*, 10, 2014. doi:10.5880/icgem.2015.1.
- B. Fox-Kemper, H. T. Hewitt, C. Xiao, G. Adalgeirsdottir, S. S. Drijfhout, T. L. Edwards, N. R. Golledge, M. Hemer, R. E. Kopp, G. Krinner, A. Mix, D. Notz, S. Nowicki, I. S. Nurhati, L. Ruiz, J.-B. Sallée, A. B. A. Slangen, and Y. Yu. *Ocean, Cryosphere and Sea Level Change*, pages 1211–1362. Cambridge University Press, 2021. doi:10.1017/9781009157896.011.
- S. P. Francis, D. A. Shaddock, A. J. Sutton, G. De Vine, B. Ware, R. E. Spero, W. M. Klipstein, and K. McKenzie. Tone-assisted time delay interferometry on GRACE Follow-On. *Physical Review D*, 92(1):012005, 2015. doi:10.1103/PhysRevD.92.012005.

- F. Frappart and G. Ramillien. Monitoring groundwater storage changes using the Gravity Recovery and Climate Experiment (GRACE) satellite mission: a Review. *Remote Sensing*, 10(6):829, 2018. doi:10.3390/rs10060829.
- B. Frommknecht, H. Oberndorfer, F. Flechtner, and R. Schmidt. Integrated sensor analysis for GRACE—development and validation. *Advances in Geosciences*, 1:57–63, 2003. doi:10.5194/adgeo-1-57-2003.
- B. Frommknecht, U. Fackler, and J. Flury. Integrated sensor analysis GRACE. *Observation of the Earth system from space*, pages 99–113, 2006. doi:10.1007/3-540-29522-4_8.
- H. Gerdener, J. Kusche, K. Schulze, P. Döll, and A. Klos. The global land water storage data set release 2 (GLWS2. 0) derived via assimilating GRACE and GRACE-FO data into a global hydrological model. *Journal of Geodesy*, 97(7): 73, 2023. doi:10.1007/s00190-023-01763-9.
- M. S. Gockenbach. *Linear inverse problems and Tikhonov regularization*, volume 32. American Mathematical Soc., 2016. ISBN 978-0-88385-141-8.
- S. Goswami, S. P. Francis, T. Bandikova, and R. E. Spero. Analysis of GRACE Follow-On Laser Ranging Interferometer derived inter-satellite pointing angles. *IEEE Sensors Journal*, page 1, 2021. ISSN 1530-437X. doi:10.1109/JSEN.2021.3090790.
- C. Gramling, S. Hur-Diaz, A. Liounis, B. Azimi, M. Romeo, G. Crum, J. Small, N. Stacey, S. Semper, R. Pritchett, and W. Yu. Low SWaP Onboard Satellite Navigation, Guidance, and Control Technology. In *Presentation to Applied Physics Laboratory (APL)*, 2024.
- T. Gruber and M. Willberg. Signal and error assessment of GOCE-based high resolution gravity field models. *Journal of Geodetic Science*, 9(1):71–86, 2019. doi:10.1515/jogs-2019-0008.
- T. Gruber, T. Peters, and L. Zenner. *The Role of the Atmosphere for Satellite Gravity Field Missions*. Springer Berlin Heidelberg, Berlin, Heidelberg, 2009. ISBN 978-3-540-85426-5. doi:10.1007/978-3-540-85426-5_13.
- T. Gruber, J. Bamber, M. Bierkens, H. Dobslaw, M. Murböck, M. Thomas, L. Van Beek, T. van Dam, L. Vermeersen, and P. Visser. Simulation of the time-variable gravity field by means of coupled geophysical models. *Earth System Science Data*, 3(1):19–35, 2011. doi:10.5194/essd-3-19-2011.
- R. Haagmans and L. Tsaoussi. Next generation gravity mission as a Mass-change And Geosciences International Constellation (MAGIC) mission requirements document. *Earth and Mission Science Division, European Space Agency; NASA Earth Science Division*, 2020. doi:10.5270/esa.nasa.magic-mrd.2020.
- R. Haagmans, C. Siemes, L. Massotti, O. Carraz, and P. Silvestrin. ESA’s next-generation gravity mission concepts. *Rendiconti Lincei. Scienze Fisiche e Naturali*, 31, 2020. doi:10.1007/s12210-020-00875-0.

- R. Hackney and W. Featherstone. Geodetic versus geophysical perspectives of the ‘gravity anomaly’. *Geophysical Journal International*, 154(1):35–43, 2002. doi:10.1046/j.1365-246X.2003.01941.x.
- H. Halloin, P. Prat, and J. Brossard. Long term characterization of voltage references. *arXiv preprint arXiv:1312.5101*, 2013. doi:10.48550/arXiv.1312.5101.
- P. C. Hansen. The L-curve and its use in the numerical treatment of inverse problems. 1999.
- M. Hauk and R. Pail. Treatment of ocean tide aliasing in the context of a next generation gravity field mission. *Geophysical Journal International*, 214(1):345–365, 2018. doi:10.1093/gji/ggy145.
- M. Hauk and D. Wiese. New methods for linking science objectives to remote sensing observations: A concept study using single-and dual-pair satellite gravimetry architectures. *Earth and Space Science*, 7(3):e2019EA000922, 2020. doi:10.1029/2019EA000922.
- A. E. Hedin, E. Fleming, A. Manson, F. Schmidlin, S. Avery, R. Clark, S. J. Franke, G. Fraser, T. Tsuda, F. Vial, et al. Empirical wind model for the upper, middle and lower atmosphere. *Journal of atmospheric and terrestrial physics*, 58(13):1421–1447, 1996. doi:10.1016/0021-9169(95)00122-0.
- G. Heinzel, A. Rüdiger, and R. Schilling. Spectrum and spectral density estimation by the Discrete Fourier transform (DFT), including a comprehensive list of window functions and some new at-top windows. *Technical report*, 2002.
- G. Heinzel, C. Braxmaier, R. Schilling, A. Rüdiger, D. Robertson, M. t. Plate, V. Wand, K. Arai, U. Johann, and K. Danzmann. Interferometry for the LISA technology package (LTP) aboard SMART-2. *Classical and Quantum Gravity*, 20(10):S153–S161, May 2003. ISSN 0264-9381, 1361-6382. doi:10.1088/0264-9381/20/10/318.
- W. A. Heiskanen and H. Moritz. Physical geodesy. *Bulletin Géodésique (1946-1975)*, 86(1):491–492, 1967. doi:10.1007/BF02525647.
- B. Heller-Kaikov, R. Pail, and I. Daras. Mission design aspects for the mass change and geoscience international constellation (MAGIC). *Geophysical Journal International*, 235(1):718–735, 2023. doi:10.1093/gji/ggad266.
- E. Hinds. NASA selects UF mission to better track the Earth’s water and ice, 2024. URL <https://news.ufl.edu/2024/05/grattis-mission-chosen-by-nasa/>. Last accessed: 13.06.2024.
- B. Hofmann-Wellenhof and H. Moritz. *Physical Geodesy*. Springer Science & Business Media, 2006. ISBN 978-3-211-33544-4.
- M. Horwath, B. D. Gutknecht, A. Cazenave, H. K. Palanisamy, F. Marti, B. Marzeion, F. Paul, R. Le Bris, A. E. Hogg, I. Otosaka, et al. Global sea-level budget and ocean-mass budget, with a focus on advanced data products and

- uncertainty characterisation. *Earth System Science Data*, 14:411–447, 2022. doi:10.5194/essd-14-411-2022.
- A. HosseiniArani, B. Tennstedt, M. Schilling, A. Knabe, H. Wu, S. Schön, and J. Müller. Kalman-filter based hybridization of classic and cold atom interferometry accelerometers for future satellite gravity missions. 2022. doi:10.1007/1345_2022_172.
- A. HosseiniArani, M. Schilling, Q. Beaufile, A. Knabe, B. Tennstedt, A. Kupriyanov, S. Schön, F. Pereira dos Santos, and J. Müller. Advances in atom interferometry and their impacts on the performance of quantum accelerometers on-board future satellite gravity missions. *Advances in Space Research*, 2024. doi:10.1016/j.asr.2024.06.055.
- V. Huarcaya, G. Apelbaum, V. Haendchen, Q. Wang, G. Heinzl, and M. Mehmet. Five degrees of freedom test mass readout via optical levers. *Classical and Quantum Gravity*, 37(2):025004, Jan 2020. ISSN 0264-9381, 1361-6382. doi:10.1088/1361-6382/ab5c73.
- M. Huckfeldt, F. Wöske, B. Rievers, and M. List. GRACE Follow-On accelerometer data recovery by high-precision environment modelling. *Advances in Space Research*, 73(12):5783–5805, 2024. doi:10.1016/j.asr.2024.03.068.
- V. Humphrey, M. Rodell, and A. Eicker. Using satellite-based terrestrial water storage data: a review. *Surveys in Geophysics*, 44(5):1489–1517, 2023. doi:10.1007/s10712-022-09754-9.
- E. S. Ince, F. Barthelmes, S. Reißland, K. Elger, C. Förste, F. Flechtner, and H. Schuh. ICGEM–15 years of successful collection and distribution of global gravitational models, associated services, and future plans. *Earth System Science Data*, 11(2):647–674, 2019. doi:10.5194/essd-11-647-2019.
- S. Iran Pour, T. Reubelt, N. Sneeuw, I. Daras, M. Murböck, T. Gruber, R. Pail, M. Weigelt, T. van Dam, P. Visser, et al. Assessment of satellite constellations for monitoring the variations in earth gravity field. *SC4MGV, ESA/ESTEC Contract No. AO/1-7317/12/NL/AF*, 2015.
- S. Iran Pour, N. Sneeuw, M. Weigelt, and A. Amiri-Simkooei. Orbit optimization for future satellite gravity field missions: Influence of the time variable gravity field models in a genetic algorithm approach. In *IX Hotine-Marussi Symposium on Mathematical Geodesy: Proceedings of the Symposium in Rome, June 18–22, 2018*, pages 3–9. Springer, 2021.
- A. Jäggi and D. Arnold. Precise orbit determination. *Global Gravity Field Modeling from Satellite-to-Satellite Tracking Data*, pages 35–80, 2017. doi:10.1007/978-3-319-49941-3_2.
- K. H. Jones and J. N. Gross. Reducing size, weight, and power (SWaP) of perception systems in small autonomous aerial systems. *14th AIAA Aviation Technology, Integration, and Operations Conference*, page 2705, 2014. doi:10.2514/6.2014-2705.

- V. Josselin, P. Touboul, and R. Kielbasa. Capacitive detection scheme for space accelerometers applications. *Sensors and Actuators A: Physical*, 78(2-3):92–98, 1999. ISSN 09244247. doi:10.1016/S0924-4247(99)00227-7.
- JPL-NASA. GRACE-FO 3D Model, 2024. URL <https://gracefo.jpl.nasa.gov/resources/86/grace-fo-3d-model/>. Last accessed: 01.08.2024.
- K. Kang, S. Zhong, A. Geruo, and W. Mao. The effects of non-newtonian rheology in the upper mantle on relative sea level change and geodetic observables induced by glacial isostatic adjustment process. *Geophysical Journal International*, 228(3):1887–1906, 2022. doi:10.1093/gji/ggab428.
- Z. Kassas, M. Neinavaie, J. Khalife, N. Khairallah, S. Kozhaya, J. Haidar-Ahmad, and Z. Shadram. Enter LEO on the GNSS stage: Navigation with Starlink satellites. *InsideGNSS*, 2021.
- W. M. Kaula. *Theory of satellite geodesy: applications of satellites to geodesy*. Courier Corporation, 2000. ISBN 978-0-486-41465-2.
- J. Kim and S. W. Lee. Flight performance analysis of GRACE K-band ranging instrument with simulation data. *Acta Astronautica*, 65(11-12):1571–1581, 2009. doi:10.1016/j.actaastro.2009.04.010.
- R. W. Kingsbury, T. Nguyen, K. Riesing, and K. Cahoy. Fast-steering solutions for cubesat-scale optical communications. *International Conference on Space Optics—ICSO 2014*, 10563:124–130, 2017. doi:10.1117/12.2304229.
- R. Klees, R. Koop, P. Visser, and J. Van den Ijssel. Efficient gravity field recovery from GOCE gravity gradient observations. *Journal of geodesy*, 74:561–571, 2000. doi:10.1007/s001900000118.
- B. Klinger and T. Mayer-Gürr. The role of accelerometer data calibration within GRACE gravity field recovery: Results from ITSG-Grace2016. *Advances in Space Research*, 58(9):1597–1609, 2016. doi:10.1016/j.asr.2016.08.007.
- A. Knabe. *New concepts for gravity field recovery using satellites*. PhD thesis, Wissenschaftliche Arbeiten der Fachrichtung Geodäsie und Geoinformatik der Leibniz Universität Hannover; ISSN 0174-1454, Nr. 391, 2023.
- A. Knabe, M. Schilling, H. Wu, A. HosseiniArani, J. Müller, Q. Beaufils, and F. P. d. Santos. The benefit of accelerometers based on cold atom interferometry for future satellite gravity missions. International Association of Geodesy Symposia. Springer Berlin Heidelberg, Berlin, Heidelberg, 2022. doi:10.1007/1345_2022_151.
- K. Koch, H. Kuhlmann, and W.-D. Schuh. Approximating covariance matrices estimated in multivariate models by estimated auto-and cross-covariances. *Journal of geodesy*, 84:383–397, 2010. doi:10.1007/s00190-010-0375-5.
- K.-R. Koch and J. Kusche. Regularization of geopotential determination from satellite data by variance components. *Journal of Geodesy*, 76:259–268, 2002. doi:10.1007/s00190-002-0245-x.

- R. Koop. Global gravity field modelling using satellite gravity gradiometry. 1993.
- R. Koop, P. Visser, and C. Tscherning. Aspects of GOCE calibration. In *International GOCE user workshop*, volume 188, 2001.
- R. P. Kornfeld, B. W. Arnold, M. A. Gross, N. T. Dahya, W. M. Klipstein, P. F. Gath, and S. Bettadpur. GRACE-FO: The Gravity Recovery and Climate Experiment Follow-On Mission. *Journal of Spacecraft and Rockets*, 56(3):931–951, 2019. ISSN 0022-4650. doi:10.2514/1.A34326.
- A. Kupriyanov, A. Reis, A. Knabe, N. Fletling, A. HosseiniArani, M. Romeshkani, M. Schilling, V. Müller, and J. Müller. Analysis of novel sensors and satellite formation flights for future gravimetry missions. *International Association of Geodesy Symposia*, 2024a. doi:10.1007/1345_2024_279.
- A. Kupriyanov, A. Reis, M. Schilling, V. Müller, and J. Müller. Benefit of enhanced electrostatic and optical accelerometry for future gravimetry missions. *Advances in Space Research*, 73, 2024b. doi:10.1016/j.asr.2023.12.067.
- J. Kusche and T. Mayer-Gürr. On the iterative solution of ill-conditioned normal equations by the use of lanczos methods. In *Vistas for Geodesy in the New Millennium: IAG 2001 Scientific Assembly, Budapest, Hungary September 2–7, 2001*, pages 248–252. Springer, 2002. doi:10.1007/978-3-662-04709-5_41.
- A. Kvas, S. Behzadpour, M. Ellmer, B. Klinger, S. Strasser, N. Zehentner, and T. Mayer-Gürr. ITSG–Grace2018: overview and evaluation of a new GRACE–only gravity field time series. *Journal of Geophysical Research: Solid Earth*, 124(8):9332–9344, 2019. ISSN 21699313. doi:10.1029/2019JB017415.
- A. Kvas, E. Boergens, H. Dobslaw, A. Eicker, T. Mayer-Guerr, and A. Güntner. Evaluating long-term water storage trends in small catchments and aquifers from a joint inversion of 20 years of GRACE/GRACE-FO mission data. *Geophysical Journal International*, 236(2):1002–1012, 2024. doi:10.1093/gji/ggad468.
- F. W. Landerer, F. M. Flechtner, H. Save, F. H. Webb, T. Bandikova, W. I. Bertiger, S. V. Bettadpur, S. H. Byun, C. Dahle, H. Dobslaw, et al. Extending the global mass change data record: GRACE Follow-On instrument and science data performance. *Geophysical Research Letters*, 47(12):e2020GL088306, 2020. doi:10.1029/2020GL088306.
- Latvian Space Office. Welcome IRIS²: EU’s new communication satellite infrastructure. <https://latviaspace.gov.lv/en/news-events/welcome-iris-eus-new-communication-satellite-infrastructure/>, 2024. Last accessed: 2024-09-05.
- A. Leipner, A. Kupriyanov, A. Reis, A. Knabe, M. Schilling, V. Müller, M. Weigelt, J. Müller, and M. List. Evaluation of deployable solar panels on GRACE-like satellites by closed-loop simulations. *Journal of Geodesy*, (under revision, 2nd round), 2025. doi:10.48550/arXiv.2503.21651.

- T. Lévêque, C. Fallet, J. Lefebve, et al. CARIOQA: Definition of a quantum pathfinder mission. 12777:1536–1545, 2023. doi:10.1117/12.2690536.
- W. Liang, R. Pail, X. Xu, and J. Li. A new method of improving global geopotential models regionally using GNSS/levelling data. *Geophysical journal international*, 221(1):542–549, 2020. doi:10.1093/gji/ggaa047.
- F. Liorzou, V. Lebat, B. Christophe, et al. ONERA accelerometers for future gravity mission. 2023. doi:10.5194/egusphere-egu23-8155.
- Y. Liu, J. Li, X. Xu, H. Wei, Z. Li, and Y. Zhao. Simulation analysis of recovering time-varying gravity fields based on Starlink-like constellation. *Geophysical Journal International*, 239(1):402–418, 2024. doi:10.1093/gji/ggae273.
- B. Loomis, S. Luthcke, and T. Sabaka. Regularization and error characterization of GRACE mascons. *Journal of geodesy*, 93(9):1381–1398, 2019. doi:10.1007/s00190-019-01252-y.
- J. Lotters, W. Olthuis, P. Veltink, and P. Bergveld. A sensitive differential capacitance to voltage converter for sensor applications. *IEEE Transactions on Instrumentation and Measurement*, 48(1):89–96, 1999. doi:10.1109/19.755066.
- B. Lu, C. Förste, F. Barthelmes, S. Petrovic, F. Flechtner, Z. Luo, B. Zhong, H. Zhou, X. Wang, and T. Wu. Using real polar ground gravimetry data to solve the GOCE polar gap problem in satellite-only gravity field recovery. *Journal of Geodesy*, 94:1–12, 2020. doi:10.1007/s00190-020-01361-z.
- S. B. Luthcke, T. Sabaka, B. Loomis, A. Arendt, J. McCarthy, and J. Camp. Antarctica, Greenland and Gulf of Alaska land-ice evolution from an iterated GRACE global mascon solution. *Journal of Glaciology*, 59(216):613–631, 2013. doi:10.3189/2013JoG12J147.
- F. H. Lyard, D. J. Allain, M. Cancet, L. Carrère, and N. Picot. FES2014 global ocean tide atlas: design and performance. *Ocean Science*, 17(3):615–649, 2021. doi:10.5194/os-17-615-2021.
- D. Mance. *Development of electronic system for sensing and actuation of test mass of the inertial sensor LISA*. PhD thesis, Faculty of Electrical Engineering, Mechanical Engineering and Naval Architecture, University of Split, 2012.
- K. Maquaire, N. Portier, B. Christophe, J. Barge, and M. Rodrigues. Studies of the thermal bias of electrostatic accelerometers. Feedback from MICROSCOPE. In *ESA-NASA MAGIC Workshop*, 2023.
- J.-P. Marque, B. Christophe, and B. Foulon. Accelerometers of the GOCE mission: return of experience from one year of in-orbit. In *Proceedings of the ESA Living Planet Symposium, 28.06 - 02.07.2010, Bergen, Norway*, 2010. ISBN 978-92-9221-250-6.
- L. Massotti, C. Siemes, G. March, R. Haagmans, and P. Silvestrin. Next Generation Gravity Mission elements of the Mass Change and Geoscience International

- Constellation: from orbit selection to instrument and mission design. *Remote Sensing*, 13(19):3935, 2021. doi:10.3390/rs13193935.
- T. Mayer-Gürr, R. Savcenko, W. Bosch, I. Daras, F. Flechtner, and C. Dahle. Ocean tides from satellite altimetry and GRACE. *Journal of geodynamics*, 59: 28–38, 2012. doi:10.1016/j.jog.2011.10.009.
- T. Mayer-Gürr, S. Behzadpour, A. Eicker, M. Ellmer, B. Koch, S. Krauss, C. Pock, D. Rieser, S. Strasser, B. Süsser-Rechberger, et al. GROOPS: A software toolkit for gravity field recovery and GNSS processing. *Computers & geosciences*, 155:104864, 2021. doi:10.1016/j.cageo.2021.104864.
- P. M. Mehta, A. C. Walker, E. K. Sutton, and H. C. Godinez. New density estimates derived using accelerometers on board the CHAMP and GRACE satellites. *Space Weather*, 15(4):558–576, 2017. doi:10.1002/2016SW001562.
- B. Metzler and R. Pail. GOCE data processing: the spherical cap regularization approach. *Studia Geophysica et Geodaetica*, 49:441–462, 2005. doi:10.1007/s11200-005-0021-5.
- F. Migliaccio, M. Reguzzoni, K. Batsukh, G. M. Tino, G. Rosi, F. Sorrentino, C. Braitenberg, T. Pivetta, D. F. Barbolla, and S. Zoffoli. MOCASS: A satellite mission concept using cold atom interferometry for measuring the Earth gravity field. *Surveys in Geophysics*, 40(5):1029–1053, 2019. doi:10.1007/s10712-019-09566-4.
- A. L. Miller and L. Mendes. First search for ultralight dark matter with a space-based gravitational-wave antenna: LISA Pathfinder. *Physical Review D*, 107(6):063015, 2023. doi:10.1103/PhysRevD.107.063015.
- O. Montenbruck, E. Gill, and F. Lutze. Satellite orbits: models, methods, and applications. *Appl. Mech. Rev.*, 55(2):B27–B28, 2002. doi:10.1115/1.1451162.
- H. Moritz. Advanced physical geodesy. *Advances in Planetary Geology*, 1980.
- V. Müller, M. Hauk, M. Misfeldt, L. Müller, H. Wegener, Y. Yan, and G. Heinzel. Comparing GRACE-FO KBR and LRI ranging data with focus on carrier frequency variations. *Remote Sensing*, 14(17):4335, 2022. doi:10.3390/rs14174335.
- M. Murböck, R. Pail, I. Daras, and T. Gruber. Optimal orbits for temporal gravity recovery regarding temporal aliasing. *Journal of Geodesy*, 88:113–126, 2014. doi:10.1007/s00190-013-0671-y.
- NASA. *GRACE Launch. Press Kit*. National Aeronautics and Space Administration, Washington, DC, 2002.
- National Academies of Sciences, Engineering, and Medicine. *Thriving on Our Changing Planet: A Decadal Strategy for Earth Observation from Space*. The National Academies Press, Washington, DC, 2018. ISBN 978-0-309-46757-5. doi:10.17226/24938.
- T. NGGM-D Team, T. Gruber, M. Murböck, M. Baldesarra, P. Brieden, K. Danzmann, B. Daras, B. Doll, D. Feili, F. Flechtner, et al. e2. motion-Earth System

- Mass Transport Mission (Square)-Concept for a Next Generation Gravity Field Mission-Final Report of Project "Satellite Gravimetry of the Next Generation (NGGM-D)". *Geodätische Kommission bei der Bayerischen Akademie der Wissenschaften Reihe B, Angewandte Geodäsie*. München: Verlag der Bayerischen Akademie der Wissenschaften and in Kommission beim Verlag C.H. Beck., 318, 2014.
- W. Niemeier. *Ausgleichsrechnung: Statistische Auswertemethoden*. Walter de Gruyter GmbH Co. KG, 10785 Berlin, 2008. ISBN 978-3-11-019055-7.
- NOAA. National centers for environmental information. *National Centers for Environmental Information (NOAA), Solar-Terrestrial Physics (STP), Space Weather*, 2024.
- H. Oberndorfer. Integrierte Sensoranalyse am Beispiel des Satelliten CHAMP. Technical report, Tech. Rep. Mu 1141/2-1, Institut für Physikalische und Astronomische Geodäsie, TU München, 2000.
- I. N. Otosaka, A. Shepherd, E. R. Ivins, N.-J. Schlegel, C. Amory, M. van den Broeke, M. Horwath, I. Joughin, M. King, G. Krinner, et al. Mass balance of the Greenland and Antarctic ice sheets from 1992 to 2020. *Earth System Science Data Discussions*, 2022:1–33, 2022. doi:10.5194/essd-15-1597-2023.
- R. Pail. Global gravity field model derived from orbit and gradiometry data applying the time-wise method. In *ESA Living Planet Symposium 2010, Bergen, Norway, June 27-July 2*, 2010.
- R. Pail and G. Plank. Assessment of three numerical solution strategies for gravity field recovery from GOCE satellite gravity gradiometry implemented on a parallel platform. *Journal of Geodesy*, 76:462–474, 2002. doi:10.1007/s00190-002-0277-2.
- R. Pail, R. Bingham, C. Braitenberg, H. Dobsław, A. Eicker, A. Güntner, M. Horwath, E. Ivins, L. Longuevergne, I. Panet, et al. Science and user needs for observing global mass transport to understand global change and to benefit society. *Surveys in Geophysics*, 36(6):743–772, 2015. ISSN 0169-3298. doi:10.1007/s10712-015-9348-9.
- R. Pail, J. Bamber, R. Biancale, R. Bingham, C. Braitenberg, A. Eicker, F. Flechtner, T. Gruber, A. Güntner, G. Heinzl, et al. Mass variation observing system by high low inter-satellite links (MOBILE)—a new concept for sustained observation of mass transport from space. *Journal of Geodetic Science*, 9(1):48–58, 2019. doi:10.1515/jogs-2019-0006.
- R. Pail, P. Abrykosov, F. Flechtner, S. Bruinsma, P. Visser, A. Güntner, and V. Müller. Extended numerical simulation studies for a Mass change And Geosciences International Constellation (MAGIC). In *XXVIII General Assembly of the International Union of Geodesy and Geophysics (IUGG)*. GFZ German Research Centre for Geosciences, 2023. doi:10.57757/IUGG23-0604.
- I. Panet, C. Narteau, J.-M. Lemoine, S. Bonvalot, and D. Remy. Detecting

- preseismic signals in GRACE gravity solutions: application to the 2011 Tohoku M w 9.0 earthquake. *Journal of Geophysical Research: Solid Earth*, 127(8), 2022. ISSN 2169-9313. doi:10.1029/2022JB024542.
- A. Peidou and S. Pagiatakis. Stripe mystery in GRACE geopotential models revealed. *Geophysical Research Letters*, 47(4):e2019GL085497, 2020. doi:10.1029/2019GL085497.
- A. Peidou, F. Landerer, D. Wiese, M. Ellmer, E. Fahnestock, C. McCullough, R. Spero, and D.-N. Yuan. Spatiotemporal characterization of geophysical signal detection capabilities of GRACE-FO. *Geophysical Research Letters*, 49(1), 2022. ISSN 0094-8276. doi:10.1029/2021GL095157.
- G. Petit and B. Luzum. The 2010 reference edition of the IERS conventions. In *Reference frames for applications in geosciences*, pages 57–61. Springer, 2013. doi:10.1007/978-3-642-32998-2_10.
- N. Pfaffenzeller and R. Pail. Small satellite formations and constellations for observing sub-daily mass changes in the earth system. *Geophysical Journal International*, 234(3):1550–1567, 2023. doi:10.1093/gji/ggad132.
- A. F. Purkhauser and R. Pail. Triple-pair constellation configurations for temporal gravity field retrieval. *Remote Sensing*, 12(5):831, 2020. doi:10.3390/rs12050831.
- A. F. Purkhauser, C. Siemes, and R. Pail. Consistent quantification of the impact of key mission design parameters on the performance of next-generation gravity missions. *Geophysical Journal International*, 221(2):1190–1210, 2020. doi:10.1093/gji/ggaa070.
- C. Reigber, G. Balmino, P. Schwintzer, R. Biancale, A. Bode, J.-M. Lemoine, R. König, S. Loyer, H. Neumayer, J.-C. Marty, F. Barthelmes, F. Perosanz, and S. Y. Zhu. A high-quality global gravity field model from CHAMP GPS tracking data and accelerometry (EIGEN-1S). *Geophysical Research Letters*, 29(14):37-1–37-4, 2002. ISSN 0094-8276. doi:10.1029/2002GL015064.
- C. Reigber, H. Lühr, P. Schwintzer, and J. Wickert. Earth observation with CHAMP. *Results from three years*, 2005.
- C. Reigber, H. Lühr, L. Grunwaldt, C. Förste, R. König, H. Massmann, and C. Falck. CHAMP mission 5 years in orbit. *Observation of the Earth system from space*, pages 3–15, 2006. doi:10.1007/3-540-29522-4_1.
- A. Reis, A. Kupriyanov, and V. Müller. A Tool for accelerometer modeling. In *EGU General Assembly Conference Abstracts*, 2022a. doi:10.5194/egusphere-egu22-1168.
- A. Reis, A. Kupriyanov, and V. Müller. A framework for modeling and simulating accelerometers. In *COSPAR 44th Scientific Assembly*, 2022b.
- A. Reis, A. Kupriyanov, V. Müller, J. Müller, and M. Schilling. Modeling and simulating of accelerometers and gradiometers concepts. In *XXVIII General*

-
- Assembly of the International Union of Geodesy and Geophysics (IUGG)*, 2023. doi:10.57757/IUGG23-0583.
- T. Reubelt, N. Sneeuw, and S. Iran-Pour. Quick-look gravity field analysis of formation scenarios selection. *GEOTECHNOLOGIEN Science Report*, 17:126–133, 2010.
- S. Rispens and J. Bouman. Calibrating the GOCE accelerations with star sensor data and a global gravity field model. *Journal of Geodesy*, 83:737–749, 2009. doi:10.1007/s00190-008-0290-1.
- M. Rodell and J. T. Reager. Water cycle science enabled by the GRACE and GRACE-FO satellite missions. *Nature Water*, 1(1):47–59, 2023. doi:10.1038/s44221-022-00005-0.
- M. Rodell, J. S. Famiglietti, D. N. Wiese, J. T. Reager, H. K. Beaudoin, F. W. Landerer, and M.-H. Lo. Emerging trends in global freshwater availability. *Nature*, 557(7707):651–659, 2018. doi:10.1038/s41586-018-0123-1.
- M. Rodrigues, J. Bergé, D. Boulanger, B. Christophe, M. Dalin, V. Lebat, and F. Liorzou. Space accelerometers for micro and nanosatellites: Fundamental Physics and Geodesy missions from MICROSCOPE, GOCE and GFO return of experience. In *4S symposium 2022*, 2022.
- M. Romanazzo, C. Steiger, G. Sechi, M. Saponara, M. Rezazad, A. Piris Niño, A. Da Costa, M. Fehringer, R. Floberghagen, G. André, et al. In-orbit experience with the drag-free attitude and orbit control system of ESA’s gravity Mission GOCE. In *8th International ESA Conference on Guidance, Navigation & Control Systems*, pages 5–10, 2011.
- K. Roy and W. Peltier. GRACE era secular trends in Earth rotation parameters: A global scale impact of the global warming process? *Geophysical Research Letters*, 38(10), 2011. doi:10.1029/2011GL047282.
- R. Rummel. Spherical spectral properties of the Earth’s gravitational potential and its first and second derivatives. *Geodetic Boundary Value Problems in View of the One Centimeter Geoid*, pages 359–404, 2005. doi:10.1007/BFb0011710.
- R. Rummel, W. Yi, and C. Stummer. GOCE gravitational gradiometry. *Journal of Geodesy*, 85(11):777–790, 2011. doi:10.1007/s00190-011-0500-0.
- R. Savcenko and W. Bosch. EOT11a-empirical ocean tide model from multi-mission satellite altimetry. *DGFI Report No. 89*, 2012. doi:10.1594/PANGAEA.834232.
- D. Savoie, M. Altorio, B. Fang, et al. Interleaved atom interferometry for high-sensitivity inertial measurements. *Science advances*, 4(12):eaau7948, 2018. doi:10.1126/sciadv.aau7948.
- E. J. Schrama, B. Wouters, and D. A. Lavallée. Signal and noise in Gravity Recovery and Climate Experiment (GRACE) observed surface mass

- variations. *Journal of Geophysical Research: Solid Earth*, 112(B8), 2007. doi:10.1029/2006JB004882.
- W.-D. Schuh. *Tailored numerical solution strategies for the global determination of the Earth's gravity field*. na, 1996.
- G. Sechi, M. Buonocore, F. Cometto, M. Saponara, A. Tramutola, B. Vinai, G. Andrè, and M. Fehringner. In-flight results from the drag-free and attitude control of GOCE satellite. *IFAC Proceedings Volumes*, 44(1):733–740, 2011. doi:10.3182/20110828-6-IT-1002.02966.
- L. F. Shampine. Computer solution of ordinary differential equations. *The initial value problem*, 1975.
- B. Sheard, G. Heinzel, K. Danzmann, D. Shaddock, W. Klipstein, and W. Folkner. Intersatellite laser ranging instrument for the GRACE Follow-On mission. *Journal of Geodesy*, 86:1083–1095, 2012. doi:10.1007/s00190-012-0566-3.
- L. Shihora, K. Balidakis, R. Dill, C. Dahle, K. Ghobadi-Far, J. Bonin, and H. Dobslaw. Non-tidal background modeling for satellite gravimetry based on operational ECWMF and ERA5 reanalysis data: AOD1B RL07. *Journal of Geophysical Research: Solid Earth*, 127(8), 2022. ISSN 2169-9313. doi:10.1029/2022JB024360.
- L. Shihora, K. Balidakis, R. Dill, and H. Dobslaw. Assessing the stability of AOD1B atmosphere–ocean non-tidal background modelling for climate applications of satellite gravity data: long-term trends and 3-hourly tendencies. *Geophysical Journal International*, 234(2):1063–1072, 2023. doi:10.1093/gji/ggad119.
- L. Shihora, Z. Liu, K. Balidakis, J. Wilms, C. Dahle, F. Flechtner, R. Dill, and H. Dobslaw. Accounting for residual errors in atmosphere–ocean background models applied in satellite gravimetry. *Journal of Geodesy*, 98(4):27, 2024. doi:10.1007/s00190-024-01832-7.
- Y. Shimizu, Y. Kudo, Y.-L. Chen, S. Ito, and W. Gao. An optical lever by using a mode-locked laser for angle measurement. *Precision Engineering*, 47:72–80, 2017. doi:10.1016/j.precisioneng.2016.07.006.
- C. Siemes. *Digital filtering algorithms for decorrelation within large least squares problems*. PhD thesis, 2008.
- C. Siemes. Improving GOCE cross-track gravity gradients. *Journal of Geodesy*, 92:33–45, 2017. doi:10.1007/s00190-017-1042-x.
- C. Siemes, R. Haagmans, M. Kern, G. Plank, and R. Floberghagen. Monitoring GOCE gradiometer calibration parameters using accelerometer and star sensor data: methodology and first results. *Journal of Geodesy*, 86:629–645, 2012. doi:10.1007/s00190-012-0545-8.

- C. Siemes, P. Ditmar, R. Riva, D. Slobbe, X. Liu, and H. H. Farahani. Estimation of mass change trends in the Earth's system on the basis of GRACE satellite data, with application to Greenland. *Journal of Geodesy*, 87:69–87, 2013. doi:10.1007/s00190-012-0580-5.
- SILSO World Data Center. The international sunspot number. *International Sunspot Number Monthly Bulletin and online catalogue*, 1954-2024.
- N. Sneeuw and M. Van Gelderen. The polar gap. *Geodetic boundary value problems in view of the one centimeter geoid*, pages 559–568, 1997.
- N. Sneeuw, R. Dorobantu, C. Gerlach, J. Müller, H. Oberndorfer, R. Rummel, R. Koop, P. Visser, P. Hoyng, A. Selig, et al. Simulation of the GOCE gravity field mission. In *IV Hotine-Marussi symposium on mathematical geodesy*, pages 14–20. Springer, 2001. doi:10.1007/978-3-642-56677-6_5.
- C. C. Speake and P. L. Andrews. Capacitive sensing for drag-free satellites. *Classical and Quantum Gravity*, 14(6):1557–1565, June 1997. ISSN 0264-9381, 1361-6382. doi:10.1088/0264-9381/14/6/027.
- M. M. Srinivasan, M. Rodell, J. T. Reager, B. Doorn, and L. Rogers. Mass change mission applications-assessing user needs for the next NASA mass change designated observable (MCDO) mission. In *AGU Fall Meeting Abstracts*, volume 2019, pages G51B–0575, 2019.
- C. Stummer. *Gradiometer data processing and analysis for the GOCE mission*. PhD thesis, Technische Universität München, 2012.
- C. Stummer, C. Siemes, R. Pail, B. Frommknecht, and R. Floberghagen. Upgrade of the GOCE Level 1b gradiometer processor. *Advances in Space Research*, 49(4):739–752, 2012. doi:10.1016/j.asr.2011.11.027.
- T. J. Sumner, G. Mueller, J. W. Conklin, P. J. Wass, and D. Hollington. Charge induced acceleration noise in the LISA gravitational reference sensor. *Classical and Quantum Gravity*, 37(4):045010, 2020. doi:10.1088/1361-6382/ab5f6e.
- A. Y. Sun, B. R. Scanlon, A. AghaKouchak, and Z. Zhang. Using GRACE satellite gravimetry for assessing large-scale hydrologic extremes. *Remote Sensing*, 9(12):1287, 2017. doi:10.3390/rs9121287.
- B. D. Tapley, S. Bettadpur, M. Watkins, and C. Reigber. The Gravity Recovery and Climate Experiment: Mission overview and early results. *Geophysical research letters*, 31(9), 2004. doi:10.1029/2004GL019920.
- B. D. Tapley, M. M. Watkins, F. Flechtner, C. Reigber, S. Bettadpur, M. Rodell, I. Sasgen, J. S. Famiglietti, F. W. Landerer, D. P. Chambers, J. T. Reager, A. S. Gardner, H. Save, E. R. Ivins, S. C. Swenson, C. Boening, C. Dahle, D. N. Wiese, H. Dobslaw, M. E. Tamisiea, and I. Velicogna. Contributions of GRACE to understanding climate change. *Nature Climate Change*, 5(5):358–369, 2019. ISSN 1758-678X. doi:10.1038/s41558-019-0456-2.

- I. The MathWorks. *Second-Order Integrator Limited*. The MathWorks Inc., Natick, Massachusetts, United States, 2024a. URL <https://www.mathworks.com/help/simulink/slref/secondorderintegratorlimited.html>.
- I. The MathWorks. *Inverse fast Fourier transform*. The MathWorks Inc., Natick, Massachusetts, United States, 2024b. URL <https://www.mathworks.com/help/matlab/ref/ifft.html>.
- I. The MathWorks. *Variable Step Solvers in Simulink*. The MathWorks Inc., Natick, Massachusetts, United States, 2024c. URL <https://www.mathworks.com/help/simulink/ug/variable-step-solvers-in-simulink-1.html>.
- S. Theil. *Satellite and test mass dynamics modeling and observation for drag-free satellite control of the STEP mission*. PhD thesis, Department of Production Engineering, University of Bremen, 2002.
- A. Tikhonov. Regularization of incorrectly posed problems: Soviet math. In *Dokl*, volume 4, pages 1035–1038, 1963a.
- A. Tikhonov. O reshenii nekorektno postavlenykh zadach i metode regulyariizacii [Solution of Incorrectly Formulated Problems and the Regularized Method]. *Doklady Akademii Nauk SSSR [Doklady Mathematics]*, 151(3):501–504, 1963b.
- A. N. Tikhonov and V. Arsenin. Solutions of ill-posed problems. *VH Winston*, 1977.
- W. Torge, J. Müller, and R. Pail. *Geodesy*. De Gruyter Oldenbourg, 2023. doi:10.1515/9783110723304.
- P. Touboul, E. Willemenot, B. Foulon, and V. Josselin. Accelerometers for CHAMP, GRACE and GOCE space missions: synergy and evolution. *Boll. Geof. Teor. Appl*, 40(3-4):321–327, 1999.
- P. Touboul, B. Foulon, B. Christophe, and J. Marque. CHAMP, GRACE, GOCE instruments and beyond. In *Geodesy for Planet Earth: Proceedings of the 2009 IAG Symposium, Buenos Aires, Argentina, 31 August 31-4 September 2009*, pages 215–221. Springer, 2012. doi:10.1007/978-3-642-20338-1_26.
- P. Touboul, S. Metris, O. Le Traon, A. Bresson, N. Zahzam, B. Christophe, and M. Rodrigues. Gravitation and geodesy with inertial sensors, from ground to space. *AerospaceLab*, 12, 2016. doi:10.12762/2016.AL12-11.
- M. J. Tourian, J. T. Reager, and N. Sneeuw. The total drainable water storage of the Amazon river basin: A first estimate using GRACE. *Water Resources Research*, 54(5):3290–3312, 2018. ISSN 0043-1397. doi:10.1029/2017WR021674.
- A. Trimeche, B. Battelier, D. Becker, A. Bertoldi, P. Bouyer, C. Braxmaier, E. Charron, R. Corgier, M. Cornelius, K. Douch, et al. Concept study and preliminary design of a cold atom interferometer for space gravity gradiometry. *Classical and Quantum Gravity*, 36(21):215004, 2019. doi:10.1088/1361-6382/ab4548.

- M. Tröbs and G. Heinzel. Improved spectrum estimation from digitized time series on a logarithmic frequency axis. *Measurement*, 39(2):120–129, 2006. doi:10.1016/j.measurement.2005.10.010.
- M. van Camp, F. P. dos Santos, M. Murböck, G. Petit, and J. Müller. Lasers and ultracold atoms for a changing Earth. *Eos, Transactions American Geophysical Union*, 102, 2021. doi:10.1029/2021EO210673.
- M. van der Meijde, R. Pail, R. Bingham, and R. Floberghagen. GOCE data, models, and applications: a review. *International Journal of Applied Earth Observation and Geoinformation*, 35:4–15, 2015. doi:10.1016/j.jag.2013.10.001.
- M. van Lonkhuyzen, R. Klees, and J. Bouman. Regularization for the Gravity Field Recovery from GOCE Observations. In *Gravity, Geoid and Geodynamics 2000: GGG2000 IAG International Symposium Banff, Alberta, Canada July 31–August 4, 2000*, pages 117–122. Springer, 2002. doi:10.1007/978-3-662-04827-6_19.
- P. Visser. GOCE gradiometer: estimation of biases and scale factors of all six individual accelerometers by precise orbit determination. *Journal of Geodesy*, 83(1):69–85, 2009. doi:10.1007/s00190-008-0235-8.
- P. N. A. M. Visser and J. A. A. van den IJssel. Calibration and validation of individual GOCE accelerometers by precise orbit determination. *Journal of Geodesy*, 90:1–13, 2016. doi:10.1007/s00190-015-0850-0.
- J. Wahr, M. Molenaar, and F. Bryan. Time variability of the Earth’s gravity field: Hydrological and oceanic effects and their possible detection using GRACE. *Journal of Geophysical Research: Solid Earth*, 103(B12):30205–30229, 1998. doi:10.1029/98JB02844.
- G. Wanner. Space-based gravitational wave detection and how LISA Pathfinder successfully paved the way. *Nature Physics*, 15(3):200–202, 2019. ISSN 1745-2481. doi:10.1038/s41567-019-0462-3.
- W. J. Weber, D. Bortoluzzi, P. Bosetti, G. Consolini, R. Dolesi, and S. Vitale. Application of LISA gravitational reference sensor hardware to future intersatellite geodesy missions. *Remote Sensing*, 14(13):3092, 2022. doi:10.3390/rs14133092.
- H. Wegener, V. Müller, G. Heinzel, and M. Misfeldt. Tilt-to-length coupling in the GRACE Follow-On laser ranging interferometer. *0022-4650*, pages 1–10, 2020. ISSN 0022-4650. doi:10.2514/1.A34790.
- M. Weigelt. *The acceleration approach*, pages 97–126. Springer, 2017. doi:10.1007/978-3-319-49941-3_4.
- P. L. Whitehouse, N. Gomez, M. A. King, and D. A. Wiens. Solid Earth change and the evolution of the Antarctic Ice Sheet. *Nature communications*, 10(1):503, 2019. doi:10.1038/s41467-018-08068-y.
- D. N. Wiese, W. Folkner, and R. Nerem. Alternative mission architectures for

- a gravity recovery satellite mission. *Journal of Geodesy*, 83:569–581, 2009. doi:10.1007/s00190-008-0274-1.
- D. N. Wiese, B. Bienstock, C. Blackwood, J. Chrone, B. D. Loomis, J. Sauber, M. Rodell, R. Baize, D. Bearden, K. Case, S. Horner, S. Luthcke, J. T. Reager, M. Srinivasan, L. Tsaoussi, F. Webb, A. Whitehurst, and V. Zlotnicki. The mass change designated observable study: overview and results. *Earth and Space Science*, 9(8):e2022EA002311, 2022. doi:10.1029/2022EA002311.
- S. Williams, P. Moore, M. A. King, and P. L. Whitehouse. Revisiting GRACE Antarctic ice mass trends and accelerations considering autocorrelation. *Earth and Planetary Science Letters*, 385:12–21, 2014. doi:10.1016/j.epsl.2013.10.016.
- F. Wöske. *Gravity field recovery from GRACE satellite data and investigation of sensor, environment and processing-option influences by closed loop mission simulation*. PhD thesis, University of Bremen, 2021.
- F. Wöske, T. Kato, M. List, and B. Rievers. Development of a high precision simulation tool for gravity recovery missions like GRACE. In R. Zanetti, R. Russel, M. Ozimek, and A. Bowes, editors, *Proceedings of the 26th AAS/AIAA space flight mechanics meeting held February*, volume 158, pages 2445–2457, 2016.
- F. Wöske, T. Kato, B. Rievers, and M. List. GRACE accelerometer calibration by high precision non-gravitational force modeling. *Advances in Space Research*, 63(3):1318–1335, 2018. ISSN 02731177. doi:10.1016/j.asr.2018.10.025.
- B. Wouters, J. A. Bonin, D. P. Chambers, R. E. Riva, I. Sasgen, and J. Wahr. GRACE, time-varying gravity, Earth system dynamics and climate change. *Reports on Progress in Physics*, 77(11):116801, 2014. doi:10.1088/0034-4885/77/11/116801.
- B. Wouters, A. S. Gardner, and G. Moholdt. Global glacier mass loss during the GRACE satellite mission (2002-2016). *Frontiers in earth science*, 7:96, 2019. doi:10.3389/feart.2019.00096.
- H. Wu. *Gravity field recovery from GOCE observations*. PhD thesis, Wissenschaftliche Arbeiten der Fachrichtung Geodäsie und Geoinformatik der Leibniz Universität Hannover; ISSN 0174-1454, Nr. 324, 2016.
- Y. Xiao, Y. Yang, Z. Pan, X. Liu, and Z. Sun. Performance and application of the Chinese satellite-to-satellite tracking gravimetry system. *Chin. Sci. Bull.*, 68:2655–2664, 2023. doi:10.1360/TB-2022-1057.
- W. Yi. *The Earth’s gravity field from GOCE*. PhD thesis, Technische Universität München, 2012.
- N. Zahzam, B. Christophe, V. Lebat, E. Hardy, P.-A. Huynh, N. Marquet, C. Blanchard, Y. Bidel, A. Bresson, P. Abrykosov, et al. Hybrid electrostatic–atomic accelerometer for future space gravity missions. *Remote Sensing*, 14(14):3273, 2022. doi:10.3390/rs14143273.
- J. Zhang, W. You, B. Yu, and D. Fan. GRACE-FO accelerometer performance

- analysis and calibration. *GPS Solutions*, 27(4):158, 2023. doi:10.1007/s10291-023-01487-5.
- P. Zingerle, T. Gruber, R. Pail, and I. Daras. Constellation design and performance of future quantum satellite gravity missions. *Earth, Planets and Space*, 76(1):101, 2024. doi:10.1186/s40623-024-02034-3.
- A. Zoellner, S. Tan, S. Saraf, A. Alfauwaz, D. DeBra, S. Buchman, and J. A. Lipa. Differential optical shadow sensor for sub-nanometer displacement measurement and its application to drag-free satellites. *Optics Express*, 25(21):25201–25211, 2017. doi:10.1364/OE.25.025201.
- L. Zotov, C. Bizouard, C. Shum, C. Zhang, N. Sidorenkov, and V. Yushkin. Analysis of Earth’s polar motion and length of day trends in comparison with estimates using second degree stokes coefficients from satellite gravimetry. *Advances in Space Research*, 69(1):308–318, 2022. doi:10.1016/j.asr.2021.09.010.

Wissenschaftliche Arbeiten der Fachrichtung Geodäsie und Geoinformatik der Leibniz Universität Hannover

(Eine vollständige Liste der Wiss. Arb. ist beim Geodätischen Institut, Nienburger Str. 1, 30167 Hannover erhältlich.)

- Nr. 378 MEHLTRETTER, Max: Uncertainty Estimation for Dense Stereo Matching using Bayesian Deep Learning (Diss. 2021)
- Nr. 379 KAZIMI, Bashir: Self Supervised Learning for Detection of Archaeological Monuments in LiDAR Data (Diss. 2021)
- Nr. 380 PETERS, Torben: Learning Multi-View 2D to 3D Label Transfer for Semi-Supervised Semantic Segmentation of Point Clouds (Diss. 2022)
- Nr. 381 WASSINK, Martin: Kommunal- und Regionalentwicklung durch Kooperation und Teilung von Verantwortung in ländlichen Räumen - eine multiperspektivische Untersuchung an Beispielen aus dem Raum Steinwald/Fichtelgebirge (Diss. 2022)
- Nr. 382 GOLDSCHMIDT, Jürgen: Die Berücksichtigung künftiger Entwicklungen bei der Verkehrswertermittlung (Diss. 2022)
- Nr. 383 KRUSE, Christian: Impact maps from bomb craters detected in aerial wartime images using marked point processes (Diss. 2023)
- Nr. 384 ZOURLIDOU, Stefania: Traffic Regulation Recognition from GPS Data (Diss. 2023)
- Nr. 385 SLEDZ, Artuom: Thermal anomaly detection based on information fusion from optical and infrared images (Diss. 2023)
- Nr. 386 WITTICH, Dennis: Deep Domain Adaptation for the Pixel-wise Classification of Aerial and Satellite Images (Diss. 2023)
- Nr. 387 SINGH, Vishwa Vijay: Lunar Laser Ranging - Improved Modelling and Parameter Estimation (Diss. 2023)
- Nr. 388 HARTMANN, Jens: Hochgenaue 3D-Erfassung von Großstrukturen durch kinematisches terrestrisches Laserscanning (Diss. 2023)
- Nr. 389 ZHUGE, Xia: Characterizing slope instability kinematics by integrating multi-sensor satellite remote sensing observations (Diss. 2023)
- Nr. 390 DOROZYNSKI, Mareike Marianne: Image Classification and Retrieval in the Context of Silk Heritage using Deep Learning (Diss. 2023)
- Nr. 391 KNABE, Annike: New Concepts for Gravity Field Recovery using Satellites (Diss. 2023)
- Nr. 392 KALIA, Andre: Landslide activity detection based on nationwide Sentinel-1 PSI datasets (Diss. 2023)
- Nr. 393 BROCKMEYER, Marco: Modellierung von Bodenbewegungen anhand heterogener Messverfahren am Beispiel der niedersächsischen Landesfläche (Diss. 2023)
- Nr. 394 ZHANG, Mingyue: Characteristics and Benefits of Differential Lunar Laser Ranging (Diss. 2023)
- Nr. 395 DENNIG, Dirk: Entwicklung eines kinematischen Profilvermessungssystems am Beispiel Kranbahnvermessung (Diss. 2024)
- Nr. 396 FUEST, Stefan: Nudging travelers to societally favorable routes by means of cartographic symbolization (Diss. 2024)
- Nr. 397 MOFTIZADEH, Rozhin: Advanced Particle Filtering for Vehicle Navigation based on Collaborative Information (Diss. 2024)
- Nr. 398 VASSILEVA, Magdalena Stefanova: Satellite Radar Interferometry for Geohazards: from ground deformation to processes understanding (Diss. 2024)
- Nr. 399 MALINOVSKAYA, Anna: Statistical Process Monitoring of Networks (Diss. 2024)
- Nr. 400 BANNERT, Jörn: Der Einfluss von Straßenverkehrslärm und Umgehungsstraßen auf Grundstückswerte in Ortslagen - Bestimmung mittels Expertenbefragung nach der Delphi-Methode (Diss. 2024)
- Nr. 401 AXMANN: Jeldrik: Maximum consensus localization using LiDAR (Diss. 2024)
- Nr. 402 TENNSTEDT, Benjamin: Concept and Evaluation of a Hybridization Scheme for Atom Interferometers and Inertial Measurement Units (Diss. 2024)
- Nr. 403 HAKE, Frederic: Schadenserkenkung an Bauwerken mittels maschinellem Lernens (Diss. 2025)
- Nr. 404 KARIMIDOONA, Ali: On Integrity Prediction for Network-RTK Positioning in Urban Environments (Diss. 2025)
- Nr. 405 ORTEGA, Mabel: Domain Adaptation for Deforestation Detection in Remote Sensing: Addressing Class Imbalance and Performance Estimation (Diss. 2025)

